Fast Multi-Photon Single-Qubit Operations in Arrays of Strontium Atoms

Maximilian Ammenwerth

SIGILL. UNIVERSITAT. LUDOVIC. MAXIM.

München 2026

Fast Multi-Photon Single-Qubit Operations in Arrays of Strontium Atoms

Maximilian Ammenwerth

Dissertation
an der Fakultät für Physik
der Ludwig-Maximilians-Universität
München

vorgelegt von

Maximilian Ammenwerth

geboren in Münster

München, den 20. Januar 2026

Erstgutachter:
Prof. Dr. Immanuel Bloch

Zweitgutachter:
Prof. Dr. Sebastian Hofferberth

Tag der mündlichen Prüfung:
9. März 2026

Zusammenfassung

Neutrale Atome bilden eine vielseitige Plattform für Quantensimulations-, Quantencomputing und Metrologie-Anwendungen und sind für verschiedene atomare Spezies etabliert. Die elektronischen Zustände werden hierbei mit Hilfe von Laserpulsen kontrolliert, welche oftmals auf dem Ein-Teilchen-Level angewandt werden. Diese Arbeit umfasst die schnelle Kontrolle von langlebigen Uhrenzuständen in Strontium basierend auf kohärenten Drei-Photon-Übergängen. Verglichen mit der direkten Ein-Photon-Anregung wird hierbei eine deutlich schnellere Rabifrequenz bei deutlich schwächeren Magnetfeldern erreicht. Durch Anlegen eines Magnetfeldes unter einem bestimmten Winkel in Bezug zur linearen Polarisation der optischen Pinzetten wird ein optisches Qutrit realisiert, welches neben dem Grundzustand $^1\mathrm{S}_0$ beide Uhrenzustände $^3\mathrm{P}_0$ und $^3\mathrm{P}_2$ umfasst. Eine detaillierte Charakterisierung der Kohärenz des Feinstrukturqubits (bestehend aus den Zuständen $^3\mathrm{P}_0$ und $^3\mathrm{P}_{2,m_j=0}$) zeigt eine bemerkenswerte Kohärenzzeit von $715(30)$ ms. Diese Demonstration zeigt, dass kompetitive Kohärenzzeiten auch in Potentialen auf Basis von optischen Pinzetten erreicht werden können, trotz der Existenz von Polarisationsgradienten und der Polarisationsabhängigkeit des Potentials. Die Güte der Zwei- und Drei-Photon-Kopplungen ist aktuell durch optisches Phasenrauschen limitiert und zutreffende Methoden zur Charakterisierung, Modellierung und Unterdrückung von optischem Phasenrauschen werden im Details diskutiert. Einzeln adressierbare Atome in optischen Potentialen haben in den letzten Jahren eine umfassende und schnelle Entwicklung hinsichtlich der Systemgrößen, Gattergüten und kohärenten "Mid-Circuit" Operationen erlebt. Eine zentrale Herausforderung im Kontext von Neutralatom-Quantencomputern besteht in der weiteren Skalierung bei gleichzeitiger Erhaltung der Adressierbarkeit. Die Kombination von skalierbaren optischen Gitterpotentialen mit der Einzelplatzkontrolle durch bewegliche optische Pinzetten eröffnet hier neue Möglichkeiten welche in dieser Arbeit beschrieben und demonstriert werden. Wir zeigen, dass einzelne Atome in einer einzelnen Ebene eines zwei-dimensionalen optischen Gitters, geladen direkt aus einer Magneto-optischen Falle, mit Hilfe von optischen Pinzetten in beliebige Konfigurationen sortiert werden können. Des Weiteren präsentieren wir ein Protokoll für das iterative Sortieren von Atomarrays und demonstrieren den kontinuierlichen Dauerbetrieb in dem Gitterpotential. Diese Techniken umgehen Skalierungslimitierungen indem Atome über mehrere Ladezyklen erhalten bleiben und eröffnen völlig neue Möglichkeiten zum Betrieb von Atomarrays. Um eine schnelle Bildverarbeitung zu gewährleisten stellen wir einen Machine-Learning-Algorithmus basierend auf einem Faltungsnetzwerk vor und demonstrieren die schnelle Rekonstruktion des gesamten optischen Gitters und eine reduzierte Abhängigkeit auf Rauschen der Eingangsbilder. Abschließend stellen wir einen neuartigen Phasenmodulator basierend auf einer Senkspiegelmatrix vor, welcher neue Möglichkeiten zur holografischen Strahlformung mit schnellen Updateraten eröffnet und mit Wellenlängen bis in den ultravioletten Bereich kompatibel ist.

Abstract

Neutral atoms are a ubiquitous platform for various quantum sciences with applications in quantum computing, simulation, and metrology across many different atomic species. In these systems, control over the electronic states is given by suitable laser pulses typically applied at the single-particle level. Here, we present fast coherent control over the meta-stable clock states in bosonic strontium-88 using two- and three-photon couplings. Compared to the direct single-photon drive on these transitions, the realistically achievable Rabi frequencies are substantially higher at significantly relaxed magnetic field strength. By applying a magnetic quantization axis under a judiciously chosen angle with respect to the linear trap polarization, we realize an optical qutrit comprising the ground state $^1S_0$ as well as both clock states $^3P_0$ and $^3P_2$, and characterize in detail the coherence of the system. Remarkably, the observed coherence time on the fine-structure qubit (given by the $^3P_0$ and $^3P_{2,m_j=0}$ states) of $715(30)$ ms demonstrates, for the first time, that state-of-the-art coherences times are compatible with tweezer-based polarizability-engineered trapping potentials, which is applicable across a broad range of wavelength and atomic species. We identify laser phase noise as the main limitation of the current operation fidelity and discuss methods for characterizing, modelling, and compensating optical phase noise. The multi-photon couplings not only allow for substantially faster Rabi frequencies under realistic experimental conditions, but additionally offer controlled dissipation via the $^3P_1$ state, which we use to demonstrate a measurement-free qubit reset. Combined with three-photon couplings to the $^3P_2$ clock state, we realize resolved sideband cooling in an optical lattice potential and benchmark the fine-structure qubit at various infrared wavelengths. In addition, we introduce a hybrid lattice-tweezer setup and demonstrate the preparation of programmable atom configurations in a single plane of the two-dimensional optical lattice potential. Using single-site addressing with optical tweezers, we present a protocol for the iterative assembly of large-scale atom arrays. Furthermore, we use the lattice-tweezer combination to continuously operate a configurable atom array, which provides means to overcome scaling limitations by repeatedly adding atoms to the system and enables entirely novel approaches to operating neutral-atom arrays. To enable reliable image processing with a fast reconstruction of the lattice occupation, we introduce a novel algorithm based on a convolutional neural network, which provides a rapid and noise-resilient reconstruction compatible with arbitrary lattice geometries. Moreover, we benchmark a new phase-only spatial light modulator based on a micromirror array, which paves the way towards holographic beam shaping at fast update rates compatible with a broad range of wavelengths, including the ultraviolet spectral range.

Contents

To my family

Chapter 1

Introduction

1.1 Applications of neutral atoms in quantum sciences

Neutral atoms are a versatile and ubiquitous platform for quantum simulation [1–6], quantum computing [7–10] and metrology applications [11–13]. Trapped in optical lattices, the coherent tunneling of atoms in the periodic potential can be used to realize the Hubbard model, and access to the single-site density is given by established quantum gas microscopy techniques [14–18]. Complementary to this approach, arrays of optical tweezers provide highly configurable potentials, which can be used, for example, to study spin models based on long-range Rydberg interactions [19–22]. Besides analog quantum simulation applications, atomic ensembles controlled at the single-particle level are a powerful platform for quantum computing [23–25]. Various species have been explored, and universal gate sets have been demonstrated as well as first realizations of error-corrected logical qubits [26–28]. Additionally, the ultranarrow linewidth of selected atomic transitions enables precision time keeping using atomic clocks [29–33].

1.1.1 Analog quantum simulation

Hubbard simulators The (Fermi) Hubbard model (FHM) is a central tool for our understanding of the properties of electrons in materials and covers a variety of interesting quantum mechanical phases. To overcome the limitations of exact numerical simulations of fermionic systems, quantum simulators have been invented, which make use of neutral atoms in optical lattices to study the FHM in regimes challenging for classical computers [1, 34]. Early experiments in the field observed the phase transition of a superfluid state to a Mott-insulating state, using bosonic atoms, by probing the phase coherence of an atomic ensemble after time-of-flight expansion [35]. Direct access to the site-resolved atom density, for bosonic as well as fermionic species, was demonstrated by quantum gas microscopes using high-resolution imaging techniques [36–38]. The simultaneous readout of density and internal spin state allows for the extraction of spin-charge-resolved correlation functions [39, 40], and anti-ferromagnetic long-range order was detected in a repulsively interacting Fermi gas [41]. Using the spin- and density-resolved detection, the coherent delocalization of a single hole within an antiferromagnetic background was characterized, which gives rise to the formation of magnetic polarons [42, 43]. These quasiparticles locally distort the spin background, which affects their mobility [44, 45]. Analog quantum simulation performed by quantum gas microscopes is thus a powerful tool to test our understanding of the Hubbard model in highly controllable setups [46, 47]. Despite the significant experimental progress in preparing, controlling, and detecting individual atoms, the main bottleneck lies in the accessible temperatures of the ensembles. Considering the optical lattice material analogs, the achievable temperatures are typically far above room temperature, and following Ref. [48] correspond to about 700 K for the cuprates, far too high to uncover their superconducting properties [49]. Recently, significant progress towards the preparation of cold ensembles was demonstrated [48], which offers access to probe the physics of the FHM beyond the reach of numerical tools [50].

Furthermore, extended versions of the Hubbard model can be realized by utilizing long-range interactions based on Rydberg or molecular dipolar interactions enabling a variety of quantum-simulation experiments [51–57].

Rydberg-tweezer-based many-body simulators In addition to lattice-based systems, neutral atoms are often used in combination with optical tweezer arrays, which provide programmable trap configurations in one, two, and three spatial dimensions [58–60]. Combined with long-range Rydberg interactions, these setups offer a powerful platform for the analog simulation of Ising-type spin models [20, 21, 61], topological phases [62, 63], atomic clocks [29], optimization tasks [64], anisotrophic XYZ models [65, 66], lattice gauge theories [67–69] and more.

1.1.2 Digital quantum computing

Neutral-atom-based quantum computing has recently experienced tremendous progress and qubits have been realized in several alkali [23, 70] and alkaline-earth-like species [31, 71, 72] using different qubit implementations [73, 74] and universal gate sets have been demonstrated [75, 76]. In these systems, single atoms are trapped in optical tweezer arrays and individually addressed, either in stationary setups [77] or in combination with mobile tweezers to coherently shuttle atoms [24, 78] for enhanced connectivity. Compared to other platforms, the distinct advantage of the neutral-atom platform is given by the excellent scalability, and the state of the art nowadays comprises several 1000 coherently controlled qubits [25, 70, 79], which can be addressed at the single-particle level. Recently, the mid-circuit readout of atomic qubits was demonstrated in several setups [27, 73, 80–83], based on rapid fluorescense imaging of ancilla atoms [75, 84, 85] and supported by dual species setups [86] to minimize cross talk or based on metastable qubits in alkaline-earth atoms. Realizing the computational subspace outside the electronic ground state offers the additional advantage of (mid-circuit) erasure detection [87–89], to detect leakage errors, which is beneficial for quantum error correction codes [90–92]. First realizations of logical qubits have been demonstrated with neutral atoms [26, 93] (and also other platforms [94]) and introduce the era of logical quantum processors. Recently, the continuous operation of atom arrays was demonstrated, which provides the means of handling the inevitable atom loss by coherently replacing data qubits and ancillas [25, 95–97]. Combined with above-threshold gate fidelities this opens up the exciting perspective of high-fidelity logical operations [26, 94] in universally programmable machines with parameters beyond the capability of modern supercomputers and requires further optimized setups and tailored error correction codes [91, 98, 99]. To satisfy the need for physical qubits in logical architectures, future neutral-atom-based quantum processors might be based on interconnected modules [100, 101].

1.1.3 Metrology

Besides quantum computing and simulation applications, the ultranarrow transitions in neutral atoms are perfect systems for realizing clocks and provide the most precise and accurate measurements of time [11] with uncertainties corresponding to less than a second over the entire lifetime of the universe of 13.8 billion years. Owing to enormous progress in laser development and their frequency stabilization, modern atomic clocks operate close to the standard quantum limit [12, 13, 102]. Considering an idealized system where the laser frequency is stabilized to an atomic resonance via Ramsey spectroscopy, the fractional stability $\sigma_N(\tau)$ for a Ramsey dark time T and averaging duration τ is given by (1.1). Here, ω_{eg} corresponds to the transition frequency, N denotes the number of atoms, and the scaling $\sigma_N \propto \frac{1}{\sqrt{N}}$ is known as the standard quantum limit (SQL) [11].

$$\sigma_N(\tau) = \frac{1}{\omega_{eg}\sqrt{N\,T\,\tau}} \tag{1.1}$$

To realize a low fractional uncertainty, experiments thus aim to maximize the atom number and the interrogation duration. However, the ability of single-site control in tweezer clocks opens up new possibilities of utilizing entangled quantum states in metrological applications. For certain metrologically useful states [103–105] the clock stability can be substantially improved $\sigma_N \to \xi\sigma_N$ approaching the Heisenberg limit $\xi \propto \frac{1}{\sqrt{N}}$ [32, 106–108]. Similarly, the sensitivity of the LIGO gravitational wave detector is improved using vacuum-squeezed photon states [109]. Generating suitable entangled states is often discussed via the one-axis twisting (OAT) Hamiltonian $H \propto J_z^2$ with the collective spin operator $J_z = \frac{1}{2}\sum_i \sigma_z^{(i)}$. Here, the Pauli matrix $\sigma_z^{(i)}$ acts on the i-th atom and infinite-range interactions are required to accurately realize this Hamiltonian, which was demonstrated with cavity-mediated interactions [110]. Similarly, OAT-like interactions can be realized for atom arrays using Rydberg interactions [111]. Here, Rydberg dressing, the off-resonant coupling to the highly-excited Rydberg state, can be used to induce long-range interactions at prolonged lifetimes and gives rise to an Ising-type Hamiltonian [19]. For Rydberg blockade radii smaller than the system size, the interaction is not OAT-like; however, Rydberg-mediated interactions nonetheless give rise to entangled states, and metrologically useful states can be generated following various proposals [103–105, 112, 113].

1.2 Preparation of atom arrays in optical lattices and tweezers

Historically, neutral atoms have been prepared in the context of quantum simulation applications by initially loading atoms into a trapping potential and cooling the atomic gas to quantum degeneracy by means of evaporative cooling, either in magnetic or optical traps [114, 115]. In this case, a Bose-Einstein condensate or degenerate Fermi gas is subsequently loaded into an optical lattice, and an ensemble with one atom per site can be realized [116] for suitably tuned tunneling rate and on-site interaction. This *top down* approach exploits the self-assembly of atoms in Hubbard-regime lattices and large-scale systems can be realized for several atomic species [36, 37, 55, 117–120].

Complementary to this approach, optical tweezer systems became a powerful platform for quantum simulation and computing applications [19–28]. Here, the distribution of the number of atoms loaded from a magneto-optical trap is typically Poissonian, and the ensemble is projected onto either zero or one atom per site via light-assisted collisions that give rise to pair-wise atom loss. The distribution of filled sites in the tweezer array is, therefore, probabilistic with a typical filling fraction of approximately 50 % unless enhanced loading schemes are utilized [72, 121]. In order to deterministically prepare atom arrays in these systems, active resorting protocols are used, where the ensemble is initially imaged nondestructively to allow for the subsequent rearrangement of atoms using mobile optical tweezers, typically controlled with acousto-optic deflectors [20, 58, 59]. In this *bottom up* assembly, arbitrary atom configurations in two or even three spatial dimensions can be prepared [60, 122] and continuously operated [25, 95–97].

Recently, the single-site control of optical tweezers was applied to rearrange atoms in an optical lattice potential to generate configurable starting conditions for quantum walk experiments [123]. Combining the single-site control of optical tweezers with the scalability of optical lattices offers new possibilities for the generation of scalable atom arrays [96].

1.3 This thesis

This thesis presents building blocks for generating large-scale atom arrays of strontium in optical lattice and tweezer potentials, which offer new approaches to scaling up neutral atom arrays for applications in quantum simulation, computing, or metrology. In addition, we realize an optical qutrit, demonstrate a state-of-the-art coherence time in the engineered trapping potentials, and characterize fast three-photon-based manipulations of the long-lived clock states.

Outline

In Chapter 2 we introduce our hybrid lattice-tweezer experiment and discuss the most important properties of strontium. In particular, we give an overview of the rich level structure of strontium and estimate the polarizability of the electronic states for various optical trapping potentials. Throughout the thesis, we will often encounter tailored trapping conditions, where we make use of sufficiently strong magnetic fields applied under specific angles with respect to the linearly polarized light field in order to suppress differential light shifts on certain transitions. This chapter contains a discussion of engineered trapping potentials and introduces the toolbox offered by our experiment.

In Chapter 3, this is applied to the creation and detailed characterization of an optical qutrit in strontium-88, which contains the electronic ground state $^1S_0$, as well as both meta-stable clock states $^3P_0$ and $^3P_2$, separated by optical transition frequencies. Using phase-coherent two- and three-photon transitions, we realize optical control over all qutrit states and carry out a detailed characterization of the coherence times. Remarkably, we experimentally demonstrate state-of-the-art coherence times on the fine-structure qubit, which are en-par with alkali-based qubit systems, using XY-4 dynamical decoupling sequences. We characterize the effect of polarization gradients across the tweezer array and provide a detailed discussion of techniques suitable for the characterization, modelling and suppression of laser phase noise, which is the main limitation so far.

In Chapter 4 we present high-fidelity and low-loss imaging of strontium atoms in a scalable optical lattice setup using the repulsive Sisyphus cooling mechanism. Combined with stationary and mobile optical tweezer potentials, we demonstrate the repeated transfer of atoms between the trapping potentials and introduce a protocol for an iteratively assembled atom array in optical lattices. This provides the means to continuously operate atomic arrays with programmable shape and overcomes scaling bottlenecks in atom-array setups. We demonstrate resolved sideband cooling in the lattice potential based on a three-photon transition to the long-lived $^3P_2$ clock state.

In Chapter 5, a fast and noise-resilient atom detection algorithm based on a deep convolutional neural network is presented. We introduce a new algorithm, which is compatible with arbitrary lattice geometries and characterize its performance, reaching a full-frame lattice reconstruction with 30.000 sites in 15 ms.

In Chapter 6, we introduce a new type of phase-only spatial light modulator based on micromirror arrays, which extends the applicability of holographic beam shaping into the ultraviolet spectral range and opens interesting perspectives towards dynamic and parallelized light modulation, for example, for parallel rearrangement of atoms along arbitrary trajectories.

We conclude in Chapter 7 and present a short outlook on several exciting directions for future experiments.

1.4 Publications

The following articles have been published in the context of this thesis.

- **High-Fidelity Detection of Large-Scale Atom Arrays in an Optical Lattice**
  Renhao Tao*, Maximilian Ammenwerth*, Flavien Gyger*, Immanuel Bloch, and Johannes Zeiher
  Phys. Rev. Lett. **133**, 013401 (2024).
  * contributed equally

- **Continuous operation of large-scale atom arrays in optical lattices**
  Flavien Gyger, Maximilian Ammenwerth, Renhao Tao, Hendrik Timme, Stepan Snigirev, Immanuel Bloch, and Johannes Zeiher
  Phys. Rev. Research **6**, 033104 (2024).

- **Realization of a Fast Triple-Magic All-Optical Qutrit in ^{88}Sr**
  Maximilian Ammenwerth, Hendrik Timme, Flavien Gyger, Renhao Tao, Immanuel Bloch, and Johannes Zeiher
  Phys. Rev. Lett. **135**, 143401 (2025).

- **Dynamical spatial light modulation in the ultraviolet spectral range**
  Maximilian Ammenwerth*, Hendrik Timme*, Veronica Giardini, Renhao Tao, Flavien Gyger, Ohad Lib, Dirk Berndt, Dimitrios Kourkoulos, Tim Rom, Immanuel Bloch, and Johannes Zeiher
  Phys. Rev. Applied **24**, 034031 (2025)
  * contributed equally

The following article has appeared as a pre-print.

- **Universal gates for a metastable qubit in strontium-88**
  Renhao Tao, Ohad Lib, Flavien Gyger, Hendrik Timme,
  Maximilian Ammenwerth, Immanuel Bloch, and Johannes Zeiher
  arXiv:2506.10714 (2025).

Chapter 2

A hybrid lattice-tweezer quantum gas microscope

To carry out experiments with neutral atoms, methods and procedures have been developed to trap, cool and control individual atoms in table-top experiments using light [124–126]. Early research in the field of atomic, molecular and optical (AMO) physics has established laser cooling and trapping techniques [127, 128] of bulk atomic gases and building on decades of research we can nowadays detect and control atom arrays at the single particle level [58, 59, 129, 130]. In this chapter, we present the experimental apparatus and summarize the most important laser systems to realize the single-site control. In addition, the properties of the optical trapping potentials are discussed, and suitable laser cooling techniques are summarized.

2.1 Level structure of strontium

The level structure of strontium, shown in Fig. 2.1, contains several transitions making it an intriguing candidate for quantum computing and simulation as well as metrology applications [131, 132]. Due to the presence of two valence electrons, the level structure partitions into a singlet and triplet subspace. This gives rise to fast transitions within each subspace and slow, narrow transitions connecting them. The 461 nm transition with a linewidth of approximately 31 MHz enables fast high-resolution imaging, and is used in the first stage of magneto-optical trapping. This transition is not entirely closed, and atoms may decay to the $^1\mathrm{D}_2$ state with a probability of approximately $1 : 50000$, from where they populate the long-lived $^3\mathrm{P}_2$ clock state [133, 134]. To repump atoms back into the cooling cycle, we apply beams at 707 nm and 679 nm. This transfers the population into the $^3\mathrm{P}_1$ state from where the atoms decay further to the ground state.

In addition to the stable ground state, strontium features two metastable clock states $^3\mathrm{P}_0$ and $^3\mathrm{P}_2$, which have versatile use cases for quantum computing, simulation, and metrology applications. For example, the ultranarrow $^1\mathrm{S}_0 \leftrightarrow {}^3\mathrm{P}_0$ transition at 698 nm is used for ultraprecise atomic clocks and can be used to implement a qubit [31, 32, 135]. Chapter 3 provides a detailed discussion of an optical qutrit encoded in the ground and both clock states, and presents all-to-all control realized via two- and three-photon transitions. Considering a subset of this qutrit, given by the two

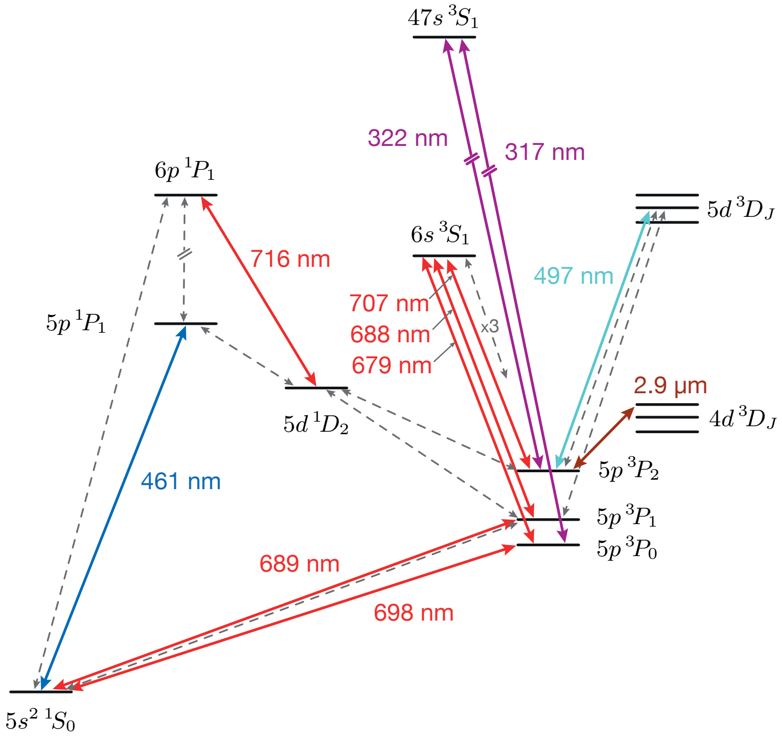

Figure 2.1: Strontium-88 level diagram. The wavelengths relevant for this work are shown, where arrows denote a laser resonant with the respective transition. For optical pumping, we exploit that atoms decay from higher-lying states. The relevant decay channels used for that purpose are shown and other decay channels are suppressed for simplicity. In addition to the $^1S_0$ ground state, bosonic strontium offers two meta-stable clock states, $^3P_0$ and $^3P_2$.

clock-states alone, realizes the so-called fine-structure (FS) qubit in strontium, for which we have demonstrated a universal gate set [75, 136]. Here, the two-qubit gates make use of a direct single-photon excitation from the clock states to Rydberg states in order to implement a controlled phase (CZ) gate. In comparison to alkali atoms, where two-photon excitations to Rydberg S-states are used [137], the direct single photon excitation sidesteps imperfections such as off-resonant scattering and strong light shifts associated with the intermediate state. To implement a state-resolved detection of the FS states, we sequentially repump and image them [75]. This makes use of a repumper at 497 nm to repump $^3P_2$ atoms into the ground state.

To cool atoms within the optical potentials, we use the narrow intercombination line at 689 nm with a linewidth of 7.4 kHz. This linewidth is well below the typical trap-induced differential light shift, enabling multiple laser cooling techniques, which are discussed in Section 2.1.3.

2.1.1 Polarizability

Controlling arrays of neutral atoms relies on trapping them in far-off-resonant dipole traps. Precise knowledge of the trapping potential is required to assess the feasibility of measurements and estimate the scalability of realistic experimental setups. In this section, we calculate the atomic polarizability [134, 138–140].

The potential U generated by an optical trapping potential is proportional to the spatially-dependent intensity I, and is characterized by the state-dependent polarizability α_{SI}, which is determined by the wavelength of the trapping light.

$$U = -\frac{\alpha_{SI}}{2c\epsilon_0} \cdot I$$

Here, c denotes the speed of light and ϵ_0 denotes the vacuum permittivity. It is common to express the polarizability in atomic units $\alpha_{AU} = \alpha_{SI}/4\pi\epsilon_0 a_0^3$, where a_0 denotes the Bohr-radius, and in the following we will quote polarizabilities in atomic units. Optical dipole trapping relies on the off-resonant interaction of the light field with the atomic dipole moment and the resulting polarizability can be computed as a sum over all such couplings for all relevant atomic transitions. For a trapping light frequency ω and electronic state Φ_0 with energy E_0 and dipole matrix element D_0, the bare scalar α_0 (2.1), bare vector α_1 (2.2) and the bare tensor polarizability α_2 (2.3) are defined as:

$$\alpha_0(\omega) = \frac{2}{3(2j+1)} \sum_k \frac{(E_k - E_0)|\langle \Phi_0 | D_0 | \Phi_k \rangle|^2}{(E_k - E_0)^2 - \omega^2} \tag{2.1}$$

$$\begin{aligned} \alpha_1(\omega) = &- \sqrt{\frac{6j}{(j+1)(2j+1)}} \sum_{n',l',j'} (-1)^{j+j'+1} \begin{Bmatrix} j & 1 & j' \\ 1 & j & 1 \end{Bmatrix} |\langle \Phi_0 | D_0 | \Phi_{n,l,j} \rangle|^2 \\ &\times \left(\frac{1}{(E_{n,l,j} - E_0) - \omega} - \frac{1}{(E_{n,l,j} - E_0) + \omega} \right) \end{aligned} \tag{2.2}$$

$$\alpha_2(\omega) = 4\sqrt{\frac{5j(2j-1)}{6(j+1)(2j+1)(2j+3)}} \sum_{n',l',j'} (-1)^{j+j'} \begin{Bmatrix} j & 1 & j' \\ 1 & j & 2 \end{Bmatrix} \frac{(E_{n,l,j} - E_0)|\langle \Phi_0 | D_0 | \Phi_{n,l,j} \rangle|^2}{(E_{n,l,j} - E_0)^2 - \omega^2} \tag{2.3}$$

The total polarizability for the electronic state with quantum numbers j and m_j is then given by (2.4).

$$\alpha = \alpha_{\text{core}} + \alpha_0 + \alpha_1 \frac{m_j}{2j} 2\,\text{Im}(\epsilon_x^* \epsilon_y) + \alpha_2 \frac{3m_j^2 - j(j+1)}{j(2j-1)} \tag{2.4}$$

Here α_{core} is an offset added to fit calculations to experimentally measured polarizabilities. The contribution of the vector polarizability depends on the polarization of the

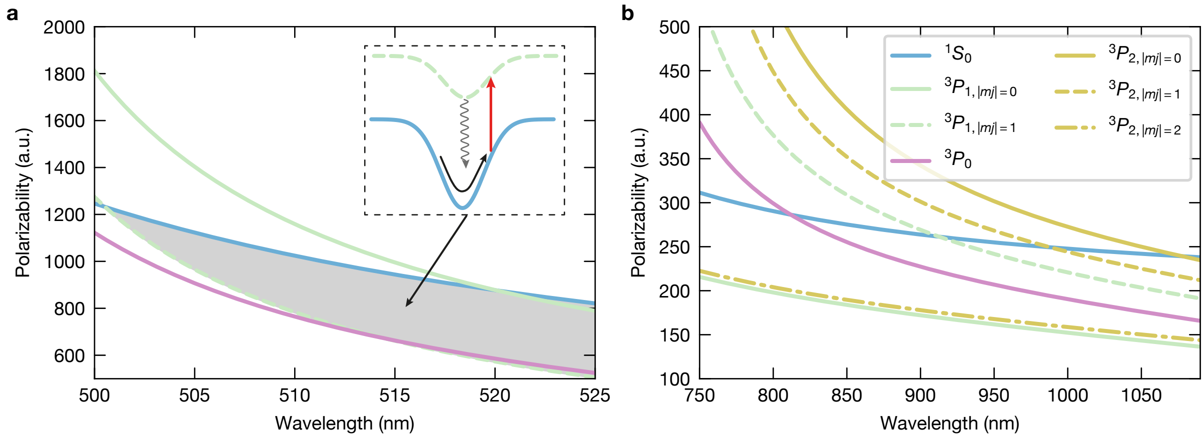

Figure 2.2: Polarizability for different electronic levels in linearly polarized trapping potentials. In the green wavelength regime (a), the polarizability is higher compared to the IR regime (b). The m_j-dependence is caused by the strong tensor-polarizability contribution.

light field, which is often parametrized by the so called "ellipticity angle" γ defined by (2.5) for the normalized polarization vector $\vec{\epsilon} = (\epsilon_x, \epsilon_y, \epsilon_z)^T$.

$$2\,\mathrm{Im}(\epsilon_x^* \epsilon_y) = \sin(2\gamma) \tag{2.5}$$

To compute the polarizability, we prepare a tabulated list of transition frequencies and matrix elements[1], taken from Ref. [142], and compute the sum over all available states.

Linearly polarized optical traps For linearly polarized traps, the vector polarizability does not contribute, and only the scalar and tensor polarizability determine the polarizability of the state. In these cases, it is still possible to tune the effective polarizability of electronic states with $J \neq 0$ by applying a magnetic quantization axis under a suitable angle with respect to the linear light polarisation [138].

2.1.2 Engineered trapping potentials

In this section, we discuss the effect of a strong magnetic field applied under an angle θ with respect to a linearly polarized optical trapping potential. For states with magnetic quantum number $m_j = 0$ this offers the possibility to tune the resulting polarizability within certain boundaries. Under the combined action of electric and magnetic field,

---

[1] Recently, tabulated transition wavelength and matrix elements as well as the resulting polarizabilities for various electronic states in strontium were added to the PORTAL FOR HIGH-PRECISION ATOMIC DATA AND COMPUTATION at https://www1.udel.edu/atom/, which provides a convenient interface to look up atomic data [141].

the Hamiltonian of an atom with total angular momentum operator $\vec{J}$ is given by $H = H_B + H_E$. Here, $H_B = \mu_B g \vec{J} \cdot \vec{B}$ is the magnetic field part with Bohr-magneton μ_B and Landé factor g, and the electric field Hamiltonian corresponding to the trapping light is given by (2.6) [134].

$$H_E = -\frac{1}{4}|E|^2 \left(\alpha_0 + \alpha_t \frac{6(\vec{\epsilon} \cdot \vec{J})(\vec{\epsilon} \cdot \vec{J}) - 2J(J+1)}{2J(2J-1)} \right) \tag{2.6}$$

Considering linearly polarized trapping light, we have already set the vector contribution of the polarizability to zero. The amplitude of the electric field is related to the trap depth via $U = -\frac{\alpha_{SI}}{4}|E|^2$. In order to find the eigenstates, we numerically diagonalize the total Hamiltonian, which provides us with the resonance shift in combined electric and magnetic fields.

Magic angle tuning for a $J = 0 \to J = 1$ transition For sufficiently strong magnetic quantization axes, the magnetic quantum number m_j is defined with respect to the magnetic field, and the decomposition in the frame of the electric field is given by a basis rotation with angle θ [134]. In this case, the eigenstate in the frame of the magnetic field $|0^B\rangle$ is given by:

$$|0^B\rangle = |0^E\rangle \cos\theta + 1/\sqrt{2} \sin\theta \left(|1^E\rangle - |-1^E\rangle \right)$$

Given the strong tensor-polarizability in strontium, the total polarizability of $|0^B\rangle$ can be tuned via the angle θ. Note that the polarizability remains unaffected for the $|J = 0\rangle$ states in strontium like the $^1\mathrm{S}_0$ and $^3\mathrm{P}_0$ states. We can apply suitably aligned magnetic fields, for example, to cancel differential light shifts between the states $^1\mathrm{S}_0$ and $^3\mathrm{P}_{1,m_j=0}$ [134, 138]. These so-called magic trapping conditions are useful to implement direct resolved sideband cooling on the narrow intercombination line, which we discuss in Section 2.1.3. The differential light shift between the $|J = 0\rangle$ and the $|J = 1, m_j = 0\rangle$ state is then given by:

$$\Delta E = E_0 \cos^2\theta + E_1 \sin^2\theta \tag{2.7}$$

Here, $E_i \propto \left(\alpha_{J=1,|m_j|=i} - \alpha_{J=0} \right)$ denotes the light shift of the $|J = 1, |m_j| = i\rangle$ state with respect to the $|J = 0\rangle$ state. In this case, the magic angle is given by:

$$\theta^{J=1}_{\text{magic}} = \arctan\left(\sqrt{-\frac{E_0}{E_1}} \right) \tag{2.8}$$

The requirement for the existence of a magic angle is, therefore, that the polarizability of the $|J = 1, |m_j| = 0\rangle$ ($|J = 1, |m_j| = 1\rangle$) state is stronger (weaker) than the polarizability of the $|J=0\rangle$ state or vise versa. Due to the strong tensor-polarizability contribution, this constraint is fulfilled across a broad range of wavelengths as illustrated in Fig. 2.3b. Note that additionally, the magnetic field has to be sufficiently strong for this approximation to hold.

Magic angle tuning for a $J=0 \to J=2$ transition For a $J=0 \to J=2$ transition, we can carry out a similar decomposition taking into account the additional $|m_j|=2$ Zeeman states and obtain:

$$\begin{aligned} |0^B\rangle = &\frac{1}{4}(1+3\cos(2\theta))\,|0^E\rangle \\ &+\frac{1}{\sqrt{2}}(\sqrt{3}\cos\theta\sin\theta)\left(|1^E\rangle - |{-1}^E\rangle\right) \\ &+\sqrt{\frac{3}{8}}\sin^2\theta\left(|2^E\rangle - |{-2}^E\rangle\right) \end{aligned}$$

The resulting differential light shift and magic angle are given by:

$$\Delta E = 3(E_1 - E_0)\sin^2\theta + E_0 \tag{2.9}$$

$$\theta_{\text{magic}}^{J=2} = \arcsin\left(\sqrt{-\frac{E_0}{3(E_1-E_0)}}\right) \tag{2.10}$$

Magic angle tuning on the ${}^1\mathrm{S}_0 \leftrightarrow {}^3\mathrm{P}_{2,m_j=0}$ transition is feasible in strontium for a broad range of wavelengths in the IR regime, as shown in Fig. 2.3b.

2.1.3 Cooling techniques

Cooling atoms trapped in optical potentials makes use of the narrow intercombination line at a wavelength of 689 nm. Because of the narrow transition linewidth of $\Gamma_{^3\mathrm{P}_1}/2\pi = 7.4\,\mathrm{kHz}$, the light shift induced by the trapping potential $|\Delta U|/\hbar \gg \Gamma_{^3\mathrm{P}_1}$ typically exceeds the linewidth. Therefore, the resonance condition depends on the position within the potential giving rise to the Sisyphus cooling mechanism. In the following, we provide a semi-classical discussion of the cooling mechanism and explain its applicability. A visualization of the different regimes is shown in Fig. 2.3a.

If the ground-state polarizability exceeds the excited-state polarizability, hot ground-state atoms can be predominantly excited on the slope of the potential. Since typical trap frequencies $\omega_{tr} \gg \Gamma_{^3\mathrm{P}_1}$ exceed the decay rate, the atoms can significantly move within the excited state potential before decaying back to the ground state. For a decay event occurring further towards the trap center, the potential energy difference of the ground-state potential, at the excitation and decay position, is removed from the system. However, if the decay happens further outwards compared to the point of excitation, the potential energy difference is added as kinetic energy. The choice of the

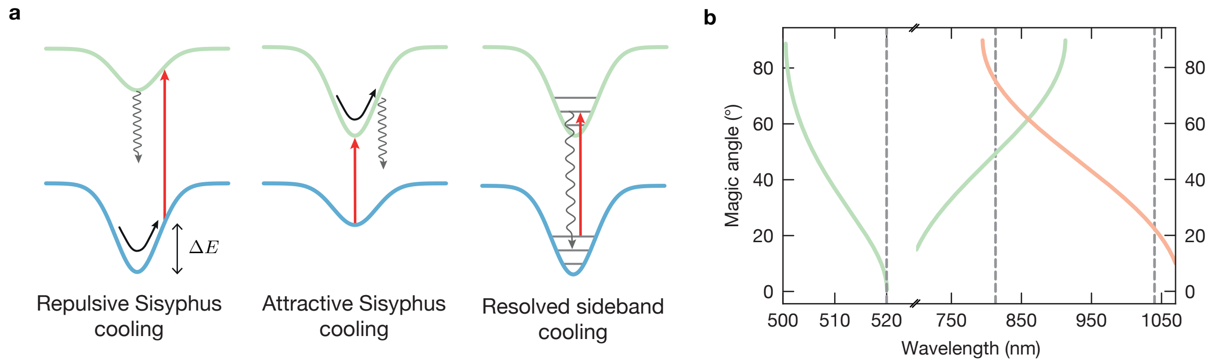

Figure 2.3: Overview of laser cooling techniques. a To cool atoms trapped in optical potentials, we use light resonant with the $^1\mathrm{S}_0 \leftrightarrow {}^3\mathrm{P}_1$ intercombination transition, and depending on the trap-induced light shifts, apply three different cooling techniques. The repulsive and attractive Sisyphus cooling techniques exploit that the differential light shift exceeds the transition linewidth of about 7.4 kHz and the resonance condition thus depends on the position. Repulsive Sisyphus cooling is applicable if the polarizability of the ground state exceeds the polarizability of the excited state. In this case, hot ground-state atoms explore a certain volume of the trap and can be predominantly excited on the slope of the potential. If the decay occurs further towards the trap center, the resulting potential energy difference is removed from the system. In the inverse case, where the excited-state polarizability exceeds the ground-state polarizability, attractive Sisyphus cooling can be realized. In magic trapping conditions, with vanishing differential light shift, direct resolved sideband cooling allows cooling the atoms into the motional ground state. See the main text for a more detailed discussion. **b** Magic trapping conditions can be realized across a broad range of wavelengths by applying a sufficiently strong magnetic field under a suitable magic angle with respect to the linear trap polarization. The magic angle for the $^1\mathrm{S}_0 \leftrightarrow {}^3\mathrm{P}_{1,m_j=0}$ (green) and for the $^1\mathrm{S}_0 \leftrightarrow {}^3\mathrm{P}_{2,m_j=0}$ (red) transition is shown. The relevant wavelength 520 nm, 813 nm and 1040 nm are indicated by dashed vertical lines.

cooling frequency can thus be understood as a repelling barrier for the atoms' energy, defining the name *repulsive* Sisyphus cooling [134, 138]. Atoms colder than a given threshold, called the Sisyphus cap in the following, are further cooled, and hotter atoms are heated. A careful adjustment of the cooling frequency is needed to generate sufficiently cold ensembles and, at the same time, limit losses due to the repulsive nature of the cooling mechanism.

For the inverse case, where the ground-state polarizability is smaller than the excited-state polarizability, *attractive* Sisyphus cooling can be used [143]. Here, the cooling frequency is adjusted to excite atoms in the trap center, and decay events further outwards of the trap result in cooling. This cooling mechanism is called attractive Sisyphus cooling and provides cooling without temperature-dependent heating effects. Exploiting either of the two Sisyphus cooling effects requires parameters that fulfill $|\Delta U|/\hbar \gg \omega_{tr} \gg \Gamma_{^3\mathrm{P}_1}$ [144].

To prepare atoms in the motional ground-state, we use direct resolved sideband cooling, exploiting once again that $\omega_{tr} \gg \Gamma_{^3\mathrm{P}_1}$. An efficient preparation of the ground state requires magic trapping conditions with vanishing differential light shift $\Delta U = 0$. In this case, we can resolve the harmonic oscillator levels of the trap and can drive the cooling sideband to lower the number of motional excitations from $n \to n-1$. In the Lamb-Dicke regime, the decay back to the ground state preserves the number of excitations such that excitations are sequentially removed [145, 146]. Realizing the required magic trapping conditions relies on magic angle tuning, discussed in Section 2.1.2. This technique is applicable to a broad class of wavelengths as shown in Fig. 2.3b. Unfortunately, for linearly polarized traps with wavelength above 914 nm, magic trapping conditions on the intercombination line are not available for strontium. To provide ground-state cooling for atoms in the optical lattice at 1040 nm, we thus need a different cooling strategy. In Section 4.5, we present resolved sideband cooling based on a scalable three-photon process driving the $^1\mathrm{S}_0 \leftrightarrow {}^3\mathrm{P}_{2,m_j=0}$ transition to overcome this limitation.

2.2 Main experimental setup

To isolate the atoms from collisions with ambient particles, the experiment takes place within an ultra-high vacuum apparatus. We use a rectangular glass cell (JapanCell custom design) which offers large optical access from all sides. The atomic flux is generated by a commercial source (AOSense Sr Beam RevC), starting with an atomic oven that we typically operate at a temperature of 400 °C. The atoms are axially slowed using a Zeeman slower and transversally cooled in a two-dimensional magneto-optical trap (2D-MOT) section generated using in-vacuum permanent magnets. The Zeeman window is heated to avoid accumulation of atoms on the inside of the Zeeman window, which could otherwise limit the transmission of (near-)resonant light. Activating the light in the 2D-MOT section provides transversal cooling and, at the same time, deflects the atomic beam into a differential pumping tube pointing at the glass cell. The vacuum is maintained by ion-getter pumps and one titanium-sublimation pump, which we activated only once after closing the vacuum assembly. To facilitate work in the close vicinity of the glass cell where the experimental setup is the most dense, we mounted the entire vacuum apparatus on a translation stage (LinTech 251242-WC0-2-S022-M00-C000-L00-E00-B00) as shown in Fig. 2.4. Thereby, the glass cell can be removed, which provides access to the focal plane of the objectives. This possibility turned out to be very useful for the installation of the high-resolution imaging system

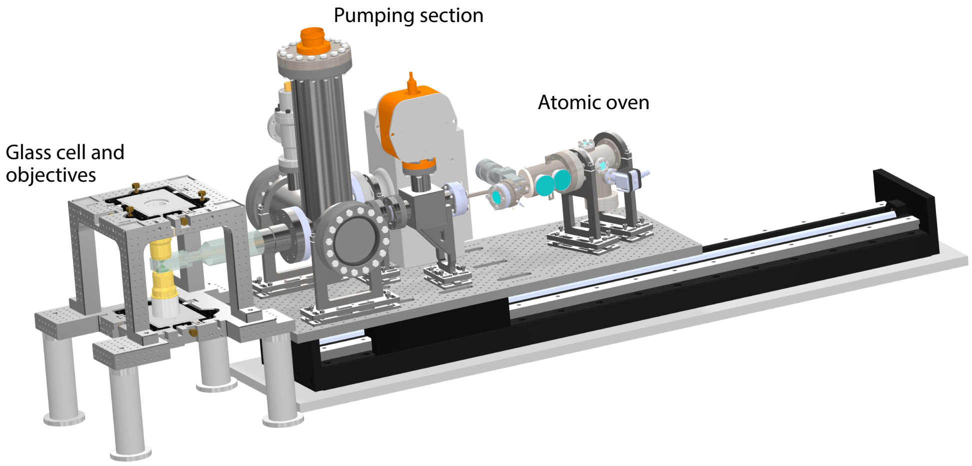

Figure 2.4: Computer rendering of the vacuum apparatus and objectives. The vacuum apparatus consists of an atomic oven which provides, on demand, a stream of precooled atoms, which travel through differential pumping tubes to the glass cell. Two high-NA objectives are focused onto a common plane within the glass cell. The vacuum is maintained by ion-getter pumps and one titanium-sublimation pump and the entire vacuum assembly is installed on a translation stage.

and the suppression of initially present aberrations. We installed two high-resolution objectives (Special Optics 57-31-24) with a numerical aperture (NA) of 0.65, which are focused onto a common plane within the glass cell. The lower objective is used to collect the fluorescence of the atoms and to image the atomic plane onto a camera. In addition, the same objective is used to project tweezer arrays in the green wavelength regime of 515 nm - 520 nm onto the atoms. Similarly, the upper objective is used for the generation of tweezer arrays at various wavelengths in the red and infrared regimes. Using a stack of longpass dichroics, we combine tweezer systems at 813 nm and ≈689 nm, see Fig. 2.5a.

To facilitate modular development of the experiment, we designed a central mounting structure that surrounds the glass cell. This monolithic “cube”-like structure, shown in Fig. 2.5b, features multiple M6 threads, which act as mechanical support and reference for additional attachments, which we added over time. For example, the optics of the horizontal lattice, further discussed below, are directly attached to the cube, and the objectives are supported by the same structure. In the direct vicinity of the glass cell, we installed multiple magnetic field coils to realize the quadrupole field for magneto-optical trapping and apply fields under arbitrary orientations. This is realized with one pair of water-cooled coils in Helmholtz configuration, which can each generate a magnetic field of at least 15 G, currently limited by the power supply. The resulting field strengths are sufficient to exploit magic-angle tuning schemes discussed in Section 2.1.2. An additional pair of coils with horizontal orientation in (anti-)Helmholtz configuration is used to generate the quadrupole field for the MOT and to apply strong magnetic fields of several 100 G to open the ultranarrow clock transition in strontium. The material of the mechanical coil support (TECAFORM) exhibits a resistivity that allows for a rapid dissipation of patch charges, while suppressing eddy currents.

The objectives are located within the vertical coils about 1 mm above the glass cell and are each attached to a piezo-positioner (Mad City Labs Nano-Z100) with a travel range of $\pm 50\,\mu\mathrm{m}$ to enable a computer-controlled finetuning of the focal plane. The objective scanners are subsequently mounted in a custom-developed 5-axis stage, which controls the tilt of the objective with respect to the glass cell as well as the position. We use fine-threaded screws (Radiant dyes Model 5 with 150 µm per revolution) to precisely adjust the angle of the objectives to better than 0.01°, as discussed in Section 2.2.2, which is an important requirement to suppress coma. To suppress vibrations that might occur during the switching of the magnetic field coils, the mechanical support of the coil assembly and the cube are fully separate and are resting on heavy sand-filled posts. Multiple optical modules are attached to the cube, for example, to retroreflect MOT beams, to attach horizontal breadboards around the glass cell, and to support a vertical shallow-angle lattice and tweezer systems above the upper objective. The following sections provide a short summary of the most important systems to realize single-particle trapping and detection.

2.2.1 A power-efficient folded optical lattice

Scaling up neutral-atom arrays offers new possibilities for quantum computing, simulation, and metrology applications. Typically, gases with several million atoms or more can be readily trapped, and the remaining challenge is to prepare scalable arrays without sacrificing the single-site control. Since individual atoms are typically trapped in off-resonant dipole traps, the optical power requirements grow with system size. A scalable method for generating a large-scale array of traps is given by optical lattices, generated by interfering laser beams. In this section, we discuss the horizontal lattice setup installed in the experiment.

We implement a horizontal two-dimensional lattice at a wavelength of 1040 nm. The light of an external-cavity diode laser (Toptica DLpro) is used to seed a Ytterbium-doped fiber amplifier (Azur Light Systems ALS-IR-1036-50-A-CC-SF (now Toptica)), which delivers up to 45 W of power. The light is passed through an acousto-optic modulator (AOM) for switching and is delivered to the experiment via a photonic crystal fiber (Alphanov LMA-PM-15 with SMA-6 connectors). The setup on the experiment side is shown in Fig. 2.6a. To protect the fiber against back reflections, the collimated light is sent through an isolator, and the power is monitored with a photodetector, which is used to actively stabilize the power. Using a cylindrical telescope, the beam

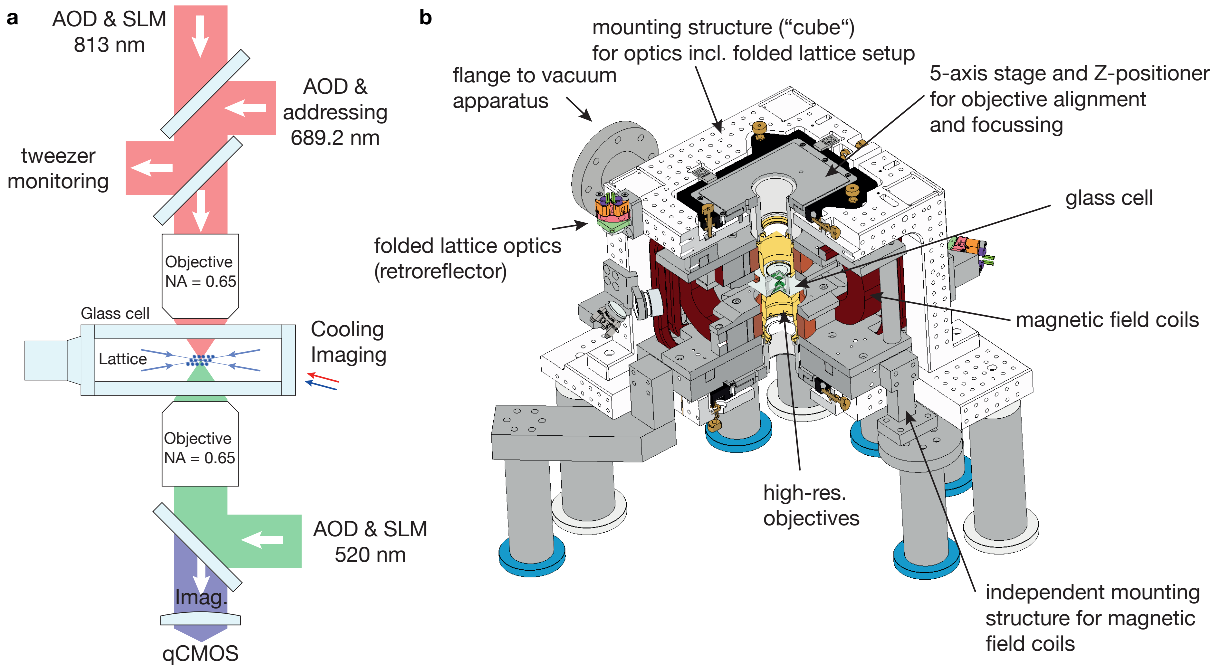

Figure 2.5: Main experimental setup. a Sketch of the main components of the apparatus. Two high-resolution objectives are focused onto a common plane within the glass cell. The bottom objective is used for fluorescence imaging of atomic ensembles, which are imaged onto a qCMOS camera. At the same time, tweezer arrays at a wavelength of ≈520 nm are projected onto the atoms using the same objective. The top objective is used for the generation of additional tweezer systems at wavelengths in the red and infrared, which are combined using a stack of dichroic mirrors. In the horizontal plane, we generate an optical lattice and globally apply various beams for optical (re-)pumping, cooling, pushout, imaging, and single- and two-qubit gate operations. **b** Computer rendering of the central part of the experiment. The glass cell is connected to the vacuum apparatus and is surrounded by multiple pairs of magnetic field coils in Helmholtz configuration. In addition to three pairs of bias coils, we installed another horizontally oriented pair for the generation of strong magnetic fields and the quadrupole field required for magneto-optical trapping. To facilitate a modular development of the experiment, we designed a central mounting structure surrounding the assembly. This "cube"-like structure features multiple M6 threads, which are used to mount, for example, the lattice optics and act as the starting point for future developments. The objectives are each attached to a piezo-based Z-positioner, which is mounted in a 5-axis stage for angle and position control. The mechanical supports of the cube and the coil assembly are entirely independent to avoid that vibrations caused by the switching of the coils or the water cooling affect the optical systems.

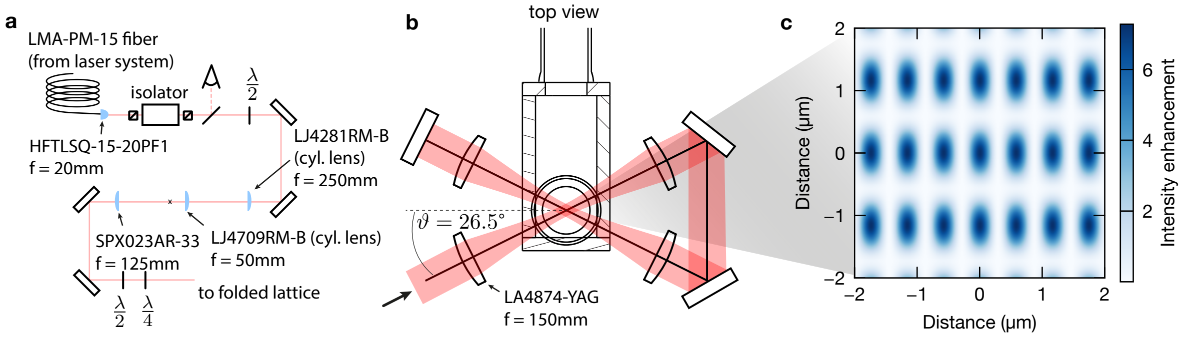

Figure 2.6: A power-efficient folded optical lattice. **a** The optical setup of the horizontal folded lattice is shown. The light at a wavelength of 1040 nm is delivered via a photonic-crystal fiber and is sent through an optical isolator. The optical power is monitored with a photodetector, and a cylindrical telescope is used to prepare an aspect ratio of 1:5 before the beam is focused onto the atoms. **b** The optical lattice is generated by focusing the beam to a horizontal (vertical) focus of 100 μm (20 μm). Subsequently, the beam is recollimated and focused again onto the atoms before it is retro-reflected. This gives rise to 4-fold interference of the vertically polarized beam, which provides a power-efficient two-dimensional single-plane optical lattice. The beams interfere under a half-opening angle of 26.5°, which gives rise to an asymmetric lattice spacing with an aspect ratio of 1:2. **c** The intensity of the resulting lattice pattern is shown in units of the single-beam intensity. Due to 4-fold interference, we expect a 16-fold enhanced intensity, however, due to reflection losses on the uncoated glass cell, the effective enhancement is reduced. We reach a typical trap depth of about 1.5 mK at about 11 W of optical power. Note that the effect of losses on the lattice contrast is negligible.

is shaped into an aspect ratio of 1:5, before the light is focused down to a horizontal (vertical) focus of 100 μm (20 μm). The transmitted beam is recollimated and focused again onto the atoms from a different direction, as shown in Fig. 2.6b. Finally, the beam is collimated again and retro-reflected, which gives rise to 4-fold interference in the crossing volume of all beams. Generating a stationary lattice requires phase stability between the individual beams after the interferometer is opened by the incident beam. To minimize mechanical drifts, we mount all optics of the lattice interferometer to the same monolithic structure. Indeed, we observe that the lattice phase drifts by one site on the time scale of approximately 6 hours if the experiment is thermalized and runs continuously. These drifts of the lattice phase have to be tracked and corrected to allow for tweezer-based single-site addressing as discussed in Section 4.2.3.

We interfere the lattice beams under a half-opening angle of $\arctan(1/2) = 26.5°$, which gives rise to a lattice geometry with an aspect ratio of 1:2. At our wavelength of 1040 nm, the resulting lattice spacings in the two horizontal directions are 1.15 μm and

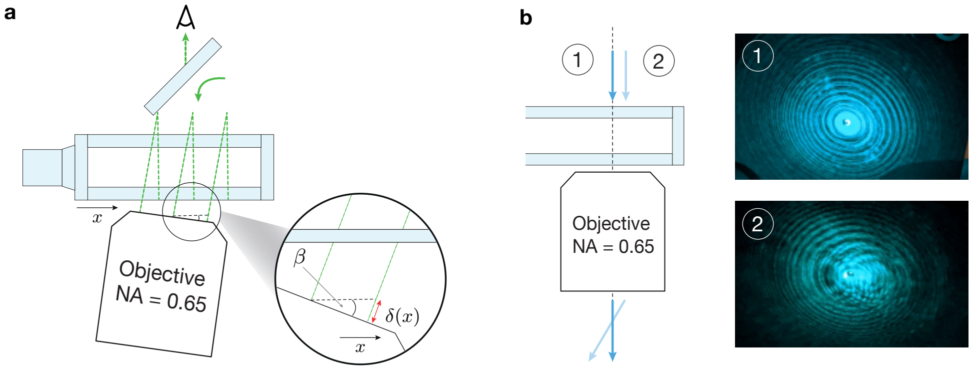

Figure 2.7: Alignment of the high-resolution objectives. **a** To minimize coma aberrations, the angle of the objective has to be precisely set with respect to the glass cell. We measure the angle interferometrically, exploiting that the last objective surface is flat. A collimated input beam with diameter of about 1 cm is launched onto the objective, and reflections from multiple surfaces of the glass cell and the objective interfere. A tilt of the objective lens with respect to the glass cell results in an interference pattern with a regular lattice structure, and the periodicity provides information on the tilt angle. **b** Aligning the imaging and tweezer systems onto the optical axis defined by the objective requires a guiding beam to center the optical components. The centration of the guiding beam on the optical axis is crucial to align all optics onto a common axis. To center the guiding beam, we observe the reflections from the inner curved surfaces of the objectives. In case of a well-centered beam, the resulting interference pattern forms concentric rings ①, which are distorted for a decentered beam ②.

0.57 µm, respectively. Because of the 4-fold interference, we would in principle expect a 16-fold enhanced intensity in comparison to the single-beam intensity. However, due to reflection losses at the uncoated glass cell, the effective intensity enhancement is approximately 7-fold, see Fig. 2.6c. Remarkably, despite the strong losses of the retro-reflected beam, the lattice contrast is not significantly reduced, making this setup a robust and power-efficient implementation for large-scale optical lattices. The scaling perspectives of this design are further discussed in Section 4.4.4.

Resolving the lattice spacing of 0.57 µm requires a suitable high-resolution imaging system. In the following, we discuss the alignment strategy of the high-NA objectives in our apparatus in order to minimize optical aberrations.

2.2.2 A high-resolution imaging system

In addition to the high-resolution fluorescence detection of neutral atoms on the short lattice spacings, the objectives are used to generate stationary and mobile optical tweezer arrays. To ensure high-quality potentials and provide high spatial resolution in detection, we require a diffraction-limited imaging system. A critical parameter for achieving this is given by the angle of the objective lens with respect to the surfaces of the glass cell. A Zemax simulation of the objective reveals that angles as small as 0.02° result in significant coma. Initially, we adjusted the angle of the objective with respect to the glass cell by observing the residual reflection of a small laser beam and adjusted the objective tilt such that the reflection of the objective overlapped with the reflection from the glass cell after a few meters of propagation. A more precise method for setting the relative angle is given by an interferometric measurement. We launch a collimated laser beam with a diameter of about 1 cm from the top onto the glass cell and objective. The reflections of the various flat surfaces interfere and give rise to a periodic intensity modulation depending on the tilt direction, which is caused by the position-dependent phase difference $\Delta\Phi(x) = 2\pi\delta(x)/\lambda$ (see Fig. 2.7a). The lattice spacing is determined by the position-dependent path-length difference $\delta(x) = 2\sin(\beta)x + \delta_0$ and the tilt angle β. Measuring the lattice spacings $L = \lambda/(2\sin(\beta))$ with a camera, thus, provides information about the tilt angle and a residual tilt of $\beta = 100\,\mu\mathrm{rad}$ corresponds to a periodicity of about 2.5 mm at our probe wavelenth of 520 nm. We use an uncoated fused-silica substrate in the experiment to separate the incoming beam from the reflection. The residual reflection of the substrate is used as a probe beam, as shown in Fig. 2.7a, and access to the interference pattern is conveniently given in transmission of the glass piece.

Besides the angle between the objective lens and the glass cell, the optics of the tweezers and imaging systems have to be precisely aligned. To facilitate an accurate positioning, we set up a guiding beam aligned with the optical axis of the objective lens. Aligning the guiding beam is again based on observing the reflections from the objective. Here, we exploit the interference of reflections from various curved surfaces within the objective. These reflections give rise to a pattern of interferometric rings if the beam is centered on the objective. For a decentered guiding beam, the reflection exhibits an interference pattern of non-concentric rings, which is shown in Fig. 2.7b. Subsequently, the optical components of the imaging system are positioned with respect to the centered guiding beam.

To characterize the performance of our imaging system, we make use of the ability to remove the vacuum apparatus and insert a dummy vacuum window of exactly the same thickness and a test target (Technologie Manufaktur TC-RT01) into the focal plane of the objective, where we make use of the interferometric alignment technique to fix the angles of the glass plate. The test target features various line pairs with well-defined spacings, which can be used to accurately measure the magnification of the imaging system. Furthermore, it includes multiple sets of pin-holes, including one at a sub-wavelength diameter of 250 nm with which we estimate the point-spread-function of the system. To ensure that the camera field of view and the position of the optical tweezer arrays overlap, we insert the test target and observe the reflection of the tweezer array from the metallic test target. Here, the target is illuminated from the top to image a pattern onto the camera, and the tweezer array is projected onto the same plane backwards through the objective. Observing the target pattern as well as the reflection of the tweezer array provides the means to overlap their fields of view and approximately focus them onto the same plane, which drastically simplifies the search for the first signal using atoms in tweezers.

Stationary and mobile optical tweezer arrays

To generate stationary tweezer arrays, we use a liquid-crystal-on-silicon spatial light modulator (LCOS-SLM) and configure arbitrary array configurations by generating suitable phase masks. A collimated laser beam is reflected from the SLM (Hamamatsu X15213-02R and X15213-16R), and the SLM plane is subsequently relayed onto the backfocal plane of the objective. The imprinted spatial phase profile then determines the intensity distribution in the focal plane. Details of our SLM-based tweezer setups can be found in Ref. [136], and we generate holographic phase patterns following established algorithms [147–149].

To generate mobile optical tweezers, we use acousto-optic deflectors (AOD) and configure the deflection angle with a suitable radio-frequency signal. Two crossed AODs are installed in a Fourier plane of the system such that the deflection angle translates to programmable positions, which enables control over the tweezer depth and trajectory.

2.2.3 Laser systems and experimental sequences

Trapping, cooling, and manipulating atoms within the vacuum apparatus relies on lasers, which generate either an off-resonant dipole trapping potential or provide a resonant excitation. We have constructed various laser systems, tabulated in Tab. 2.1, to provide a versatile experimental toolbox. This section provides an overview of the available laser systems and contains a short summary of the typical experimental sequence. The control system in the experiment is given by an Adwin timing system (Jäger Messtechnik GmbH ADwin-Pro II-BM), which is programmed via the in-house developed control software Qcontrol.

Magneto-optical trapping

Each experimental cycle starts with a pre-cooled cloud of atoms trapped in a MOT. We realize a MOT on the broad ${}^1\mathrm{S}_0 \leftrightarrow {}^1\mathrm{P}_1$ transition, which provides confinement for a broad range of velocity classes of the atoms arriving from the Zeeman slower. The corresponding laser system (Toptica TA SHG pro) is based on amplifying an external-cavity diode laser (ECDL) at a wavelength of 922 nm with a tapered-amplifier (TA) followed by resonant doubling in a bow-tie cavity. The generated power of up to 1.4 W is distributed into individual beams for the Zeeman slower, 2D- and 3D-MOT, imaging and more. Because of the broad linewidth of the 461 nm transition, the resulting temperature is typically on the order of up to a few mK, which prevents efficient loading into trapping potentials. To reach lower temperatures, we subsequently realize a sawtooth-wave-adiabatic-passage MOT on the narrow intercombination line at 689 nm [150]. The laser system consists of an ECDL locked to an ultralow-expansion (ULE) cavity. During both MOT stages, we additionally apply resonant repumping light at 679 nm and 707 nm to repump atoms from the long-lived $^3P_0$ and $^3P_2$ state, respectively.

Trapping potentials

The apparatus features multiple systems for site-resolved trapping of atoms, which cover various wavelengths. The optical power for the green tweezer system is generated by amplifying an ECDL-based laser with a Ytterbium-doped fiber amplifier (YDFA) by second-harmonic generation in a single pass through a periodically-poled magnesium-oxide-doped lithium-tantalate crystal. With about 30 W of IR power, the system provides up to about 10 W of green light. Using a multi-grating crystal that contains several different periodicities, the system covers the wavelength range of 515 nm to 520 nm. For clock-magic trapping, we use an additional tweezer system at a wavelength of 813 nm. Two-fiber lasers at 1550 nm and 1067 nm are used to seed fiber amplifiers and the 1067 nm light is frequency doubled. It is subsequently used in a difference-frequency-generation step with the 1550 nm light, resulting in about 3.5 W of power at 813 nm. The entire laser system, including the non-linear frequency conversion module, is commercially available (NKT Photonics). An additional tweezer system is designed for the $^1S_0$ tune-out wavelength at approximately 689.2 nm. We use a Titanium:Saphir laser (Sirah Matisse CS), which provides up to 7 W at this wavelength. The optical lattice setup at a wavelength of 1040 nm is powered by a Ytterbium-doped fiber amplifier, which is seeded by an ECDL.

Cooling and optical pumping

To cool atoms in the optical potentials, as discussed in Section 2.1.3, we use light resonant with the narrow intercombination line at 689 nm, which is provided by an ECDL. The laser is locked to an ultralow-expansion (ULE) reference cavity with a Finesse of about 50000. The cavity resonance drifts by approximately 7 kHz within one day, and we compensate for this drift by recalibrating the resonance of the intercombination line every morning. In addition, light at 716 nm and 688 nm and 497 nm is used for optical (re-)pumping and provided by diode lasers. The shelving light at 688 nm and the repumping light at 716 nm is locked to a reference cavity and the 497 nm laser is stabilized to a wavemeter.

Single-qubit operations

We use a diode laser at 698 nm, to drive the ultranarrow clock transition. The laser is locked to a high-finesse ULE reference cavity using the Pound-Drever-Hall technique and is amplified by an injection-locked amplifier. The ULE resonance frequency drifts by about 5 Hz/min which quickly limits the available duration for data taking in the absence of a suitable drift compensation. To correct for the laser frequency drift, we create a beat signal between the 698 nm laser and an independently dedrifted frequency comb. The correction is then applied by adjusting the RF frequency of the AOM used to generate the light pulses. To realize coherent two- and three-photon transitions, we utilize a set of lasers at 679, 688, 689 and 707 nm locked to the frequency comb. This setup is discussed in more detail in Section 3.2.

Rydberg

To excite atoms from the $^3P_0$ clock state into Rydberg states, we use light at a wavelength of 317 nm. Two fiber amplifiers provide high-power sources at 1570 nm and 1071 nm, which are used for the generation of red light at a wavelength of 633 nm, which is subsequently doubled in a resonant enhancement cavity. We use the red light to generate a PDH error signal with respect to a ULE cavity and apply the feedback to the 1071 nm ECDL seed laser. The 1570 nm seed light is provided by a free-running fiber-laser. A similar setup at a wavelength of 322 nm is used to excite atoms from $^3P_2$ to Rydberg states.

2.3 Summary and outlook

This chapter gives a brief introduction to the experimental apparatus and the versatile toolbox comprising multiple laser systems for trapping and state manipulation. In addition, we summarized the main features of the strontium level structure and how to engineer tailored optical potentials. In the following chapters, these considerations are applied to demonstrate building blocks for scalable quantum computing and simulation experiments. Chapter 3 contains a detailed characterisation of two- and three-photon couplings to implement fast gate operations within a novel optical qutrit. Here, we engineer the polarizability as described in Section 2.1.2. Furthermore, Chapter 4 presents a technique for iteratively assembling and continuously operating atom arrays in large-scale optical lattices. This technique combines the scalability of the optical lattices architecture discussed in Section 2.2.1 with the single-site control offered by optical tweezers and opens new possibilities for operating neutral atom arrays. Finally, we utilize the three-photon couplings to demonstrate resolved sideband cooling in the lattice potential using the magic-angle-tuned $^1S_0 \leftrightarrow {}^3P_{2,m_j=0}$ clock transition.

Wavelength	Application	Laser technology	Locking
1040 nm	Horizontal optical lattice	ECDL + YDFA	free-running
813 nm	Clock-magic tweezer trapping	SFG + SHG	free-running
689.2 nm	Tune-out tweezer system	Titanium:Saphir laser	Wavemeter lock
520 nm	Green tweezer-system	ECDL + YDFA + SHG	free-running
707 nm	$^3P_2$ repumping	ECDL	PDH lock to ULE
679 nm	$^3P_0$ repumping	ECDL	PDH lock to ULE
689 nm	Red-MOT	ECDL	PDH lock to ULE
461 nm	Blue-MOT & imaging	922nm ECDL + SHG	PDH lock to ULE
716 nm	$^1D_2$ repumping	ECDL	PDH lock to ULE
688 nm	Shelving from $^3P_1$	ECDL	PDH lock to ULE
698 nm	Single-photon clock transfer	ECDL + ILA	PDH lock to high-finesse ULE
707 nm	Two- and three-photon transitions	ECDL	offset lock to comb
679 nm	Two- and three-photon transitions	ECDL	offset lock to comb
688 nm	Three-photon transitions	ECDL	offset lock to comb
689 nm	Three-photon transitions	ECDL	offset lock to comb
497 nm	FS state resolved detection	ECDL	wavemeter lock
408 nm	Rydberg autoionisation	ECDL	PDH lock to cavity
322 nm	Rydberg excitation from the $^3P_2$ state	fiber lasers + SFG + SHG	PDH lock of fundamental
317 nm	Rydberg excitation from the $^3P_0$ state	fiber lasers + SFG + SHG	PDH lock of fundamental

Table 2.1: Overview of relevant wavelengths and laser systems. This table gives an overview of the relevant laser systems to trap, cool, and manipulate strontium atoms in the experiment. Some wavelengths exist multiple times as we use them for different purposes.

Chapter 3

Fast two- and three-photon single-qubit operations in strontium

3.1 Introduction

The level structure of strontium features two metastable clock states which are the fundament of state-of-the-art atomic clocks [32, 151–153] and have applications for quantum simulation [87] and computing [31, 89]. Direct coupling from the electronic ground state is doubly dipole-forbidden, which gives rise to their long lifetime, but also limits the achievable coupling rates on the clock transitions. In this chapter, we present an alternative method for coherent manipulations based on three-photon transitions mediated via two short-lived intermediate excited states [154, 155]. At our trapping wavelength of 813 nm, we realize an all optical qutrit comprising the ground state $^1\mathrm{S}_0$ as well as the clock states $^3\mathrm{P}_0$ and $^3\mathrm{P}_{2,m_j=0}$, demonstrate coherent all-to-all couplings using two- and three-photon transitions, and characterize the coherence time. We analyze the current limitations of the coupling fidelity, which are dominated by laser phase noise, and discuss methods for the characterisation and feedforward suppression of high-frequency laser phase noise. The demonstrated two- and three-photon transitions, coupling the qutrit states, open up new possibilities, for example, for a measurement-free qubit reset and three-photon-based sideband cooling discussed in Section 4.5. The experimental results presented in this chapter are partially based on the publication [71].

3.1.1 Opening the ultra-narrow clock transition

Driving the ultranarrow clock transition $^1\mathrm{S}_0 \leftrightarrow {}^3\mathrm{P}_0$ in bosonic isotopes directly requires strong magnetic fields to open the transition by admixing the state $^3\mathrm{P}_1$. In a suitable reference frame, corotating with the laser at wavelength 698 nm, the Hamiltonian is given by Eq. (3.1). Here, Δ is the detuning of the clock laser from resonance, Δ_{FS} is the fine-structure energy splitting between the states $^3\mathrm{P}_0$ and $^3\mathrm{P}_1$, d_{689} denotes the dipole matrix element on the intercombination line, E_{698} refers to the clock-laser electric field strength, B denotes the magnetic field strength and $\mu_{FS} = 0.816\mu_B$ denotes the reduced matrix element for the magnetic dipole transition $^3\mathrm{P}_1 \leftrightarrow {}^3\mathrm{P}_0$ [156, 157].

$$\begin{aligned} H = &-\Delta_{FS} \left|^3\mathrm{P}_1\right\rangle \left\langle^3\mathrm{P}_1\right| - \Delta \left|^3\mathrm{P}_0\right\rangle \left\langle^3\mathrm{P}_0\right| \\ &+ \Big(d_{689} E_{698} \left|^1\mathrm{S}_0\right\rangle \left\langle^3\mathrm{P}_1\right| + \mu_{FS} B \left|^3\mathrm{P}_0\right\rangle \left\langle^3\mathrm{P}_1\right| + h.c.\Big) \end{aligned} \tag{3.1}$$

This Hamiltonian resembles the form of a "resonant two-photon process" mediated via the state $^3\mathrm{P}_1$ and we obtain the resulting Rabi frequency $\Omega_C = d_{689}\, E_{698} \cdot \frac{B\cdot\mu_{FS}}{2\Delta_{FS}}$ proportional to the magnetic field strength B. For a realistic magnetic field strength of 1000 G the admixture of $^3\mathrm{P}_1$ population remains below 10^{-7}, which typically limits the achievable Rabi frequency on the clock transition to a few kHz for realistic laser intensities. Applying strong magnetic fields experimentally is typically constrained to one specific direction along the orientation of one pair of high-field coils, which limits the compatibility of magic-angle tuning techniques with coherent manipulations of the clock states. This motivates the development of alternative techniques to enable fast coherent manipulations on the ground-to-clock transitions at intermediate magnetic field strengths. In the following, we introduce three-photon ground-to-clock couplings mediated by off-resonantly coupling to the $^3\mathrm{P}_1$ and $^3\mathrm{S}_1$ states, starting with a description of the laser system.

3.2 A frequency-comb-based laser system for coherent two- and three-photon transitions

To realize coherent two- and three-photon transitions, for coupling both $^3\mathrm{P}_0$ and $^3\mathrm{P}_2$ to each other and additionally to $^1\mathrm{S}_0$, we require a laser system that provides mutually phase-coherent light fields at the wavelength 679, 688, 689, 707 nm. This section describes the corresponding laser system, which is based on phase-locking all lasers to a common frequency comb (Menlo Systems FC1500). The whole system contains a ULE reference cavity (Menlo Systems ORS), acting as reference for a transfer laser at a wavelength of 1542 nm, which is locked to the cavity via the PDH-technique [158]. The frequency comb, with its main oscillator operating in the near-infrared, is then stabilized via phase-locking to the transfer laser. The spectrum of the frequency comb consists of multiple comb teeth and is parametrized by the carrier envelope offset (CEO) frequency f_{CEO} and the repetition rate (REP) f_{REP}, as shown in Eq. (3.2). The CEO frequency is independently measured using a $f - 2f$ interferometer, which is based on frequency-doubling the entire spectrum. In case of a sufficiently broad spectrum, where the n-th and the $2n$-th component are present in the optical spectrum, one obtains a beating signal at the CEO frequency when superimposing the light with its frequency-doubled version.

$$f_n = f_{\mathrm{CEO}} + n \cdot f_{\mathrm{REP}} \tag{3.2}$$

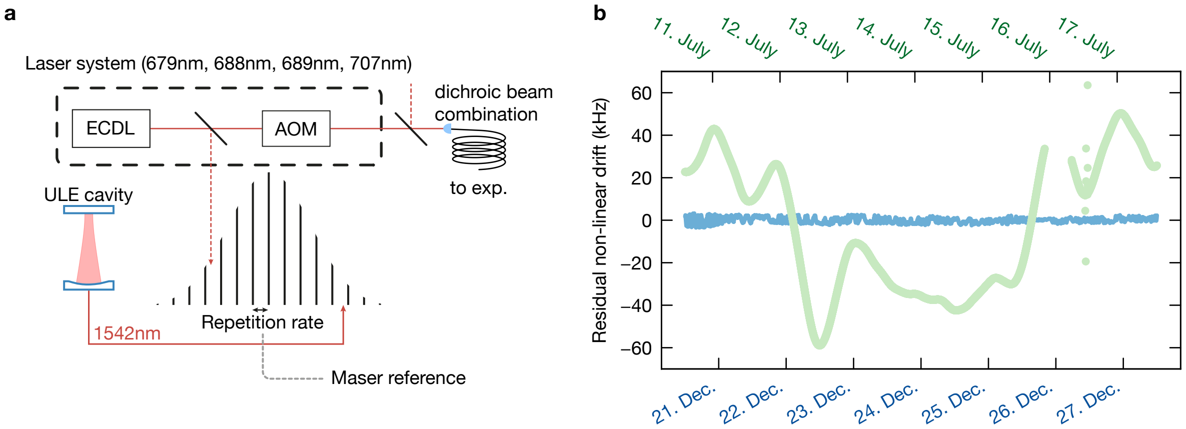

Figure 3.1: Frequency-comb-based laser system for coherent multi-photon couplings. **a** A sketch of the laser system is shown. The stability of a ULE reference cavity is transferred onto the frequency comb by first locking a transfer laser at 1542 nm to the cavity and subsequently locking the frequency comb to that laser. We phase-lock 4 lasers at 679, 688, 689 and 707 nm to the comb to establish their mutual phase coherence. The residual drift of the ULE reference cavity translates to a corresponding drift of the frequency comb spectrum. We track this drift by measuring the comb's repetition rate and reference it to a long-term stable maser signal. This provides the means to dedrift the comb as discussed in the main text. Each light field is controlled via an acousto-optic modulator (AOM) in double-pass configuration, to control the intensity and apply programmable phase modulations. **b** The residual non-linear drift of the ULE reference cavity is shown, which translates to an equal drift of the frequency comb spectrum. Using a reference cavity with crystalline mirror coatings (green, 2024) we observe a substantially stronger non-linear drift compared to IBS-coated mirrors (blue, 2025).

At the same time, the beat frequency between the comb and transfer laser is used to transfer the stability of the cavity onto the comb, which narrows the optical linewidth of the individual comb tooth by applying feedback to the comb's repetition rate. The resulting frequency comb spectrum, thus, inherits the spectral properties of the cavity and provides a reference for locking the lasers of interest [159–163]. For that purpose, the spectrum has to be broadened to cover the red wavelength regime. This is achieved in a so-called supercontinuum module that exploits self-phase modulation in a non-linear fiber and provides beat detection ports by filtering out suitable wavelength ranges [164].

Since the frequency comb is effectively referenced to the ULE cavity, it also inherits the slow drift of the cavity. This drift can be understood as small and slow variations in the cavity length and a corresponding modulation of the resonance frequency with a typical rate of a few Hertz per minute. While this drift rate is negligible in the case of MHz-regime transition linewidth, it may become relevant when addressing the ultranarrow clock transition. We therefore compensate for the ULE aging and dedrift the entire frequency comb. Since the CEO frequency is independently stabilized, the drift of the ULE cavity translates to small variations in the repetition rate. These variations are approximately $1.2 \cdot 10^6$ smaller than the corresponding drift in the optical domain. For a drift of a few 100 Hz in the optical domain, that occurs on the timescale of a few minutes, we thus have to resolve a frequency variation of a few 100 μHz in the RF domain. The repetition rate is measured using a frequency counter, which is locked to a long-term stable maser signal, and its deviation with respect to a programmable target value acts as an error signal for the drift compensation. The deviation is subsequently compensated by smoothly adjusting the target frequency of the phase-lock between the transfer laser and comb. Using a software PID controller to process the error signal, we thereby dedrift the entire comb spectrum and provide a long-term-stable absolute frequency reference. We use this feature, for example, to dedrift the clock-laser setup, which is locked to an independent ULE cavity. A beat of the clock light and the dedrifted frequency comb accurately tracks the drift of the clock-ULE cavity, which we subsequently compensate for by adjusting the RF frequency of the AOM in the clock setup for each experimental repetition.

Successfully dedrifting the frequency comb requires a sufficiently slow cavity drift rate to allow for sufficient averaging of the repetition rate frequency. In other words, the servo bandwidth of the PID controller has to be purposefully limited to avoid the addition of high-frequency noise that is not present in the intrinsically slow cavity drift. Our setup initially used a ULE cavity with crystalline mirror coatings. In this case, we observed a strongly non-linear drift behaviour of the cavity with local rates as high as 100 Hz/min and above. These locally rapid and varying drift rates initially limited the performance of the dedrifting, since they require a higher servo bandwidth to be compensated. After exchanging the crystalline mirrors with standard ion-beam-sputtering-coated (IBS) mirrors, we obtain a rather linear drift with substantially smaller non-linear residuals, shown in Fig. 3.1b.

3.3 Realization of an optical qutrit in strontium-88

3.3.1 Three-photon coupling from the ground to the clock state

To benchmark the three-photon couplings from ground to clock states, we trap atoms in a 9×9-site tweezer array at a wavelength of 813 nm. The setup is shown in Fig. 3.2a including the objectives to generate the tweezer arrays and to image the atomic ensemble. The light fields used to drive two- and three-photon transitions are delivered to the experiment via a single polarization-maintaining optical fiber, which guarantees a good spatial overlap of all colors. All light fields at wavelength 679, 688, 689 and

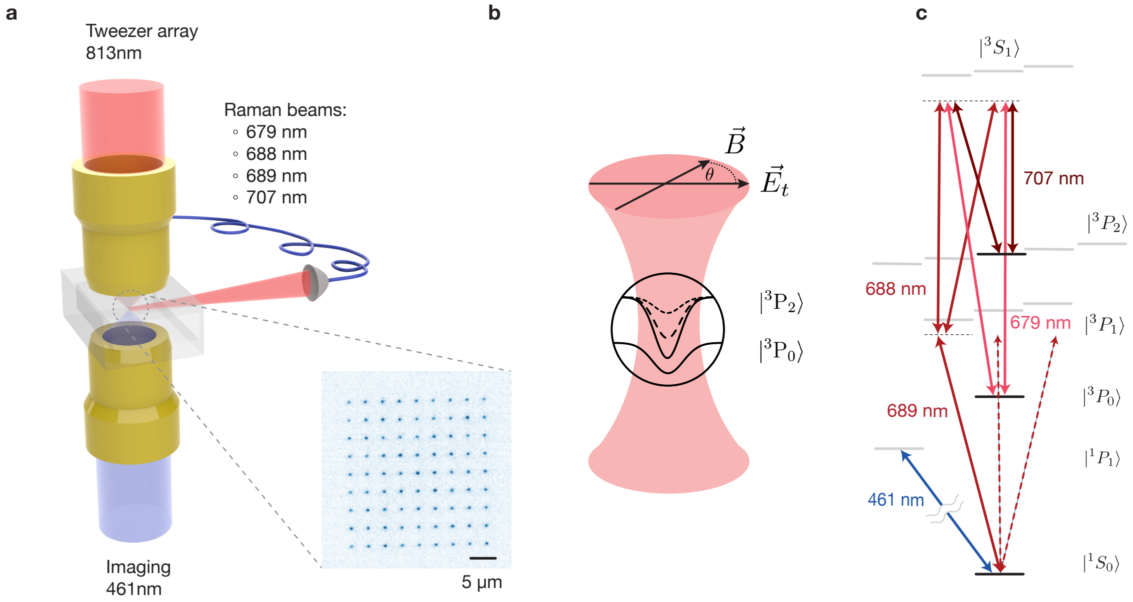

Figure 3.2: Overview of the setup for coherent two- and three-photon couplings. **a** The optical setup relevant for the characterisation of the two- and three-photon couplings is shown. We trap atoms in a 9x9 spot tweezer array at a wavelength of 813 nm projected onto the atoms via the upper objective and detect the fluorescence with the bottom objective. To drive multi-photon transitions, we apply mutually phase coherent light fields at wavelengths 679, 688, 689 and 707 nm delivered from a common polarization maintaining fiber. **b** A priori, the $^3P_0$ state and $^3P_2$ state experience different polarizabilities, causing a strong differential light shift between the fine-structure qubit states. We engineer magic trapping conditions by applying a 19 G magnetic field under a suitable angle with respect to the linear tweezer polarization. **c** Three-photon couplings from the ground to either of the clock states are mediated by two intermediate states, namely the $^3P_1$ and the $^3S_1$ states. Here, we show the relevant levels and the excitation path. Note that all beams are delivered with a common linear polarization, which contains π and $\sigma^{\pm}$ projections as discussed in the main text.

707 nm have the same linear polarization, which is tilted about 55° out of the horizontal plane. This ensures an approximately equal projection onto the three polarization components π, σ^+, σ^-, with respect to the horizontally oriented magnetic field.

The experimental sequence starts by trapping atoms in a two-stage magneto-optical trap before loading the tweezer array and inducing parity projection. Afterwards, we cool atoms to their radial motional ground state using light on the intercombination line at 689 nm [134, 138]. State-sensitive detection of the atoms is performed by pushing out ground-state atoms via rapidly scattering photons at 461 nm before repumping and imaging the remaining atoms.

To find the three-photon resonance, we first identify the individual single-photon resonances for the 689, 688 and 679 nm light fields. We apply a magnetic field with a strength of 19 G, which separates the m_j-substates within $^3\mathrm{P}_1$ by about ±38 MHz and choose a detuning of -6 MHz with respect to the $^1\mathrm{S}_0 \leftrightarrow {}^3\mathrm{P}_{1,m_j=-1}$ transition. This detuning is sufficient to suppress off-resonant scattering on the transition due to its narrow 7.4 kHz-broad linewidth. To suppress off-resonant scattering on the $^3\mathrm{S}_1$ state, we detune the 688 and 679 nm light fields by 12 GHz to the red with respect to the previously found single-photon resonances. The relevant electronic states and laser couplings are shown in Fig. 3.2c, including multiple excitation paths due to the presence of all polarization components for all colors. We purposefully apply a Zeeman splitting much larger than the intermediate state detuning with respect to $^3\mathrm{P}_1$, in order to avoid a destructive interference of excitation path mediated via the $^3\mathrm{P}_{1,m_j=\pm1}$ states [154]. To find the three-photon resonance, given by Eq. (3.3), we account for the single-photon light shifts and obtain the resonance by varying the RF frequency used to drive the 688 nm AOM.

$$\Delta_{679} = \Delta_{688} + \Delta_{689} - \frac{1}{4}\left(\frac{\Omega_{679}^2}{\Delta_{679}} - \frac{\Omega_{689}^2}{\Delta_{689}}\right) \tag{3.3}$$

Using optical powers of $P_{689} = 75\,\mu\mathrm{W}$, $P_{688} = 8.2\,\mathrm{mW}$ and $P_{679} = 850\,\mu\mathrm{W}$ focussed to a horizontal (vertical) waist of 240 µm (90 µm), we obtain a Rabi frequency of 19.16(2) kHz, see Fig. 3.4a. In the following, we use three-photon π-pulses to initialize atoms in the $^3\mathrm{P}_0$ clock state. To identify triple-magic trapping conditions between the states $^1\mathrm{S}_0$, $^3\mathrm{P}_0$, and $^3\mathrm{P}_{2,m_j=0}$, we probe the trap-induced differential light shift between the fine-structure (FS) states $^3\mathrm{P}_0$ and $^3\mathrm{P}_{2,m_j=0}$. A more detailed theoretical discussion of the three-photon coupling in 4-level approximation is provided in Appendix A.

3.3.2 Triple-magic trapping conditions

At our trapping wavelength of 813 nm, the ground state $^1\mathrm{S}_0$ and the clock state $^3\mathrm{P}_0$ experience an equal trapping potential, which is unaltered by magnetic fields due to the absence of total angular momentum $J = 0$. Realizing triple-magic conditions relies on tuning the polarizability of the $^3P_{2,m_j=0}$ to the same value by applying a magnetic field in the horizontal plane under a suitable angle with respect to the tweezer polarization, as sketched in Fig. 3.2b. To find the magic angle, we initialize atoms in $^3P_0$ and perform spectroscopy on the two-photon transition to $^3P_{2,m_j=0}$ by varying the frequency of the 707 nm light field. A state-selective detection between the FS states is done by transferring the $^3P_0$ population to $^1S_0$ using a three-photon π-pulse combined with a ground-state pushout.

To measure an approximate estimate of the magic angle, we initially record the resonance frequency of the spectroscopy sequence as a function of trap depth. To get a more precise characterization of the magic angle, we subsequently use a Ramsey-type sequence. We apply two $\pi/2$-pulses on the fine-structure states separated by a variable waiting time, and fit the oscillation frequency. This Ramsey frequency is given by the differential light shifts between the FS states, which are caused by the light shifts of the two-photon Raman beams and contain a trap-induced contribution. To measure the trap-induced contribution, we record the Ramsey frequency as a function of trap depth, see Fig. 3.3a. The slope of the Ramsey frequency as a function of trap depth represents the trap-induced differential light shift and is independent of the light shift induced by the Raman beams. Repeating the measurement for various magnetic field angles, shown in Fig. 3.3b, yields a magic angle of about 78.5° in the close vicinity of expectations.

Magic-angle tuning for the $^3P_2$ clock state is applicable across a broad range of wavelengths and can be used to realize qubits combined with either $^1S_0$ or $^3P_0$. The expected magic angles for the two qubit candidates are shown in Fig. 3.3c and cross at 813 nm where a qutrit can be realized. In Section 3.3.7 we characterize the trapping conditions in our scalable optical lattice at 1040 nm and experimentally measure the cut-off wavelength for magic-angle tuning of the FS states.

3.3.3 All-to-all optical control over the qutrit states

Under common triple-magic trapping conditions, control over the qutrit states is realized by fast two- and three-photon couplings. Since the magnetic field is constrained by the magic-angle conditions the available field strength in our experiment (and also other typical cold-atom experiments) is limited. Currently, we can generate magnetic fields with a strength of up to 19 G in the correct orientation, which is insufficient for direct single-photon driving of the ground-to-clock transitions. The three-photon transfer is thus an important tool to use the qutrit in experiments.

To demonstrate coherent control over all qutrit states, we drive Rabi oscillations between any pair of states as shown in Fig. 3.4. The three-photon coupling from $^1S_0$ to $^3P_0$ exhibits a rapid dephasing dominated by laser phase noise, see Fig. 3.4a. To estimate the influence of laser phase noise, we record the phase noise power spectral density (PSD) for each laser by analyzing the in-loop beat signal between the laser and

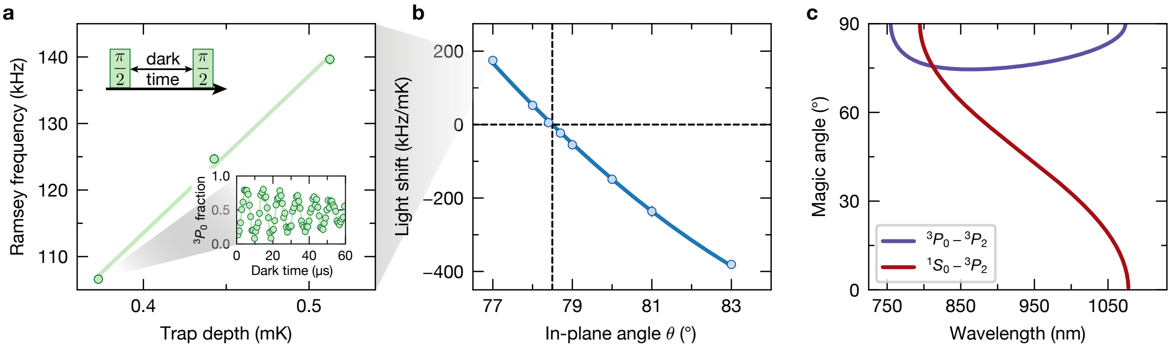

Figure 3.3: Fine-structure magic angle spectroscopy. To realize triple-magic trapping conditions, we apply a 19 G magnetic field in the horizontal plane under a specific angle. **a** To find the magic angle, we measure the trap-induced differential light shift in a Ramsey sequence by varying the waiting time between two fine-structure $\pi/2$-pulses. We obtain the Ramsey frequency (see inset) as a function of trap power, which provides a differential measurement independent of the light shift induced by the Raman beams. **b** The trap-induced differential light shift is detected as a function of the in-plane magnetic field angle. For an angle of 78.5° with respect to the tweezer polarization, the differential light shifts cancel, and we obtain triple magic trapping conditions for $^3\mathrm{P}_0$ and $^3\mathrm{P}_{2,m_j=0}$. **c** The magic angle is shown as a function of wavelength for the $^3\mathrm{P}_0 \leftrightarrow {}^3\mathrm{P}_{2,m_j=0}$ (purple) and $^1\mathrm{S}_0 \leftrightarrow {}^3\mathrm{P}_{2,m_j=0}$ (red) transition. At our wavelength of 813 nm, the $^1\mathrm{S}_0$ and $^3\mathrm{P}_0$ states experience magic trapping conditions independent of magnetic fields, enabling triple-magic conditions.

the common frequency comb. The noise densities are plotted in Fig. 3.5a, showing that the 688 nm laser exhibits significantly stronger noise than the other lasers. Given this measurement, we approximate the effective noise density of the three-photon coupling with the phase noise PSD of the 688 nm laser alone.

Estimating the effect of laser phase noise

Considering this noise density, we compute the expected dephasing of the Rabi oscillations in a two-level approximation. The Hamiltonian used for this simulation is given by a resonantly-driven two-level system with a time-dependent phase term:

$$H = \frac{\Omega}{2} \left|g\right\rangle \left\langle e\right| e^{-i\Phi(t)} + h.c. \tag{3.4}$$

To compute the dephasing of the Rabi oscillations, we average over 1000 repetitions of the simulation for different instances of the time-dependent phase $\Phi(t)$. The phase traces are characterized by the measured phase noise PSD S_Φ, and we initially interpolate the phase noise measurement to an equidistant spacing $\mathrm{d}f$. Samples of the time-dependent phase are then given by Eq. (3.5), where $\Phi_f \in [0, 2\pi)$ is a randomly selected phase [165].

$$\Phi(t) = \sum_f \sqrt{2S_\Phi \mathrm{d}f} \cos\left(2\pi f t + \Phi_f\right) \tag{3.5}$$

With this simple model, we estimate the expected dephasing of the three-photon Rabi oscillations, which is shown as the solid red line in Fig. 3.4a. The simulation has no free parameter, and the excellent agreement with the measurement indicates that laser phase noise is currently the main limitation of the fidelity. In addition to numerical simulations of the two-level Hamiltonian (3.4), a modelling based on the linear response formalisms, which is discussed in Appendix B, provides an efficient description of the influence of laser phase noise and provides additional information about the importance of spectrally-resolved noise components.

Numerical simulations of the three-photon couplings

To estimate the fundamental limitations of the three-photon coupling at the experimental settings, we numerically simulate a noise-free system, taking the entire Zeeman substructure of the $^3\mathrm{P}_1$ and $^3\mathrm{S}_1$ states into account together with the qutrit states $^1\mathrm{S}_0$, $^3\mathrm{P}_0$ and $^3\mathrm{P}_2$. The numerical simulation, visualized in Fig. 3.4a (gray line), includes all dipole-allowed couplings for which we compute the corresponding Rabi frequencies between states $|J_0, m_0\rangle$ and $|J_1, m_1\rangle$ according to:

$$\begin{aligned}\Omega_i = p_q \cdot E_i/\hbar \cdot D_i \cdot \begin{pmatrix} J_0 & 1 & J_1 \\ m_0 & q & -m_1 \end{pmatrix} \\ \times \sqrt{2J_1 + 1} \cdot (-1)^{J_0 + J_1 + J_> - m_1}.\end{aligned} \tag{3.6}$$

Here, p_q is a polarization projection factor, $q = -1, 0, 1$ labels the polarization σ^-, π, σ^+ of the light field ($i = 679, 688, 689$) and $J_>$ denotes the larger value of J_0, J_1 [166]. The Rabi frequency depends on the electric field strength $E = \sqrt{4P/(\pi w_0 c \epsilon_0)}$ for given power P and beam waist w_0 and the reduced dipole matrix element $D = \sqrt{3\epsilon_0 \hbar \lambda_0^3 \Gamma/(8\pi^2)}$ on the transition with the inverse lifetime Γ and the transition wavelength λ_0. In addition to the unitary Rabi couplings, we also include incoherent decay from the states $^3\mathrm{S}_1$ and $^3\mathrm{P}_1$ and simulate the dynamics via a Lindblad master equation. The numerical simulation, which is in more detail discussed in Appendix C, indicates that the three-photon coupling can be used at significantly higher fidelities, compared to the demonstrated dephasing rate of $1/\tau = 3.9(1)$ kHz and the corresponding $\Omega/2\pi \cdot \tau \approx 4.9$.

Coherent two- and three-photon couplings

In addition to the three-photon coupling from ground to clock state $^1\mathrm{S}_0 \leftrightarrow {}^3\mathrm{P}_0$, we realize a three-photon coupling between $^1\mathrm{S}_0 \leftrightarrow {}^3\mathrm{P}_{2,m_j=0}$ by substituting the 679 nm

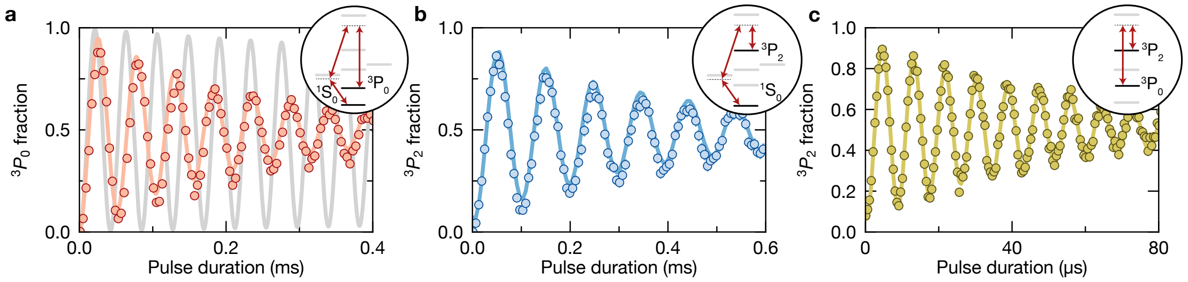

Figure 3.4: Three- and two-photon Rabi oscillations. **a** Three-photon Rabi oscillations between the ground state $^1S_0$ and the clock state $^3P_0$ driven by three phase-coherent light fields at 689, 688 and 679 nm. The red line shows an estimation of the expected dephasing based on the independently measured laser phase noise. For a noise-free system, we compute the expected dephasing due to off-resonant scattering (gray trace). See the main text for details regarding the phase-noise modelling and numerical simulations. **b** To drive three-photon couplings from $^1S_0$ to $^3P_2$, we substitute the 679 nm light field with a beam at a wavelength of 707 nm. **c** The meta-stable clock states are connected by a two-photon process using the 679 and 707 nm beams, enabling fast couplings. Here, the dephasing is also limited by laser phase noise as discussed further in the main text.

light field with a phase-coherent beam at 707 nm. Using optical powers of $P_{689} = 75\,\mu\text{W}$, $P_{688} = 5\,\text{mW}$ and $P_{707} = 900\,\mu\text{W}$, we observe a three-photon Rabi frequency of $10.27(3)$ kHz on this transition, see Fig. 3.4b. We attribute the dephasing again to laser phase noise dominated by the excess noise of the 688 nm laser.

Scalability of the three-photon coupling We experimentally demonstrate a three-photon Rabi frequency of $19.16(2)$ kHz using optical powers of $P_{689} = 75\,\mu\text{W}$, $P_{688} = 8.2\,\text{mW}$ and $P_{679} = 850\,\mu\text{W}$ focused to an elliptical waist of approximately 240 μm (90 μm) along the horizontal (vertical) direction at detunings of $\Delta_{689} = 6\,\text{MHz}$ and $\Delta_{688,679} \approx 12\,\text{GHz}$. To estimate the feasibility of drastically enhanced three-photon Rabi frequency, we consider scaling up the power of the 688 nm and 679 nm beams by a common ratio β. In this case, the individual Rabi frequencies $\Omega_{688,679}$ are enhanced by a factor $\sqrt{\beta}$, implying that the three-photon Rabi frequency scales up linearly $\Omega_3 \propto \beta$. Since the single-photon scattering rates of the 688 and 679 nm beams depend as well linearly on β, the scattering-induced infidelity per π-pulse is unaffected, until off-resonant two-photon scattering on the $^3P_1$ state has to be considered. Realizing a three-photon Rabi frequency of 1 MHz at our given beam waist and detunings, thus corresponds to optical powers of approximately 410 mW at 688 nm, 43 mW at 679 nm while maintaining the power of 75 μW at 689 nm [71]. This demonstrates the scaling potential of three-photon couplings, and further Rabi frequency boosts are conceivable by increasing the power of the 689 nm beam. However, compensating for the enhanced off-resonant scattering in this case requires detuning the beam further, which gives rise to (destructive) interference of excitation paths mediated by different $^3P_1$ Zeeman levels [154]. To reach a Rabi frequency of approximately 1 MHz at equal beam waists, the direct single-photon coupling would require a prohibitively high optical power of 1 kW at a magnetic field strength of 1000 G.

Two-photon fine-structure manipulations Significantly faster coupling rates can be realized by coupling the two clock states $^3\mathrm{P}_0 \leftrightarrow {}^3\mathrm{P}_{2m_j=0}$ directly using a two-photon process mediated via the excited $^3\mathrm{S}_1$ state using light fields at 679 nm and 707 nm. Using optical powers of only $P_{707} = 900\,\mu\mathrm{W}$ and $P_{679} = 850\,\mu\mathrm{W}$ (focussed to an elliptical Gaussian spot with waists 240 µm and 90 µm), we obtain a Rabi frequency of 117 kHz on two-photon resonance. For this measurement, the applied polarization, which is angled by approximately 55° with respect to the quantisation axis, is suboptimal and effectively lowers the achievable coupling rate. This polarization choice, however, maximizes the three-photon coupling rates , and we choose to characterize the qutrit system under common conditions. The two-photon fine-structure Rabi oscillations, shown in Fig. 3.4c, exhibit dephasing on a timescale of 50.1(14) µs obtained from an exponential fit. To understand the limitations of the achievable coherence times in our angle-tuned trapping potentials, we carry out a detailed benchmarking of the T_2^* and T_2 times of the fine-structure qubit, which are discussed in the following.

3.3.4 Ramsey and spin-lock measurements

In order to bypass the excess phase noise of the 688 nm light field, we characterize the coherence times of the FS qubit. For the measurements discussed here, we initialize the atoms in the FS-subspace using a three-photon pulse in triple-magic conditions. During the initialization, we use a trap depth of approximately 0.5 mK, which gives rise to a radial trap frequency of 100 kHz. In this case, the three-photon pulse operates in the sideband-resolved regime and provides a motional-state-preserving initialization of the qubit register for the radial direction.

To measure the T_2^* time of the system, we use a Ramsey sequence on the FS qubit and vary the duration between two $\pi/2$-pulses. We observe Ramsey oscillations, which probe the differential light shift induced by the two Raman beams. While the two-photon coupling is resonant in the presence of both beams, their absence gives rise to an effective detuning, which causes the Ramsey oscillations. Our measurement, shown in Fig. 3.5b, reveals a tweezer-averaged T_2^* time of 463(7) µs obtained from an exponential fit. This rapid drop in Ramsey contrast is caused by an inhomogeneous distribution of the Ramsey frequency, i.e. a tweezer-dependent differential light shift, which we discuss in more detail in Section 3.3.5. To understand the limitations of the FS Rabi oscillations, we carry out a spin-lock measurement in comparison to the Ramsey sequence. Here, we first apply a FS $\pi/2$-pulse along the Y-axis of the Bloch sphere, which transfers the system into the state $|+\rangle = \frac{1}{\sqrt{2}}\left(|^3\mathrm{P}_0\rangle + |^3\mathrm{P}_{2,m_j=0}\rangle\right)$ aligned

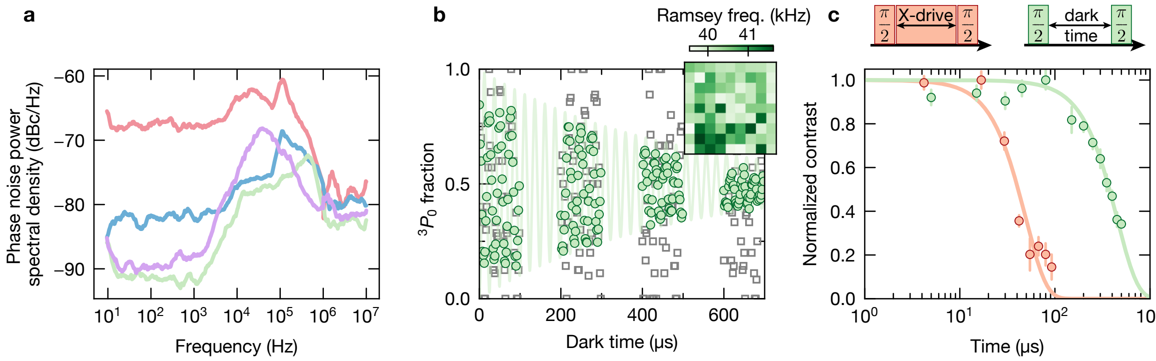

Figure 3.5: Fine-structure Ramsey and spin-lock measurement. a Phase noise power spectral density measurements for the light fields at 688 nm (red), 689 nm (blue), 707 nm (purple), and 679 nm (green). To estimate the noise densities, we analyze the in-loop radio-frequency beat signal of the respective laser and the common frequency comb. **b** Ramsey measurement on the fine-structure qubit carried out by varying the dark time between two $\pi/2$-pulses. The tweezer-averaged Ramsey contrast (green) rapidly drops due to an inhomogeneous distribution of Ramsey frequencies (inset). In contrast, the single-tweezer Ramsey contrast (gray squares) shows no noticeable drop on the shown timescales. The inhomogeneous distribution of the Ramsey frequencies is caused by polarization gradients across the tweezer array and is discussed in detail in the main text. **c** Comparison of Ramsey and spin-lock measurement. The Ramsey contrast (green) decays exponentially with a time constant of $\tau_R = 463(7)$ µs. For comparison, the spin-lock measurement (red) exhibits decay with a time constant of $49(4)$ µs. Here, we first apply a $\pi/2$ pulse around the y-axis of the Bloch sphere to align the system in the state $|+\rangle$ along the x-axis. The subsequently applied x-drive stabilizes the system before another $\pi/2$ pulse closes the interferometer. This technique provides insight into the laser phase noise as discussed in the main text.

along the X-axis. Subsequently, we turn on an X-drive, which stabilizes the system, before another $\pi/2$-pulse with variable analyzer phase translates the atomic phase back to measurable populations. We measure the contrast of the fringe when varying the analyzer phase for multiple X-drive durations. The spin-lock measurement, shown in Fig. 3.5c, exhibits a significantly faster dephasing than the Ramsey sequence on a time scale of $\tau_{se} = 49(4)$ µs. The observation that the driven system (spin-lock) dephases more rapidly compared to a sequence where the atoms spend most of the time in the dark (Ramsey) indicates that laser phase noise is limiting the contrast of the Rabi oscillations and hence the gate fidelity.

Probing the noise density with spin-lock measurements

Going beyond the comparison to Ramsey sequences, spin-lock measurements can be used to experimentally probe the phase noise of light fields at the position of the atoms, and in our case, can be used to measure the two-photon phase noise power spectral density directly. For sufficiently long probe durations, the exponential decay rate $\Gamma_{sl} = 1/\tau_{se}$ of the spin-lock can be directly related to the frequency noise power spectral density [165] as given by Eq. (3.7). A spin-lock measurement can then be used to measure the noise power spectral density at the Rabi frequency. Intuitively, this can be understood in a dressed state picture, where the $|+\rangle$ and $|-\rangle$ eigenstates of the driving field are separated energetically by the Rabi frequency Ω. The system remains in the $|+\rangle$ eigenstate throughout the evolution unless phase noise at the Rabi frequency, and hence at the energy splitting, drives the system into the $|-\rangle$ eigenstate.

$$\Gamma_{sl} = \pi^2 S_\nu(\Omega/(2\pi)) \tag{3.7}$$

$$S_\Phi = S_\nu/f^2 \tag{3.8}$$

In our case the measurement of $\tau_{se} = 49(4)$ µs translates to a frequency noise power spectral density of 2068(169) $\mathrm{Hz}^2/\mathrm{Hz}$. To compare this result to the measurements in Fig. 3.5a, we compute the phase noise power spectral density in units of dBc/Hz, which is given by $\mathcal{L}_\Phi = \log_{10}(S_\Phi/2) \cdot 10$ [167]. For the Rabi frequency of $\Omega/2\pi =$ 117 kHz we obtain a phase noise PSD of approximately −71 dBc/Hz in good agreement to the in-loop measurements in Fig. 3.5a. In conclusion, the spin-lock measurements, which probe the out-of-loop phase noise at the atomic position, indicate that currently laser phase noise is the main limitation for the two- and three-photon couplings, while numerical simulations show that limitations due to off-resonant scattering allow for substantially better fidelities. A detailed description of the linear response formalism, used here to relate the spin-lock measurement to the frequency noise density, is provided in Appendix B.

3.3.5 Coherence times

The fine-structure Ramsey measurement in Fig. 3.5b exhibits an ensemble-averaged contrast decay on the time scale of $\tau_R = 463(7)$ µs, caused by an inhomogeneous distribution of Ramsey frequencies. Indeed, the contrast of a single tweezer shows no noticeable dephasing on the experimentally-tested time scales of up to 700 µs, highlighting that the T_2^* time is limited by a inhomogeneous trap-induced differential light shift. Such inhomogeneities can be mitigated with dynamical decoupling techniques, characterized by the measurements shown in Fig. 3.6. Using a single spin-echo pulse, we obtain a T_2 time of $\tau_{se} = 36(2)$ ms on the FS qubit. The coherence time is further boosted using a XY-4 dynamical decoupling sequence that makes use of alternating π-pulses around the X- and Y-axis of the Bloch sphere, as sketched in Fig. 3.6c. At our trap depth of 46 µK we obtain a coherence time $\tau_{dd'} = 97(6)$ ms, which is further boosted to $\tau_{dd} = 346(37)$ ms upon lowering the trap depth to approximately 5 µK. We additionally benchmark the coherence time for a XY-8 dynamical decoupling protocol

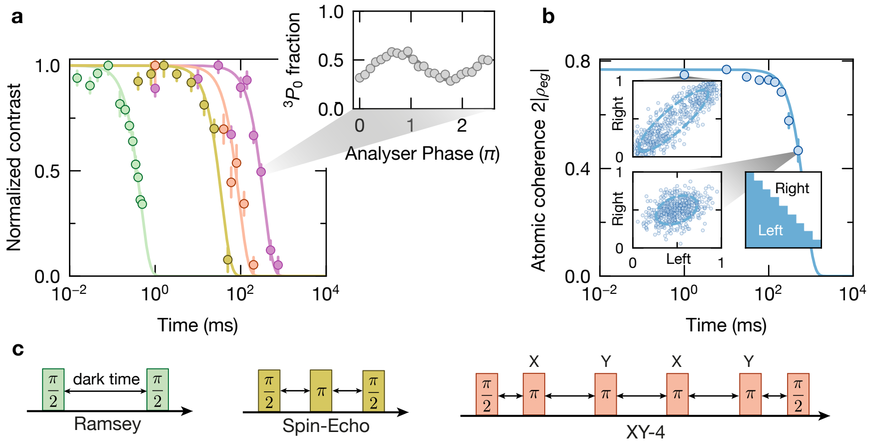

Figure 3.6: Fine-structure coherence time in triple-magic conditions. **a** Comparison of the measurements to benchmark the atom-laser coherence. We obtain a T_2^* time (green) of $\tau_R = 463(7)\,\mu\text{s}$, measured with a Ramsey sequence, at a trap depth of $46\,\mu\text{K}$. Applying a single spin-echo, we obtain a T_2 time of $\tau_{se} = 36(2)\,\text{ms}$ (olive-green), which is further boosted using a XY-4 dynamical decoupling sequence reaching $\tau_{dd'} = 97(6)\,\text{ms}$. At a lowered trap depth of $5\,\mu\text{K}$ we obtain an atom-laser coherence time of $\tau_{dd} = 346(37)\,\text{ms}$ using a XY-4 sequence. The inset shows a single measurement of the contrast obtained by varying the phase of the last $\pi/2$ pulse. **b** To additionally benchmark the atom-atom coherence time, we analyze correlations in the measurement and compute a lower limit for the coherence time. The analysis is based on averaging over all possible pairs of $g^{(2)}$ correlation functions and can be formally related to the off-diagonal entries of the density matrix; see the main text for details. To visualize the measurement, we divide the 9x9-site tweezer array into a left and right portion to correlate the excitation probability in each subset (insets). The eccentricity of the fitted ellips drops as a function of waiting time, which visualizes the drop in mutual atom-atom coherence. **c** Sketch of the pulse sequences used for benchmarking the coherence time. The total waiting time, indicated by the black arrows, is varied.

that makes use of more π-pulses; however, we obtain a low contrast and no noticeable enhancement of the coherence times, which we attribute to the limited π-pulse fidelity. We expect that longer coherence times are accessible using higher-order decoupling sequences and improved single-qubit gates. However, even the demonstrated atom-laser coherence time of 346(37) ms opens up interesting quantum computing perspectives due to the fast achievable coupling rates of several 100 kHz.

To benchmark the fundamental limits of the coherence time in tweezer-based angle-tuned trapping potentials, we estimate the atom-atom coherence time following an analysis presented in Ref. [32]. For a two-level system with states $|g\rangle$ and $|e\rangle$, a lower bound of the atomic coherence is given by (3.9). Here, C_b denotes the average of the $g^{(2)}_{ij} = \langle S_i S_j \rangle - \langle S_i \rangle \langle S_j \rangle$ correlator across all pairs of tweezers with indices i and j within a subset b, as defined by (3.10). The expectation value of the spin operator S_i with eigenvalues -1 $(+1)$ for the states $|g\rangle$ $(|e\rangle)$ is obtained by averaging over all repetitions of the experiment and over all phase values of the Ramsey-type sequence.

$$|\rho_{eg}| \geq \sqrt{\langle C_b \rangle / 2} \tag{3.9}$$

$$C_b = \frac{1}{N(N-1)} \sum_{i \neq j} g^{(2)}_{ij} \tag{3.10}$$

We obtain the expectation value $\langle C_b \rangle$ by dividing the tweezer array into subsets of 2×2 neighboring tweezer sites and average over all possible subsets. The resulting lower bound for the atomic coherence time of 715(30) ms is obtained from a Gaussian fit. To visualize the degree of mutual atom-atom correlations, we divide the tweezer array into two parts and correlate the excitation fractions as shown in Fig. 3.6b. The eccentricity of an ellipse fitted by a singular value decomposition visualizes the atomic coherence time, which can exceed the atom-laser coherence time significantly.

Our measurements demonstrate that state-of-the-art coherence times can be realized in systems of optical tweezer arrays that rely on magic angle tuning techniques despite the presence of polarization gradients within the tweezers, which give rise to position-dependent light shifts and motion-induced dephasing [168]. Demonstrating competitive coherence times for these systems marks an important achievement due to its applicability across a broad range of wavelengths and other atomic species. Our measurements also show the relevance of polarization gradients across the array, which are analyzed in Section 3.3.6.

Three-photon coherence times

In addition to the detailed benchmarking of the FS coherence time, we characterize the coherence times currently achievable on the three-photon transfer, which are summarized in Fig. 3.7a. We obtain a T_2^* time on the ${}^1\mathrm{S}_0 \leftrightarrow {}^3\mathrm{P}_{2,m_j=0}$ transition of $\tau_R^{{}^3\mathrm{P}_2} = 470(18)\,\mu\mathrm{s}$, measured with a Ramsey sequence. The T_2^* time obtained for the

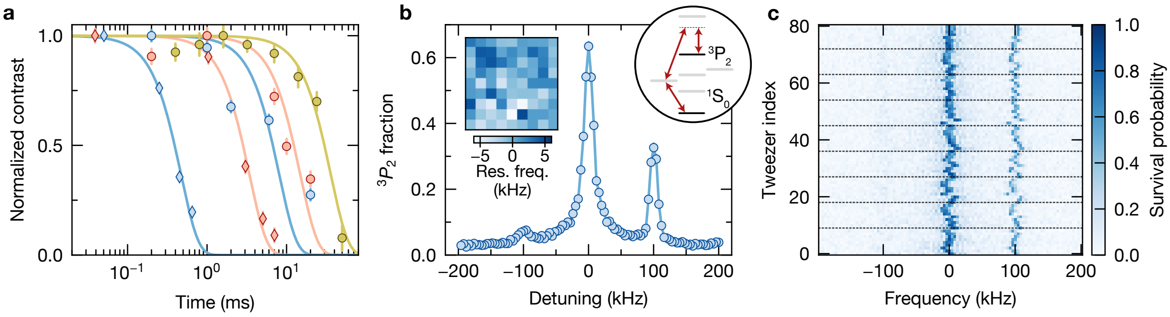

Figure 3.7: Three-photon coherence time & spectroscopy. **a** Comparison of the three-photon coherence times obtained in Ramsey- and spin-echo-type sequences. For the three-photon coupling on the $^1\mathrm{S}_0 \leftrightarrow {}^3\mathrm{P}_0$ and $^1\mathrm{S}_0 \leftrightarrow {}^3\mathrm{P}_{2,m_j=0}$ transition, we obtain a T_2^* time of $\tau_R^{^3\mathrm{P}_0} = 3.4(2)$ ms (red diamonds) and $\tau_R^{^3\mathrm{P}_2} = 470(18)$ µs (blue diamonds), respectively. Using a spin-echo sequence, the resulting T_2 times are $\tau_{se}^{^3\mathrm{P}_0} = 14.8(22)$ ms (red circles) and $\tau_{se}^{^3\mathrm{P}_2} = 8.1(24)$ ms (blue circles), respectively. For comparison, the spin-echoed T_2 time on the fine-structure states under equal conditions is $\tau_{se} = 36(2)$ ms (olive-green circles). **b** Three-photon spectroscopy on the $^1\mathrm{S}_0 \leftrightarrow {}^3\mathrm{P}_{2,m_j=0}$ transition in triple-magic conditions. The carrier in the center is accompanied by a cooling (heating) sideband on the left (right) offset by the trap frequency of about 100 kHz from the carrier. The imbalance of the cooling and heating sidebands confirms that near ground-state cooling is achieved with a mean residual excitation number of $\bar{n} = 0.14(4)$. A tweezer-resolved analysis of the carrier frequency (inset) shows a tweezer-dependent resonance shift that we attribute to polarization gradients across the array. **c** Tweezer-resolved spectroscopy of the three-photon $^1\mathrm{S}_0 \leftrightarrow {}^3\mathrm{P}_{2,m_j=0}$ resonance.

ground-to-$^3\mathrm{P}_2$-clock transition resembles the T_2^* duration on the fine-structure qubit, since both qubit choices are limited by the susceptibility of the $^3\mathrm{P}_2$ state to polarization gradients. This gets evident by the enhanced T_2^* duration of $\tau_R^{^3\mathrm{P}_0} = 3.4(2)$ ms observed on the three-photon $^1\mathrm{S}_0 \leftrightarrow {}^3\mathrm{P}_0$ transition, which is insensitive to a locally varying polarization angle. Using a spin-echo sequence, the resulting T_2 times are $\tau_{se}^{^3\mathrm{P}_0} = 14.8(22)$ ms and $\tau_{se}^{^3\mathrm{P}_2} = 8.1(24)$ ms, respectively. This demonstrates that dynamical decoupling sequences can also be applied to the three-photon couplings to mitigate inhomogeneous effects and suppress the influence of low-frequency noise sources. With improved phase noise densities, we expect also significantly enhanced atom-laser coherence times on the three-photon couplings.

3.3.6 Polarization gradients

Polarization gradients across the tweezer-array

To characterize the tweezer-dependent light shifts, we carry out precision spectroscopy on the three-photon ${}^1\mathrm{S}_0 \leftrightarrow {}^3\mathrm{P}_{2,m_j=0}$ transition. Our measurements, shown in Fig. 3.7b,c, resolve the radial motional sidebands of the tweezer array, which are offset by about 100 kHz from the carrier. The three-photon spectroscopy confirms the efficiency of the sideband cooling, reaching a mean residual number of motional excitations of $\bar{n} = 0.14(4)$ corresponding to a radial ground-state occupation of 88(3) %. The tweezer-resolved analysis reveals a tweezer-dependent shift of the carrier resonance, which resembles the distribution of Ramsey frequencies already encountered in Fig. 3.5b.

The resonance shift is caused by a position-dependent polarization, which gives rise to polarization gradients across the tweezer array. To estimate the local polarization tilt, the tweezer-dependent resonance shift Δf_{res} at a given trap depth U_0 is converted to a polarization angle correction following Eq. (3.11). Here, $\nu = 6.03\,\mathrm{kHz}/(\mathrm{mK}\,\mathrm{mrad})/k_B$ is the measured slope of the light shift as a function of magnetic field angle, obtained from the measurement in Fig. 3.3b.

$$\Delta\theta = \frac{\Delta f_{\mathrm{res}}}{U_0}\frac{1}{\nu} \tag{3.11}$$

The observed resonance shift of a few kHz (see inset in Fig. 3.7b) translates to an angular spread of about ±1.6 mrad across the tweezer array as shown in Fig. 3.8a. This distribution of locally varying polarizations is compatible with a small mismatch of the tweezer optics from a telecentric configuration. The optical setup, sketched in Fig. 3.8c, includes an SLM installed in the Fourier plane of the first lens with focal length f_1. Using a simple ABCD-matrix calculation, we estimate the effect of an axial displacement $\delta = d_1 - f_1 \neq 0$ onto the tilt φ' in the focal plane within the paraxial approximation. The model includes the lenses with focal length f_i and the free propagation over distances d_i. Assuming a centered input beam ($r = 0$), the tilt is given by Eq. (3.12). Here, $M = \frac{f_2}{f_1} = 3$ is the magnification of the relay telescope that images the SLM onto the back-focal plane of the microscope objective with focal length $f_3 = 24\,\mathrm{mm}$. Within our ABCD-matrix model, we find that the strongest sensitivity for tilts in the focal plane is given by a displacement of the first lens, and neglect additional deviations from a telecentric configuration.

$$\varphi' = \frac{M\varphi}{f_3}\delta \tag{3.12}$$

For the 9×9 tweezer array, the individual tweezers cover an angular spread of about $\varphi = \pm 2.5\,\mathrm{mrad}$ in the Fourier plane of the SLM system. This indicates a plausibel mismatch of $\delta \approx 5.3\,\mathrm{mm}$ with respect to a telecentric system in order to explain the

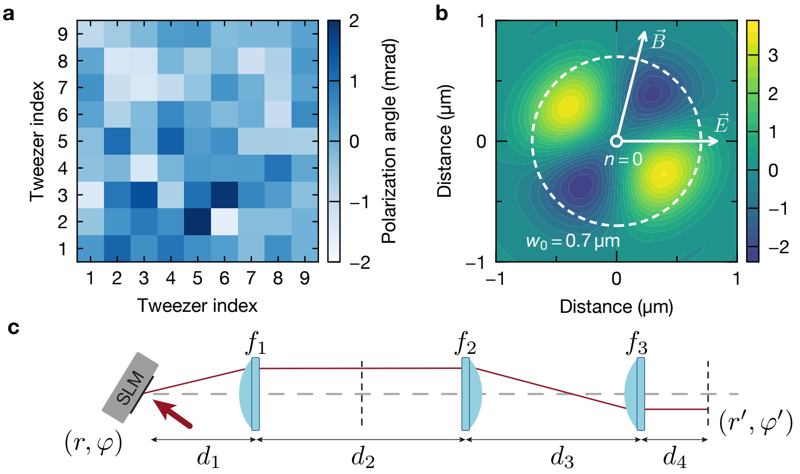

Figure 3.8: Polarization gradients. **a** The tweezer-dependent resonance shift on the $^1\mathrm{S}_0 \leftrightarrow {}^3\mathrm{P}_{2,m_j=0}$ transition is caused by polarization gradients across the tweezer array. Using the known sensitivity obtained from the magic-angle measurements, the resonance shift is translated to a locally varying polarization angle. This position-dependency is compatible with a small mismatch of the tweezer system from a telecentric configuration. **b** In addition to gradients across the tweezer array, the polarization within each tweezer exhibits gradients due to the high numerical aperture used to focus the beam. We compute the local polarization numerically by solving the vector Debye integrals and obtain the resulting differential light shifts for a ground-state trap depth of 46 μK and magnetic field strength of 19 G. The white dashed ring indicates the tweezer waist of about 700 nm and the inner solid ring indicates the root-mean-square extent of the ground state $\sqrt{\langle \hat{x}^2_{n=0} \rangle}$. **c** To generate the optical tweezer array, we use a SLM installed in a Fourier plane of the imaging system. For a telecentric configuration, the angle φ' in the focal plane is independent of the position. However, for small deviations $\delta = d_1 - f_1 \neq 0$ one obtains a position dependent angle and thus a spatially-dependent polarization gradient.

polarization gradients across the tweezers. For a larger tweezer array the polarization gradients across the array give rise to a larger spread of resonance frequencies and would further reduce the ensemble-averaged T_2^* duration, however, with an improved axial alignment of the optical system, this effect can be eliminated. To provide a sufficiently precise alignment, it is advisable to confirm the axial placement of the lenses using an infinity corrected camera. To that end, one first prepares an infinity corrected camera by imaging a target that is sufficiently far away. To avoid chromatic shifts, a suitable filter is installed in front of the camera. We typically image a pattern, like a tree, a sign, or a building, at a distance of several 10s of meters and lock the lens-camera-assembly to a fixed distance. Subsequently, the SLM can be placed precisely in the Fourier plane by imaging the phase pattern through the first lens and the infinity-corrected camera assembly. If the SLM shows a pattern with sharp corners, e.g., a checkerboard pattern, the relative distance can be accurately set in order to generate a sharp image.

In addition to polarization gradients across the tweezer array, each individual tweezer exhibits a spatially varying polarization due to the high numerical aperture of the focusing lens [146]. This gives rise to a spatially varying differential light shift, which is discussed in the following.

Polarization gradients within each tweezer

To compute the energy landscape within each tweezer, we first compute the local polarization by solving numerically the vector Debye integrals [169]. Afterwards, we compute numerically the eigenstates of the Hamiltonian, which includes the light field and the magnetic field $H = H_E + H_B$. The magnetic part $H_B = \mu_B \, g_J \, \vec{J} \cdot \vec{B}$ contains the coupling of the angular momentum operator $\vec{J}$ to the magnetic field $\vec{B}$ with the Bohr magneton μ_B and the Landé factor g_J. The electric field contribution is given by Eq. (2.6) for the special case of a linearly polarized trap [138, 168]. Solving the eigenstates numerically for our magnetic field strength of 19 G and a ground-state trap depth of 46 µK, we find the differential energy landscape shown in Fig. 3.8b. This calculation shows that tweezer-arrays are susceptible to polarization gradients, which give rise to sizeable differential light shifts even at shallow trap depth. Realizing long coherence times in these systems thus requires cold ensembles to minimize the inhomogeneous distribution of differential light shifts sampled by a thermal ensemble.

Importantly, our measurements have shown that long coherence times in tweezer-based angle-tuned trapping potentials are feasible despite the polarization gradients within each tweezer even in the absence of three-dimensional ground-state cooling [168]. This is a decisive demonstration that makes the fine-structure qubit an intriguing candidate for large-scale quantum computing. To minimize the effect of polarization gradients, we envision trapping the atoms in optical lattices instead of tweezer arrays. This not only minimizes polarization gradients, but also provides a favourable scaling of the number of trapping sites with the available laser power, which is discussed in Section 4.4.4. The following section provides a detailed characterization of the FS qubit at different trapping laser wavelength in the IR regime, where high-power laser sources are readily available.

3.3.7 Fine-structure qubits trapped in IR wavelength

To characterize the fine-structure qubit for trapping wavelength in the infrared regime, we first load single atoms into a tweezer array at a wavelength of 520 nm and subsequently implant the atoms into well-defined sites within our horizontal two-dimensional

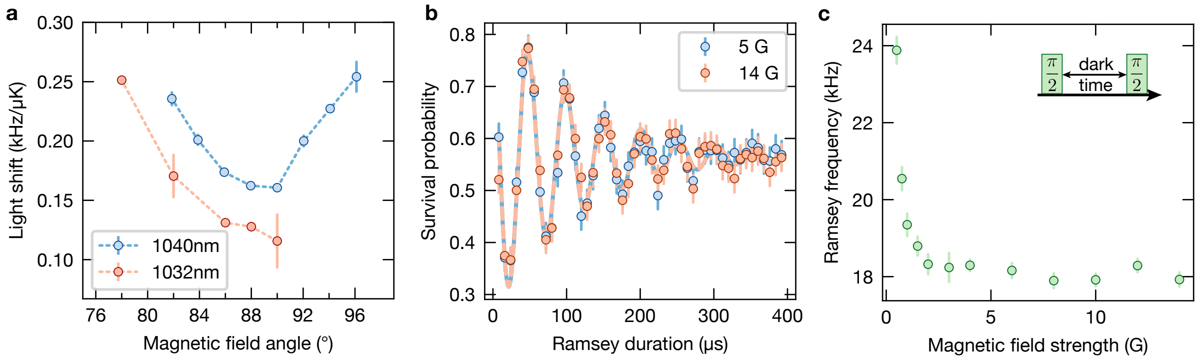

Figure 3.9: Fine-structure magic angle spectroscopy in an IR lattice. a To characterize the trapping conditions in the lattice, we repeat the Ramsey-based magic angle spectroscopy and extract the trap-induced differential light shift as a function of the magnetic field angle. At our wavelength, we expected a magic angle just below 90°; however, we find that magic conditions on the FS qubit are not available at this wavelength. To exclude an uncontrolled tilt between magnetic field and light polarization, we vary the angle and even invert the polarity of the vertical coil pair to access angles above 90° in our parametrization. **b** Ramsey oscillations between the fine-structure states in the optical lattice at 1040 nm. To rule out that the rapid dephasing is caused by an insufficient magnetic field strength, we measure the Ramsey frequency as a function of field strength without changing the field angle. **c** The Ramsey frequency probes the trap-induced differential light shift, and a sufficiently strong magnetic quantization axis is required for magic angle tuning. Here, a trap depth of about 75 μK is used, and a magnetic field of at least 3 G is sufficient to define the quantization axis.

optical lattice. The loading procedure is in detail described in Chapter 4, and this section instead focuses on the properties of the FS qubit.

In order to obtain the trap-induced differential light shift, we measure the Ramsey frequency as a function of trap depth for various magnetic field angles, as already outlined before. According to theoretical estimates, shown in Fig. 3.3c, we expect a magic angle in the close vicinity of 90°. At the trapping wavelength of 1040 nm we, however, observe no zero-crossing of the light shift and obtain the lowest differential light shift for a 90° angle, see Fig. 3.9a. Given the close vicinity to a right angle, this could, in principle, be caused by a tilt of the coil assembly or the lattice polarization with respect to each other. To test this experimentally, we change the polarity of the vertically-oriented bias coils and benchmark angles above 90° in the chosen parametrization. The measurement confirms that the lowest differential light shift is reached for right angles, which confirms the correct orientation of coils and polarization and implies that magic angle tuning of the FS qubit is not possible at a wavelength of 1040 nm. The discrepancy to our theoretical estimates is caused by residual uncertainties of the polarizability on the order of $\mathcal{O}(10\,\%)$. While these uncertainties are typically negligible for the estimation of realistically feasible trap depth in experiments, they sensitively affect the magic angles, which depend on the polarizability difference of electronic states, see Eq. (2.8).

Magic angle tuning requires a sufficiently strong magnetic field to avoid a competition of quantization axes with the electric field polarization. To rule out that the measurement is limited by an insufficient field strength, we measure the Ramsey frequency as a function of magnetic field strength, see Fig. 3.9b,c. The measurement shows that a magnetic field strength of about 3 G is sufficient to define the quantization axis at the trap depth of approximately 75 µK used here.

Despite the residual differential light shift of about 150 Hz/µK, we benchmark the coherence time of the system. The T_2^* time, measured with a Ramsey sequence, shows a rapid dephasing on the time scale of 133(4) µs, obtained from an exponential fit. To mitigate inhomogeneities, we apply a spin-echo pulse and observe significantly longer coherence times shown in Fig. 3.10. The spin-echo contrast exhibits revivals with a modulated amplitude that varies on the time scale of about 1 ms. We attribute this modulation to an oscillation of atoms along the vertical direction, where the trap frequency for this measurement was approximately 1.3 kHz. In this case, the spin-echo sequence used here can give rise to rephasing, which counteracts the effect of the residual inhomogeneous differential light shift given by the envelope of the lattice beam. This measurement highlights the need for magic trapping conditions in order to decouple the internal and the motional degrees of freedom.

To confirm the assumption that the differential light shift drops at lower wavelength, we tune the lattice wavelength to 1032 nm and repeat the characterization of the FS magic angle, see Fig. 3.9a. Indeed, at this wavelength, the light shift is reduced, which indicates that magic angle tuning is feasible for some cut-on wavelength below 1032 nm. Recently published ab-initio calculations predict a wavelength of 1010(170) nm, where a magic angle of 90° is reached [141]. Due to the large uncertainty in the prediction, an experimental validation is required. Unfortunately, our optical lattice system is limited to wavelengths above 1032 nm because of the finite optical bandwidth of the high-power Ytterbium-doped fiber amplifier. To carry out the spectroscopy with a tunable light source, we make use of a Titanium:Saphir laser as described in the following.

Fine-structure 90° magic wavelength spectroscopy

In order to find the wavelength which provides magic trapping conditions for the FS qubit under a magnetic field angle of 90°, we focus an IR probe beam to a waist of 20 µm onto tweezer-trapped atoms. The tweezer array operates at a wavelength of 813 nm and the magnetic field is applied in the horizontal plane to generate FS-magic trapping conditions with respect to the tweezer potential. Additionally, the probe beam is provided with vertical polarization, which satisfies the right-angle constraint with respect to the magnetic field. Using a Ramsey sequence, we measure the differential

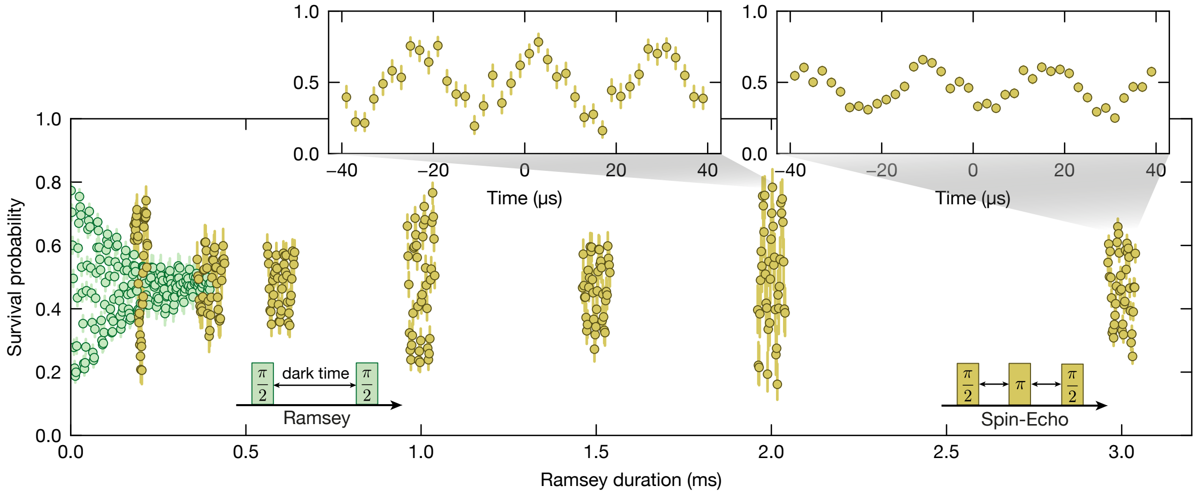

Figure 3.10: Fine-structure Ramsey measurement in the optical lattice. To benchmark the coherence time of the fine-structure qubit trapped in the optical lattice, at a wavelength of 1040 nm, we implant individual atoms from the tweezer array into the lattice and carry out a Ramsey sequence (green). Because of the residual light shift, the atoms quickly dephase on a time-scale of 133(4) µs obtained from an exponential fit. For comparison, we add a single spin-echo pulse, which considerably boosts the coherence time (yellow). The contrast of the spin-echo sequence exhibits a modulation on the 1 ms time scale, which we attribute to oscillations of the atoms along the vertical direction of the lattice, where the vertical trap frequency is approximately 1.3 kHz. The insets show the revival of the contrast due to the spin-echo.

light shift induced by the probe beam and calibrate the probe-induced trap depth via shelving spectroscopy on the intercombination line. At the available laser power of up to approximately 3 W, we can generate a trap depth of a few 10s of µK. To align the beam initially, we couple resonant light at 689 nm into the probe beam fiber and align the beam onto the atoms by addressing a Sisyphus heating resonance, which removes atoms from the trap. The correct alignment is confirmed with a tweezer-resolved probe shift measurement, from which we extract the beam waist at the atomic position. The measurement is presented in Fig. 3.11a and reveals a 90° magic wavelength for the strontium fine-structure states of 997(1) nm. This measurement provides the means to benchmark theoretical calculations in order to provide more accurate estimations of atomic polarizabilities. Furthermore, it implies that FS-magic trapping conditions can be realized at wavelengths below 997(1) nm, which may guide future experiments in this direction.

At this point, we can propose an efficient and robust architecture for quantum computing applications that makes use of the FS qubit, see Fig. 3.11b. A vertically polarized

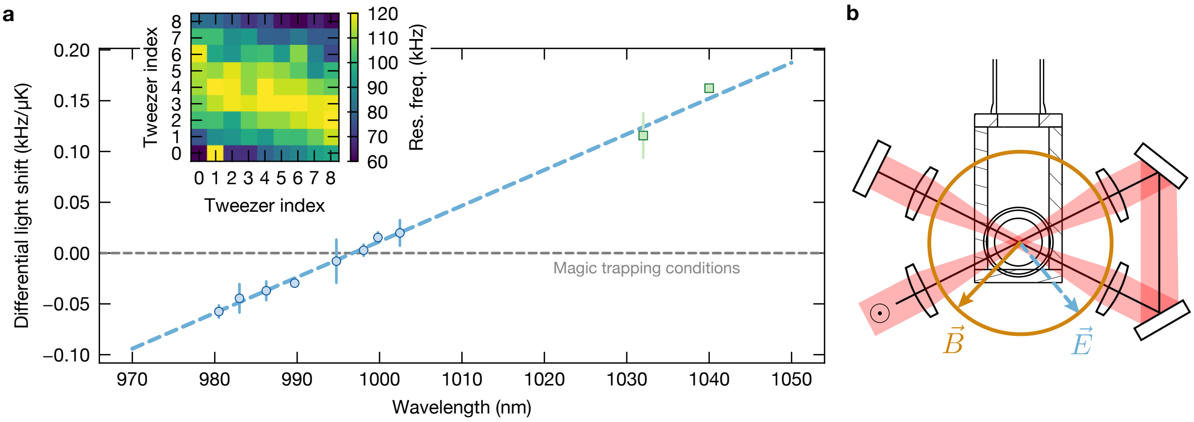

Figure 3.11: Fine-structure 90° magic wavelength spectroscopy. a We measure the wavelength for fine-structure magic trapping conditions for an angle of 90° between the trap polarization and the magnetic field. Here, we trap atoms in a 9x9 tweezer array at a wavelength of 813 nm and apply a magnetic field to generate magic conditions with respect to the tweezer array. In addition, we superimpose a vertically polarized probe laser beam at a variable wavelength and carry out a Ramsey sequence to obtain the probe-induced differential light shift (blue dots). The normalization to trap depth is done via shelving spectroscopy on the intercombination line, yielding a magic wavelength of $997(1)$ nm. For comparison, the measurements in the optical lattice at 1040 nm and 1032 nm are shown (green squares) in excellent agreement. The inset shows the probe-beam-induced tweezer-resolved light shift on the intercombination line, which confirms the correct centration of the probe beam on the tweezer array. **b** The 90° magic wavelength offers the possibility for a simple and robust architecture. A vertically polarized lattice provides fine-structure magic trapping conditions for any in-plane-oriented magnetic field. This flexibility can be used to additionally generate magic conditions for an in-plane polarized tweezer array, for example, at a wavelength of 813 nm. Using an in-plane magnetic field to satisfy both magic angle constraints has the advantage that the spurious effect of polarization gradients is suppressed, compared to an out-of-plane field.

lattice at 997 nm is generated in a power-efficient folded configuration. Individual atomic qubits are shuttled in the lattice geometry using tweezer arrays, for example, operating at a wavelength of 813 nm. The magic angle constraint for the optical lattice is conveniently fulfilled for any in-plane magnetic field. This freedom can be exploited to generate, at the same time, magic conditions for the vertically propagating and horizontally polarized tweezer array. Using an in-plane magnetic field is advantageous since it suppresses the effect of spurious gradients with a spatially varying out-of-plane polarization contribution. Such a setup combines the scalability of lattice-based systems with the single-site control of tweezers and the arbitrary connectivity enabled by the coherent shuttling of atoms. Chapter 4 contains a discussion of the assembly of atom arrays in optical lattice potentials. Recently, we demonstrated the coherent transport of atomic FS qubits using a AOD-driven tweezer at a wavelength of 813 nm, which paves the way to utilizing the FS qubit in zone-based architectures.

The multi-photon couplings are not only advantageous due to their relaxed magnetic field strength requirements, but also offer new possibilities that are not available in setups relying on direct single-photon transitions, such as the ability to realize a probe-shift-free coupling. In the following, we discuss a protocol for a measurement-free qubit reset exploiting the arbitrary two-photon control within the $^3\mathrm{P}_J$ manifold.

3.3.8 Measurement-free qubit reset

When driving three-photon Rabi oscillations, as discussed in Section 3.3.3, the system decoheres after some time to a mixed state which is no longer suitable for quantum information processing. Here, we present a protocol for a measurement-free qubit reset based on a dissipative reset via the state $^3\mathrm{P}_1$. For the three-photon $^1\mathrm{S}_0 \leftrightarrow {}^3\mathrm{P}_0$ qubit, we first drive three-photon Rabi oscillations. When the system decoheres we couple the state $^3\mathrm{P}_0$ to $^3\mathrm{P}_{1,m_j=-1}$ using a two-photon transfer via the phase-coherent light fields at 679 nm and 688 nm. Subsequently, the atoms decay to $^1\mathrm{S}_0$ where the population accumulates and thereby resets the qubit state. Afterwards, we resume the three-photon oscillations as shown in Fig. 3.12b. To realize the reset we implement a pulsed sequence of 1.1 µs-long two-photon pulses followed by a 50 µs waiting time during which atoms decay. This pulsed protocol minimizes unwanted Rabi oscillations during the reset in order to minimize off-resonant scattering from the intermediate excited state $^3\mathrm{S}_1$. We demonstrate the reset with a proof-of-principle experiment shown in Fig. 3.12a, where the residual $^3\mathrm{P}_0$ population is recorded as a function of the number of reset pulses. With improved laser phase noise and a more accurate calibration of the two-photon $^3\mathrm{P}_0 \leftrightarrow {}^3\mathrm{P}_{1,m_j=-1}$ π-duration, we envision that fewer cycles are needed to reset qubits.

Applied to the FS subspace, the dissipative reset protocol outlined here offers the possibility to selectively transfer the qubit states to $^1\mathrm{S}_0$ for state-resolved imaging. Compared to alternative approaches based on repumping the $^3\mathrm{P}_2$ directly, for example, using light at a wavelength of 497 nm, the two-photon transfer is sensitive to the m_j-substate of $^3\mathrm{P}_2$, which can be used to detect unwanted scattering events into $^3\mathrm{P}_{2,m_j\neq 0}$. Furthermore, the dissipative reset protocol may have application for recently proposed measurement-free quantum computation [170].

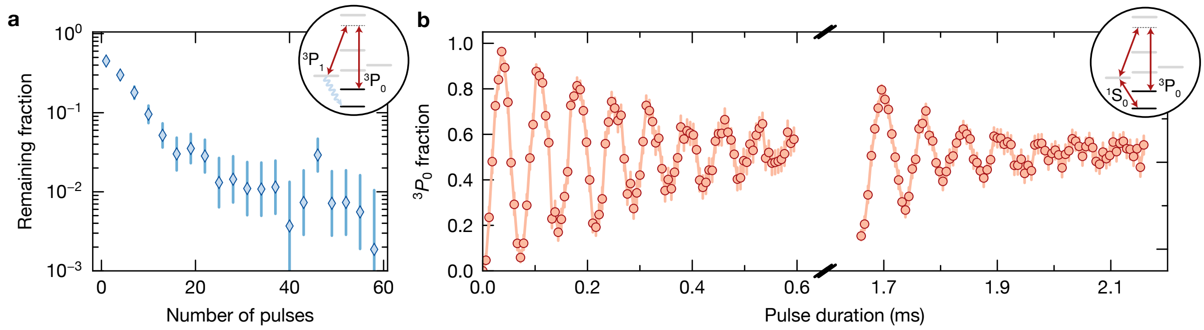

Figure 3.12: Measurement-free qubit reset. **a** To reset qubits without a projective measurement, we apply a two-photon pulse coupling the $^3P_0$ state to $^3P_{1,m_j=-1}$ from where they decay further to the electronic ground state. To avoid unwanted Rabi oscillations between the two states, we demonstrate a pulsed qubit reset starting with a 1.1 µs-long two-photon pulse followed by a 50 µs waiting time during which atoms decay. **b** We demonstrate a measurement-free qubit reset and drive three-photon Rabi oscillations from $^1S_0$ to $^3P_0$ until the system dephases. Afterwards, we apply the dissipative reset and resume Rabi oscillations.

3.4 Towards a low-phase-noise laser system

The measurements presented in this chapter have shown that laser phase noise is an important figure of merit for two- and three-photon transitions. This section provides additional technical details regarding the measurement of phase noise power spectral densities directly in the optical regime and presents techniques to reach substantially lower noise densities using feedforward noise suppression.

3.4.1 Measuring phase noise

Estimating the effect of laser phase noise relies on accurate measurements of the applicable noise densities in the experiment. Measuring phase noise can be done via a comparison to an optical reference. In this case, the light field of interest is superimposed with an optical reference, and the beat signal is recorded with a fast photodetector. The phase noise density can then be extracted by analyzing the electronic signal of the photodetector, which, however, requires a suitable low-noise optical reference. Practically, it is more convenient to measure the noise density of a light field directly in the optical domain using a fiber-coupled light field provided to a suitable analyzer. In this section, we characterize a home-built frequency noise analyzer following Ref. [171].

The working principle is based on a delayed self-homodyne detection in an imbalanced fiber-interferometer, and the setup is sketched in Fig. 3.13b. The input light,

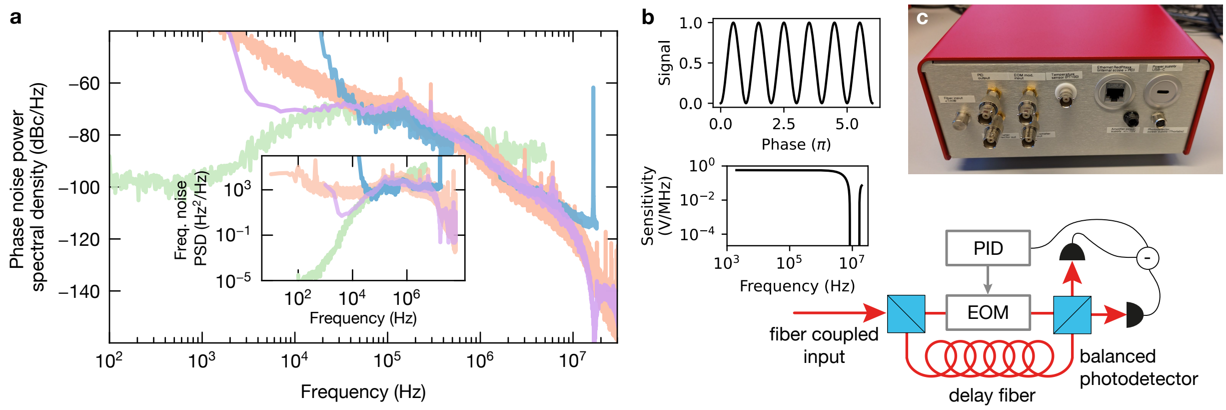

Figure 3.13: Phase noise measurement with an imbalanced fiber-based interferometer. **a** The phase noise power spectral density (PSD) of a test laser at 688 nm is measured with different devices. The laser is phase-locked to an optical frequency comb, and the phase noise PSD of the in-loop beat signal (green) is shown. For comparison, the noise density is measured with a LWA-10k from Highfinesse (orange), which exhibits a detection limit just slightly below the noise density. A lower detection limit is reached by a fiber-interferometer-based analyzer from Highfinesse (purple) and our home-built delayed self-homodyne interferometer (blue). The inset shows the same data in frequency noise power spectral density units. **b** The working principle of the delayed self-heterodyne interferometer is shown. The input light is separated into two arms, which feature a path-length difference, before being recombined on a balanced photodetector (PD). The signal of the PD depends on the relative phase of the interferometer arms. A linear dependency between output voltage and instantaneous laser frequency is guaranteed with a low-bandwidth lock. **c** Picture of the interferometer setup. We mount all components in a metallic box, which makes the interferometer a transportable, easy-to-use device for phase noise measurements in the optical regime.

delivered by a single-mode polarization-maintaining fiber, is split using a one-to-two-port fiber beamsplitter (Thorlabs PN670R5A1). One arm of the interferometer contains a 10m-long delay fiber and a fiber EOM (Jenoptik PM705), to control the relative phase with respect to the reference arm, before the arms are combined in a two-to-two-port fiber splitter (Thorlabs PN670R5A2). The output ports of the combiner are connected to a balanced photodetector (Thorlabs PDB425A). The voltage measured by the photodetector depends on the relative phase of the two interferometer arms as given by Eq. (3.13). Here, τ is the delay between the two interferometer arms and V_{pp} denotes the peak-to-peak voltage of the interferometer. Using the approximation $\nu(t) = \frac{1}{2\pi}\frac{d\Phi}{dt} \approx \frac{1}{2\pi}\frac{\Phi(t)-\Phi(t-\tau)}{\tau}$, the interferometer-voltage is proportional to the time-dependent instantaneous laser frequency $\nu(t)$ with the sensitivity $s_0 = V_{pp}\pi\tau$.

$$\begin{aligned} V(t) &= \frac{1}{2}V_{pp}\cos\left(2\pi v_0\tau + \Phi(t) - \Phi(t-\tau)\right) \\ &\approx \frac{1}{2}V_{pp}\left(\Phi(t) - \Phi(t-\tau)\right) \\ &\approx s_0 \times \nu(t) \end{aligned} \tag{3.13}$$

Since the PD voltage depends on the relative phase following a cos-dependency, which we approximate linearly, the interferometer path length difference has to be actively stabilized using a low-bandwidth lock. In the absence of activate feedback, we observe phase drifts of 2π on timescales of about 1 s, which are given by thermal fluctuations. Without restricting the interferometer to the linear slope of an interference fringe, the sensitivity is modulated, which prevents accurate phase noise measurements. To set up a low-bandwidth feedback, we use a microcontroller (RedPitaya STEMlab 125-14) which runs a software PID controller (PyRPL [172]) and apply feedback to the relative phase via the fiber EOM. The output voltage of the RedPitaya is amplified using an operational amplifier (OPA544), which can provide sufficiently high currents for the 50 Ω input impedance. The entire interferometer is mounted in an aluminium box (Thorlabs EC2030BR) featuring a fiber feedthrough and connections for various electronic signals, as shown in Fig. 3.13c. Thereby, the interferometer becomes a transportable device suitable for phase noise measurements directly from an optical fiber. The phase noise results, shown in Fig. 3.13a, agree with reference measurements taken with other devices.

The choice of the delay τ determines the interferometer sensitivity. In principle, a long delay is desirable to maximize the DC-sensitivity $s_0 \propto \tau$. However, the delay also determines the frequency-dependency of the sensitivity (3.14), which exhibits zero-crossings at integer multiples of $1/\tau$.

$$s(f) = s_0 \frac{\sin\left(\pi f \tau\right)}{\pi f \tau} e^{-i\pi f \tau} \tag{3.14}$$

For example, at our delay length of approximately 12 m (given by the 10 m fiber and the fiber EOM, which are installed in the same path), we obtain the first zero-crossing at about 16 MHz. Practically, a delay length of a few meters is thus a good choice and causes only low losses of the optical power. Taking phase noise measurements requires the interferometer to remain locked during the entire sampling duration, which is currently limited by the finite dynamic range of the EOM. Using a fiber-stretcher, based on a piezo-electric or a voice coil actuator, might provide better long-term stable locking due to the larger dynamic range, which can ultimately be combined with thermal control to keep the actuator close to its dynamic center.

To take measurements, we sample the interferometer voltage with an electrical spectrum analyzer, ensuring that the interferometer is locked during the entire duration.

Translating the output spectrum in units of a voltage noise PSD to a frequency noise PSD, we divide by the sensitivity (3.14). In order to measure s_0 precisely, we observe the output voltage for several seconds on an oscilloscope to obtain the peak-to-peak voltage V_{pp}. The delay is measured by extracting the frequency of zero-sensitivity directly from the spectrum. In the experiment, we read out the interferometer using a digital oscilloscope (PicoScope PQ290) and compute the spectrum via Fast Fourier Transform. In this setup, the outlined interferometer provides a low-cost solution to monitor the phase noise power spectral densities of critical laser systems and can generate updated measurements upon pressing a button to facilitate debugging and monitoring on a day-to-day basis. The following section contains a discussion of a new laser system optimized for coherent two- and three-photon transitions using a feedforward phase noise suppression technique with respect to a high-finesse ULE reference cavity.

3.4.2 Feedforward phase-noise correction

The phase noise PSDs of the comb-based laser system exhibit high noise levels in the range around 100 kHz due to the low locking bandwidth. The bandwidth is partially limited by the long cable and fiber length in the rack-based system and also suffers from excess noise picked up in the lock chain. In this system, the stability of a high-finesse ULE reference cavity is transferred onto the comb by first locking a transfer laser at 1542 nm to the cavity and subsequently phase-locking the frequency comb to the transfer laser. In a third step, the lasers of interest are referenced to the comb, implying that the noise density at each Fourier frequency is given by the worst phase lock in the chain, which gives rise to excess noise.

Here, we describe a different approach based on locking all lasers to a 4-bore high-finesse ULE reference cavity (Stable Laser Systems). The direct lock for each laser avoids excess noise caused by lock chains and the usage of a 4-bore reference cavity ensures a (mostly) common-mode drift of the lasers and provides a space- and cost-efficient implementation. We use 4 ECDLs (DLpro Toptica) at wavelengths 679, 688, 689, and 707 nm which are locked to the cavity with a Finesse of about 100k using the PDH technique. The cavity reflection is detected with a fast photodetector and the demodulated error signal is fed into a fast PID-controller (FALC pro Toptica) using a minimal cable length reaching a locking bandwidth of about 2.6 MHz.

The demodulated PDH error signal contains information about the instantaneous laser phase as given in (3.15) and is used for feedback onto the laser current and piezo, and is additionally used for feedforward noise suppression.

$$V_{\mathrm{PDH}} \propto E_0^2 J_0(\beta) J_1(\beta) \sin(\Phi(t)) \tag{3.15}$$

Here, E_0 denotes the electric field strength of the light field coupled to the cavity, J_i is the Bessel function of the first kind, and $\Phi(t)$ denotes the laser phase. The feedforward

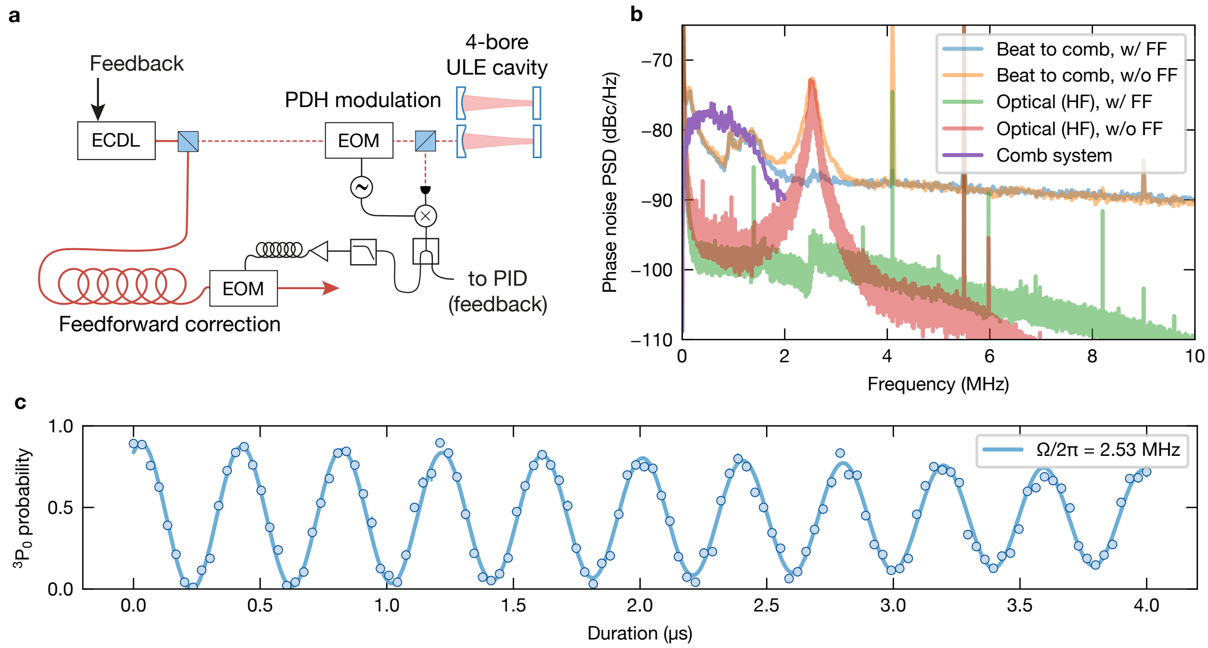

Figure 3.14: Feedforward phase noise suppression. **a** Improved laser system for coherent two- and three-photon transitions. We set up a 4-bore high-finesse ultralow-expansion cavity (ULE) and stabilize 4 external cavity diode lasers (ECDL) via the Pound-Drever-Hall (PDH) technique. The demodulated PDH error signal contains information about the instantaneous laser phase and is used for feedforward noise suppression. For that purpose, the light field is delayed in a 30 m-long delay fiber before a correction signal with suitably chosen gain and delay is applied via a fiber electro-optic modulator (EOM). The 4-bore cavity provides a cost and space-efficient solution and a common-mode resonance drift. Locking directly to the cavity sidesteps noise originating from the lock-chain required for comb-based systems and avoids shot-noise-induced detection limits. **b** Comparison of the noise densities of different laser systems and the effect of feedforward noise suppression. We analyze the noise density of a laser at 707 nm locked to the 4-bore reference cavity using an optical analyzer based on a delayed self-homodyne interferometer (red and green) and via a beat signal with the frequency comb (blue and yellow). The servo-bump at a frequency of 2.6 MHz is suppressed by 20-25dB when activating the feedforward suppression (green, yellow). The noise densities obtained with respect to the frequency comb, are detection-limited due to shot noise on the PD. **c** Preliminary demonstration of fine-structure Rabi oscillations at a Rabi frequency of 2.53 MHz.

noise suppression is based on delaying the light field in a 30 m-long delay fiber, which provides a delay of about 150 ns sufficient to obtain the demodulated and low-pass filtered error signal. Using a high-bandwidth DC-compatible power splitter, the error signal is divided into two branches used for feedback and feedforward correction. The feedforward noise suppression relies on applying a suitable signal to a fiber EOM. In order to compensate for the noise, it is critical to choose an overall circuit gain of unity and to combine the light field and the electronic correction signal with vanishing differential delay at the position of the EOM. To realize this experimentally, we use the setup sketched in Fig. 3.14a. The feedforward path is first low-pass filtered to suppress spurious contributions at the PDH-modulation frequency and then fed into a variable gain amplifier and a cable of adjustable length to match the delay with respect to the light field. Using this technique, we obtain a 20-25dB suppression of the phase noise PSD at the position of the servo-bump as shown in Fig. 3.14b. The noise densities are substantially improved compared to the comb-based system and pave the way towards MHz-regime coupling rates on the fine-structure qubit, as demonstrated in Fig. 3.14c.

Noise suppression

The suppression of the feedforward-corrected power spectral density $S_{out}/S_{in} = |1-G|^2$ depends on the overall circuit gain G to ensure that the noise is neither under- nor over-corrected. A deviation of about 3 % already limits the noise suppression to 30 dB, and an even higher suppression of 40 dB requires the gain to be accurate at the sub 1 % level. Since the PDH error signal (3.15) is proportional to the coupled optical power, this constraint is often violated because of thermal fluctations, for example, due to polarization rotation in fiber-optical components. Indeed, we observe a time-varying noise suppression at the 25 dB level corresponding to power variations of a few %. To mitigate this problem, we prepared an adaptive gain circuit [173], which provides a voltage-controlled amplification to scale the overall gain inversely proportional to the optical power transmitted through the cavity. This approach requires no additional optical components and was shown to support a long-term stable noise suppression at the 40 dB level [173].

Optimizing the feedforward parameters

To obtain the first indication for feedforward (FF) noise suppression, we make use of a two-channel function generator, which we connect to the AC-coupled current modulation port of the laser and directly to the feedforward EOM. We then modulate the laser current at a frequency around or slightly above the servo-bump to purposefully add noise, which we monitor with an imbalanced fiber interferometer. Subsequently, we deactivate the current modulation and apply a similar modulation at the same frequency to the FF-EOM and choose the modulation strength such that the noise amplitude approaches the previously observed noise amplitude. Next, we activate both signals and optimize their relative phase in order to counteract the current modulation with the FF-EOM. The optimal suppression is reached by iteratively varying the amplitude and phase of the signal provided to the EOM, which is simultaneously monitored on an oscilloscope. Afterwards, the FF circuitry is connected to the EOM, and the amplitude and delay are set to resemble the previously applied modulation. However, now the signal is generated via the demodulated PDH error signal and the FF electronics, which gives rise to broadband noise suppression. Finally, the parameters delay and gain are optimized based on the optically measured noise densities. In addition to the interferometer-based characterization, it is convenient to interfere the feedforward-corrected light field with the cavity transmission and monitor the phase noise of the beat signal. Our setup includes the fiber-ports to realize suitable beat signals; however, we have so far reserved the transmitted light for the purpose of stabilizing the FF gain using the adaptive gain circuit.

The noise suppression in Fig. 3.14b is currently limited, likely by a detection noise floor on the PDH reflection photodetector, which is above the shot noise limit [158]. Overcoming these limitations unlocks access to even lower noise densities down to $-120\,\mathrm{dBc/Hz}$ and below to effectively remove phase noise from the relevant infidelity budget of future setups. Alternatively, a feedforward noise suppression can also be set up based on the noise density measured with the fiber interferometer. In this case, the time-dependent voltage characterizes the instantaneous laser frequency, while the high-bandwidth correction via an EOM acts on the laser phase. Setting up an interferometer-based FF noise correction thus requires an integrator which can be conveniently realized via a simple low-pass filter with a sufficiently low cut-off frequency [171]. Compared to the PDH-based setup, this approach has the disadvantage of a frequency-dependent gain limited in the low-frequency regime by the low-pass filter and by the interferometer-sensitivity at high Fourier frequencies, but provides a flexible and low-cost solution to high-frequency noise suppression.

3.5 Summary and outlook

In this chapter, we have described the experimental realization and thorough characterization of an optical qutrit in strontium-88, which contains the electronic ground state ${}^1\mathrm{S}_0$ as well as both meta-stable clock states ${}^3\mathrm{P}_0$ and ${}^3\mathrm{P}_2$, separated by optical transition frequencies. Using two- and three-photon couplings, we have demonstrated all-to-all optical control over the qutrit states in magic-angle tuned trapping potentials. Here, the polarizability of the ${}^3\mathrm{P}_2$ state is tuned by applying a magnetic field under a suitable angle with respect to the linearly polarized tweezer array. Compared to the typically used single-photon clock excitation, the three-photon approach has the distinct advantage of requiring only a weak magnetic field. This enables coherent manipulations of the qutrit, since strong magnetic fields, required to drive the clock transition with a single photon, are constrained to one direction in our apparatus and are thus incompatible with magic angle tuning. Coupling either of the ^3P_J states to a Rydberg state, we envision creating three-dimensional entanglement in future studies [174].

Furthermore, the detailed benchmarking of the FS coherence demonstrates that state-of-the-art coherence times are feasible in tweezer-based angle-tuned trapping potentials despite the presence of polarization gradients within the trap. This technique is applicable across a broad wavelength range and even different atomic species and may enable new design choices of neutral atom processors for quantum simulation and computing. Exploiting the long coherence time of the FS qubit, we recently demonstrated a universal gate set on this meta-stable qubit, including a Rydberg-mediated two-qubit controlled-phase (CZ) gate [75, 136].

In the following chapter, we discuss the assembly of scalable atom arrays using combined lattice-tweezer potentials, which have been used for some experiments to characterize the FS qubit at IR wavelengths. In addition, we will demonstrate a novel sideband cooling technique based on the long-lived $^3P_2$ clock state, which utilizes three-photon transitions in the lattice potential.

Chapter 4

Large-scale atom arrays in an optical lattice

4.1 Introduction

Neutral atoms in optical lattices are a powerful tool and have been successfully used, for example, for the analog quantum simulation of the Hubbard model [16, 17]. The simultaneous readout of density and internal spin state, enabled by quantum gas microscopes, was demonstrated for bosons as well as fermions and allows for the extraction of spin-charge-resolved correlation functions [36–38, 175], enabling a wide variety of quantum-simulation experiments [51–55]. In these systems, the initial state is typically realized as a Mott-insulating state with one atom per site. Starting with evaporative cooling, a degenerate gas of atoms is loaded into a single lattice plane with typical spacings of $0.5 - 1\mu$m. Under the action of on-site interaction and tunneling, the atoms self-assemble in the optical lattice potential [17, 129, 176, 177].

Complementary to this approach, optical tweezer arrays offer a platform to prepare individual atoms in configurable potentials, providing a versatile toolbox for the simulation of spin models [61, 148, 178–180], lattice-gauge theories [67, 68] and for digital quantum computing [20, 24, 26, 181]. Due to light-assisted collisions, the loading of atoms in optical tweezers is a stochastic process with typically half the tweezer sites remaining empty, and the preparation of defect-free ensembles relies on the direct assembly of arrays with mobile tweezers [58–60]. Compared to lattice systems, the interatomic spacings are typically larger and on the order of $\geq 2\,\mu$m, which enables (cross-talk-free) addressing with focused laser beams.

In this chapter, we combine the scalability of optical lattice systems with the single-site control offered by optical tweezers. We realize low-loss and high-fidelity imaging of individual strontium atoms trapped in our 1040 nm lattice potential using the repulsive Sisyphus cooling mechanism already introduced in Section 2.1.3, and demonstrate a survival probability as high as $99.80(5)\,\%$. By superimposing individual tweezers with specific lattice sites, we repeatedly transfer atoms between the lattice and the tweezer potential. This enables new experimental protocols, for example, to prepare the initial state of quantum walk experiments by implanting atoms at a configurable location [123]. Furthermore, we demonstrate a novel protocol to iteratively assemble large-scale atom arrays in the optical lattice. This overcomes scaling bottlenecks of tweezer-based systems by repeatedly adding atoms to the system. In addition, we demonstrate continuous operation of arbitrary atom arrays where inevitably occurring defects are refilled, maintaining an atom array of more than 1000 atoms for more than 1 hour. Finally, we discuss the direct loading of our horizontal two-dimensional optical lattice directly from a MOT and the preparation of sorted atom array in a single lattice plane. This offers a new approach to generate scalable atom arrays for quantum simulation, computing, and metrology applications. We demonstrate magic trapping conditions for the $^1S_0 \leftrightarrow {}^3P_2$ transition at 1040 nm and introduce a sideband cooling technique based on three-photon transitions in the lattice. Some of the results presented in this chapter are based on the publications [96, 182].

4.2 Preparation and fluorescence imaging of individual atoms

4.2.1 Imaging atoms trapped in green tweezers

Historically, the first trapping system of our experiment was given by a tweezer setup at a wavelength of 518 nm, which exploits the enhanced polarizability in the visible regime compared to the IR regime, see Fig. 2.2. To image atoms at this wavelength, we scatter photons at 461 nm and simultaneously cool on the intercombination line. A typical single-shot fluorescence image is shown in Fig. 4.1b for a rectangular tweezer array of 19×21 sites. At the green trapping wavelength, cooling is feasible either via repulsive Sisyphus cooling or resolved sideband cooling using the control given by magic angle tuning on the 689 nm transition. We optimize the imaging parameter for both settings in order to minimize atom loss; however, we find in both cases a residual loss probability of approximately 5 %. The losses are likely limited by a trap-induced ionization process, which drives electronic states other than the ground state above the ionisation threshold in a two-photon process [183]. The observed loss probability prevents the assembly of large-scale atom arrays.

4.2.2 Preparing and imaging atoms in the optical lattice

To remedy this issue, we installed a two-dimensional optical lattice in the horizontal plane, which is introduced in Section 2.2.1. The optical lattice provides spacings of 1.15 µm and 0.57 µm in the two horizontal directions, and we adjust the tweezer spacing to about 3.5 µm commensurate with the lattice grid, as shown in Fig. 4.1a. This allows transferring the atoms from the tweezer array into the optical lattice, which is generated at the wavelength of 1040 nm, and thereby sidesteps trap-induced ionisation losses. By implanting atoms from the tweezer array into well-defined lattice sites, we obtain images like Fig. 4.1c. At the lattice wavelength, the polarizabilities on the

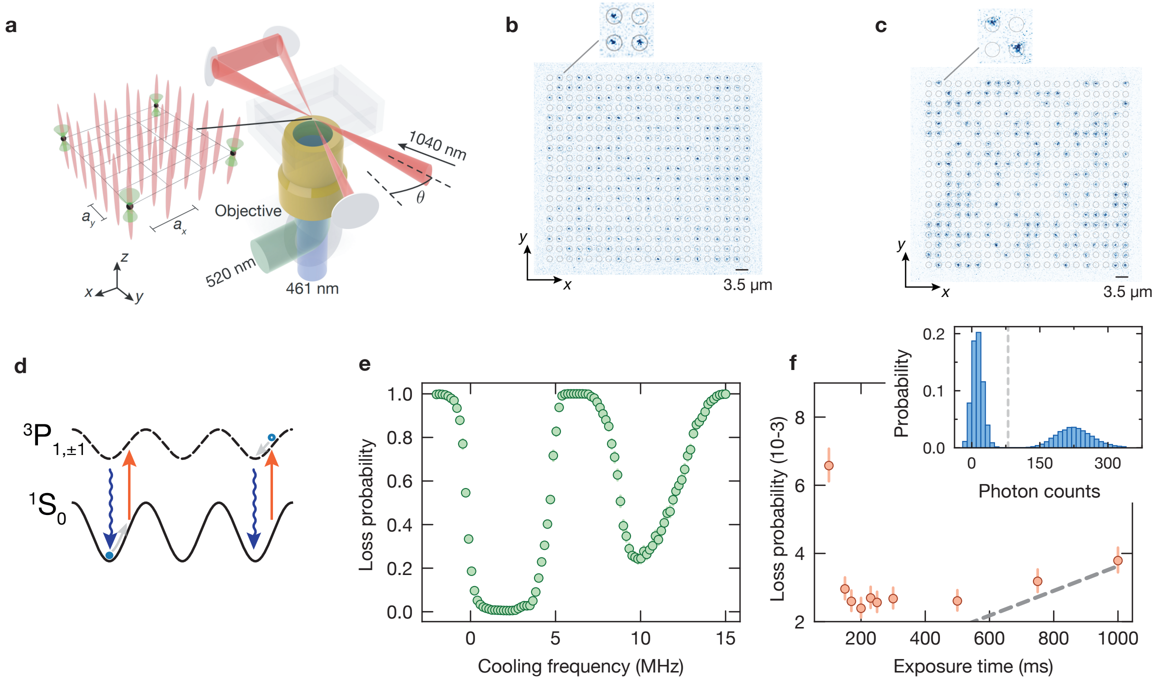

Figure 4.1: Fluorescence imaging in the lattice. **a** Sketch of the setup. To realize low-loss high-fidelity imaging and prepare single atoms at well-defined lattice sites, we first load atoms into tweezers and subsequently implant them into the optical lattice. This is realized by carefully adjusting the tweezer spacings in order to make them commensurate with the lattice spacings. **b** Fluorescence image of atoms trapped in the optical tweezer array at a wavelength of 520 nm. **c** Fluorescence image of atoms taken in the optical lattice. The occupation resembles the shape of the tweezer array since the lattice is loaded by implanting atoms from the tweezer array into the optical lattice. Due to the weaker vertical confinement, the fluorescence shows a broader distribution compared to images taken in the tweezers. **d** To cool the atoms during imaging, we implement repulsive Sisyphus cooling on the intercombination line. At our trapping wavelength of 1040 nm, the polarizability of the ground state exceeds the polarizability of the $^3P_1$ state. Cooling is most efficient on the σ-transition as evident from the cooling frequency scan. **e** Scan of the cooling frequency for repulsive Sisyphus cooling. We measure the survival probability of atoms during a fixed duration of imaging conditions and obtain a survival probability as high as 99.80(5) %. **f** High-fidelity and low-loss detection requires balancing the heating and cooling rates. We maintain an approximately constant number of scattered photons and vary the scattering rate and exposure time accordingly. For fast exposures, the cooling cannot compensate for the heating, giving rise to enhanced losses. In the other extreme, for very low scattering rates and long exposures, losses can be vacuum-limited (dashed line). The integrated photon count in a given ROI shows a bimodal distribution (inset), used to obtain the lattice occupation.

intercombination line allow for repulsive Sisyphus cooling, and we choose the cooling frequency in order to minimize atom loss during the exposure. The frequency scan, shown in Fig. 4.1e exhibits a robust low-loss regime for a blue detuning of a few MHz with respect to the free-space resonance. Note that the chosen frequency is red detuned with respect to the light-shifted (σ) resonance in order to realize the repulsive Sisyphus cooling mechanism sketched in Fig. 4.1d. A second cooling feature, corresponding to Sisyphus cooling on the $^3\mathrm{P}_1$ π transition shows an enhanced loss probability, which we attribute to simultaneous Sisyphus heating on the σ transitions.

In order to implement low-loss imaging, the scattering-induced recoil heating has to be compensated by a sufficiently high cooling rate. At fixed cooling power and frequency, we vary the scattering rate of the imaging beam while maintaining an approximately constant number of detected photons. As shown in Fig. 4.1f, the loss probability for short exposures rapidly rises, which corresponds to a setting where the heating rate exceeds the cooling rate. On the other side, for very long exposure times, the loss becomes vacuum-limited despite the vacuum-lifetime of about 270 s. We obtain the lowest loss probability for exposure times around 200 ms where the reported loss is limited by hopping of hot atoms in the lattice potentials, which we classify as lost with respect to the initially loaded site. The rather long exposure time is currently required due to insufficient vertical trap frequency in the lattice potential. Since the vertical confinement is only given by the Gaussian envelope of the lattice beam, the atoms explore a volume beyond the depth of focus of the objective, which results in an effective loss of photons. Additionally, the vertical motion of atoms broadens the single-atom fluorescense distribution which is noticeable in Fig. 4.1b, c. Resolving the lattice spacing down to 0.57 µm in the presence of a broadened point-spread-function requires a high signal-to-noise ratio, which further prolongs the imaging duration. With stronger vertical confinement, we envision that high-fidelity and low-loss images are feasible on shorter time scales. The outlook in Section 4.6 contains a short discussion of suitable setups. These upgrades would also be beneficial for transferring atoms between lattice and tweezer potentials, which we discuss in the following.

4.2.3 Repeated transfer of single atoms from tweezers to lattice

To characterize the transfer of individual atoms between the lattice and tweezer potentials, we first load the tweezer array and sideband-cool the atoms to their radial motional ground state. We then superimpose the lattice potential at maximal trap depth of about 1.5 mK and ramp down the tweezer intensity, thereby implanting atoms at specifically chosen lattice sites. To return them to the tweezer potential, we follow the sequence outlined in Fig. 4.2a starting with Sisyphus cooling in the lattice potential alone with a depth of about 1.5 mK. Subsequently, we ramp up the tweezer potentials to a depth of 0.3 mK and afterwards ramp down the lattice potential to a residual depth of about 0.15 mK. Again, we cool atoms in the combined optical

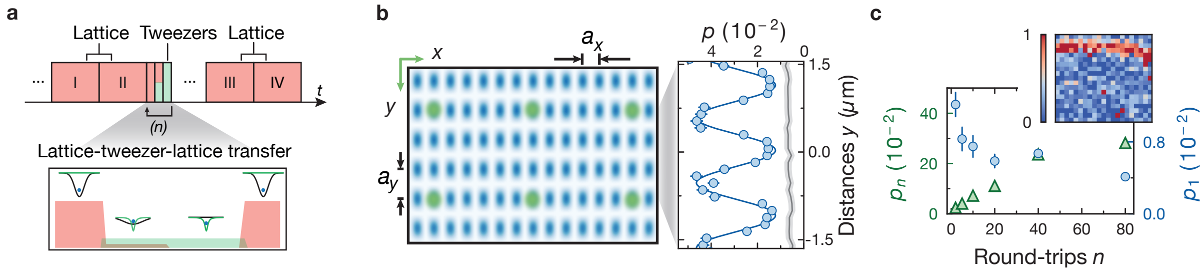

Figure 4.2: Repeated transfer between lattice and tweezers. **a** Sequence for benchmarking the repeated transfer from atoms between the tweezer and lattice potential. The atoms are initially implanted into the lattice from the tweezer array and imaged. Afterwards, the atoms are cooled in the deep lattice potential alone using repulsive Sisyphus cooling. Subsequently, the lattice depth is lowered, and the tweezers are superimposed, enabling cooling in the combined lattice and tweezer potential. Finally, the lattice is ramped down, thereby transferring the atoms back to the tweezer array. **b** Efficient repeatable tweezer-lattice transfer requires to carefully superimpose the potentials. The lattice potential (blue) is given by an equidistant grid of lattice sites with spacings 579(2) nm and 1187(18) nm along the x- and y-direction, respectively. The tweezer-positions (green) are adjusted to overlap with every 6th and 3rd lattice site, respectively. Long-term stable transfer between the potentials requires tracking the phase drift of the lattice potential (see inset). We ensure a common mode drift of the lattice and tweezer potential by applying a suitable diffraction grating to the SLM. **c** To benchmark the loss probability of the transfer, we carry out up to 80 transfer rounds (green). Assuming an exponential scaling, we obtain the single-round loss probability (blue) as low as 0.4 %. Here, the losses are dominated by an inhomogeneity of the system, as evident from the tweezer-resolved loss probability (inset).

potential before smoothly switching off the lattice potential. At this point, the atoms are again entirely trapped by the tweezer potential, which concludes one round of tweezer-lattice-tweezer transfer. Currently, the potential transfer does not preserve the temperature of the atoms that get heated during the process. However, being trapped in the tweezer potentials, the atoms can be reinitialized in the motional ground state via sideband cooling. We attribute the heating in parts to the strong mismatch of vertical trap frequencies. While the tweezers typically provide a vertical trap frequency of $20 - 30$ kHz, the optical lattice reaches only about 7 kHz at full depth.

Nonetheless, the controlled parallel implantation of atoms at configurable sites opens interesting perspectives to prepare initial states for quantum simulation experiments in the optical lattice [123]. In addition, the ability to transfer atoms back to the tweezer potentials decouples the power-demanding imaging procedure from the rest of the sequence. This provides the means to overcome scaling limitations of the tweezer system given by the finite available laser power. Specifically, the tweezer array may be operated at a shallow depth suitable for the physically-relevant part of the sequence and can be transferred to the optical lattice for imaging. This technique is compatible with arbitrary tweezer wavelengths and is favourable in cases where high-power laser sources are not available or where the trapping wavelength is not suitable for low-loss imaging.

Compensating slow drifts of the lattice phase

In our experiment, the phase of the optical lattice is freely drifting due to thermal fluctuations of the path length in the lattice interferometer. This gives rise to a continuous shift of the lattice sites with respect to the camera and also with respect to the tweezer potentials. To ensure a long-term stable overlap of the potentials, we extract the phase of the optical lattice from every image and store the result in a database for monitoring and postprocessing purposes. To compensate for the drift, we predict the lattice phase based on the recorded phase drift history and apply feedback to the global diffraction grating displayed on the SLM. Thereby, the entire tweezer array is displaced by a programmable amount to follow the drift of the optical lattice. Stabilizing the relative phase is a crucial requirement in order to minimize losses during the transfer as shown in Fig. 4.2b. When the experiment is thermalized and continuously running, we observe drift rates as low as 1 lattice site in 6 hours, given by the passive stability of the optomechanical setup. In addition to drifts of the optical lattice, we also observe slow variations of the tweezer position with respect to the camera, which we attribute to thermal expansion in the optical setup. The amplitude of these drifts reaches up to 600 nm, and we compensate for the drift by calibrating the position of the tweezers with respect to the camera in regular intervals. For that purpose, the control computer is configured to automatically interrupt the running sequence in a configurable interval of typically 30 min in order to run a calibration sequence. The data is automatically analyzed with a predefined procedure, and an updated grating-to-position calibration is written to a database and used for subsequent runs.

Transfer efficiency

Efficiently transferring atoms between the optical potentials requires precisely overlapping the tweezers with the center of the chosen lattice sites. In order to determine the lattice and tweezer spacings, we average several images and compute the Fourier transform, which exhibits peaks at multiples of the spacing in units of inverse camera pixels. Similarly, the rotation angles with respect to the camera can be determined by rotating the images in postprocessing and fitting the width of the peaks in the Fourier spectrum for each rotation angle. The lowest width corresponds to the case where the image is rotated along the eigenaxis of the optical potentials, which is used to accurately overlap the orientations of the grid-like potentials [136]. Finally, the remaining degree of freedom is given by a relative offset of the potentials.

To benchmark the efficiency of the tweezer-lattice-tweezer transfer, we carry out repeated rounds of transfers with up to 80 repetitions and record the loss probability of atoms, as shown in Fig. 4.2c. After 80 rounds we obtain an accumulated loss of about 30 %, which translates to a per-round loss probability of 0.4 % assuming an exponential scaling with run-independent loss probabilities. We observe that the per-round loss probability drops with a growing number of repetitions, which indicates limitations due to inhomogeneous effects. Indeed, we find that the losses after 80 round-trips exhibit a strong spatial dependence. These spatially dependent losses may be caused either by a suboptimal centration of the tweezer array in the lattice potential or an insufficient alignment to the relative spacings, which could give rise to a finite beating length modulating the losses as a function of position. Both effects can be readily suppressed with an improved relative alignment of the potentials. Optical tweezer arrays registered to individual sites of two-dimensional optical lattices facilitate new methods to overcome scaling bottlenecks of pure tweezer systems, and in the following, we discuss a protocol to iteratively assemble atom arrays.

4.3 Iterative assembly and continuous operation of atom arrays in the optical lattice

Scalable arrays of neutral atoms are a powerful and rapidly developing platform for several quantum technologies. For applications that require single-site addressing with negligible cross-talk, atoms are usually trapped in optical tweezer arrays and the feasible system size is typically limited by available laser power. Realizing large-scale systems is possible by merging tweezer setups at slightly different wavelengths, preferably in the infrared regime [70]. However, due to the finite transmission and associated optical losses in the objective, further scaled-up versions require additional developments, like a thermal management at the objective lens assembly.

4.3.1 Sequence for iterative assembly of atom arrays

Here, we present a different approach to scaling up atom arrays and introduce a protocol to iteratively assemble atom arrays starting with a finite-sized tweezer-based loading array. The experimental setup and sequence is outlined in Fig. 4.3 and Fig. 4.4. We partition the optical lattice into two zones, a loading zone and a storage zone, and repeatedly pick up atoms from the loading zone and position them in the storage zone. Atoms in the loading zone are initially loaded into a 19 × 21-site tweezer array at a wavelength of 520 nm and implanted into the lattice potential. Because of the finite laser power, the number of tweezers available for loading atoms is limited, and we use the iterative assembly procedure to overcome this limitations and provide a continuously growing number of atoms in the storage zone. To this end, we pick up atoms from the loading zone using an AOD-driven optical tweezer and position them

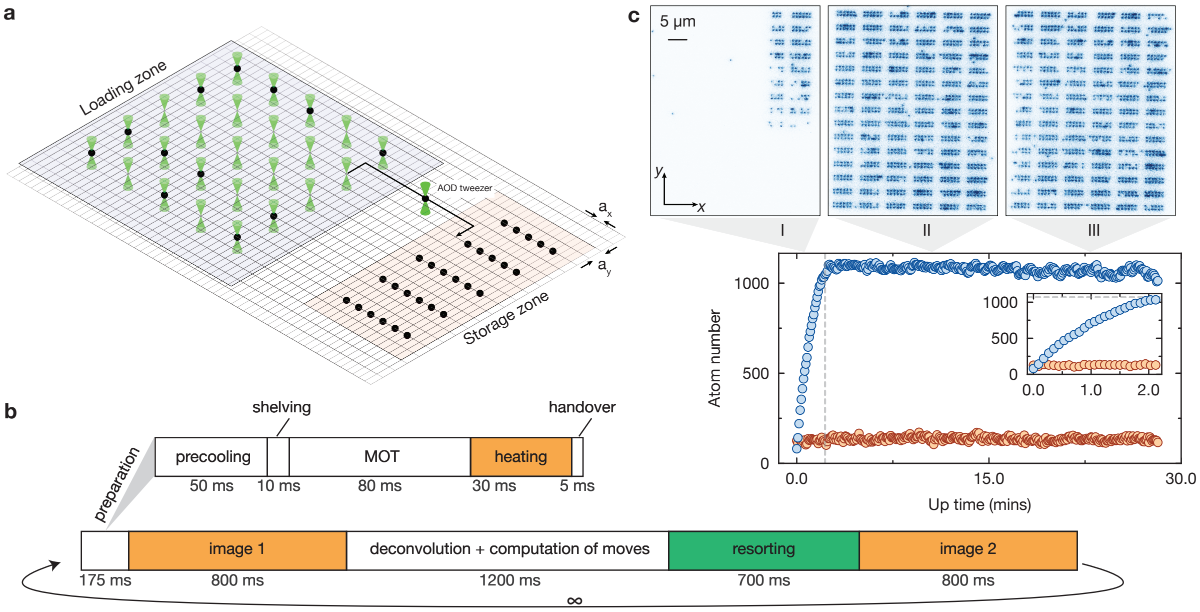

Figure 4.3: Iterative assembly of atom arrays. **a** To iteratively assemble atom arrays in the optical lattice, we partition the system into two zones. Atoms are repeatedly implanted into the loading zone, which is superimposed with a tweezer array loading individual sites. Using mobile optical tweezers, generated with acousto-optic deflectors (AODs), the atoms are moved into the storage zone where subsequent experiments can take place. **b** Sequence and timing diagram for iterative assembly. To restart a new round, we first cool ground-state atoms and subsequently shelve them into the long-lived $^3P_0$ state, before generating a new magneto-optical trap (MOT) to load the potentials. To constrain the loading to a few selected sites in the loading zone, which are shielded by the tweezers, we apply a selective heating pulse to empty unwanted direct loading into unshielded lattice sites. Afterwards, the atoms are imaged, the fluorescence image is deconvolved and processed, and the atoms are resorted. At this point, we take another image to benchmark the resorting. **c** The atom number in the loading zone (red) and the storage zone (blue) is shown as a function of time during the iterative assembly procedure. Using this technique, the atom array overcomes the size limit given by the number of available atoms per round. In the storage zone, the atoms are distributed following a configurable target distribution (insets). Here, we purposefully choose a target containing blocks of atoms separated by free “corridors” along which atoms can be shuttled.

on programmable target locations in the storage zone. Technical details of the image processing are discussed in Section 4.4, and here we initially focus on the experimental protocol.

Images of the atom distribution in the storage zone are shown in Fig. 4.3c. We purposefully choose a target pattern consisting of groups of atoms separated by free corridors. Each target position is connected in at least one direction to a corridor to facilitate the delivery of atoms from the loading zone to the target site along these corridors, in order to minimize disturbances to stored atoms on nearby target sites. We envision that groups of atoms can be shuttled as one unit in future studies and may act, for example, as logical qubits or multiplexed copies of analog simulations. When shuttling atoms, we choose a trajectory along the corridors to avoid collisions with atoms along the way. Similarly, the role of the implanting tweezer array is to provide atoms at addressable spacings in the lattice potential and to bypass the need for initially separating atoms at short spacings. Modifications of the initial loading procedure are conceivable, for example, to bypass the loading tweezer array in favour of other trapping potential, such as a nearby or overlapped dipole trap. However, care has to be taken to provide atoms at sufficiently large spacings to ensure a well-resolved selection of single atoms for the transport. This is relevant, in particular for the loading of a directly loaded lattice system, as discussed in Section 4.4, where the interatomic distances are randomly distributed.

The experimental sequence used for the iterative assembly is shown in more detail in Fig. 4.3c. Initially, we image the atoms in both the loading and the storage zone. To obtain the site-resolved occupation in the lattice potential, we apply a deconvolution algorithm [184] and compute the required moves to fill defects in the storage zone, before the moves are carried out. Finally, we image the atoms again to conclude the repetition. The iterative assembly protocol, in principle, allows adding an arbitrary number of atoms; however, due to losses, the achievable atom number is limited. In the steady state, the number of atoms added on each round is equal to the number of atoms lost per round. Parametrized in terms of the resorting infidelity α_r and the loss probability per cycle α_c, the final atom number N_∞ is given by (4.1). Here, N_L denotes the number of atoms loaded in each round.

$$N_\infty = N_L \frac{1-\alpha_r}{\alpha_c} \tag{4.1}$$

In our case, the amplification N_∞ / N_L is approximately 10-fold, limited by the losses per cycle, and significantly higher amplification factors are, in principle, feasible. In the following, we discuss in more detail the experimental procedure to connect individual resorting cycles.

Data processing

For this proof-of-concept demonstration, the repetition rate was limited by the time required for image processing and RF synthesis. Since then, we drastically reduced the technical overhead on all relevant substeps. Chapter 5 presents a new atom detection algorithm based on a deep convolutional neural network, which outperforms our previous algorithm in terms of noise resiliance and provides a full-frame reconstruction within less than 15 ms. In addition, we significantly lowered the signal processing duration of the RF generation, which is now based on an AWG PCI extension card (Spectrum Instrumentation M4i.6631-x8). The recently published firmware option for multi-carrier DDS-type signal synthesis (Spectrum Instrumentation M4i.66xx-DDS20) allows to program a parametrized waveform in terms of signal frequency, amplitude and phase for up to 23 channels.

4.3.2 Continuous operation

Maintaining atom arrays in optical potentials, while reloading a dedicated loading zone, enables the continuous operation of atom arrays. This not only boosts the number of atoms available for experiments, but also reduces the preparation time, since on each round it is sufficient to fix defects rather than assembling an entirely new array. The details of the protocol are outlined in Fig. 4.4. The cycle starts by creating a magneto-optical trap, which is located at the same position as tweezer and lattice systems. Therefore, both tweezer array and the optical lattice are loaded with atoms. In order to avoid problems with uncontrolled loading in the storage zone and insufficient inter-atomic distances, we need to restrict the loading to a few selected lattice sites within the loading zone. To select suitable sites, we overlap them with green tweezers, generating an extra tweezer-induced light shift on those sites. Subsequently, a selective Sisyphus heating pulse removes ground-state atoms from lattice sites that are not shielded by a tweezer. At the same time, we maintain the loading in sites protected by the tweezer-induced light shift. We observe a contrast of approximately 30 dB and maintain a loading fraction of 0.45 for the desired sites, see Fig. 4.4b. Subsequently, the atoms in both zones are imaged, and newly loaded atoms are moved to the storage zone to fill defects. At this point, the atoms are available for the experiment of interest and can be reused for the next cycle due to the non-destructiveness of the imaging process. To ensure that already existing atoms are not disturbed by the MOT of the next cycle, we shelve atoms into the long-lived $^3P_0$ state. The MOT is created without the 679 nm repumper, and the atoms are thus insensitive to the MOT light and the magnetic quadrupole field. To shelve atoms we address the $^1S_0 \leftrightarrow {}^3P_1$ resonance at 689 nm and additionally switch on a beam at 688 nm resonant with the $^3P_1 \leftrightarrow {}^3S_1$ transition and the $^3P_2$ repumper at 707 nm. In this configuration, the atoms accumulate in the $^3P_0$ dark state. The efficiency of the shelving process, shown in Fig. 4.4a as a function of the duration, saturates with a residual unshelved fraction of 3 %. This

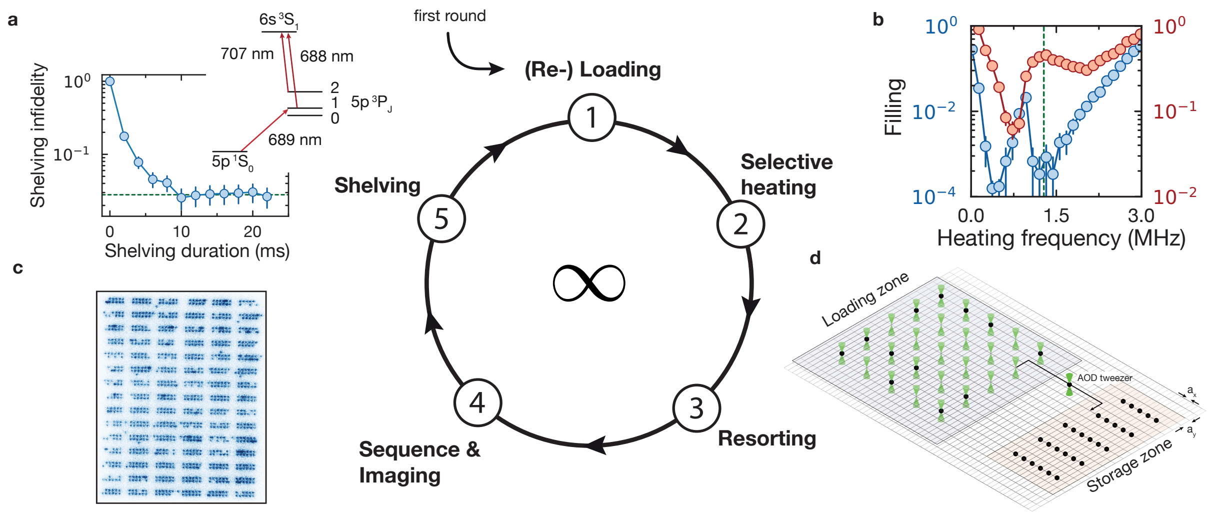

Figure 4.4: Continuous operation of atom arrays. The continuous operation of atoms is divided into 5 steps, starting with the loading of atoms in the loading zone on the first iteration. Creating a new magneto-optical trap gives rise to the loading of atoms in the entire lattice potential. Using a selective heating pulse, atoms trapped in lattice sites that are not overlapped with a tweezer are heated via Sisyphus heating and removed from the trap. Afterwards, the atoms are arranged in the storage zone and imaged nondestructively after using them for a sequence of interest. Subsequently, atoms in the storage zone are shelved in the long-lived $^3\mathrm{P}_0$ state before the continuous loading procedure repeats. **a** Efficiency of the optical shelving as a function of time. Using beams at 689 and 688 nm, the atoms are excited to the $^3\mathrm{S}_1$ state and decay back to the ^3P_J-manifold. Using a repumper at 707 nm ensures that all atoms accumulate in $^3\mathrm{P}_0$. **b** Efficiency of the selective heating pulse. For a suitable laser detuning (dashed line) on the intercombination line, we obtain a loading probability of approximately 0.45 for lattice sites superimposed with a tweezer (red trace). At the same time, unprotected sites (blue) exhibit a high loss probability with a contrast of about 30 dB. **c** Fluorescence image of atoms in the storage zone. We purposefully choose a target containing free corridors along which atoms can be moved without disturbing neighboring sites. Each target position is accessible from at least one direction without passing through filled sites. **d** The optical lattice is partitioned into two zones. Atoms are repeatedly implanted in the loading zone and subsequently arranged in the storage zone.

error sets the main limitation of the achievable array size in our iterative assembly protocol and is attributed to an inhomogeneous distribution of the narrow 689 nm resonance. Since the intercombination line is not magically trapped in the optical lattice, the Gaussian envelope of the lattice beams give rise to spatially varying light shifts, which limit the shelving efficiency. For the measurements presented here, the three-photon couplings were not yet available, and alternative shelving procedures are conceivable in future realizations. For example, the three-photon transfer from $^1S_0$ to $^3P_{2,m_j=0}$, where magic conditions can be realized in the lattice potential, could be utilized to decouple atoms from the MOT fields. In this case, the leakage from $^1P_1$ into the $^3P_2$ states could be suppressed by repumping the $^1D_2$ state directly, for example, at a wavelength of 716 nm (see Fig. 2.1 for a reminder of the strontium level structure).

4.3.3 Move trajectories in the lattice

Compared to the established shuttling of atoms in optical tweezer arrays, the movement of atoms in the lattice is complicated by the presence of additional lattice sites in between the initial and the target position. This gives rise to a substantial trap depth modulation during the transport, which heats the atoms and can lead to atom loss. This gets evident from the measurement in Fig. 4.5b. If the trajectory is taken through the center of lattice sites, we observe significantly higher losses compared to a trajectory along the potential valley, where the modulation is the weakest. Conveniently, our folded optical lattice provides asymmetric spacings, which give rise a long spacing of 1.1 µm. This feature can be exploited by resorting algorithms in order to favour moves along the minimal potential modulation, and the orientation of the loading and storage zone already exploits this. To ensure an efficient transport, it is required to maintain a sufficiently large distance from untargeted atoms at all times. We typically choose a trap depth of the resorting tweezer to be approximately 10-fold deeper than the lattice potential. At our tweezer waist of 472(3) nm, obtained from independent characterizations of trap depth and radial sideband frequency, a distance of ±1 µm is sufficient to satisfy this requirement. To characterize the distance requirements, we move a single tweezer linearly through the lattice and record the probability of atom loss as a function of distance with respect to the tweezer trajectory, as shown in Fig. 4.5c. This constraint is particularly relevant if the atoms are not initially positioned on well-defined locations and can occupy arbitrary sites. In this case, it can be challenging to find a suitable trajectory, ideally with a small number of turns. Additionally, for insufficient distances, the resorting tweezer may pick up neighboring atoms in addition to the addressed site. If these atoms are implanted onto the same site, light-assisted collisions during the next image will remove them from the trap. Furthermore, for isotopes and species with non-vanishing on-site interaction, additional heating effects may occur. Despite these technical difficulties, the direct sorting of atoms loaded into a single lattice plane opens up new possibilities for the generation of scalable atom arrays and is discussed in the following.

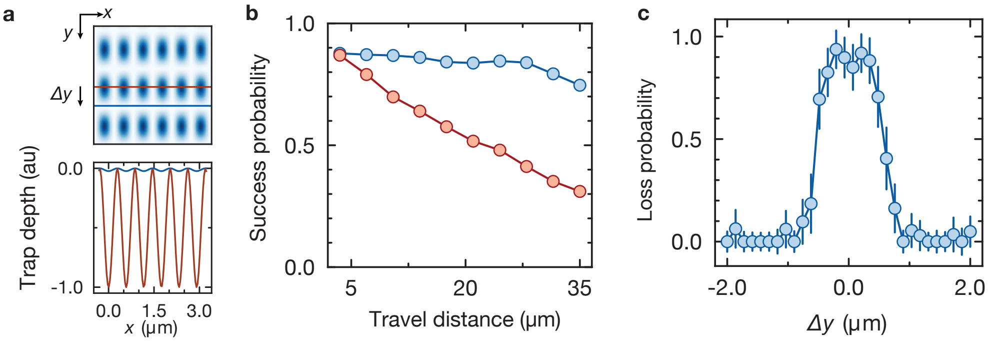

Figure 4.5: Trajectories for sorting in an optical lattice. a Modulation of the potential landscape for different trajectories within the lattice. Moving along the center of the lattice sites (red) gives rise to a significantly stronger potential compared to a trajectory in between sites (blue). **b** Success probability for different move trajectories as a function of distance. The blue trace is measured for trajectories in between vertical lattice sites, and the red trace is considering moves through the center (see (a)). **c** Moving atoms within the potential landscape requires a minimal distance between the mobile tweezer and the stationary atoms. Here, we show the loss probability of atoms as a function of distance with respect to a moving mobile tweezer. A distance of $\pm 1\,\mu\mathrm{m}$ is required to avoid unwanted loss.

4.4 Direct loading and resorting in a scalable optical lattice

Lattice-based systems facilitate the creation of large-scale atom arrays [182]. In our experiment, a single lattice plane is loaded directly from a MOT, and the scalability is demonstrated by Fig. 4.6, which covers more than 20000 sites. In this section, we discuss details of the site-resolved atom detection and show that the ensemble is parity-projected in the lattice potential. Furthermore, we demonstrate the active sorting of atoms within the lattice plane.

4.4.1 Site-resolved atom detection

To compute the site-resolved occupation of atoms in the lattice, we make use of the algorithm presented in Ref. [184] and outline the steps here. Initially, we take fluorescence images of atoms in the lattice after transferring the atoms from the tweezer array. This ensures well-separated atoms, and we subsequently compute an estimate of the point spread function (PSF) by averaging over filled sites, which are aligned to a common center. To compute the convolutional kernel for the site reconstruction, the Moore-Penrose inverse of the PSF is computed. Finally, during the reconstruction, the algorithm computes an emission for each lattice site by convolving the lattice image

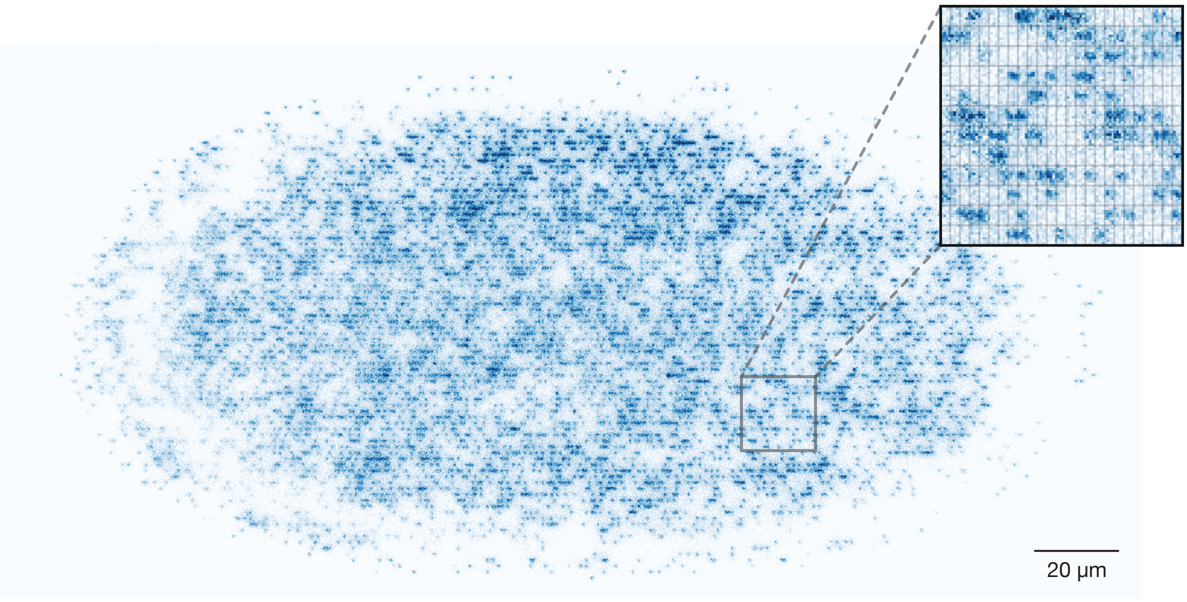

Figure 4.6: Fluorescence image of atoms in the optical lattice. The single-plane optical lattice is generated by 4-fold interference of a laser beam at 1040 nm and atoms are loaded directly from a magneto-optical trap. A fluorescence picture of the atomic ensemble is shown, demonstrating the scalability of the optical lattice. The inset shows a zoom-in, demonstrating the site-resolved detection.

with the kernel and integrating the ROI. The occupation matrix is then obtained by thresholding the emission for each site. Noteably, the emission is proportional to the brightness of atoms and depends linearly on the number of detected photons. Because of the linear relation, the projected emission is a useful tool to study the occupation statistics of atoms in the lattice. An example image snippet is shown in Fig. 4.7a and reconstructed in Fig. 4.7b. To obtain the emission for each lattice site, the algorithm initially detects the phase of the lattice grid with respect to the camera, which is required to define the center coordinates for the subsequent analysis. This phase detection is based on the position of individual and well-separated outlier atoms.

4.4.2 Parity projection in the optical lattice

Using the reconstruction algorithm, we obtain the histograms shown in Fig. 4.7c where the bimodal structure, corresponding to the 0-atom and 1-atom peak, is clearly noticeable. For the analysis shown here, we vary the MOT loading duration, which provides the means to control the filling fraction of the lattice and take two consecutive images by scattering photons on the 461 nm transition while simultaneously cooling the atoms using repulsive Sisyphus cooling on the 689 nm transition. The histogram of the first

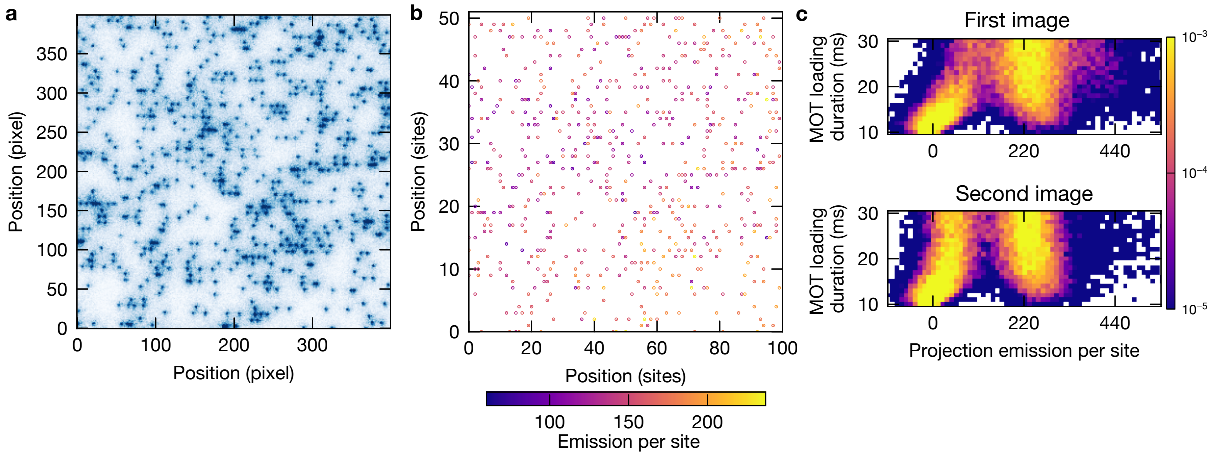

Figure 4.7: Parity projection and site-resolved detection in the optical lattice. a Section of a fluorescence image of atoms in the optical lattice used to obtain the site-resolved occupation. **b** Occupation matrix of atoms in the lattice obtained from the image in (a). The occupation per site is obtained by convolving the fluorescence image with a suitable kernel and summing the resulting "emission" for each site. Due to the linearity of the convolution, the emission is proportional to the number of detected photons for each site. The occupation is then obtained by thresholding the emission, which is shown here for the occupied sites. **c** Emission histogram of images taken in the lattice as a function of the MOT loading duration. The upper panel shows the distribution before parity projection and the 0-atom and 1-atom peaks are merging. After parity projection (lower panel), which takes place during the first image, the peaks are separated, and the onset of the 2-atom peak is removed. This measurement shows that individual atoms can be loaded directly from a MOT into a single plane of the two-dimensional lattice.

image exhibits the onset of the 2-atom peak and shows a bridge between the 0-atom and 1-atom peaks, which are both absent in the histogram of the second image. This shows that, despite the weak vertical confinement in our lattice, the atomic ensemble is parity projected and constitutes a scalable platform for individual atoms. To exploit the scalability of lattice systems, for example in quantum computing applications, the atoms have to be individually addressed and in the following we demonstrate the tweezer-based resorting in the lattice potential.

4.4.3 Assembly of atom arrays at addressable spacings

To demonstrate the direct resorting of atoms loaded to a single plane of a two-dimensional lattice in a proof-of-concept experiment, we configure the MOT loading duration to realize a sparse filling, see Fig. 4.8a. This provides the means to tune the filling fraction of atoms loaded in the lattice potential and is used to equalize the density of loaded atoms with respect to the chosen target pattern. The assembly of atom arrays follows three steps.

1. State detection
   Input: Image, Output: Occupation matrix (sites) and lattice phase
2. Resorting algorithm
   Generate a list of moves from start coordinates $\vec{s_0}$ to the destination $\vec{s_1}$
3. Generate RF to perform the moves
   Translate sites to frequencies and generate RF

When generating the RF frequencies to drive the acousto-optic deflectors, we have to account for the phase drift of the lattice and compensate for variations of the frequency-to-position mapping caused by thermal drifts in the apparatus. Starting with a position in units of sites $\vec{s}$ of the lattice, we first compute the corresponding position in terms of camera pixel coordinates $\vec{p} = M_{s\to p} \cdot \vec{s} + \vec{p_0}$. The transformation $M_{s\to p}$ takes into account the lattice spacings and rotation angles and is provided to the reconstruction algorithm. Translating the parametrization in terms of sites back to the pixel-space on the camera accounts for the lattice phase ($\vec{p_0} = M_{s\to p} \cdot \vec{\Phi}$, with $\vec{\Phi}$ referring to the lattice phases) and provides the means to compensate for drifts of the AOD frequency-to-position calibration. To generate the RF driving signal, we subsequently translate the positions to frequencies, which are parametrized by (4.2).

$$\vec{f} = M_{p\to f} \cdot \vec{p} + \vec{f_0} \tag{4.2}$$

While the sites-to-pixel mapping is completely known from the image itself, the pixels-to-frequency mapping is subject to small drifts on thermal timescales. To track these drifts, we repeatedly calibrate the AOD position on the atoms by generating a 3×3 tweezer array and computing an averaged fluorescence image of atoms trapped in the tweezer array. We then obtain the center positions of the tweezers and fit Eq. (4.2) to obtain an updated AOD calibration. On every resorting run, we query the latest calibration from a database in order to counteract the slow drifts. The database logging also allows a convenient visualization of the drift over time, and we observe drifts of the AOD tweezer that correspond to a displacement of up to 600 nm throughout a day.

To carry out the moves, we typically start in the center of the array and then arrange atoms further outwards. A typical set of moves is shown in Fig. 4.8c. For the first demonstration shown here, we make use of a single tweezer only and perform around 1200 moves. Here, the initial loading aims to approximate the density of the target pattern, and the algorithm is chosen to find the closest atom for each site. However, depending on local variations of the loading, some sites remain empty due to an insufficient number of atoms in the direct vicinity. The target definition used here

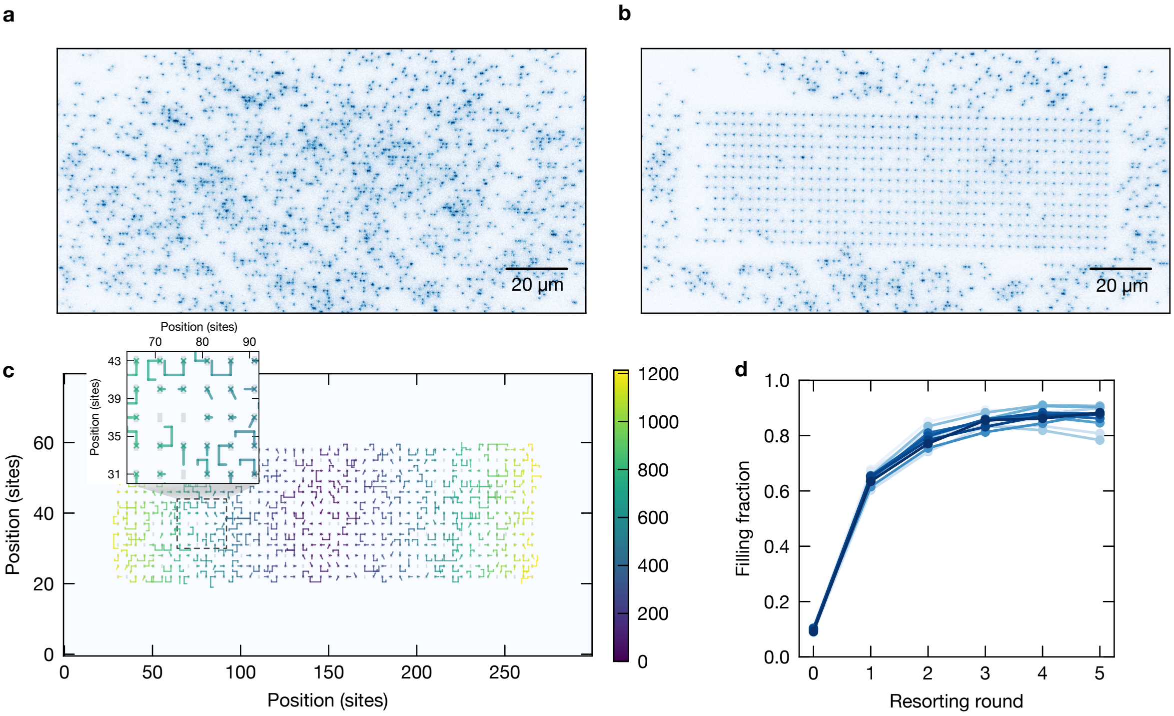

Figure 4.8: Resorting a directly loaded single lattice plane. a Fluorescence image of atoms after loading a single plane of the two-dimensional lattice directly from the MOT. The filling fraction can be smoothly adjusted by varying the MOT loading duration. **b** Fluorescence image of atoms after sorting. Here, we configured a target pattern with spacings of approximately 3.5 µm, corresponding to an occupation of every 6th (3rd) site along the horizontal (vertical) direction. The chosen target ignores sites in between the grid, which explains the presence of off-grid atoms in the central region. **c** Visualization of moves used to resort atoms in the lattice. The target pattern (light grey) is filled by sequentially moving atoms onto target sites, and the trajectories are shown. The resorting starts in the center and advances further outwards (see colorbar), containing about 1200 moves. **d** Filling fraction of the given target as a function of the number of resorting rounds. After the first round of sorting, the atoms are imaged again, and the sorting is applied again to fill defects. Note that the algorithm used here does not guarantee that sites are filled if no atom is available in the close vicinity (see inset in c). The colors correspond to individual repetitions of the experiment.

ignores excess atoms in between the target sites, which explains the deviations from a perfect rectangular grid in the final image, see Fig. 4.8b. Using more sophisticated algorithms, we envision preparing defect-free arrays in the optical lattice system at inter-atomic spacings suitable for cross-talk-free addressing through the objective. Despite the imperfections at the algorithmic level, we benchmark the filling fraction of the target positions as a function of the number of resorting attempts and reach a typical filling of about 90 % as shown in Fig. 4.8d.

Loading and resorting a single plane of a two-dimensional optical lattice provides the means to create large-scale atom arrays. Compared to tweezer-based systems, an additional complication is given by the presence of densely-spaced intermediate sites undesired for the final arrangement. To mitigate this issue, we propose a two-step protocol for the assembly of individual atoms. In this case, the first resorting step after imaging aims to equalize the density and separate individual atoms in order to allow a well-defined rearrangement in a second step. To avoid that atoms at short relative spacings are shuttled together, the dense areas are initially emptied, either by heating atoms out of the trap using an intensity-modulated tweezer or by moving them out of the region of interest. In a second step, starting with a new fluorescence image, the successful separation of atoms can be confirmed before the actual sorting attempt begins. This step may also benefit from presorting in the first round, to prepare free corridors along which atoms can be moved. This lowers the number of turns and hence boosts the success probability of the second round. In conclusion, overcoming the complications imposed by the additional trapping sites offers access to a very scalable platform and provides exciting opportunities for further optimizations. In the following, we discuss a comparison of the scalability of lattice-based systems compared to tweezer setups.

4.4.4 Scalability of lattice-based systems

For neutral-atom-based quantum information processors, available laser power typically limits the number of achievable qubits. Here, we summarize the scalability of different approaches.

Tweezers

For tweezer-based approaches, each tweezer has to contain a certain power P_{trap} to generate the required potential U_{trap}. Generating tweezer arrays with phase-only spatial light modulators requires a total laser power of

$$P_{\text{SLM}} \propto N \cdot U_{\text{trap}}$$

where N is the number of tweezers with a typical spacing of $2\,\mu\text{m}$ and above. In the case of AODs, where each tweezer corresponds to a radio-frequency tone, we additionally have to consider the maximally allowed RF input power. For suitably chosen phases of the RF tones, the Crest ratio (also known as peak-to-average power ratio) saturates at about 10. In this case, the average power still grows linearly with the number of tweezers N, which implies that the RF power for each tone has to be scaled with $\frac{1}{N}$ to comply with the RF damage threshold. This lowers the diffraction efficiency per tone, which has to be compensated by increasing the optical power. Assuming that the diffraction efficiency is approximately linearly dependent on the RF power, we obtain a scaling for the required optical power for AODs:

$$P_{\mathrm{AOD}} \propto 10\,N \cdot U_{\mathrm{trap}}$$

Note that residual nonlinearities in the RF electronics or the AOD crystal give rise to intermodulation, which lowers the diffraction efficiency. Furthermore, the diffraction efficiency of both SLM and AOD-generated tweezers is non-uniform across the array. To generate homogeneous tweezer arrays, the diffraction efficiency of the deep tweezers has to be purposefully lowered to match the shallow tweezers. This is accompanied by an additional effective loss of optical power. The drop in diffraction efficiency depends on device-specific details and the system size. For example, for tweezer arrays with a few hundred traps, we obtain a power efficiency of about 1/3 using an SLM accepting 1%-regime residual inhomogeneities across the array.

Optical lattices

Optical lattices generate sites at shorter spacings depending on the lattice architecture and wavelength. To allow for a fair comparison with the tweezer platform, we assume that the atoms get resorted to "addressable spacings", meaning that the spacing between neighbouring qubits has to be large enough to allow for individual addressing with sufficiently low crosstalk. In our case, suitable spacings of around 3.5 µm can be realized using every 3rd and 6th site, which corresponds to a filling factor of about 5.5 %, but does not affect the scaling of the number of sites with laser power.

We assume an elliptical lattice beam and note that the intensity of the setup is constant if the power scales with the horizontal waist $P \propto w_{\mathrm{hor}}$ while maintaining a constant vertical waist. For a 2D horizontal lattice, the area spanned by the lattice scales as $A \propto w_{\mathrm{hor}}^2$ and the number of qubits grows with $N \propto A$. The required power as a function of qubits, thus, scales as

$$P_{\mathrm{lattice}} \propto N^{1/2}$$

which holds for any lattice geometry. Note that the prefactor depends on the type of lattice geometry (folded lattice, textbook retro-reflected lattice, shallow angle lattice). For our lattice parameters with a vertical waist of 20 µm the Rayleigh length is about 1.2 mm. This shows that the horizontal waist could be, in principle, scaled up 10-fold, which corresponds to a 100-fold increase in lattice area and demonstrates the scalability of this setup.

Textbook retro-reflected lattice We assume that the total power P is split into two parts, one for each horizontal axis. The total potential is then given by

$$U \propto 2|2E|^2 = 2|\,2\sqrt{\frac{P}{2}}\,|^2 = 4P$$

This setup is, in principle, compatible with dynamic phase modulation schemes where a spatial phase modulator is installed in the retro path to realize spatially-dependent and dynamically modulated shifts of the lattice phase, which would allow for the highly-parallelized displacement of atoms within the lattice potential.

Folded lattice This lattice setup exploits 4-fold interference of a single input beam, which makes it particularly power efficient.

$$U \propto |4E|^2 = 16P$$

Note that the achievable trap depth drops by a factor of approximately 2 if an uncoated glass cell is used. In this case, the optical losses lower the trap depth, however, without affecting the lattice contrast.

Shallow angle lattice In this setup, the lattice spacing a can be arbitrarily tuned by adjusting the angle of interference θ between the two arms:

$$a = \frac{\lambda}{2\sin(\theta)}$$

In addition, this type of lattice can be made robust against laser phase noise if the path length difference between the interferometer arms is set to $\Delta L = 0$ [185]; however, the power efficiency is reduced, since the available power is distributed across 4 laser beams.

$$U \propto 2|2E|^2 = 2|\,2\sqrt{\frac{P}{4}}\,|^2 = 2P$$

4.5 Resolved sideband cooling with three-photon couplings

To support the creation of large-scale atom arrays, high-power laser sources have to be used and a particularly robust and established technology is given by Ytterbium-doped fiber amplifiers, which support wavelength just above 1 µm. To realize high-fidelity operations in these systems, the atoms have to be sufficiently cold, which is usually implemented via resolved sideband cooling. Unfortunately, in the case of strontium, the intercombination line does not support magic trapping conditions for linearly

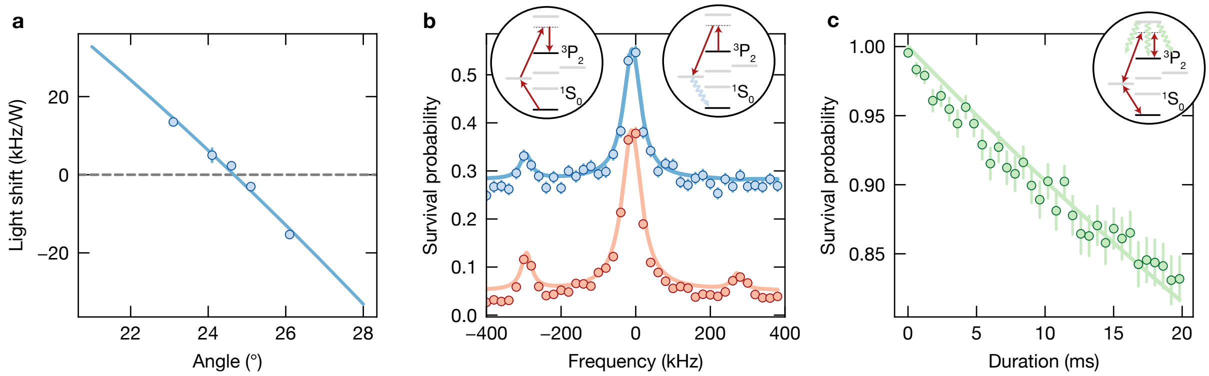

Figure 4.9: Three-photon sideband spectroscopy. a To obtain magic trapping conditions for the $^1S_0 \leftrightarrow {}^3P_{2,m_j=0}$ transition, we measure the trap-induced light shift with a Ramsey sequence at our wavelength of 1040 nm as a function of the angle between the magnetic field and vertically polarized lattice. The solid line is a fit following Eq. (2.10). **b** Under magic conditions, we perform sideband spectroscopy (red) and observe a heating sideband on the left of the carrier and a cooling sideband on the right when varying the detuning of the 707 nm light field. Repeating the spectroscopy after sideband cooling (blue) shows a suppression of the cooling sideband, however, at the expense of an enhanced background caused by off-resonant scattering from $^3S_1$. **c** Estimation of the off-resonant single-photon scattering rate. The 707 and 688 nm beams give rise to off-resonant scattering which effectively pumps population in the $^3P_{2,m_j\neq0}$ states.

polarized traps at this wavelength, see Fig. 2.3b. At this wavelength, magic conditions can be realized on the $^1S_0 \leftrightarrow {}^3P_{1,m_j=-1}$ transition for a suitable elliptical polarization of the light field. Remarkably, the folded lattice geometry, in principle, supports a well-defined ellipticity angle at the position of the lattice sites, given by the highest intensities, but due to polarization rotations on the mirrors, we could not realize the magic conditions experimentally.

Instead, alternative methods are required to carry out resolved sideband cooling, and here we present an approach based on the $^3P_2$ clock state using a three-photon drive, which is in detail introduced in Chapter 3.

4.5.1 Magic angle spectroscopy

To realize magic conditions, we apply a magnetic field with a strength of 19 G under a variable angle with respect to the vertically polarized lattice and initially characterize the resonance shift as a function of lattice trap depth. To perform a more accurate characterization of the magic angle on the $^1S_0 \leftrightarrow {}^3P_{2,m_j=0}$ transition, we use a Ramsey sequence and extract the frequency of Ramsey oscillations as a function of the dark time between two $\pi/2$-pulses. Repeating the measurement for different lattice trap depths reveals the trap-induced differential light shift. The measurement is shown in Fig. 4.9a and is fitted with Eq. (2.10) for a $J = 0 \rightarrow J = 2$ transition.

4.5.2 Sideband spectroscopy & cooling

Under magic trapping conditions, we carry out sideband spectroscopy by varying the frequency of the 707 nm beam and observe motional sidebands at detunings of approximately ±300 kHz with respect to the carrier, shown in Fig. 4.9b, which correspond to the short lattice spacing collinear with the probe direction. Implementing cooling with unitary operations alone is not possible, and instead, a dissipative step is required. Here, we realize the dissipative "repumping" of atoms by coupling $^3\mathrm{P}_2$ to $^3\mathrm{P}_1$, using a two-photon drive at 707 and 688 nm, from where the atoms decay back to the ground state. To avoid heating due to dipole force fluctuations caused by the non-magically-trapped $^3\mathrm{P}_1$ state, we purposefully detune the two-photon repumping by 1 MHz [186, 187]. Initially, we drive a three-photon π-pulse on the cooling sideband to remove one motional excitation and subsequently reset the atoms via $^3\mathrm{P}_1$, as described in Section 3.3.8. Currently, the efficiency of this process is limited by off-resonant scattering from the intermediate state $^3\mathrm{S}_1$, which gives rise to a high baseline in the subsequent spectroscopy and corresponds to an effective loss of atoms from the cooling cycle. In order to experimentally measure the off-resonant scattering rate, we detune the 707 nm light field by 20 MHz and drive off-resonant three-photon couplings, before the remaining ground-state atoms are pushed out. We obtain an effective scattering rate of 10.2(2) Hz, plotted in Fig. 4.9c, which provides a plausible explaination for the baseline in Fig. 4.9b, where we applied the sideband cooling for about 30 ms. Alternatively, resonant repumping at 707 nm is conceivable, which would, however, require multiple scattering events that would give rise to additional heating. Instead, we choose to repump atoms via a two-photon pulse and expect to suppress the scattering error using larger intermediate state detunings. Since the cooling transition is driven by a three-photon process, the effective power-broadened linewidth can be accurately controlled via the applied laser power at intermediate magnetic field strength. Alternative couplings based on the single-photon coupling at 671 nm would allow for only slow Rabi frequencies due to the weak coupling of the magnetic quadrupole transition [188].

4.6 Summary and outlook

In this chapter, we demonstrated building blocks combining the scalability of optical lattice setups with the single-site control of tightly focused optical tweezers. By choosing the tweezer spacings to be commensurate with the lattice grid, we implanted atoms in parallel at individual lattice sites and presented the repeated transfer of atoms between the tweezer and lattice potential. This provides the means to decouple, for example, the trap-depth-demanding imaging from the rest of the sequence and facilitates the creation of larger tweezer systems at wavelengths where high-power sources are not available.

Furthermore, we demonstrated the loading of a single lattice plane directly from a MOT and rearranged atoms in the two-dimensional lattice system using AOD-driven tweezers. This approach paves the way for the assembly of scalable atom arrays, potentially beyond the current state-of-the-art of tweezer arrays and sidesteps thermal issues in the objective lens occurring in tweezer-based approaches [70]. Additionally, the precise positioning of atoms in the lattice offers new possibilities for experiments, for example, to prepare an initial state for quantum walk experiments or to create deterministically loaded tweezer arrays at 100 % filling by transfering atoms into the tweezer array after presorting in the lattice.

Moreover, the combination of tweezers and lattice potentials facilitates new protocols for the generation of atom arrays, and we demonstrated a protocol for the iterative assembly and continuous operation of atom arrays. This provides the means to overcome scaling limitations by repeatedly adding atoms to the system and relies on the low-loss imaging introduced at the beginning of this chapter. Exploiting the presence of long-lived metastable states in strontium, this protocol also enables the continuous operation of atom arrays, which substantially reduces the timing overhead of experiments, since the resorting has to fix only the defects instead of assembling an entirely new ensemble.

Finally, we presented a new method for resolved sideband cooling of strontium at IR wavelength, where magic trapping conditions for linearly polarized traps are not available on the intercombination line. Instead, we made use of a three-photon coupling from the $^1S_0$ ground state to the $^3P_2$ clock state. This technique is compatible with intermediate magnetic field strength, which facilitates creating magic trapping conditions on this transition. Combined with the site-resolved assembly of atom arrays, this paves the way towards assembled Hubbard systems. Here, the sideband-resolved two-photon coupling of $^3P_2$ to $^3P_1$ may be exploited in future experiments to realize algorithmic cooling protocols or for erasure detection of atoms out of the motional ground state. To create atom arrays in a Hubbard-regime optical lattice, the vertical confinement has to be enhanced. The following section provides a brief discussion of possible setups.

4.6.1 Improved vertical confinement

The measurements presented in this chapter would benefit from a stronger vertical confinement, for example, to suppress broadening of the single-atom fluorescence distribution and to match the vertical trap frequencies of tweezers and lattice. In our system, the confinement in the vertical direction is entirely given by the Gaussian envelope of the beam, which could be focused to a smaller vertical waist of about 10 µm in order to provide a higher vertical trap frequency. However, a stronger vertical focus limits the Rayleigh length of the beam and reduces the scalability of the system. At our lattice wavelength of 1040 nm and the 20 µm vertical waist, the resulting Rayleigh length is about 1.2 mm. The demonstrations presented in the chapter are thus scalable up to 100-fold larger areas and associated atom numbers.

Enhanced vertical confinement can be realized by superimposing the lattice with a vertically tightly-focused and highly elliptical light sheet [120]. However, this approach is limited to intermediate system sizes due to the diffraction-limited divergence inherent to tightly-focused Gaussian beams.

Alternatively, shallow-angle lattices are a promising approach where the angle of interference provides the means to choose the lattice spacing, which can even be smoothly adjusted in "accordeon-type" setups [189, 190]. Choosing the lattice spacing requires a trade-off between the strength of the vertical confinement in terms of its trap frequency (favoured by short spacings) and the ability to load only a single plane. If the lattice spacing is too short, atoms might be loaded into multiple planes, and the subsequent preparation would require an involved "slicing" procedure in a vertical magnetic field gradient [188]. Considering a sequence of vertical confinement steps using, for example, a combination of optical potentials, the atoms can finally be loaded into a retro-reflected optical lattice, which provides the strongest vertical confinement. Generating such a lattice in the presence of two vertically oriented objectives may rely on a hole in the center of the objective lenses [179].

4.6.2 Perspectives for parallel assembly

For the resorting demonstrations presented in the chapter, we have, for simplicity, used only a single AOD-driven tweezer. In order to speed up the resorting process, future experiments can exploit multiple tweezers to move atoms in parallel along the eigenaxis of the AODs. In this case, the eigenaxes of the AODs are ideally aligned with the eigenaxes of the lattice to allow for parallelized moves within the lattice grid. However, even in this case, the ability to perform moves in parallel is limited by the inherent properties of the AOD-based setup, which prevents arbitrary parallelized moves beyond the grid spanned by the AODs. Recently, an alternative approach for parallelized atom shuttling was demonstrated, which relies on fast LCOS-SLMs. Here, the tweezer position can be arbitrarily programmed holographically, and atoms can be moved by smoothly displacing atoms in several steps [191–194]. Currently, the achievable resorting durations are limited by the update rates of commercially available light modulators, with the fastest devices operating at rates of about 1 kHz (Meadowlark HSP1K-488-850-PC8-TCS4). Recently, a new type of spatial light modulator, based on microelectromechanical system (MEMS) phase-only light modulation, was introduced [195]. This device makes use of a micromirror array (MMA) to imprint a configurable phase mask onto a laser beam and is described further in Chapter 6. Currently, the update rate of the MMA is limited as well to 1 kHz, which may be increased further, approaching the rates achievable with DMD setups.

The main data-processing bottleneck in our apparatus is, however, currently given by the deconvolution and state detection algorithm. In the following chapter, we present a scalable reconstruction algorithm based on a deep convolutional neural network, which exploits the parallel execution on modern graphics cards and offers a fast noise-resilient reconstruction applicable to arbitrary lattice geometries.

Chapter 5

A deep learning algorithm for scalable deconvolution

5.1 Introduction

Detecting the atomic distribution in optical lattices is a ubiquitous requirement of quantum gas microscopes and has been used very successfully, for example, to simulate the Hubbard model. Compared to systems based on optical tweezers, the interatomic spacings are significantly smaller and are typically of the order of 500 nm or, in some cases, even below at the 300 nm level [196]. In most setups, this gives rise to a substantial overlap of the single-atom fluorescence emitted from neighboring sites, which complicates the site-resolved detection. For sufficiently localized atoms, the fluorescence distribution can be understood as a convolution of the point-like atom position with the point-spread-function (PSF) of the imaging system. The inverse operation, termed deconvolution, aims to recover the point-like distribution and is mathematically based on the convolution theorem, which states that the Fourier transform of the fluorescence image is given by the product of the Fourier transform of the point-like distribution with the Fourier transform of the PSF. However, in the presence of experimental noise, for example, the fundamentally given Shot noise, the division in the reciprocal space is ill-defined, and several methods have been invented to mitigate this [197].

In this chapter, we introduce a novel deconvolution algorithm based on a deep convolutional neural network (CNN). Combined with a state-detection postprocessing algorithm, this offers a fast and noise-resilient approach to obtain the site-resolved lattice occupation.

5.2 Learning predictions of the site-resolved occupation

Previous work on neural networks for quantum optics image processing is based on network architectures which provide directly a site-resolved classification at the output [198–200]. To build a scalable network architecture, we work exclusively with convolutional elements and choose an input dimension of the first layer of 64×64 pixels, substantially smaller than the full-frame camera ROI. The small input dimension limits the number of parameters and ensures a fast execution of the network and the usage of convolutional layers allows for a straightforward upscaling to larger ROIs.

Inspired by previous work [198, 200], we train an encoder network to translate image snippets with dimensions of 64×64 pixels to site-occupations on a 8×16 output grid. The network architecture is based on a modified U-Net [201] and the working principle is illustrated in Fig. 5.1a. For training, we take a few hundred images and reconstruct the lattice occupation with our reference algorithm, introduced in Section 4.4.1. We then draw randomly selected, but mutually corresponding snippets from the image and the occupation matrix and train the network to produce the occupation snippet given the image. The final layer of the network makes use of a Sigmoid activation function and the training loss function is given by a binary-crossentropy loss to minimize the Kullback-Leibler divergence between the generated and reference probability distribution [202].

5.2.1 Comparison to the reference algorithm

Compared to the reference algorithm, described in Section 4.4.1, the neural network approach can capture new effects. As shown in Fig. 5.1b the background noise level (see the two marked regions) depends on the presence of atoms surrounding an empty area. If several atoms are present in the vicinity of an empty ROI, the background level is substantially higher compared to larger empty areas. We attribute this to the insufficient vertical confinement and the corresponding long tail of the single-atom fluorescence distribution. Similarly, the brightness of atoms seems to depend on the distance to other atoms, and groups of atoms seem to exhibit superradiance, a collective emission, which occurs when the interparticle spacing approaches the transition wavelength [203]. The linear kernel-based approach of our reference algorithm [184] cannot capture this non-linear behaviour, but the network may learn a suitable non-linear mapping to allow for a more accurate reconstruction. While the supervised training approach used here inherently implies that the network learns to reproduce the reference algorithm, it may still produce more accurate predictions, in particular, in densely filled areas. In addition, the learned reconstruction can be made more noise resilient by purposefully adding random noise to the images during training. This so-called noise regularization prevents overfitting and forces the model to learn relevant features. At the same time, it also favours robustness of the model against noise. Since fluorescence images of atoms have limited signal-to-noise ratios, it also serves as a data augmentation technique if only a limited number of images is available. Furthermore, to ensure that the detection is not limited by possible imperfections of the reference algorithm, unsupervised training approaches are feasible and are discussed in more detail in Section 5.5.1.

While the training is based on small image snippets, we typically need to reconstruct a larger lattice ROI. Applying the convolutional network to a larger image directly

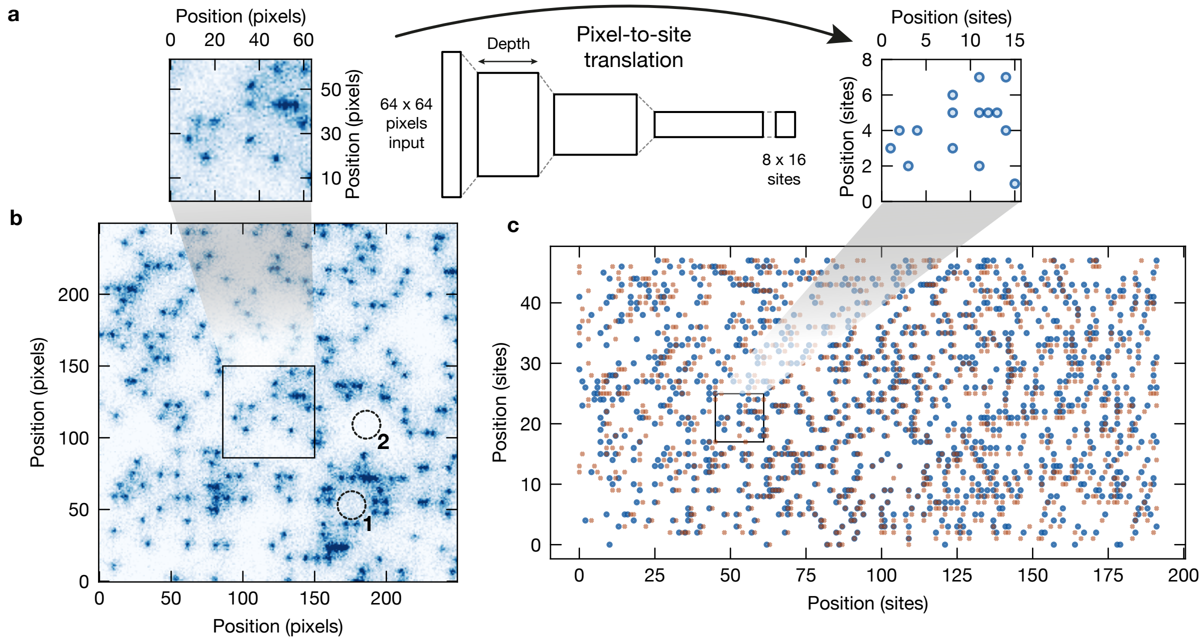

Figure 5.1: Image to site translation with a neural network. **a** The data processing of a convolutional encoder network is shown, which translates images to occupation matrices. The input of the network is given by a 64 × 64 pixel area of the image, and a set of learned convolutional kernels and non-linear activation functions is applied. The output of the network is given by an 8 × 16-sites output representing the occupation matrix. **b** Snippet of a fluorescence image of atoms loaded directly into the optical lattice. The brightness of atoms and the background level vary depending on the local filling fraction. Areas surrounded by atoms (1) exhibit a higher background level than empty areas (2), indicating a large extent of the single-atom fluorescence distribution likely caused by insufficient vertical confinement. Atoms in the close vicinity of other atoms appear brighter, which we attribute to superradiant effects and the overlap of their fluorescence distribution. This observation motivates the usage of convolutional neural networks to learn the detailed fluorescence distribution and potential nonlinear effects. **c** Comparison of the occupation matrix obtained from the encoder network (blue dots) with the output of the reference algorithm (orange crosses). The two occupation matrices exhibit a spatially varying shift. In the upper left part, the results are shifted horizontally by two sites. Further towards the center, the shift is reduced to an offset of one site , and in the lower right area of the occupation, the shift appears along the vertical direction. Since the encoder network has an input (output) area of only 64 × 64 pixels (8 × 16 sites), it fails to generate a phase-coherent grid when applied to a larger area. See the main text for a more detailed discussion.

produces a correspondingly larger occupation matrix. The result is shown in Fig. 5.1c compared to the output of the reference algorithm. Remarkably, the two occupation matrices exhibit a spatially varying phase shift. In the upper left area, the occupation matrices are horizontally shifted, and the lower right area exhibits a vertical shift. This discrepancy is caused by difficulties of the neural network to “phase-coherently” stitch together smaller areas. The data presented during training includes only small-scale areas, where residual phase shifts, caused, for example, by the rounding in the site-to-pixel translation, are not relevant. However, for large-scale images, a small mismatch of the learned lattice spacing may give rise to a locally varying lattice phase and a resulting position-dependent mismatch of the assigned lattice site. This problem is inherent to all setups where the lattice spacing is incommensurate with the pixel spacing, and prior work [198] has used upsampling to reduce the effect of rounding. Here, we follow a different approach and instead separate the deconvolution from the state detection. The first step aims solely to provide a deconvolved image, and the second step subsequently assigns the emission to a lattice site. We make use of machine learning techniques for the first step only and employ a postprocessing algorithm to guarantee a phase-coherent lattice grid across the entire ROI.

5.3 Learned deconvolution of fluorescence images

Separating the deconvolution from the state detection, where the emission is assigned to individual lattice sites, has the distinct advantage of sidestepping rounding issues for incommensurate site-to-pixel translation. In addition, this approach is applicable to arbitrary lattice geometries, including kagome or triangular lattices, which would otherwise require entirely new network architectures.

5.3.1 Training

To learn the deconvolution, we again take images and reconstruct them with the reference algorithm. Afterwards, we compute the center pixel for all occupied sites and activate a single pixel at this location. Specifically, we set all pixels to zero and set the center position of occupied sites to one, as shown in Fig. 5.2a. We extend the previously used encoder network by a suitable decoder network to generate an output of 64×64 pixels and train the network to generate the sparsely filled outputs. At this point, the deconvolution task is formulated as an image-to-image translation task , and various publications describe suitable network architectures and training strategies [204–206]. To favour the binary output of the network, we again use a Sigmoid activation function in the final layer and train with binary cross-entropy loss. Before presenting the images to the network, the data is normalized to a mean of zero and a standard deviation of unity in order to facilitate the convergence of the training. During inference, we similarly subtract the image mean and divide by the standard deviation of the image.

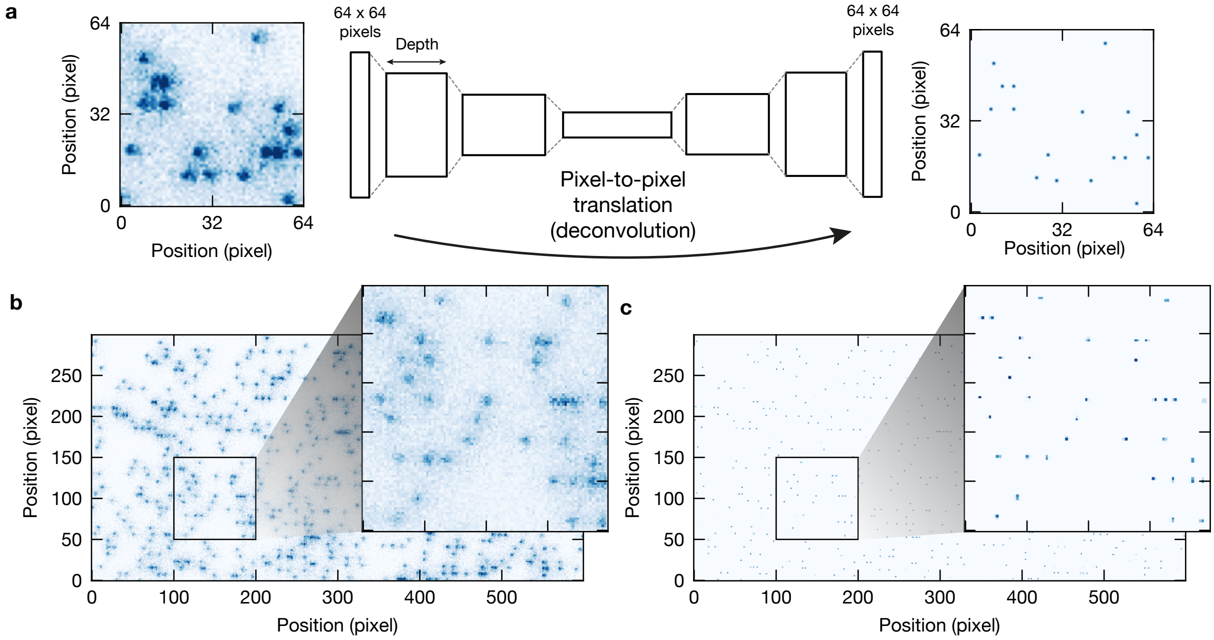

Figure 5.2: Deconvolution with a convolutional neural network. Instead of a full state detection, we train an autoencoder network to carry out the deconvolution alone without assigning the emission to specific lattice sites. **a** Layout of the autoencoder network used to carry out the deconvolution. An image snippet with 64 × 64 pixels is provided to an encoder network, which uses layers of convolutional kernels and non-linear activation functions to shrink the spatial dimensions while extending the depth before a decoder network the spatial dimensions of the input. The network is trained to provide a deconvolved version of the input image where only individual pixels are activated that correspond to the round center position of the atom. The images are taken from the training dataset. **b** Fluorescence image of atoms in the lattice provided to the input layer of the autoencoder network. Since the network is based entirely on convolutional operations, it is easily applicable to any input image dimension. **c** Output of the network for the input in (b) after completed training. The lattice structure is noticeable, and the emission can subsequently be assigned to individual lattice sites as described in the main text. The network architecture used here can be applied to arbitrary lattice geometries.

Applying the network to a large-scale lattice image yields the output shown in Fig. 5.2c. Again, the output exhibits rounding issues, caused by the incommensurability of the pixel and lattice spacing, which distributes the output emission across more than one pixel. However, in this case, the rounding errors occur on the pixel level, and multiple pixels can still uniquely be assigned to the correct lattice site. To compute the site-resolved occupation, the deconvolved image has to be divided into individual ROIs corresponding to the lattice sites, and defining the lattice ROIs requires knowledge of the lattice phases. In the following, we discuss a postprocessing algorithm to detect the lattice phase and compute the occupation matrix.

5.3.2 Postprocessing algorithm

To obtain the occupation matrix, we first need to identify the shift of the lattice grid with respect to the camera in order to uniquely fix the ROIs for each site. Extracting the phase relies on comparing the deconvolved image to a set of precomputed masks, which are computed for various x- and y-phases considering unity filling. Specifically, we assume that all sites are filled and compute the center pixel in the image ROI for each site, which we subsequently set to one in a background of zeros. These masks are computed for each combination of lattice phase for the x- and y-direction, where we typically take 20 discrete points within the range $[-0.5, 0.5)$. At our lattice spacings of approximately 4 (8) pixels along the horizontal (vertical) image direction, we can, in principle, only distinguish an equal number of different phases. However, at large ROIs, the rounding to the closest pixel gives rise to a noticeable difference due to the incommensurability of the lattice and pixel spacing.

Phase detection

The resulting set of reference masks R_{ijkl} is a four-dimensional matrix, where the first two indices i, j represent the two spatial image dimensions and the indices k, l correspond to the phases in the x- and y-direction, respectively. To estimate the lattice phase, we compute the overlap of the deconvolved image I_{ij} with the reference mask:

$$O_{kl} = \sum_{i,j} R_{ijkl} \, I_{ij}$$

The overlap is shown in Fig. 5.3a and exhibits a well-defined optimum obtained from the smoothly varying overlap and the phase is subsequently extracted as the point of highest overlap. Indeed, we confirmed that the resulting phases are in excellent agreement with the results obtained from our reference algorithm.

Emission per lattice site

To compute the emission for each lattice site, we define ROIs with dimensions of 3×3 pixels centered on each site of the deconvolved image. The usage of ROIs ensures

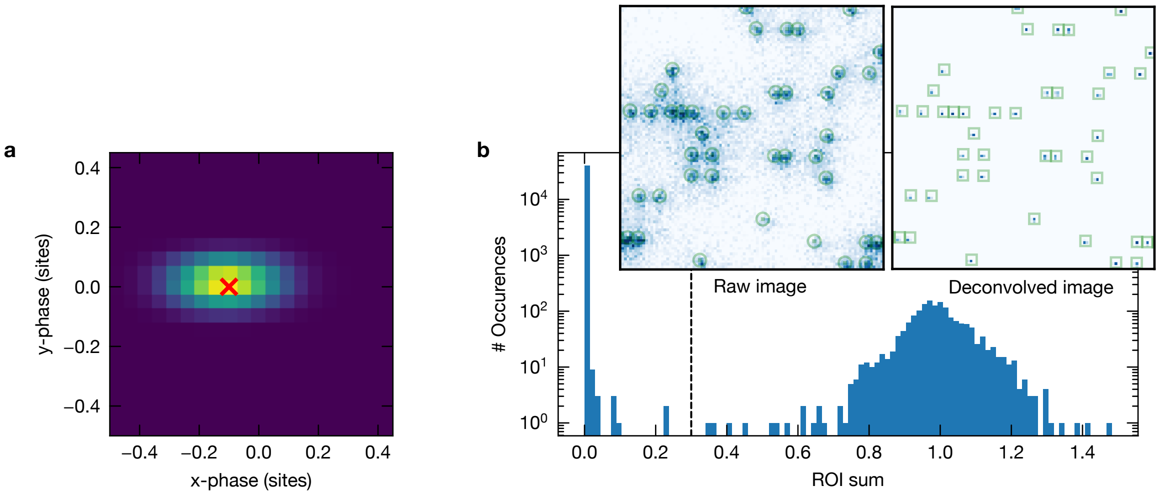

Figure 5.3: Phase detection & emission per site. a To obtain the phase of the optical lattice, we compare the autoencoder to a set of precomputed masks where only the center positions of the lattice sites are activated depending on the phases along the x- and y-directions. For each pair of phase values, we compute the product of the mask and the deconvolved image and sum it, thereby measuring the overlap of the output with the given mask. This overlap is shown here as a function of the phases, and the identified optimum is marked with a red cross. These phases are subsequently used to define the ROIs of the lattice sites on the deconvolved image. **b** Knowing the phases of the optical lattice, we compute for each lattice site a region of interest (ROI) of 3×3 pixels centered on the site coordinates. We then sum the emission for each ROI and show a histogram of the emission per site. The occupation is obtained by thresholding the emission. The insets show annotated snippets of the raw image (left) and the deconvolved image (right), where the green boxes indicate occupied sites.

that small shifts of the emission in the deconvolution (see Fig. 5.3c) are still assigned correctly to their corresponding lattice sites. We then sum over the ROI and obtain the histogram over single-site emissions shown in Fig. 5.3b, which shows a highly bimodal distribution. We observe the highest number of occurrences at near-zero emission corresponding to empty sites and obtain the 1-atom peak centered at unity. Note that the dynamic range of the deconvolved image is bound within $(0, 1)$, because of the Sigmoid activation function of the last layer. However, since we sum over small ROIs to obtain the emission, we can, in some cases, obtain integrated values larger than unity. Note that the emission obtained here is a non-linear function with respect to the image and can thus not be understood in terms of the number of photons per site.

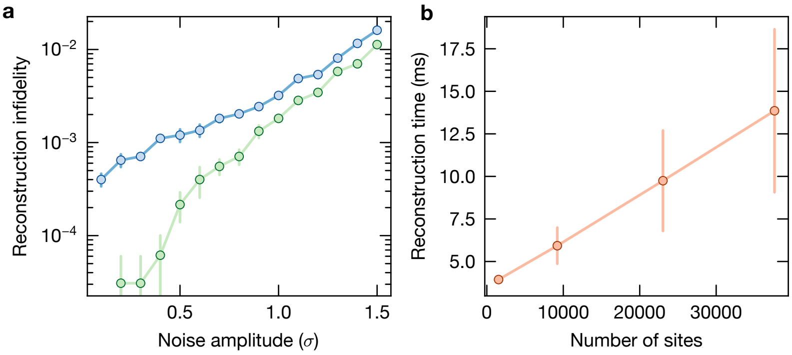

Figure 5.4: Noise resilience and timing of the reconstruction. a To benchmark the autoencoder network, we compare the noise resilience to our reference algorithm described in Chapter 4. For a set of test images, we first compute the occupation for each algorithm, which acts as a reference. We then add random noise from a Gaussian distribution with standard deviation σ and reconstruct the image again. The infidelity is computed with respect to the reference image obtained in the absence of excess noise. The autoencoder (green) shows a significantly reduced infidelity than the reference algorithm (blue). Error bars denote the standard deviation. **b** To benchmark the execution time of the autoencoder network, we select regions of interest of variable size from the set of images and measure the execution time. Here, the network is running on an A5000 GPU from Nvidia, which allows reconstructing more than 30000 sites in less than 15 ms. The error bars denote the standard deviation.

5.4 Benchmarking of the autoencoder network

To characterize the performance of the autoencoder network, we benchmark the noise resilience in comparison to the reference algorithm. Initially, we reconstruct a few images and store the resulting occupation matrices. We then add random noise to the image, perform another round of reconstruction, and compare the resulting occupation to the reference case obtained in the absence of additional noise. For occupation matrices m and n, we define the fidelity as $F = 2\sum_{i,j} m_{ij}n_{ij} / \left(\sum_{i,j} m_{ij} \sum_{i,j} n_{ij}\right)$ and plot the infidelity $1 - F$ in Fig. 5.4a. The comparison shows that the autoencoder-based state detection is substantially more noise resilient and exhibits an error probability that is suppressed by up to an order of magnitude for small to intermediate noise amplitudes. This demonstrates an advantage of machine learning techniques over single-kernel-based approaches, where the noise-resilience can be supported during training, for example, via noise regularization as discussed above. For realistic noise models, denoising routines may be developed further based on trainable networks, which exploit correlations across individual pixels.

Besides the ability to handle noise and reconstruct realistic images, the processing duration is another important figure of merit. For benchmarking purposes, we compute the average execution duration for ROIs of variable area, as shown in Fig. 5.4b. We obtain a slope of approximately 0.3 µs/site and an offset of about 3.5 ms attributed to the data transfer onto the GPU. The timings shown here include the conversion of the image into a suitable tensor object and the full state reconstruction, including the autoencoder-based deconvolution and the execution of the postprocessing algorithm. Reconstructing more than 30000 lattice sites in, on average, less than 15 ms, demonstrates the scalability of this approach and unlocks the processing of million-site-scale images within less than one second.

5.5 Summary and outlook

In this chapter, we introduced a novel atom detection algorithm based on a deep convolutional neural network suitable for reconstructing the occupation in densely filled optical lattice system. We separate the deconvolution from the site-resolved state detection and train an autoencoder-type network to provide deconvolved images of the point-like distribution of atoms. This approach mitigates position-dependent shifts of the occupation matrix, caused by the incommensurability of the lattice and pixel spacings and ensure that the outlined protocol is applicable to any lattice geometry, including, for example, kagome and triangular lattices.

To extract the site-resolved lattice occupation, we introduce a postprocessing algorithm, which assigns the emission on the deconvolved image to their individual lattice sites and provides an occupation matrix by thresholding the emission. Compared to our linear kernel-based reference algorithm, we find a substantially improved resilience against random noise, caused by the noise regularization employed during training. We envision that realistic noise models, tailored to describe the noise processes of camera readout and photon scattering, may serve as helpful extensions to train denoising layers in future CNN setups.

For the demonstration here, we used a supervised training approach, making use of the reference algorithm to produce a set of mutually corresponding images and occupation matrices. While the resulting network fulfils our requirements in terms of robustness against noise, execution time, and scalability, some applications might require an entirely unsupervised approach if other reconstruction algorithms are not applicable. In these cases, it would be desirable to train a network without a dataset of mutually corresponding pairs of images and occupation matrices.

5.5.1 Unsupervised training

In the context of image-to-image translation, various unsupervised training algorithms have been invented to transfer images from one type to another. The translation from noisy fluorescence images to clean (potentially binary) deconvolved images can be understood in this setting as translating images from the noisy class to the clean class. If supervised techniques are not feasible due to the absence of a suitable reconstruction algorithm, we can still generate pairs of real images accompanied by generated deconvolved versions, which are not mutually corresponding. In this case, the images are taken from the experimental dataset, and the deconvolved versions are randomly generated following the known lattice spacings and angles, but without reflecting the occupation of the actual fluorescence image. The resulting dataset contains snippets of both classes (fluorescence images and deconvolved images), and the network is trained to translate from one class to the other one; however, in such a way that images are mutually corresponding. This type of unsupervised image-to-image translation is realized, for example, by the CycleGAN algorithm [205] or the Contrastive Unpaired Translation (CUT) approach [206].

Training a neural network to translate images to resemble a certain type requires, in principle, a suitable loss function to guide the training. However, designing a suitable function to measure the similarity with the desired outcome is, in most cases, very difficult. Instead, the loss function itself can be learned during training following the concept of Conditional Generative Adversarial Networks (cGAN) [204]. Here, a discriminator network is trained together with the translating network to distinguish between images taken from the desired target class and the output of the translator network. As the training proceeds, the discriminator gets better at distinguishing generated and real images from the target class, thereby forcing the translating network to produce more realistic outputs. Applied to our deconvolution task, this would, so far, allow for the generation of authentic occupation matrices, however, without any correspondence to the provided images. If the forward translation is combined with another translating network for the backward translation process, the combination can be further trained to provide cycle-consistent results, thereby enforcing a mutual correspondence of the images from the two classes. In summary, a deconvolving network can be trained using a set of atomic fluorescence images and randomly generated deconvolved samples. To avoid the overhead of the backwards translation, the CUT algorithm makes use of an autoencoder setup, and the training is based on maximizing the mutual information of image patches from both classes in the latent space of the encoder network [206].

In conclusion, the deconvolution approach presented in this chapter can be extended to operate in a purely unsupervised manner. This would provide a simple-to-use setup for experimentalists, where the creation of a tailored reconstruction algorithm would be feasible upon pressing a button.

Chapter 6

Holographic tweezer generation with micromirror arrays

6.1 Introduction

Optical tweezers are a powerful tool for the study of quantum-mechanical many-body systems and the construction of neutral-atom-based quantum information processors. For stationary tweezers, the array is often generated using liquid-crystal-on-silicon spatial light modulators (LCOS-SLMs), where incident light is reflected after passing through a liquid crystal layer. With suitable control voltages applied to a grid of pixel electrodes, the refractive index is altered locally, which gives rise to a programmable phase pattern imprinted onto the laser beam. In this setup, nearly arbitrary intensity distributions in the focal plane of an objective lens can be configured by displaying a suitable phase mask on the device. The programmability of the phase pattern allows for compensating optical aberrations, and SLMs have been successfully used for the creation of tweezer arrays with several 1000 sites owing to their compatibility with high optical power [70]. Because of the limited update rate of typically $60 - 120\,\mathrm{Hz}$ of most devices, the resulting tweezer arrays are usually stationary; however, dynamic potentials have been demonstrated using specialized SLMs with up to 1 kHz update rate [193]. The available wavelength range for LCOS-SLMs is constrained to wavelengths above 355 nm due to the degradation of the liquid crystal phase under UV irradiation.

Besides SLM-based approaches, optical tweezers can also be generated with acousto-optic deflector (AOD), digital micromirror devices (DMD), or metamaterials. Complementary to the SLM-generated arrays, the AOD-driven setups are suitable for dynamic rearrangement of the tweezer position owing to the radio-frequency-based diffraction, which allows for smooth adjustments of the tweezer position at fast rates. In contrast, DMDs offer an intermediate update rate typically somewhere in the kHz-regime, and can be used either in a Fourier or an image plane of an optical system. While this opens interesting possibilities, for example, for the spatial modulation of incoherent light, it is typically not power efficient for generating optical tweezer arrays. Stationary, metamaterial-based phase masks enable large-scale tweezer arrays [207, 208], but offer no dynamic controllability.

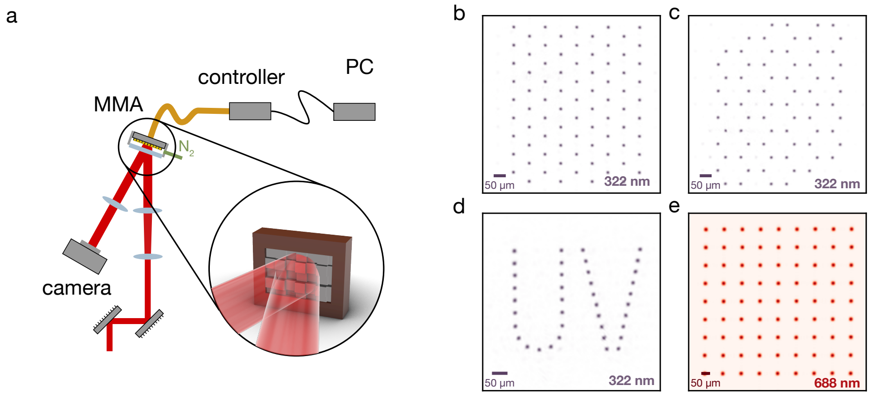

Figure 6.1: Holographic beam shaping with a micromirror array. a Setup for holographic beam shaping with a micromirror array (MMA). A collimated input beam is reflected from the device, which imprints a programmable phase mask onto the beam. The beam is focused, and the image plane is monitored with a camera. For each micromirror, the phase is set by controlling the piston stroke electrostatically, which enables holographic beam shaping at a wavelength in the ultraviolet regime. To avoid damage to the underlying control electronics under UV irradiation, the MMA is continuously flushed with nitrogen. **b-d** Tweezer arrays generated at a wavelength of 322 nm using the MMA. **e** Adjusting the piston stroke depending on the wavelength enables beam shaping across a broad wavelength range. Here, a tweezer array at a wavelength of 688 nm is shown.

In this chapter, we introduce a new type of spatial light modulator based on a micromirror array (MMA). Here, individual mirrors are electrostatically controlled to set a stroke on the nanometer-scale, which is used to imprint programmable phase masks onto laser beams reflected from the device. The device acts as a phase-only spatial light modulator and is compatible with wavelengths in the ultraviolet regime, and offers a fast update rate. The measurements presented in this chapter are based on publication [195].

6.2 Beam shaping in the ultraviolet range

The working principle of MMA-based holographic beam shaping is sketched in Fig. 6.1a. A collimated input beam is reflected from the MMA and focused onto a camera to monitor the resulting intensity distribution. The MMA itself is installed in a Fourier plane of the optical system, and the stroke of mirrors is individually configured to imprint the desired phase mask onto the light field. The prototype MMA used here (64k customer evaluation kit piston MMA α-module) features 256×256 uncoated square mirrors with a pitch of 16 µm and maximum stroke of 350 nm, which is configured

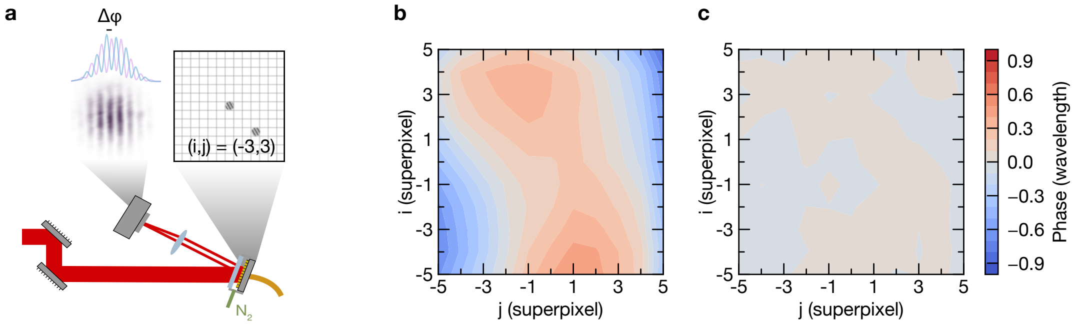

Figure 6.2: Phase shifting interferometry with a micro-mirror array. **a** To carry out phase shifting interferometry, the MMA is illuminated with a collimated beam, and the MMA displays a blazing grating within two superpixel regions only. The relative phase of the two superpixels' grating determines the position of the interference fringe detected on a camera. By varying the position of one superpixel with respect to a common reference superpixel in the center, the spatially-dependent phase profile can be mapped out. **b** Phase map obtained via phase shifting interferometry, which exhibits a wavefront distortion resembling astigmatism. **c** After wavefront correction, we obtain a residual wavefront distortion of $\lambda/100$ at the employed wavelength of 322 nm.

with a resolution of 8 bits. Starting with a collimated beam, the MMA is illuminated at an angle of incidence of approximately 7° and the optically imprinted phase profile is given by twice the path-length difference configured by the mirror stroke. A full phase modulation of $\Phi(x,y) \in [0,2\pi)$ is thus feasible for wavelength up to about 700 nm and because of the purely reflection-based working principle, the MMA is compatible with a broad range of wavelengths, including the ultraviolet range. To prevent damage to the microelectromechanical-system-based (MEMS) control components from ozone, which forms in the presence of ambient air under UV irradiation, we continuously flush the MMA surface with dry nitrogen. This is realized by installing a small enclosure with a central fused-silica window in front of the MMA and connecting a weak flow of nitrogen.

To demonstrate the possibility of holographic beam shaping in the UV spectral range, we generate various tweezer arrays at a wavelength of 322 nm, see Fig. 6.1b-d and also at a wavelength of 688 nm, see Fig. 6.1e. Generating high-quality optical potentials relies on compensating optical aberrations, which we independently characterize via phase shifting interferometry.

6.2.1 Phase shifting interferometry

To carry out phase shifting interferometry and measure the wave front distortion across the beam, we deactivate most MMA pixels and turn on only two superpixel areas which each displays a blazing grating. The light reflected from both superpixels

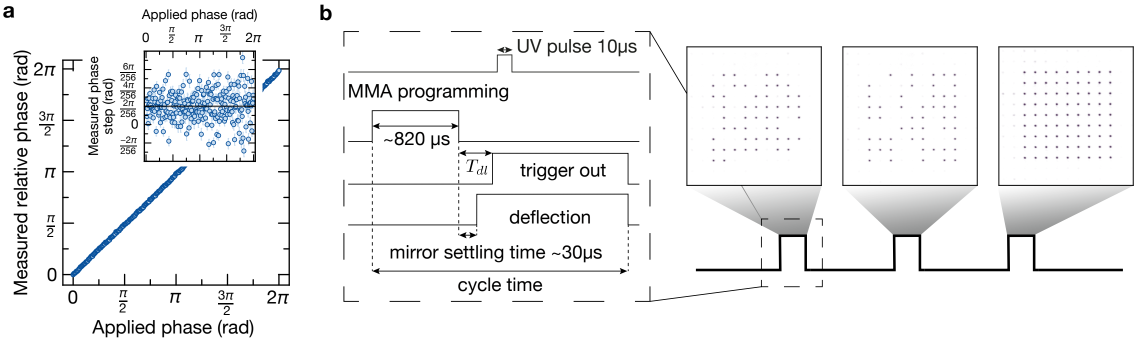

Figure 6.3: Resolution and switching speed. **a** To benchmark the resolution of the MMA, we apply phase-shifting interferometry and step the phase of one superpixel in steps of $\frac{2\pi}{256}$ and observe the phase of the resulting interference fringe. Here, the extracted phase is shown as a function of the programmed phase, and the inset shows the measured phase step of each point with respect to the previous value. The points indeed scatter around a mean step size of $\frac{2\pi}{256}$. **b** Timing diagram of the MMA. The deflection cycle of the MMA is synchronized to the experimental sequence using TTL signals.

interferes on the camera, as shown in Fig. 6.2a, and the phase of the interference pattern is extracted. By varying the position of the second superpixel with respect to the common reference in the center, the phase profile across the beam is mapped out, which includes aberrations induced by the deformation of the MMA surface, residual aberrations of the incident light field, and aberrations in the optical setup. We initially observe astigmatism, see Fig. 6.2b and reach a residual root-mean-square wavefront distortion of $\lambda/100$, within a circular aperture after applying the phase correction obtained in the first step. This demonstration, performed at a wavelength of 322 nm establishes MMAs as a powerful alternative to LCOS-SLMs and unlocks holographic beam shaping in the ultraviolet spectral range. In the following, we characterize the MMA in terms of the achievable phase resolution and timing.

6.3 Benchmarking the MMA

6.3.1 Phase resolution

Each MMA mirror is programmed with an electronic resolution of 8 bits, and to characterize the available phase resolution in the optical domain, we make use of the superpixel setup introduced for phase shifting interferometry. We vary the phase of one superpixel and measure the phase of the resulting interference fringe on the camera. In Fig. 6.3a the extracted phase relative to the initial fringe is shown as a function of the programmed phase shift on the superpixel, and the linear scaling with unity slope

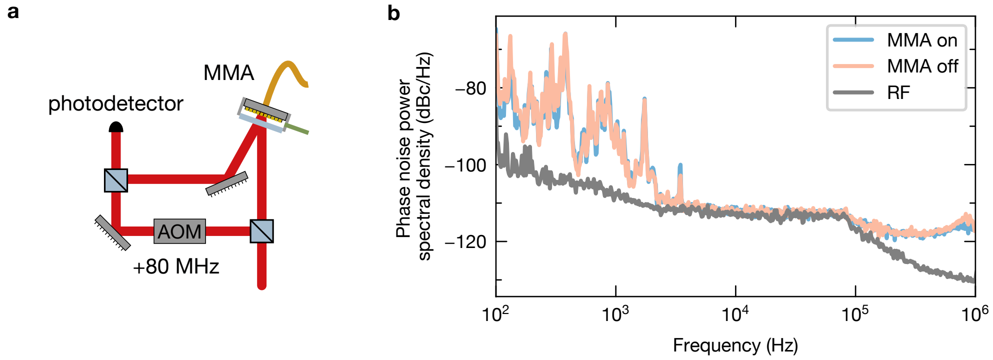

Figure 6.4: Phase noise of the MMA. a To characterize the phase noise added by the MMA, we set up a self-heterodyne interferometer. One arm of the interferometer contains the MMA, and the other arm features an AOM to offset the optical frequency by 80 MHz. The two arms are superimposed on a fast photodetector, and the phase noise of the beat signal is analyzed. **b** Phase noise power spectral densities with activated and deactivated MMA deflection. We observe no excess phase noise within our measurement sensitivity.

confirms the correct calibration for the employed wavelength. For this measurement, we step the applied phase with the smallest possible resolution of $\frac{2\pi}{256}$, given by the 8-bit resolution, and compute, for each step, the phase difference compared to the previous measurement (see inset in Fig. 6.3a). The measured phase steps indeed scatter around the programmed step size of $\frac{2\pi}{256}$. With respect to a linear fit, we obtain the largest residual deviation of $2.2 \times \frac{2\pi}{256}$ and a standard deviation of $0.91 \times \frac{2\pi}{256}$, indicating that the resolution in the optical domain is slightly reduced compared to the electronic resolution given by the MMA controller.

6.3.2 MMA timing

Besides the compatibility with UV wavelength, one intriguing feature of MMAs is given by the perspective of holographic beam shaping with fast update rates beyond the applicability of LCOS-type light modulators. For the demonstration here, we use a MMA, which supports an update rate of 1 kHz and is thus comparable to the fastest currently available LCOS-SLMs (Meadowlark HSP1K-488-850-PC8-TCS4). However, the switching speed is currently limited by the underlying MEMS-based control electronics and can be improved in future developments, which provides access to highly parallel control of focused spot arrays at fast rates.

The timing diagram for MMA-based beam shaping is shown in Fig. 6.3b and begins with a 820 µs-long programming duration where the stroke of each mirror is configured and becomes active after a mirror settling time of approximately 30 µs. At this point, the MMA deflection is active for a programmable duration, which can be synchronized with a TTL trigger output indicating the completed deflection with a configurable delay. To mimic the application of an MMA for UV beam shaping in a neutral atom experiment, we synchronize the MMA deflection with 10 µs-long UV pulses generated with an independent acousto-optic deflector. At the power level of 100 mW used here we observe no degradation of the MMA and demonstrate the rapid switching of holographic masks, see Fig. 6.3b.

6.3.3 Phase noise

The MMA is based on an array of mirrors mounted to a spring-like structure and an electrostatically configured stroke. In order to estimate the extent to which residual motion of the mirrors translates to phase noise, we set up the self-heterodyne interferometer shown in Fig. 6.4a. One arm of the interferometer contains the MMA, which is compared to a reference arm by superimposing both paths on a fast photodetector. The optical frequency in the reference arm is shifted by +80 MHz to generate a beating signal away from DC, which is subsequently analyzed to obtain the phase noise power spectral densities shown in Fig. 6.4b. Compared to the passive MMA, where the device acts purely as a flat mirror, we observe no excess phase noise when the MMA displays a phase pattern. For the measurement with activated MMA, we configure a single blazing grating and align the diffracted light onto the photodetector. The absence of excess phase noise demonstrates that MMAs are suitable for a variety of applications, including the generation of holographically programmed off-resonant tweezer arrays or the addressing of individual qubits with focused resonant laser beams, where phase noise affects the gate fidelities. Compared to LCOS-SLMs, MMAs do not require refresh cycles at around 60 Hz, which usually gives rise to excess intensity noise at the update frequency.

6.4 Applications

The UV-compatibility and the perspective of realizing high-speed switchable potentials enable multiple applications of MMAs in the context of quantum simulation and computing. For example, the ability of beam shaping in the UV range facilitates the creation of flat top beam profiles, as shown in Fig. 6.5c. This provides the means to equalize the UV intensity in a zone-based architecture to provide the same Rabi frequency to all qubits located in a gate zone. Compared to Gaussian beams, which inherently yield an intensity gradient across the beam, the flat top shapes allow for a more homogeneous illumination, and we obtain a residual RMS inhomogeneity of 0.75 % with a peak-to-peak variation of 3.65 %. To exploit the flat top illumination in quantum computing setups, neutral atoms can be stored in a dedicated storage zone and moved to single- and two-qubit gate zones for the manipulation with light,

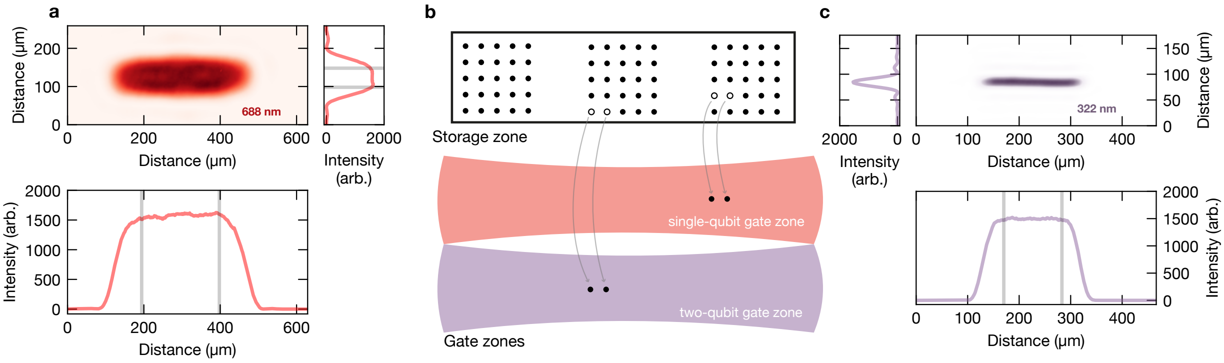

Figure 6.5: Applications of MMAs. Micromirror arrays have several applications in the field of neutral-atom-based quantum simulation and computing. Due to the compatibility with UV wavelength, they enable flat-top beam shaping, which provides a homogeneous illumination of atoms in zone-based architectures. **a** Two-dimensional flat-top beam generated at a wavelength of 688 nm, reaching an rms inhomogeneity of 1.8 % (1.4 %) and a peak-to-peak variation of 7.4 % (6.2 %) in the x (y) directions at a power efficiency of about 38 %. **b** Zone-based neutral atom quantum computing architecture. Individual atoms are moved into dedicated zones for single- and two-qubit gate operations. A homogeneous illumination within each zone is favourable and can be realized using the MMA-generated flat-top beam profiles. **c** Flat-top beam at 322 nm with a residual rms inhomogeneity of 0.75 % and a peak-to-peak variation of 3.65 %

see Fig. 6.5b. In this case, the atoms are shuttled coherently, for example, using AODs, and the MMAs are used to provide a homogeneous illumination with the gate lasers. Complementary to this configuration, MMAs may also be used to directly address individual atoms through the high-NA objectives. Making use of their fast update rates, resonant light pulses can be applied to a programmable set of atoms to perform gate operations. In addition, future setups might use MMAs in combination with off-resonant trapping light for generating rapidly configurable tweezer arrays. This offers new possibilities to rearrange atoms in parallel along arbitrary trajectories and overcomes constraints of AOD-based setups [191–193].

6.5 Summary and outlook

In this chapter, we introduced a new type of phase-only spatial light modulator based on micromirror arrays. Due to the purely reflection-based working principle and the absence of a liquid-crystal layer, the device is compatible with wavelengths in the ultraviolet regime, which facilitates new possibilities for holographic beam shaping. Furthermore, the perspective of drastically increased update rates for phase-based light modulation opens up new prospects for generating rapidly switchable spot arrays or to rearrange neutral atoms in parallel along arbitrary trajectories, thereby bypassing the limitations of AOD-based setups, which typically allow for parallel displacements only along the eigenaxes of the AODs.

Chapter 7

Conclusion and outlook

7.1 Conclusion

In this thesis, we demonstrated a new hybrid lattice-tweezer experiment for strontium atoms in optical lattice and tweezer potentials, which offers a versatile toolbox suitable for quantum simulation and computing experiments. Due to the large tensor polarizability of strontium, the trapping conditions for various electronic states can be tuned in a linearly polarized light field using magnetic fields applied under specifically chosen angles.

We utilize this to realize an optical qutrit comprising the electronic ground state $^1\mathrm{S}_0$ and both long-lived clock states $^3\mathrm{P}_0$ and $^3\mathrm{P}_2$. Separated by optical transition frequencies, we realize coherent all-to-all control over the qutrit states using two- and three-photon transitions. The direction of the magnetic quantization axis is constrained to realize triple-magic conditions, and therefore the three-photon coupling is crucial for our demonstrations, since the single-photon coupling would be prohibitively slow under realistic experimental conditions, owing to the inherently small coupling on the clock transition.

Under triple-magic conditions, we characterize the fine-structure (FS) qubit given by the $^3\mathrm{P}_0$ and $^3\mathrm{P}_{2,m_j=0}$ clock states and demonstrate state-of-the-art coherence times. This promotes the FS qubit to a competitive qubit candidate and demonstrates that state-of-the-art coherence times are realistically achievable in tweezer-based angle-tuned trapping potentials despite the existence of a polarization gradient within the tweezers caused by the high numerical aperture of the objective.

In our setup, we observe additionally polarization gradients across the tweezer array, which we attribute to a small residual misalignment with respect to a telecentric configuration and characterize the spatially varying differential light shift. These inhomogeneities rapidly limit the contrast in the tweezer-averaged measurements and can be very successfully mitigated using dynamical decoupling sequences.

The fast two-photon control over the $^3\mathrm{P}_J$ states enables not only coherent control over the clock states, but also allows for controlled dissipation when coupling either of the $^3\mathrm{P}_{0,2}$ states to $^3\mathrm{P}_1$, from where the atoms decay back to the ground state. We utilize a two-photon coupling to demonstrate a measurement-free qubit reset based on dissipatively resetting the qubit population after the system has decohered. This facilitates, for example, measurement-free fault-tolerant quantum computing [170].

The fidelity of the two- and three-photon operations is currently limited by laser phase noise, and we present tools to measure phase noise directly in the optical regime and model the effect on arbitrary gate operations. To overcome the limitations of the currently used frequency-comb-based setup, a new laser system was constructed where the four relevant wavelengths 679, 688, 689, and 707 nm are referenced to a common 4-bore ULE cavity. This setup provides a cost-efficient implementation and facilitates the direct transfer of the ULE-based stability onto the light fields without intermediate lock chains required for comb-based systems. Using the demodulated PDH signal, we set up a feedforward phase noise suppression, which paves the way for high-fidelity operations at MHz-regime coupling rates.

Besides the detailed characterization of multi-photon operations, we demonstrate the bottom-up assembly of large-scale atom arrays in the optical lattice system. The combination of the site-resolved readout enabled by quantum gas microscopes in scalable optical lattices with the single-site control offered by optical tweezers enables new possibilities to operate neutral atom experiments. We present and characterize a protocol for the iterative assembly and continuous operation of atom arrays, which overcomes scaling bottlenecks of tweezer-based systems. The iterative procedure relies on high-fidelity and low-loss imaging, which we demonstrate in our folded lattice setup at a wavelength of 1040 nm using the repulsive Sisyphus cooling mechanism. This wavelength lies within the range of Ytterbium-doped fiber amplifiers and thus offers exciting scalability prospects.

By superimposing the lattice with a tweezer array commensurate with the lattice spacing, we demonstrate the repeated transfer of atoms from the tweezers to the lattice potential and back. This provides the means to decouple, for example, the trap-depth-demanding imaging from the rest of the sequence and facilitates the creation of larger tweezer systems at a wavelength where high-power sources are not available.

Moreover, we demonstrate the sorting of atoms in a single plane of the optical lattice after loading the atoms directly from a magneto-optical trap. This paves the way for generating scalable atom arrays in the two-dimensional lattice potential, which may potentially overcome the current state of the art of large-scale tweezer-based setups. Furthermore, the precise positioning of atoms at programmable lattice sites provides means to initialize quantum walk experiments [123], configure local tunneling rates [209] or to prepare quantum optics experiments [210].

To facilitate large-scale resorting in future experiments and reduce the data-processing overhead, we developed and characterized a state detection algorithm based on a convolutional neural network. This approach offers a noise-resilient atom detection, and "learns" to account for non-linear effects such as superradiance in areas of densely spaced atoms. By separating the deconvolution from the state detection, where the emission is assigned to a lattice site, we outline an algorithm compatible with arbitrary lattice geometries.

Rearanging atoms in optical potentials is commonly done using mobile tweezers controlled with acousto-optic deflectors, which allow for parallel moves along the eigenaxes of the AOD setup. Arbitrary parallelized moves beyond the grid spanned by the AODs are, however, not feasible and require different modulators, for example, based on phase-only spatial light modulators. So far, suitable modulators offer a limited update rate, which prevents large-scale resorting based on this technology. Here, we benchmarked a new type of phase-only spatial light modulator based on arrays of micromirrors with configurable stroke. This technology offers the intriguing perspective of holographic beam shaping at fast rates and enables spatial phase-only modulation in the UV range.

In this thesis, we demonstrated control over the external degrees of freedom of atoms in terms of their position in optical potentials as well as fast control over the internal electronic states. The toolbox of our experiment enables multiple intriguing studies for future experiments, of which some are briefly outlined in the following section.

7.2 Outlook

7.2.1 Quantum optics experiments in the lattice

Most of the existing experiments focus on coherent quantum dynamics in closed systems. However, in ordered atomic arrays with interatomic spacings at the subwavelength regime, collectively enhanced dissipative interactions can become a fruitful resource. In strontium, the $^3\mathrm{P}_2 \leftrightarrow 5s4d\,^3\mathrm{D}_3$ transition occurs at a wavelength of 2.92 µm, which is more than 5-fold larger compared to our lattice spacings of 0.57 µm, which provides an exciting platform for the study of collective effects in ordered atom arrays. Superradiant dynamics have been previously studied in the context of cavity quantum electrodynamics [211] and similar effects are expected for ordered atomic arrays [212]. For initially interverted atomic arrays, with all atoms prepared in the $^3\mathrm{D}_3$ state, the dipolar interaction gives rise to a photon burst, known as a superradiant burst [203, 212, 213]. Combined with the additional control over atomic configurations, which can be resorted to arbitrary patterns within the lattice potential, this opens the possibility of exploring the influence of geometry on the collective response. Additionally, the strong confinement in the optical lattice with trap frequencies in the 100 kHz regime reduces the atomic position uncertainty, which has been an important limitation in previous work on sub-wavelength-spaced atom arrays [214]. The collective decay of atoms can be characterized by recording the photon emission rate; however, at the wavelength of 2.92 µm we expect high losses in the objective lens, and suitable single-photon detectors are not available. Instead, we will characterize the evolution of the effective two-level system on the $^3\mathrm{P}_{2,|m_j|=2} \leftrightarrow {}^3\mathrm{D}_{3,|m_j|=3}$ transition by rapidly mapping the $^3P_2$ population to $^3P_0$ via a fast two-photon coupling. The high two-photon Rabi frequency presented in Section 3.4.2 is, thus, not only of interest for digital gates, but also opens up exciting possibilities for analog simulation experiments.

7.2.2 Dense assembly of atom arrays with tune-out tweezers

Studying collective effects with atomic arrays requires the assembly of atoms at subwavelength spacings. In case of the transition wavelength of 2.92 µm for strontium, this constraint is simplified and already fulfilled, for example, for interatomic spacings of approximately 1.1 µm, which corresponds to next-nearest-neighbor occupation in the horizontal direction of our folded lattice. These spacings are addressable with focused tweezers in the visible regime; however, to unlock the full potential of our quantum simulator, atoms are ideally positioned deterministically with unity filling requiring control at the half µm level.

To realize extended atomic arrays with unity filling in the lattice potential, we envision using tweezers at the ground-state tune-out wavelength of 689.222 nm, where the polarizability of the electronic ground state vanishes and atoms are thus unaffected by resorting tweezers at this wavelength [215]. To fill a defect in an area that is densely surrounded by atoms and without a free corridor along which the atoms could be moved, we will optically pump atoms into the $^3P_0$ clock state and subsequently move them with an AOD-driven tune-out tweezer into the desired site. Afterwards, the atoms can be globally repumped to initialize the array in $^1S_0$. Optical pumping into the $^3P_0$ clock state can be conveniently realized using two resonant light fields at 689 and 688 nm, which are focussed onto the desired atom (see Section 4.3 for the electronic levels involved in the optical pumping procedure) and can be applied via the tune-out addressing setup due to the wavelength similarity.

Assembled Hubbard simulators

The ability to arrange atoms onto nearest-neighbor sites with interatomic spacings in the half to one µm range opens the possibility to carry out analog simulations of the Hubbard model with assembled atom arrays [209, 216]. The Hubbard model is described by the Hamiltonian (7.1) for bosonic species and is characterized by the nearest-neighbor tunneling rate J, the spatially-dependent chemical potential ϵ_i, and the on-site interaction U.

$$H/\hbar = -J \sum_{\langle i,j \rangle} a_i^\dagger a_j + \sum_i \epsilon_i n_i + \frac{U}{2} \sum_i n_i(n_i - 1) \tag{7.1}$$

Realizing this Hamiltonian requires the preparation of the atomic ensemble in the lowest Bloch band, which is usually achieved by means of evaporative cooling, which typically limits the repetition rate of Hubbard simulators to several seconds, owing to the slow rethermalization of atoms required for efficient evaporation. Higher cycle rates are potentially feasible with setups based on assembled atomic arrays [216]. Resorting atoms in the lattice potential will inevitably cause heating and ground-state cooling can be subsequently realized via resolved sideband cooling in a sufficiently deep lattice potential. In this light, our demonstration of the three-photon-based sideband resolved spectroscopy in Chapter 4 opens up new means to realize suitable cooling schemes for strontium. In order to realize sufficiently cold temperatures, sideband-resolved two-photon pulses allow for dissipatively resetting hot atoms from $^3\mathrm{P}_2$ via $^3\mathrm{P}_1$ back to the electronic ground state, which provides the means for postselection on the successful motional-ground-state preparation in the context of the analog simulation [89].

Preparing atoms in a Hubbard-regime setup in our experiment, furthermore, requires stronger vertical confinement in order to reach a sizeable on-site interaction $U = \frac{4\pi\hbar^2 a}{m} \int |w(r)|^4 \,\mathrm{d}r$, where a is the s-wave scattering length, m is the atomic mass and $w(r)$ is the Wannier wavefunction for a lattice site, which depends in particular on the trap frequencies [217].

7.2.3 Ising-type simulations

The tweezer-based trapping of atoms and the excitation to highly-excited Rydberg states offers an ideal testbed for analog simulations of the Ising model. Here, a two-level atom with ground state and Rydberg state is driven at (site-dependent) Rabi frequency Ω_i and detuning δ, and the Rydberg interaction gives rise to position- and state-dependent energy shifts V_{ij}. The Hamiltonian (7.2) is expressed in terms of the number $n_i \in (0, 1)$ of Rydberg atoms on the i-th site.

$$H/\hbar = \frac{1}{2} \sum_i \Omega_i \sigma_x^i - \delta \sum_i n_i + \sum_{i<j} V_{ij} n_i n_j \tag{7.2}$$

In this setup, the position control of the optical tweezer arrays enables studies of geometrical frustration [63] and multiple interesting many-body phases can be prepared via adiabatic sweeps of the parameters [20]. For suitable tuned detuning $\delta = -V/4$ Rydberg facilitation enables the two-photon coupling from the two-particle ground state to the Rydberg state, which gives rise to correlated dynamics that can be exploited for the analog simulation of lattice gauge theories [67, 136].

Appendix A

Three-photon coupling from ground to clock state

In this appendix, we discuss the three-photon coupling from the ground state $^1\mathrm{S}_0$ to the clock state $^3\mathrm{P}_0$, compute the three-photon Rabi frequency and derive an analytic estimation for the scattering-limited infidelity.

Following Ref. [218], the Hamiltonian of the system in 4-level approximation is given by (A.1). Here and in the following, we are setting $\hbar = 1$.

$$\begin{aligned} H = &-\Delta_{689} \left|^3\mathrm{P}_1\right\rangle \left\langle^3\mathrm{P}_1\right| - (\Delta_{689} + \Delta_{688}) \left|^3\mathrm{S}_1\right\rangle \left\langle^3\mathrm{S}_1\right| \\ &-(\Delta_{689} + \Delta_{688} - \Delta_{679}) \left|^3\mathrm{P}_0\right\rangle \left\langle^3\mathrm{P}_0\right| \\ &+ \left(\frac{\Omega_{689}}{2} \left|^1\mathrm{S}_0\right\rangle \left\langle^3\mathrm{P}_1\right| + \frac{\Omega_{688}}{2} \left|^3\mathrm{P}_1\right\rangle \left\langle^3\mathrm{S}_1\right| + \frac{\Omega_{679}}{2} \left|^3\mathrm{P}_0\right\rangle \left\langle^3\mathrm{S}_1\right| + h.c. \right) \end{aligned} \tag{A.1}$$

This Hamiltonian can be restructured and separated into a ground-state-like part H_g and an excited-state-like part H_e, and a coupling operator $\hat{V}_+$ which drives the system from the ground to the excited subspace

$$\begin{aligned} H_g &= -(\Delta_{689} + \Delta_{688} - \Delta_{679}) \left|^3\mathrm{P}_0\right\rangle \left\langle^3\mathrm{P}_0\right| \\ H_e &= -\Delta_{689} \left|^3\mathrm{P}_1\right\rangle \left\langle^3\mathrm{P}_1\right| - (\Delta_{689} + \Delta_{688}) \left|^3\mathrm{S}_1\right\rangle \left\langle^3\mathrm{S}_1\right| + \left(\frac{\Omega_{688}}{2} \left|^3\mathrm{P}_1\right\rangle \left\langle^3\mathrm{S}_1\right| + h.c. \right) \\ \hat{V}_+ &= \left(\frac{\Omega_{689}}{2} \left|^3\mathrm{P}_1\right\rangle \left\langle^1\mathrm{S}_0\right| + \frac{\Omega_{679}}{2} \left|^3\mathrm{S}_1\right\rangle \left\langle^3\mathrm{P}_0\right| + h.c. \right) \\ \hat{V}_- &= \hat{V}_+^\dagger \end{aligned}$$

We want to find the effective dynamics and scattering rates within the ground-state manifold upon adiabatic elimination of the excited-state subspace. To describe coherent and dissipative effects, we work with a Lindblad master equation, which describes the evolution of a density matrix. The Lindblad master equation for the density matrix ρ is given by (A.2) with the Hamiltonian H from (A.1).

$$\dot{\rho} = -i\,[H, \rho] + \sum_k \hat{L}_k \rho \hat{L}_k^\dagger - \frac{1}{2} \left(\hat{L}_k^\dagger \hat{L}_k \rho + \rho \hat{L}_k^\dagger \hat{L}_k \right) \tag{A.2}$$

The Lindblad decay operators are given by $L_1 = \sqrt{2\gamma_{^3\mathrm{P}_1}}\,|^1\mathrm{S}_0\rangle\langle^3\mathrm{P}_1|$ and $L_{2/3} = \sqrt{2\gamma_{^3\mathrm{S}_1\to s}}\,|s\rangle\langle^3\mathrm{S}_1|$ for $s = {}^1\mathrm{S}_0, {}^3\mathrm{P}_0$. Here, $\gamma_{^3\mathrm{S}_1\to s}$ denotes the decay rate of atoms in state $^3\mathrm{S}_1$ to state s. We obtain the effective dynamics and decay rates via adiabatic elimination of the excited subspace following the technique presented in Ref. [219]. The non-hermitian Hamiltonian, required for the next step of the calculation, is given by:

$$\begin{aligned}\hat{H}_{\mathrm{NH}} &= H_e - \frac{i}{2}\sum_k \hat{L}_k^\dagger \hat{L}_k \\ &= -\tilde{\Delta}_{^3\mathrm{P}_1}|^3\mathrm{P}_1\rangle\langle^3\mathrm{P}_1| - \tilde{\Delta}_{^3\mathrm{S}_1}|^3\mathrm{S}_1\rangle\langle^3\mathrm{S}_1| + \left(\frac{\Omega_{688}}{2}|^3\mathrm{P}_1\rangle\langle^3\mathrm{S}_1| + h.c.\right)\end{aligned}$$

with $\tilde{\Delta}_{^3\mathrm{P}_1} = \Delta_{689} + i\gamma_{^3\mathrm{P}_1}$ and $\tilde{\Delta}_{^3\mathrm{S}_1} = \Delta_{689} + \Delta_{688} + i\gamma_{^3\mathrm{S}_1\to{}^3\mathrm{P}_0} + i\gamma_{^3\mathrm{S}_1\to{}^1\mathrm{S}_0}$. The inverse of the non-Hermitian Hamiltonian is given by:

$$\begin{aligned}\hat{H}_{\mathrm{NH}}^{-1} = &\frac{4\tilde{\Delta}_{^3\mathrm{S}_1}}{|\Omega_{688}|^2 - 4\tilde{\Delta}_{^3\mathrm{P}_1}\tilde{\Delta}_{^3\mathrm{S}_1}}|^3\mathrm{P}_1\rangle\langle^3\mathrm{P}_1| + \frac{4\tilde{\Delta}_{^3\mathrm{P}_1}}{|\Omega_{688}|^2 - 4\tilde{\Delta}_{^3\mathrm{P}_1}\tilde{\Delta}_{^3\mathrm{S}_1}}|^3\mathrm{S}_1\rangle\langle^3\mathrm{S}_1| \\ &+ \left(\frac{2\Omega_{688}}{|\Omega_{688}|^2 - 4\tilde{\Delta}_{^3\mathrm{P}_1}\tilde{\Delta}_{^3\mathrm{S}_1}}|^3\mathrm{P}_1\rangle\langle^3\mathrm{S}_1| + h.c.\right)\end{aligned}$$

Following the effective operator formalism, we compute the effective Hamiltonian within the ground-state manifold and obtain the three-photon coupling and light shift contributions:

$$\begin{aligned}H_{\mathrm{eff}} &= -\frac{1}{2}\hat{V}_-\left(\hat{H}_{\mathrm{NH}}^{-1} + (\hat{H}_{\mathrm{NH}}^{-1})^\dagger\right)\hat{V}_+ + H_g \\ &= H_3 + H_{LS} + H_g \\ H_3 &= \frac{1}{2}\frac{\Omega_{689}\Omega_{688}\Omega_{679}^*}{|\Omega_{688}|^2 - 4\tilde{\Delta}_{^3\mathrm{P}_1}\tilde{\Delta}_{^3\mathrm{S}_1}}|^1\mathrm{S}_0\rangle\langle^3\mathrm{P}_0| + h.c \\ H_{LS} &= -\frac{|\Omega_{688}|^2}{8}\mathrm{Re}\left(\frac{8\tilde{\Delta}_{^3\mathrm{S}_1}}{|\Omega_{688}|^2 - 4\tilde{\Delta}_{^3\mathrm{P}_1}\tilde{\Delta}_{^3\mathrm{S}_1}}\right)|^1\mathrm{S}_0\rangle\langle^1\mathrm{S}_0| \\ &\quad - \frac{|\Omega_{679}|^2}{8}\mathrm{Re}\left(\frac{8\tilde{\Delta}_{^3\mathrm{P}_1}}{|\Omega_{688}|^2 - 4\tilde{\Delta}_{^3\mathrm{P}_1}\tilde{\Delta}_{^3\mathrm{S}_1}}\right)|^3\mathrm{P}_0\rangle\langle^3\mathrm{P}_0|\end{aligned}$$

These results can be simplified further assuming $\Delta_{^3\mathrm{S}_1} \gg \Omega_{688}, \gamma$ and $\Delta_{688} \approx \Delta_{679}$ to obtain a simple and intuitive result for the three-photon Rabi frequency (A.3) and the two single-photon light shifts (A.4).

$$\Omega_3 = \frac{\Omega_{679}\Omega_{688}\Omega_{689}}{4\Delta_{688}\Delta_{689}} \tag{A.3}$$

$$H_{LS} = \frac{1}{4}\frac{|\Omega_{689}|^2}{\Delta_{689}} |^1\mathrm{S}_0\rangle \langle ^1\mathrm{S}_0| + \frac{1}{4}\frac{|\Omega_{679}|^2}{\Delta_{679}} |^3\mathrm{P}_0\rangle \langle ^3\mathrm{P}_0| \tag{A.4}$$

Note that this Hamiltonian is still taken in the frame of $H_g = -(\Delta_{689} + \Delta_{688} - \Delta_{679}) |^3\mathrm{P}_0\rangle \langle ^3\mathrm{P}_0|$. We thus obtain the condition for three-photon resonance, taking the individual light shifts into account:

$$\Delta_{679} = \Delta_{688} + \Delta_{689} - \frac{1}{4}\left(\frac{\Omega_{679}^2}{\Delta_{679}} - \frac{\Omega_{689}^2}{\Delta_{689}}\right) \tag{A.5}$$

For a suitable ratio of the optical powers in the beams, the differential light shifts induced by the three-photon coupling vanish. This is a remarkable difference compared to the often employed single-photon coupling at a wavelength of 698 nm, where the probe shift inevitably grows as the power is increased. Setting $|\Omega_i|^2 = \alpha_i\, P_i$ we obtain the “magic power ratio” given by Eq. (A.6) for which the three-photon probe shift vanishes.

$$\frac{P_{689}}{P_{679}} = \frac{\alpha_{679}}{\alpha_{689}}\frac{\Delta_{689}}{\Delta_{679}} \approx 169.8\frac{\Delta_{689}}{\Delta_{679}} \tag{A.6}$$

In addition to the effective ground-state dynamics, the effective operator formalism also provides us with the effective decay and dephasing rates within the ground-state subspace. The effective rates after adiabatic elimination of the excited subspace are given by

$$\hat{L}^k_{\mathrm{eff}} = \hat{L}_k \hat{H}^{-1}_{\mathrm{NH}} \hat{V}_+$$

for all decay operators $k = 1, 2, 3$ listed above. The rates between states $|g\rangle, |g'\rangle \in (|^1\mathrm{S}_0\rangle, |^3\mathrm{P}_0\rangle)$ are then given by $\Gamma_k = |\langle g| \hat{L}^k_{\mathrm{eff}} |g'\rangle|^2$. We group the resulting contributions into population relaxation (L^{T_1}) and dephasing operators (L^{T_2}). The resulting rates of the combined population relaxation and dephasing of the remaining effective two-level system are given by:

$$L^{T_1} = \frac{1}{(4\Delta_{688}\Delta_{689})^2}\left(\Gamma_{^3\mathrm{P}_1}\Omega_{688}^2\Omega_{679}^2 + 3\Gamma_{^3\mathrm{S}_1}\Omega_{679}^2\Delta_{689}^2 + \frac{1}{4}\Gamma_{^3\mathrm{S}_1}\Omega_{688}^2\Omega_{689}^2\right)$$

$$L^{T_2} = \frac{1}{(4\Delta_{688}\Delta_{689})^2}\left(\Gamma_{^3\mathrm{P}_1}4\Omega_{689}^2\Delta_{688}^2 + \frac{3}{4}\Gamma_{^3\mathrm{S}_1}\Omega_{688}^2\Omega_{689}^2 + \Gamma_{^3\mathrm{S}_1}\Omega_{679}^2\Delta_{689}^2\right)$$

The two most important contributions describe dephasing caused by off-resonant single-photon scattering (considering $\Delta_{679} \approx \Delta_{688}$), which we combine into one effective dephasing rate.

$$\Gamma_{\text{eff}} = \Gamma_{{}^3\text{P}_1} \frac{\Omega_{689}^2}{4\Delta_{689}^2} + \Gamma_{{}^3\text{S}_1} \frac{\Omega_{679}^2}{4\Delta_{679}^2}$$

Within the 4-level approximation considered here, additional contributions to dephasing and depolarization are suppressed. We are interested in finding the optimal parameter set within the 5-dimensional parameter space (one detuning is fixed by Eq.(A.5) to stay on three-photon resonance) to maximize the fidelity. Assuming that the fidelity is optimal if the scattering rates from both excited states are equal, we find a simple analytic expression for the infidelity.

$$\epsilon = \frac{\Gamma_{\text{eff}}}{\Omega_3} = 2\sqrt{\frac{\Gamma_{{}^3\text{P}_1}}{\Gamma_{{}^3\text{S}_1}}} \frac{\Gamma_{{}^3\text{S}_1}}{\Omega_{688}} \approx \frac{1}{19.4} \frac{\Gamma_{{}^3\text{S}_1}}{\Omega_{688}}$$

We confirm numerically that this infidelity limit is indeed approximately reached throughout a large volume of the parameter space of this 4-level description. High-fidelity three-photon gates thus require the highest possible Rabi frequency on the 688 nm transition.

Appendix B

Linear response modelling

In this appendix, we discuss the influence of laser phase and intensity noise in the framework of the linear response (LR) formalism and model the resulting infidelity associated with the measured noise power spectral densities [165]. In this formalism, the infidelity $1 - F$ is given by the integral over the product of the noise power spectral density $S(f)$ multiplied with a suitable sensitivity function $I(f)$.

$$1 - F \approx \int \mathrm{d}f \, S(f) \, I(f)$$

A summary of the formalism is provided in Section B.1, which is then applied in Section B.2 to derive the sensitivity functions $I_x(f)$ for various noise types.

B.1 Linear response formalism

We consider a system with Hamiltonian $H = H_0 + \lambda \delta H$ with the ideal Hamiltonian H_0, which is perturbed by δH with a "small" parameter λ. Here, we derive the resulting infidelity of a quantum state due to δH in a perturbation theory description following Ref. [165].

In the interaction picture, governed by the operator $U(t) = \exp(iH_0 t)$, the Hamiltonian is given by $H \to U\,H\,U^\dagger - H_0 = U\,\lambda\delta H\,U^\dagger$ and the state is transformed according to $|\Psi\rangle \to |\tilde{\Psi}\rangle = U\,|\Psi\rangle$.

$$|\tilde{\Psi}\rangle = |\tilde{\Psi}_0\rangle + \lambda\,|\tilde{\Psi}_1\rangle + \lambda^2\,|\tilde{\Psi}_2\rangle + \ldots \tag{B.1}$$

Using ansatz (B.1) for the wavefunction, we can define the fidelity F with respect to the unperturbed state $|\tilde{\Psi}_0\rangle$ by (B.2), which is based on an expansion in terms of the small parameter λ.

$$F = \frac{|\langle\tilde{\Psi}_0|\tilde{\Psi}\rangle|^2}{\langle\tilde{\Psi}|\tilde{\Psi}\rangle} \approx 1 - \left(\langle\tilde{\Psi}_1|\tilde{\Psi}_1\rangle - |\langle\tilde{\Psi}_0|\tilde{\Psi}_1\rangle|^2\right)\lambda^2 + \mathcal{O}(\lambda^3) \tag{B.2}$$

The expectation values can be computed using the known time evolution of the wavefunction (B.3), which is given, in this perturbative treatment, by integrating the Schrödinger equation $i\partial_t\,|\tilde{\Psi}_1\rangle = \delta\tilde{H}\,|\tilde{\Psi}_0\rangle$.

$$|\tilde{\Psi}_1(t)\rangle = -i\int_0^t \mathrm{d}\tau\,\delta\tilde{H}(\tau)\,|\tilde{\Psi}_0\rangle \tag{B.3}$$

Here, $\lambda\delta\tilde{H} = h(t)\hat{O}(t)$ is the noise operator in the interaction picture, and we separate the operator $\hat{O}(t)$ from the noise amplitude $h(t)$. In this case, we define the time-dependent amplitude via its single-sided noise power spectral density $S(f)$, as given by (B.4), for a spectrum with equidistant spacing $\mathrm{d}f$ and randomly sampled phase Φ_f.

$$h(t) = \sum_f \sqrt{2S(f)\mathrm{d}f}\cos\left(2\pi f t + \Phi_f\right) \tag{B.4}$$

In conclusion, the resulting infidelity (B.5) is given as the integral over the power spectral density multiplied with a frequency-dependent sensitivity function (B.6), where the expectation values are computed with respect to the initial state $|\tilde{\psi}_0\rangle = |\psi(t=0)\rangle$.

$$1 - F = \int_0^\infty \mathrm{d}f S(f)\, I(f) \tag{B.5}$$

$$I(f) = \int_0^T \int_0^T \mathrm{d}t\,\mathrm{d}\tau\,\cos\left(2\pi f(t-\tau)\right)\left(\langle\hat{O}(t)\hat{O}(\tau)\rangle - \langle\hat{O}(t)\rangle\langle\hat{O}(\tau)\rangle\right) \tag{B.6}$$

Here, T is the duration over which the system is evolved and corresponds, for example, to the duration of a laser pulse. Computing the sensitivity function provides insight into the most important Fourier components, in order to minimize the resulting error. This can be used, for example, to optimize the position of the servo-bump in laser locks or, alternatively, to choose the Rabi frequency of the optical drive such that the phase-noise-induced error is reduced. A set of analytically computed sensitivity functions for various noise sources is given in the following.

B.2 Sensitivity functions for various noise types

The linear response sensitivity function can be computed as the Fourier transform of the autocorrelation of the noise operator. Here, we derive sensitivity functions for frequency, phase, and intensity noise for a resonantly driven two-level system. A description in terms of frequency or phase noise power spectral densities is, in principle, equivalent; however, care must be taken for certain pulse areas, where the LR treatment of laser frequency noise may yield incorrect predictions.

B.2.1 Intensity noise

To compute the sensitivity function for relative intensity noise (RIN), we consider a resonantly-driven two-level system $H = \frac{\Omega}{2}\sigma_x$ and a perturbation $\delta H = h(t)\sigma_x$. To relate $h(t)$ to intensity noise (instead of field noise), we note that $\Omega \propto \sqrt{I} = \sqrt{I_0}\sqrt{1+\mathrm{RIN}} \approx \sqrt{I_0}(1+\mathrm{RIN}/2)$, and we obtain $h(t) = \frac{\Omega}{4}\mathrm{RIN}(t)$. Since the noise operator commutes with the time-evolution operator, the operator in the Heisenberg picture is again given by σ_x, and we obtain the autocorrelator (B.7).

$$\langle \hat{O}(t)\hat{O}(\tau)\rangle - \langle \hat{O}(t)\rangle \langle \hat{O}(\tau)\rangle = \frac{\Omega^2}{16} \tag{B.7}$$

Here, we have again computed the expectation value with respect to $|g\rangle$, which gives rise to a vanishing expectation value $\langle \hat{O}(t)\rangle = 0$. Note that a non-vanishing expectation value would be obtained for any coherent superposition state. The sensitivity function of intensity noise is given by (B.8).

$$I_{\text{RIN}}(f) = \frac{\Omega^2}{16}\frac{\sin^2(\pi f T)}{\pi^2 f^2} \tag{B.8}$$

Note that intensity noise also gives rise to effective frequency noise in the presence of a sufficiently strong probe shift. In this case, the time-dependent detuning $\Delta(t) = \Delta_0 + \gamma\Omega^2$ is modulated depending on the intensity of the beam, where the factor γ characterizes the strength of the differential light shift induced by the coupling beam.

B.2.2 Laser frequency noise

We consider the Hamiltonian of a driven two-level system (B.9), which is perturbed by $\delta H = -\pi\sigma_z \times \nu(t)$, with the time-dependent frequency noise amplitude $\nu(t)$ characterized by a corresponding noise power spectral density $S_\nu(f)$.

$$H = -\frac{\Delta}{2}\sigma_z + \frac{\Omega}{2}\sigma_x \tag{B.9}$$

To translate the noise operator $\hat{O} = -\pi\sigma_z$ into the Heisenberg picture, we note that $\exp(i\theta\sigma_x) = \cos(\theta)\mathbb{1} + i\sin(\theta)\sigma_x$ and obtain $\hat{O}_H = -\pi(\cos(\Omega t)\sigma_z + \sin(\Omega t)\sigma_y)$. In this case, we obtain the autocorrelator (B.10), where the expectation value is taken with respect to the initial state $|\psi_0\rangle = |g\rangle$.

$$\langle \hat{O}(t)\hat{O}(\tau)\rangle - \langle \hat{O}(t)\rangle \langle \hat{O}(\tau)\rangle = \pi^2 \sin(\Omega t)\sin(\Omega\tau) \tag{B.10}$$

Integrating over t and τ up to time T yields the frequency noise sensitivity function (B.11) as a function of the Fourier frequency f.

$$\begin{aligned} I_\nu(f) = \frac{\pi^2}{16\pi^4 f^4 - 8\pi^2 f^2\Omega^2 + \Omega^4} \times \Big(& 4\pi^2 f^2 \sin^2(T\Omega) - \Omega^2\sin^2(T\Omega) \\ & -8\pi f\Omega\sin(T\Omega)\sin(\pi T f)\cos(\pi T f) \\ & +4\Omega^2\sin^2(\pi T f)\cos(T\Omega) \\ & -2\Omega^2\cos(T\Omega) + 2\Omega^2\Big) \end{aligned} \tag{B.11}$$

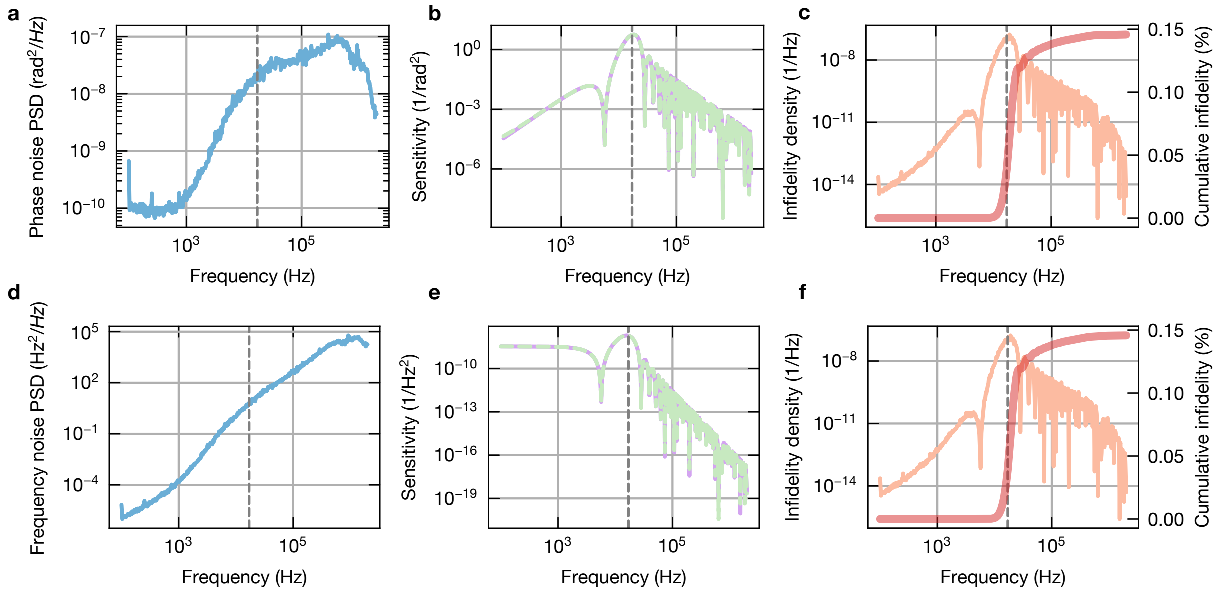

Figure B.1: Linear response phase and frequency noise modelling. The infidelity of a Rabi drive with a pulse area of $\theta = 3\pi$ is shown for a Rabi frequency of $\Omega/2\pi = 17\,\text{kHz}$ (dashed line). The upper panel contains a description in terms of a phase noise, and the lower panel in terms of a frequency noise power spectral density (PSD). **a** Phase noise PSD in units of rad^2/Hz. **b** The analytically derived sensitivity function for phase noise, following (B.17), is shown (purple) together with the numerically computed sensitivity function (green). **c** The infidelity density (orange) given by the product of the noise PSD and the sensitivity function is shown. The infidelity (red) rises strongest in the close vicinity of the Rabi frequency, and saturates towards higher Fourier components. **d** Frequency noise PSD in units of Hz^2/Hz. **e** Analytically derived sensitivity function for frequency noise, following (B.11) (purple) together with the numerically computed sensitivity function (green). **f** The infidelity density (orange) and cumulative infidelity (red) for the frequency noise description agree with the corresponding phase noise description in (c).

B.2.3 Phase noise

In this section, we first show the formal equivalence of phase and frequency noise and compare the frequency noise results from Section B.2.2 to numerical simulations. The linear response description of laser frequency noise yields incorrect predictions if the target state is given by a superposition of the basis states, and we show that more accurate predictions are feasible in a slightly modified phase noise treatment.

Equivalence of phase and frequency noise

The Hamiltonian of a driven two-level system in a frame of the laser frequency is given by (B.12) and the time-dependent phase is sampled according to (B.13) for a given single-sided phase noise power spectral density S_Φ.

$$H = -\frac{\Delta}{2}\sigma_z + \left(\frac{\Omega}{2}e^{i\Phi(t)}\sigma_+ + h.c.\right) \tag{B.12}$$

$$\Phi(t) = \sum_f \sqrt{2S_\Phi(f)\mathrm{d}f}\cos\left(2\pi f t + \Phi_f\right) \tag{B.13}$$

To show the equivalence to a frequency noise treatment, we transform into a time-dependent frame via the unitary $U = \exp(i\Phi(t)/2\sigma_z)$, and obtain the transformed Hamiltonian (B.14), where the derivative of the time-dependent phase acts as an additional detuning and describes frequency noise.

$$H' = -\frac{\Delta}{2}\sigma_z + \left(\frac{\Omega}{2}\sigma_+ + h.c.\right) - \frac{\partial_t\Phi(t)}{2}\sigma_z \tag{B.14}$$

Note that the basis states, in this frame, transform as $|\Psi'(t)\rangle = U(t)\,|\Psi(t)\rangle$, which gives rise to a time-dependent phase that is relevant for the evaluation of fidelities. We obtained the expression $\Delta(t) = \partial_t\Phi(t) = 2\pi\nu(t)$, and compute $\nu(t)$ from the time derivative of (B.13). A resulting time trace for the detuning is then given by (B.15) for the corresponding frequency noise power spectral density $S_\nu = S_\Phi f^2$ and random phase $\Phi'_f = \pi/2 + \Phi_f$.

$$\begin{aligned}\nu(t) &= \frac{1}{2\pi}\partial_t\Phi(t) = \frac{1}{2\pi}\sum_f \sqrt{2S_\Phi(f)\mathrm{d}f}\,2\pi f\,(-1)\sin\left(2\pi f t + \Phi_f\right)\\ &= \sum_f \sqrt{2\,\underbrace{S_\Phi(f)f^2}_{S_\nu}\,\mathrm{d}f}\,\cos\left(2\pi f t + \Phi'_f\right)\end{aligned} \tag{B.15}$$

A description in terms of phase or frequency noise is, thus, equivalent as long as the implicitly assumed time-dependent phase, in the case of the frequency noise description, is considered in the evaluation of fidelity.

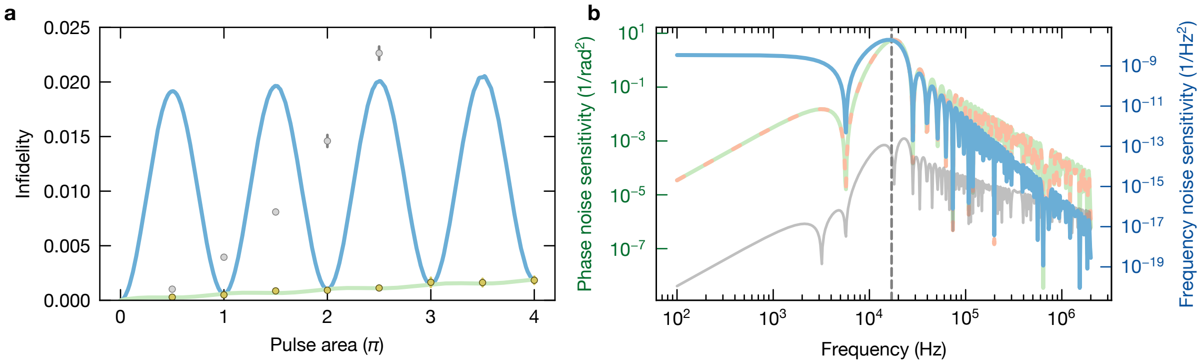

Figure B.2: Comparison of linear response to numerics. **a** To compare the results of the linear response modelling to numerical simulations, we compute the infidelity as a function of pulse area. The linear response frequency noise modelling, following (B.11), predicts an oscillatory infidelity (blue), which overestimates the error if the target state is not given by a basis state. In contrast, the linear response phase noise model, following (B.17), yields a more reasonable result (green). For comparison, we perform numerical simulations averaged over multiple instances of generated time-dependent phase traces. If the state is numerically evolved until time $T = \theta/\Omega$, the resulting infidelity (grey) rapidly rises, since the effective Rabi frequency in the presence of noise is modified. If the fidelity is defined as the best fidelity within a window around the expected pulse duration (yellow), the result agrees with the phase noise linear response description. Error bars for the numerical simulations are estimated via bootstrapping. **b** Comparison of the sensitivity functions for frequency noise and phase noise for a Rabi drive with pulse area $\theta = 3\pi$. For comparison, the frequency noise sensitivity function I_ν (blue) is scaled to the phase noise domain $I'_\Phi = I_\nu \cdot f^2$ (dashed orange), which agrees approximately with the independently derived phase noise sensitivity function I_Φ (green). The residuals $|I_\Phi - I'_\Phi|$ are shown in grey on the phase noise scale. For pulse areas incommensurate with π the deviations are substantially stronger.

Linear response description of laser phase noise

To avoid evaluating fidelity in a time-dependent reference frame, we carry out a similar analysis in a frame co-rotating with the laser and consider the Hamiltonian (B.12). We consider a Taylor expansion of the exponential phase term $\exp(i\Phi(t)) \approx 1 + i\Phi(t)$, and obtain the Hamiltonian $H = H_0 - \Phi(t) \times \frac{\Omega}{2}\sigma_y$. Remarkably, the noise operator is now σ_y instead of σ_z, and the noise amplitude is proportional to Ω, and is taken from a phase noise, rather than a frequency noise, power spectral density. We obtain the expectation value of the autocorrelator (B.16) and the sensitivity function (B.17). A comparison to the frequency noise description is given in Fig. B.1 and yields consistent results for a pulse area of $\theta = 3\pi$. Note that the resulting infidelities differ for pulse areas incommensurate with π, as shown in Fig. B.2a.

$$\langle \hat{O}(t)\hat{O}(\tau)\rangle - \langle \hat{O}(t)\rangle \langle \hat{O}(\tau)\rangle = \frac{\Omega^2}{4}\cos(\Omega t)\cos(\Omega\tau) \tag{B.16}$$

$$\begin{aligned} I_\Phi(f) = \frac{\Omega^2}{16\pi^4 f^4 - 8\pi^2 f^2\Omega^2 + \Omega^4} \times \Big(& -\pi^2 f^2 \sin^2(T\Omega) - 2\pi^2 f^2 \cos(T\Omega) \\ & +4\pi^2 f^2 \sin^2(\pi T f)\cos(T\Omega) + 2\pi^2 f^2 \\ & -2\pi f\Omega \sin(T\Omega)\sin(\pi T f)\cos(\pi T f) \\ & +\frac{\Omega^2}{4}\sin^2(T\Omega)\Big) \end{aligned} \tag{B.17}$$

Spin lock

To derive the sensitivity function for a spin lock experiment (see e.g. Section 3.3.4), we assume that the initial and final $\pi/2$ pulses are perfect, and restrict our attention to the intermediate drive, where the atom is already prepared in an eigenstate of the driving field. Even for imperfect $\pi/2$ pulses, this assumption is justified, since the decay rate of the Ramsey contrast is of interest, and independent of a potential reduction of the initial contrast. The sensitivity function is obtained, as in Section B.2.2, except that we now use the state $|+\rangle = \frac{1}{\sqrt{2}}(|g\rangle + |e\rangle)$ to compute the expectation values. We obtain the spin-lock sensitivity function (B.18), which gets arbitrarily narrow for sufficiently long probe durations T. This can be exploited to experimentally measure noise densities in experiments, following (B.19), by varying the Rabi frequency [165]. Here, we are defining the sinc-function as $\mathrm{si}(x) := \sin(x)/x$.

$$\begin{aligned} I_v^{\text{spin lock}}(f) &= \frac{2\pi^2}{16\pi^4 f^4 - 8\pi^2 f^2\Omega^2 + \Omega^4} \times \Big(-8\pi^2 f^2 \cos(\Omega T)\cos(\pi f T)^2 + 4\pi^2 f^2 \\ &\quad +4\pi^2 f^2 \cos(\Omega T) - 8\pi f\Omega \sin(\Omega T)\sin(\pi f T)\cos(\pi f T) \\ &\quad -2\Omega^2\cos(\Omega T)\cos(\pi f T)^2 + \Omega^2(1+\cos(\Omega T))\Big) \\ &= \frac{\pi^2 T^2}{2}\left(\mathrm{si}\left[\left(\frac{\Omega}{2}+\pi f\right)T\right] + \mathrm{si}\left[\left(\frac{\Omega}{2}-\pi f\right)T\right]\right) \qquad \text{(B.18)} \\ &\approx \frac{\pi^2}{2}\delta\left(f - \frac{\Omega}{2\pi}\right)T \qquad \text{(B.19)} \end{aligned}$$

B.2.4 Comparison of linear response and numerical simulations

To compare the approximate linear response modelling to numerical simulations, we generate samples of the time-dependent phase according to (B.13) and compute the dynamics under the action of the Hamiltonian (B.12). For each sampled phase trace, we obtain the density matrix and average over 100 repetitions of the simulation. To estimate uncertainties of the numerics, we use a bootstrapping procedure and estimate the variance of the fidelity by drawing randomly selected samples from the set of density matrices [220]. The results are shown in Fig. B.2 in comparison to the infidelity obtained via linear response. Remarkably, the frequency noise description yields an oscillatory behaviour which makes incorrect predictions if the pulse area is not an integer multiple of π. In other words, the time-dependent phase, discussed in Section B.2.3, gives rise to an erroneous fidelity prediction if the target state is not given by a basis state. However, the result obtained from the phase noise description agrees with numerical simulations.

B.2.5 Infidelity for parametrized noise power spectral densities

Using the LR description, we can compute the infidelity associated with parametrized noise power spectral densities. Here, we assume a simple model for the frequency noise power spectral density, given by (B.20), and find that this model represents the measured noise densities reasonably well for $m = 3$.

$$S_\nu(f) = \begin{cases} S_\nu^{\text{free}} & f \geq f_B \\ f^m \cdot S_\nu^{\text{free}} / f_B^m & \text{else} \end{cases} \tag{B.20}$$

A fit of (B.20) to the measured noise density, which we considered in Section 3.3.3, is shown in Fig. B.3b and yields a cut-off bandwidth of $f_B \approx 0.48\,\text{MHz}$. For a given bandwidth, we compute the frequency-noise-induced π-pulse infidelity as a function of the parameter S_ν^{free}, which is shown in Fig. B.3a. The calculation shows that a locking bandwidth f_B higher than the Rabi frequency offers a significant fidelity boost, as the feedback can suppress the relevant noise components in this case. However, for Rabi frequencies around or beyond the locking bandwidth, the most important Fourier components are no longer efficiently suppressed, and the infidelity depends on the noise density of the free-running laser. Here, we vary this parameter to compute the resulting infidelity for different Rabi frequencies. Fundamentally, this noise density is limited by the Schawlow-Townes limit $S_\nu^{\text{ST}} = h\nu_0\nu_c^2/P$ for given laser frequency ν_0, cavity linewidth ν_c, and output power P [171]. Assuming MHz-regime Rabi frequencies, the calculation shows that frequency noise densities of about $50\,\text{Hz}^2/\text{Hz}$ or less are required to support π-pulse infidelities on the order of a few times 10^{-5}. For Rabi frequencies well below 1 MHz, the intrinsic laser properties are less important since feedback-based laser locks typically provide an efficient noise suppression. Complementary, for Rabi frequencies of a few MHz or more, the intrinsic laser properties are an important property unless a high-bandwidth feedforward noise suppression is utilized [173, 221, 222].

In addition to this parametrized frequency noise power spectral density, we compute the π-pulse infidelities associated with white intensity, phase, and frequency noise power spectral densities, as shown in Fig. B.3c,d,e. For moderate intensity noise the resulting infidelities are negligble unless a strong probe shift gives rise to associated frequency noise. Note that lasers often exhibit more complex noise spectra compared to the simple parametrization used here. A collection of typical frequency noise densities can be found in Ref. [171].

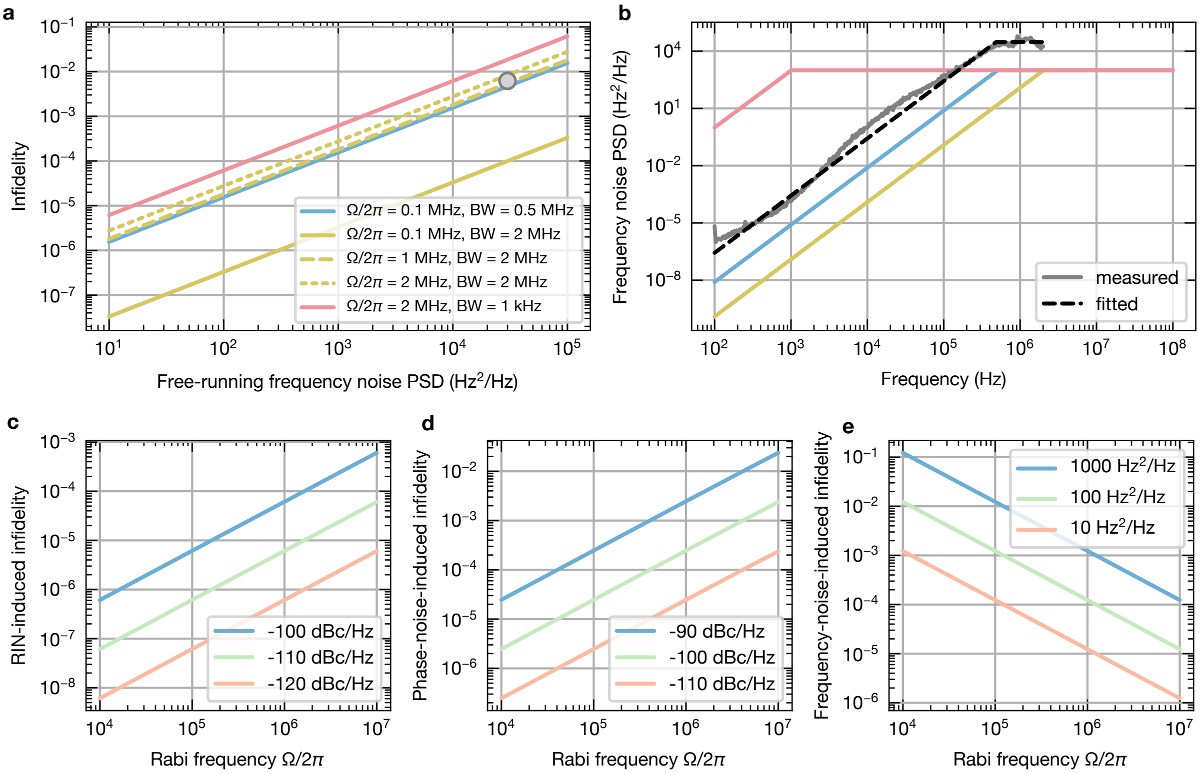

Figure B.3: Linear response applied to parametrized noise PSDs. Using the linear response formalism, the infidelity of a π-pulse due to intensity, phase, and frequency noise is estimated. The upper panel considers parametrized frequency noise and presents the associated infidelity. The lower panel shows the infidelity for white noise power spectral densities (PSD). **a** Infidelity of a resonant π-pulse for a parametrized frequency noise density as a function of the parameter S_ν^{free}, which corresponds to the frequency noise PSD obtained beyond the locking bandwidth. The infidelity is shown for various Rabi frequencies Ω (see legend). The grey dot corresponds to the infidelity obtained for the measured noise PSD (shown in b) and lies in the close vicinity of the blue curve, which assumes an approximately equal bandwidth parameter and is thus comparable. The parametrization is discussed in more detail in the main text. **b** Frequency noise PSD for different parameters corresponding to the infidelities in (a). For Fourier components beyond the bandwidth, the frequency noise PSD is assumed to be constant and is plotted here for a value of $1000\,\mathrm{Hz}^2/\mathrm{Hz}$. The measured noise PSD (grey) is approximated with the simple model given by Eq. (B.20) (dashed black). The cut-off bandwidth f_B, extracted from the fit, agrees approximately with the bandwidth of the blue curve. **c-e** Infidelity due to white intensity (c), phase (d), and frequency (e) noise as a function of the Rabi frequency.

Appendix C

Numerical multi-level simulation

In this appendix, we discuss details regarding the numerical simulations of the three-photon coupling taking into account the entire atomic Zeeman substructure. The Hamiltonian $H = H_E + H_D$ contains various energy terms H_E to account for the laser detunings (C.1) and the driving fields H_D given by the three light fields (C.2). Here, the symbols Δ_i ($i = 689, 688, 679$) denotes the detuning of the respective light field in a suitable reference frame [218] and $\Delta_B/2\pi = 2.09\,\mathrm{MHz/G} \cdot |B|$ is the Zeeman splitting. The notation $|s, m_j\rangle$ with $s \in \left({}^1\mathrm{S}_0, {}^3\mathrm{P}_1, {}^3\mathrm{S}_1, {}^3\mathrm{P}_0, {}^3\mathrm{P}_2\right)$ refers to the electronic state $|s\rangle$ with given m_j quantum number. The ${}^3\mathrm{P}_2$ state with energy $\Delta_{{}^3\mathrm{P}_2}$ is included to act as a bucket state, which gets populated only by spontaneous emission from ${}^3\mathrm{S}_1$. The Rabi frequencies Ω on the transitions are computed by (3.6) and the complex-valued polarization projection is described in Section C.1 below. We consider a magnetic field strength of 19 G and optical powers of $P_{689} = 75\,\mu\mathrm{W}$, $P_{688} = 8.2\,\mathrm{mW}$ and $P_{679} = 850\,\mu\mathrm{W}$ focused to an elliptical focus with horizontal (vertical) waist of approximately 240 µm (90 µm) at detunings of $\Delta_{689} = 6\,\mathrm{MHz}$ and $\Delta_{688,679} \approx 12\,\mathrm{GHz}$ for the numerical simulations. Furthermore, to obtain the polarization decomposition of the linearly polarized light fields onto its $\sigma_\pm$ and π contributions, we assume that the light fields are applied with a linear polarization tilted by an angle of $\Theta_R = 55°$ out of the horizontal plane.

$$\begin{aligned}
H_E = &-\Delta_{689} \left|{}^3\mathrm{P}_1, -1\right\rangle \left\langle {}^3\mathrm{P}_1, -1\right| - (\Delta_{689} + \Delta_B) \left|{}^3\mathrm{P}_1, 0\right\rangle \left\langle {}^3\mathrm{P}_1, 0\right| \\
&- (\Delta_{689} + 2\Delta_B) \left|{}^3\mathrm{P}_1, 1\right\rangle \left\langle {}^3\mathrm{P}_1, 1\right| - (\Delta_{689} + \Delta_{688}) \left|{}^3\mathrm{S}_1, -1\right\rangle \left\langle {}^3\mathrm{S}_1, -1\right| \\
&- (\Delta_{689} + \Delta_{688} + \Delta_B) \left|{}^3\mathrm{S}_1, 0\right\rangle \left\langle {}^3\mathrm{S}_1, 0\right| - (\Delta_{689} + \Delta_{688} + 2\Delta_B) \left|{}^3\mathrm{S}_1, 1\right\rangle \left\langle {}^3\mathrm{S}_1, 1\right| \\
&- (\Delta_{689} + \Delta_{688} - \Delta_{679}) \left|{}^3\mathrm{P}_0, 0\right\rangle \left\langle {}^3\mathrm{P}_0, 0\right| - \Delta_{{}^3\mathrm{P}_2} \left|{}^3\mathrm{P}_2\right\rangle \left\langle {}^3\mathrm{P}_2\right| \qquad \text{(C.1)}
\end{aligned}$$

$$\begin{aligned}
H_D = &\frac{1}{2} \sum_i \Omega_{{}^1\mathrm{S}_0 \leftrightarrow {}^3\mathrm{P}_{1,m_j=i}} \left|{}^1\mathrm{S}_0, 0\right\rangle \left\langle {}^3\mathrm{P}_1, i\right| + \frac{1}{2} \sum_i \Omega_{{}^3\mathrm{P}_0 \leftrightarrow {}^3\mathrm{S}_{1,m_j=i}} \left|{}^3\mathrm{P}_0, 0\right\rangle \left\langle {}^3\mathrm{S}_1, i\right| \\
&+ \frac{1}{2} \sum_{i,j} \Omega_{{}^3\mathrm{P}_{1,m_j=i} \leftrightarrow {}^3\mathrm{S}_{1,m_j=j}} \left|{}^3\mathrm{P}_1, i\right\rangle \left\langle {}^3\mathrm{S}_1, j\right| + h.c. \qquad \text{(C.2)}
\end{aligned}$$

In addition to the unitary dynamics, we also take into account spontaneous decay from the intermediate states ${}^3\mathrm{P}_1$ and ${}^3\mathrm{S}_1$. For each decay, from the state $|s'\rangle = |J_1, m_1\rangle$ to state $|s\rangle = |J_0, m_0\rangle$, we consider a Lindblad decay operator $\hat{L}_k = \sqrt{2\gamma_{s' \to s}}\, |s\rangle \langle s'|$ where the decay rate on the transition $\gamma_{s' \to s}$ is given by (C.3) and depends on the transition matrix element D and the transition wavelength λ_0 [166]. The resulting excited state lifetimes $1/\tau_{s'} = \sum_s \gamma_{s' \to s}$ are about 21.3 µs and 13.9 ns for the ^{3}P$_1$ and ^{3}S$_1$ state, respectively [215].

$$\gamma_{s' \to s} = \frac{1}{2J_1 + 1} \frac{8\pi^2 D^2}{3\epsilon_0 \hbar \lambda_0^3} \begin{pmatrix} J_0 & 1 & J_1 \\ m_0 & q & -m_1 \end{pmatrix} \begin{pmatrix} J_0 & 1 & J_1 \\ m_0 & q & -m_1 \end{pmatrix} \tag{C.3}$$

C.1 Polarization decomposition in the lab frame

We consider the setup shown in Fig. 3.2. A magnetic field is applied under an arbitrary orientation with respect to the pair of collinearly propagating Raman beams. We assume a linear polarization of the light field which is tilted out of the horizontal plane by an angle Θ_R. Using an in-plane projection φ of the magnetic field and an out-of-plane projection Θ, the normalized magnetic and electric field vectors are parametrized as:

$$\begin{aligned} \vec{B} &= (\sin\Theta\cos\varphi, \sin\Theta\sin\varphi, \cos\Theta)^T \\ \vec{E} &= (\cos\Theta_R, 0, \sin\Theta_R)^T \end{aligned}$$

To find the π and σ polarization projections, we consider the overlap $\vec{E}_{||} = (\vec{E} \cdot \vec{B})\vec{B}$, yielding the π projection and decompose the orthogonal vector component $\vec{E}_\perp = \vec{E} - \vec{E}_{||}$ into the σ_+ and σ_+ contributions. To this end, apply a coordinate transformation into the eigenframe of the magnetic field, where $\vec{\tilde{B}} = B\vec{e_z}$, which is given by $\tilde{R} = R_y(-\Theta)R_z(-\varphi)$. In this frame the orthogonal electric field components $\vec{E}_\perp$ is given by:

$$\vec{\tilde{E}} = \begin{pmatrix} \cos\Theta\cos\varphi\cos\Theta_R - \sin\Theta\sin\Theta_R \\ -\cos\Theta_R\sin\varphi \\ 0 \end{pmatrix}$$

Decomposing this electric field vector into the $\sigma_\pm = \frac{1}{\sqrt{2}}(\hat{x} \pm i\hat{y})$ components yields a complete set of polarization projections:

$$\begin{aligned} \pi: &\quad \sin\Theta\cos\varphi\cos\Theta_R + \cos\Theta\sin\Omega_R \\ \sigma_+: &\cos\Theta\cos\varphi\cos\Theta_R - \sin\Theta\sin\Theta_R + i\,(\cos\Theta_R\sin\varphi) \\ \sigma_-: &\cos\Theta\cos\varphi\cos\Theta_R - \sin\Theta\sin\Theta_R - i\,(\cos\Theta_R\sin\varphi) \end{aligned}$$

Note that the relative phase of the two σ-polarized components varies as

$$\Delta\Phi = 2\arctan\left(\frac{\sin\varphi}{\cos\Theta\cos\varphi - \sin\Theta\tan\Theta_R}\right)$$

Bibliography

[1] R. P. Feynman. *Simulating physics with computers*. International Journal of Theoretical Physics **21**, 467–488 (1982). (Cited on page **1**)

[2] I. Bloch, J. Dalibard, and S. Nascimbène. *Quantum simulations with ultracold quantum gases*. Nature Physics **8**, 267–276 (2012). (Cited on page **1**)

[3] F. Schäfer, T. Fukuhara, S. Sugawa, Y. Takasu, and Y. Takahashi. *Tools for quantum simulation with ultracold atoms in optical lattices*. Nature Reviews Physics **2**, 411–425 (2020). (Cited on page **1**)

[4] I. Bloch. *Ultracold quantum gases in optical lattices*. Nature Physics **1**, 23–30 (2005). (Cited on page **1**)

[5] C. Gross and I. Bloch. *Quantum simulations with ultracold atoms in optical lattices*. Science **357**, 995–1001 (2017). (Cited on page **1**)

[6] A. J. Daley, I. Bloch, C. Kokail, S. Flannigan, N. Pearson, M. Troyer, and P. Zoller. *Practical quantum advantage in quantum simulation*. Nature **607**, 667–676 (2022). (Cited on page **1**)

[7] D. S. Weiss and M. Saffman. *Quantum computing with neutral atoms*. Physics Today **70**, 44–50 (2017). (Cited on page **1**)

[8] A. J. Daley. *Quantum computing and quantum simulation with group-II atoms*. Quantum Information Processing **10**, 865–884 (2011). (Cited on page **1**)

[9] M. Saffman. *Quantum computing with neutral atoms*. National Science Review **6**, 24–25 (2019). (Cited on page **1**)

[10] L. Henriet, L. Beguin, A. Signoles, T. Lahaye, A. Browaeys, G.-O. Reymond, and C. Jurczak. *Quantum computing with neutral atoms*. Quantum **4**, 327 (2020). (Cited on page **1**)

[11] A. D. Ludlow, M. M. Boyd, J. Ye, E. Peik, and P. O. Schmidt. *Optical atomic clocks*. Reviews of Modern Physics **87**, 637–701 (2015). (Cited on pages **1** and **3**)

[12] S. L. Campbell, R. B. Hutson, G. E. Marti, A. Goban, N. Darkwah Oppong, R. L. McNally, L. Sonderhouse, J. M. Robinson, W. Zhang, B. J. Bloom, and J. Ye. *A*

Fermi-degenerate three-dimensional optical lattice clock. Science **358**, 90–94 (2017). (Cited on pages **1** and **3**)

[13] E. Oelker, R. B. Hutson, C. J. Kennedy, L. Sonderhouse, T. Bothwell, A. Goban, D. Kedar, C. Sanner, J. M. Robinson, G. E. Marti, D. G. Matei, T. Legero, M. Giunta, R. Holzwarth, F. Riehle, U. Sterr, and J. Ye. *Demonstration of* 4.8×10^{-17} *stability at* 1 *s for two independent optical clocks*. Nature Photonics **13**, 714–719 (2019). (Cited on pages **1** and **3**)

[14] M. Greiner, O. Mandel, T. Esslinger, T. W. Hänsch, and I. Bloch. *Quantum phase transition from a superfluid to a Mott insulator in a gas of ultracold atoms*. Nature **415**, 39–44 (2002). (Cited on page **1**)

[15] M. Cheneau, P. Barmettler, D. Poletti, M. Endres, P. Schauß, T. Fukuhara, C. Gross, I. Bloch, C. Kollath, and S. Kuhr. *Light-cone-like spreading of correlations in a quantum many-body system*. Nature **481**, 484–487 (2012). (Cited on page **1**)

[16] W. S. Bakr, J. I. Gillen, A. Peng, S. Fölling, and M. Greiner. *A quantum gas microscope for detecting single atoms in a Hubbard-regime optical lattice*. Nature **462**, 74–77 (2009). (Cited on pages **1** and **59**)

[17] J. F. Sherson, C. Weitenberg, M. Endres, M. Cheneau, I. Bloch, and S. Kuhr. *Single-atom-resolved fluorescence imaging of an atomic Mott insulator*. Nature **467**, 68–72 (2010). (Cited on pages **1** and **59**)

[18] R. Jördens, N. Strohmaier, K. Günter, H. Moritz, and T. Esslinger. *A Mott insulator of fermionic atoms in an optical lattice*. Nature **455**, 204–207 (2008). (Cited on page **1**)

[19] A. Browaeys and T. Lahaye. *Many-body physics with individually controlled Rydberg atoms*. Nature Physics **16**, 132–142 (2020). (Cited on pages **1** and **4**)

[20] S. Ebadi, T. T. Wang, H. Levine, A. Keesling, G. Semeghini, A. Omran, D. Bluvstein, R. Samajdar, H. Pichler, W. W. Ho, S. Choi, S. Sachdev, M. Greiner, V. Vuletić, and M. D. Lukin. *Quantum phases of matter on a 256-atom programmable quantum simulator*. Nature **595**, 227–232 (2021). (Cited on pages **1**, **2**, **4**, **59**, and **107**)

[21] H. Bernien, S. Schwartz, A. Keesling, H. Levine, A. Omran, H. Pichler, S. Choi, A. S. Zibrov, M. Endres, M. Greiner, V. Vuletić, and M. D. Lukin. *Probing many-body dynamics on a 51-atom quantum simulator*. Nature **551**, 579–584 (2017). (Cited on pages **1**, **2**, and **4**)

[22] A. Omran, H. Levine, A. Keesling, G. Semeghini, T. T. Wang, S. Ebadi, H. Bernien, A. S. Zibrov, H. Pichler, S. Choi, J. Cui, M. Rossignolo, P. Rembold, S. Montangero,

T. Calarco, M. Endres, M. Greiner, V. Vuletić, and M. D. Lukin. *Generation and manipulation of Schrödinger cat states in Rydberg atom arrays*. Science **365**, 570–574 (2019). (Cited on pages **1** and **4**)

[23] S. J. Evered, D. Bluvstein, M. Kalinowski, S. Ebadi, T. Manovitz, H. Zhou, S. H. Li, A. A. Geim, T. T. Wang, N. Maskara, H. Levine, G. Semeghini, M. Greiner, V. Vuletić, and M. D. Lukin. *High-fidelity parallel entangling gates on a neutral-atom quantum computer*. Nature **622**, 268–272 (2023). (Cited on pages **1**, **2**, and **4**)

[24] D. Bluvstein, H. Levine, G. Semeghini, T. T. Wang, S. Ebadi, M. Kalinowski, A. Keesling, N. Maskara, H. Pichler, M. Greiner, V. Vuletić, and M. D. Lukin. *A quantum processor based on coherent transport of entangled atom arrays*. Nature **604**, 451–456 (2022). (Cited on pages **1**, **2**, **4**, and **59**)

[25] N.-C. Chiu, E. C. Trapp, J. Guo, M. H. Abobeih, L. M. Stewart, S. Hollerith, P. L. Stroganov, M. Kalinowski, A. A. Geim, S. J. Evered, S. H. Li, X. Lyu, L. M. Peters, D. Bluvstein, T. T. Wang, M. Greiner, V. Vuletić, and M. D. Lukin. *Continuous operation of a coherent 3,000-qubit system*. Nature **646**, 1075–1080 (2025). (Cited on pages **1**, **2**, **3**, and **4**)

[26] D. Bluvstein, S. J. Evered, A. A. Geim, S. H. Li, H. Zhou, T. Manovitz, S. Ebadi, M. Cain, M. Kalinowski, D. Hangleiter, J. P. Bonilla Ataides, N. Maskara, I. Cong, X. Gao, P. Sales Rodriguez, T. Karolyshyn, G. Semeghini, M. J. Gullans, M. Greiner, V. Vuletić, and M. D. Lukin. *Logical quantum processor based on reconfigurable atom arrays*. Nature **626**, 58–65 (2024). (Cited on pages **1**, **3**, **4**, and **59**)

[27] S. Ma, G. Liu, P. Peng, B. Zhang, S. Jandura, J. Claes, A. P. Burgers, G. Pupillo, S. Puri, and J. D. Thompson. *High-fidelity gates and mid-circuit erasure conversion in an atomic qubit*. Nature **622**, 279–284 (2023). (Cited on pages **1**, **2**, and **4**)

[28] B. Grinkemeyer, E. Guardado-Sanchez, I. Dimitrova, D. Shchepanovich, G. E. Mandopoulou, J. Borregaard, V. Vuletić, and M. D. Lukin. *Error-detected quantum operations with neutral atoms mediated by an optical cavity*. Science **387**, 1301–1305 (2025). (Cited on pages **1** and **4**)

[29] I. S. Madjarov, A. Cooper, A. L. Shaw, J. P. Covey, V. Schkolnik, T. H. Yoon, J. R. Williams, and M. Endres. *An Atomic-Array Optical Clock with Single-Atom Readout*. Physical Review X **9**, 041052 (2019). (Cited on pages **1** and **2**)

[30] A. Cao, W. J. Eckner, T. Lukin Yelin, A. W. Young, S. Jandura, L. Yan, K. Kim, G. Pupillo, J. Ye, N. Darkwah Oppong, and A. M. Kaufman. *Multi-qubit gates and Schrödinger cat states in an optical clock*. Nature **634**, 315–320 (2024). (Cited on page **1**)

[31] A. L. Shaw, R. Finkelstein, R. B.-S. Tsai, P. Scholl, T. H. Yoon, J. Choi, and M. Endres. *Multi-ensemble metrology by programming local rotations with atom movements*. Nature Physics **20**, 195–201 (2024). (Cited on pages **1**, **2**, **9**, and **27**)

[32] A. W. Young, W. J. Eckner, W. R. Milner, D. Kedar, M. A. Norcia, E. Oelker, N. Schine, J. Ye, and A. M. Kaufman. *Half-minute-scale atomic coherence and high relative stability in a tweezer clock*. Nature **588**, 408–413 (2020). (Cited on pages **1**, **3**, **9**, **27**, and **41**)

[33] M. Takamoto, I. Ushijima, N. Ohmae, T. Yahagi, K. Kokado, H. Shinkai, and H. Katori. *Test of general relativity by a pair of transportable optical lattice clocks*. Nature Photonics **14**, 411–415 (2020). (Cited on page **1**)

[34] I. Bloch, J. Dalibard, and S. Nascimbène. *Quantum simulations with ultracold quantum gases*. Nature Physics **8**, 267–276 (2012). (Cited on page **1**)

[35] M. Greiner, O. Mandel, T. Esslinger, T. W. Hänsch, and I. Bloch. *Quantum phase transition from a superfluid to a Mott insulator in a gas of ultracold atoms*. Nature **415**, 39–44 (2002). (Cited on page **1**)

[36] L. W. Cheuk, M. A. Nichols, M. Okan, T. Gersdorf, V. V. Ramasesh, W. S. Bakr, T. Lompe, and M. W. Zwierlein. *Quantum-Gas Microscope for Fermionic Atoms*. Physical Review Letters **114**, 193001 (2015). (Cited on pages **1**, **4**, and **59**)

[37] E. Haller, J. Hudson, A. Kelly, D. A. Cotta, B. Peaudecerf, G. D. Bruce, and S. Kuhr. *Single-atom imaging of fermions in a quantum-gas microscope*. Nature Physics **11**, 738–742 (2015). (Cited on pages **1**, **4**, and **59**)

[38] M. F. Parsons, F. Huber, A. Mazurenko, C. S. Chiu, W. Setiawan, K. Wooley-Brown, S. Blatt, and M. Greiner. *Site-Resolved Imaging of Fermionic Li 6 in an Optical Lattice*. Physical Review Letters **114**, 213002 (2015). (Cited on pages **1** and **59**)

[39] M. Boll, T. A. Hilker, G. Salomon, A. Omran, J. Nespolo, L. Pollet, I. Bloch, and C. Gross. *Spin- and density-resolved microscopy of antiferromagnetic correlations in Fermi-Hubbard chains*. Science **353**, 1257–1260 (2016). (Cited on page **1**)

[40] J. Vijayan, P. Sompet, G. Salomon, J. Koepsell, S. Hirthe, A. Bohrdt, F. Grusdt, I. Bloch, and C. Gross. *Time-resolved observation of spin-charge deconfinement in fermionic Hubbard chains*. Science **367**, 186–189 (2020). (Cited on page **1**)

[41] A. Mazurenko, C. S. Chiu, G. Ji, M. F. Parsons, M. Kanász-Nagy, R. Schmidt, F. Grusdt, E. Demler, D. Greif, and M. Greiner. *A cold-atom Fermi–Hubbard antiferromagnet*. Nature **545**, 462–466 (2017). (Cited on page **1**)

[42] G. Ji, M. Xu, L. H. Kendrick, C. S. Chiu, J. C. Brüggenjürgen, D. Greif, A. Bohrdt, F. Grusdt, E. Demler, M. Lebrat, and M. Greiner. *Coupling a Mobile Hole to an Antiferromagnetic Spin Background: Transient Dynamics of a Magnetic Polaron*. Physical Review X **11**, 021022 (2021). (Cited on page **2**)

[43] D. Greif, T. Uehlinger, G. Jotzu, L. Tarruell, and T. Esslinger. *Short-Range Quantum Magnetism of Ultracold Fermions in an Optical Lattice*. Science **340**, 1307–1310 (2013). (Cited on page **2**)

[44] J. Koepsell, J. Vijayan, P. Sompet, F. Grusdt, T. A. Hilker, E. Demler, G. Salomon, I. Bloch, and C. Gross. *Imaging magnetic polarons in the doped Fermi–Hubbard model*. Nature **572**, 358–362 (2019). (Cited on page **2**)

[45] S. Hirthe, T. Chalopin, D. Bourgund, P. Bojović, A. Bohrdt, E. Demler, F. Grusdt, I. Bloch, and T. A. Hilker. *Magnetically mediated hole pairing in fermionic ladders of ultracold atoms*. Nature **613**, 463–467 (2023). (Cited on page **2**)

[46] L. Tarruell and L. Sanchez-Palencia. *Quantum simulation of the Hubbard model with ultracold fermions in optical lattices*. Comptes Rendus. Physique **19**, 365–393 (2018). (Cited on page **2**)

[47] M. Xu, L. H. Kendrick, A. Kale, Y. Gang, G. Ji, R. T. Scalettar, M. Lebrat, and M. Greiner. *Frustration- and doping-induced magnetism in a Fermi–Hubbard simulator*. Nature **620**, 971–976 (2023). (Cited on page **2**)

[48] M. Xu, L. H. Kendrick, A. Kale, Y. Gang, C. Feng, S. Zhang, A. W. Young, M. Lebrat, and M. Greiner. *A neutral-atom Hubbard quantum simulator in the cryogenic regime*. Nature **642**, 909–915 (2025). (Cited on page **2**)

[49] N. E. Hussey. *Phenomenology of the normal state in-plane transport properties of high-*T_c *cuprates*. Journal of Physics: Condensed Matter **20**, 123201 (2008). (Cited on page **2**)

[50] B. Currie, J. Sturt, and E. Kozik. *Numerical validation of an ultracold Hubbard quantum simulator*. arXiv:2508.18041 (2025). (Cited on page **2**)

[51] P. Weckesser, K. Srakaew, T. Blatz, D. Wei, D. Adler, S. Agrawal, A. Bohrdt, I. Bloch, and J. Zeiher. *Realization of a Rydberg-dressed extended Bose-Hubbard model*. Science **390**, 849–853 (2025). (Cited on pages **2** and **59**)

[52] M. Mattioli, M. Dalmonte, W. Lechner, and G. Pupillo. *Cluster Luttinger Liquids of Rydberg-Dressed Atoms in Optical Lattices*. Physical Review Letters **111**, 165302 (2013). (Cited on pages **2** and **59**)

[53] L. Christakis, J. S. Rosenberg, R. Raj, S. Chi, A. Morningstar, D. A. Huse, Z. Z. Yan, and W. S. Bakr. *Probing site-resolved correlations in a spin system of ultracold molecules*. Nature **614**, 64–69 (2023). (Cited on pages **2** and **59**)

[54] A. N. Carroll, H. Hirzler, C. Miller, D. Wellnitz, S. R. Muleady, J. Lin, K. P. Zamarski, R. R. W. Wang, J. L. Bohn, A. M. Rey, and J. Ye. *Observation of generalized* t-J *spin dynamics with tunable dipolar interactions*. Science **388**, 381–386 (2025). (Cited on pages **2** and **59**)

[55] C. Gross and W. S. Bakr. *Quantum gas microscopy for single atom and spin detection*. Nature Physics **17**, 1316–1323 (2021). (Cited on pages **2**, **4**, and **59**)

[56] J. Zeiher, J.-y. Choi, A. Rubio-Abadal, T. Pohl, R. Van Bijnen, I. Bloch, and C. Gross. *Coherent Many-Body Spin Dynamics in a Long-Range Interacting Ising Chain*. Physical Review X **7**, 041063 (2017). (Cited on page **2**)

[57] J. Zeiher, R. Van Bijnen, P. Schauß, S. Hild, J.-y. Choi, T. Pohl, I. Bloch, and C. Gross. *Many-body interferometry of a Rydberg-dressed spin lattice*. Nature Physics **12**, 1095–1099 (2016). (Cited on page **2**)

[58] M. Endres, H. Bernien, A. Keesling, H. Levine, E. R. Anschuetz, A. Krajenbrink, C. Senko, V. Vuletic, M. Greiner, and M. D. Lukin. *Atom-by-atom assembly of defect-free one-dimensional cold atom arrays*. Science **354**, 1024–1027 (2016). (Cited on pages **2**, **4**, **9**, and **59**)

[59] D. Barredo, S. De Léséleuc, V. Lienhard, T. Lahaye, and A. Browaeys. *An atom-by-atom assembler of defect-free arbitrary two-dimensional atomic arrays*. Science **354**, 1021–1023 (2016). (Cited on pages **2**, **4**, **9**, and **59**)

[60] D. Barredo, V. Lienhard, S. De Léséleuc, T. Lahaye, and A. Browaeys. *Synthetic three-dimensional atomic structures assembled atom by atom*. Nature **561**, 79–82 (2018). (Cited on pages **2**, **4**, and **59**)

[61] P. Scholl, M. Schuler, H. J. Williams, A. A. Eberharter, D. Barredo, K.-N. Schymik, V. Lienhard, L.-P. Henry, T. C. Lang, T. Lahaye, A. M. Läuchli, and A. Browaeys. *Quantum simulation of 2D antiferromagnets with hundreds of Rydberg atoms*. Nature **595**, 233–238 (2021). (Cited on pages **2** and **59**)

[62] S. De Léséleuc, V. Lienhard, P. Scholl, D. Barredo, S. Weber, N. Lang, H. P. Büchler, T. Lahaye, and A. Browaeys. *Observation of a symmetry-protected topological phase of interacting bosons with Rydberg atoms*. Science **365**, 775–780 (2019). (Cited on page **2**)

[63] G. Semeghini, H. Levine, A. Keesling, S. Ebadi, T. T. Wang, D. Bluvstein, R. Verresen, H. Pichler, M. Kalinowski, R. Samajdar, A. Omran, S. Sachdev, A. Vishwanath, M. Greiner, V. Vuletić, and M. D. Lukin. *Probing topological spin liquids on a programmable quantum simulator*. Science **374**, 1242–1247 (2021). (Cited on pages **2** and **107**)

[64] A. Byun, M. Kim, and J. Ahn. *Finding the Maximum Independent Sets of Platonic Graphs Using Rydberg Atoms*. PRX Quantum **3**, 030305 (2022). (Cited on page **2**)

[65] L.-M. Steinert, P. Osterholz, R. Eberhard, L. Festa, N. Lorenz, Z. Chen, A. Trautmann, and C. Gross. *Spatially Tunable Spin Interactions in Neutral Atom Arrays*. Physical Review Letters **130**, 243001 (2023). (Cited on page **2**)

[66] P. Scholl, H. J. Williams, G. Bornet, F. Wallner, D. Barredo, L. Henriet, A. Signoles, C. Hainaut, T. Franz, S. Geier, A. Tebben, A. Salzinger, G. Zürn, T. Lahaye, M. Weidemüller, and A. Browaeys. *Microwave Engineering of Programmable XXZ Hamiltonians in Arrays of Rydberg Atoms*. PRX Quantum **3**, 020303 (2022). (Cited on page **2**)

[67] L. Homeier, A. Bohrdt, S. Linsel, E. Demler, J. C. Halimeh, and F. Grusdt. *Realistic scheme for quantum simulation of* $\mathbb{Z}_2$ *lattice gauge theories with dynamical matter in (2 + 1)D*. Communications Physics **6**, 127 (2023). (Cited on pages **2**, **59**, and **107**)

[68] J. C. Halimeh, M. Aidelsburger, F. Grusdt, P. Hauke, and B. Yang. *Cold-atom quantum simulators of gauge theories*. Nature Physics **21**, 25–36 (2025). (Cited on pages **2** and **59**)

[69] S. Chandrasekharan and U.-J. Wiese. *Quantum link models: A discrete approach to gauge theories*. Nuclear Physics B **492**, 455–471 (1997). (Cited on page **2**)

[70] H. J. Manetsch, G. Nomura, E. Bataille, X. Lv, K. H. Leung, and M. Endres. *A tweezer array with 6,100 highly coherent atomic qubits*. Nature **647**, 60–67 (2025). (Cited on pages **2**, **65**, **81**, and **95**)

[71] M. Ammenwerth, H. Timme, F. Gyger, R. Tao, I. Bloch, and J. Zeiher. *Realization of a Fast Triple-Magic All-Optical Qutrit in* Sr^{88}. Physical Review Letters **135**, 143401 (2025). (Cited on pages **2**, **27**, and **36**)

[72] A. Jenkins, J. W. Lis, A. Senoo, W. F. McGrew, and A. M. Kaufman. *Ytterbium Nuclear-Spin Qubits in an Optical Tweezer Array*. Physical Review X **12**, 021027 (2022). (Cited on pages **2** and **4**)

[73] J. W. Lis, A. Senoo, W. F. McGrew, F. Rönchen, A. Jenkins, and A. M. Kaufman. *Midcircuit Operations Using the* omg *Architecture in Neutral Atom Arrays*. Physical Review X **13**, 041035 (2023). (Cited on page **2**)

[74] A. Senoo, A. Baumgärtner, J. W. Lis, G. M. Vaidya, Z. Zeng, G. Giudici, H. Pichler, and A. M. Kaufman. *High-fidelity entanglement and coherent multi-qubit mapping in an atom array*. arXiv:2506.13632 (2025). (Cited on page **2**)

[75] R. Tao, O. Lib, F. Gyger, H. Timme, M. Ammenwerth, I. Bloch, and J. Zeiher. *Universal gates for a metastable qubit in strontium-88*. arXiv:2506.10714 (2025). (Cited on pages **2**, **10**, and **58**)

[76] S. Ma, A. P. Burgers, G. Liu, J. Wilson, B. Zhang, and J. D. Thompson. *Universal Gate Operations on Nuclear Spin Qubits in an Optical Tweezer Array of ^{171}Yb Atoms*. Physical Review X **12**, 021028 (2022). (Cited on page **2**)

[77] A. Radnaev, W. Chung, D. Cole, D. Mason, T. Ballance, M. Bedalov, D. Belknap, M. Berman, M. Blakely, I. Bloomfield, P. Buttler, C. Campbell, A. Chopinaud, E. Copenhaver, M. Dawes, S. Eubanks, A. Friss, D. Garcia, J. Gilbert, M. Gillette, P. Goiporia, P. Gokhale, J. Goldwin, D. Goodwin, T. Graham, C. Guttormsson, G. Hickman, L. Hurtley, M. Iliev, E. Jones, R. Jones, K. Kuper, T. Lewis, M. Lichtman, F. Majdeteimouri, J. Mason, J. McMaster, J. Miles, P. Mitchell, J. Murphree, N. Neff-Mallon, T. Oh, V. Omole, C. Parlo Simon, N. Pederson, M. Perlin, A. Reiter, R. Rines, P. Romlow, A. Scott, D. Stiefvater, J. Tanner, A. Tucker, I. Vinogradov, M. Warter, M. Yeo, M. Saffman, and T. Noel. *Universal Neutral-Atom Quantum Computer with Individual Optical Addressing and Nondestructive Readout*. PRX Quantum **6**, 030334 (2025). (Cited on page **2**)

[78] J. Beugnon, C. Tuchendler, H. Marion, A. Gaëtan, Y. Miroshnychenko, Y. R. P. Sortais, A. M. Lance, M. P. A. Jones, G. Messin, A. Browaeys, and P. Grangier. *Two-dimensional transport and transfer of a single atomic qubit in optical tweezers*. Nature Physics **3**, 696–699 (2007). (Cited on page **2**)

[79] J. Zhu, C. Chen, L. Zhou, X. Xie, C. Jiang, Z. Ding, F. Wu, F. Yang, G. Wang, Q. Gong, P. Zhang, S. Zhang, and P. Peng. *High-efficiency loading of 2,400 Ytterbium atoms in optical tweezer arrays*. arXiv:2512.19795 (2025). (Cited on page **2**)

[80] E. Deist, Y.-H. Lu, J. Ho, M. K. Pasha, J. Zeiher, Z. Yan, and D. M. Stamper-Kurn. *Mid-Circuit Cavity Measurement in a Neutral Atom Array*. Physical Review Letters **129**, 203602 (2022). (Cited on page **2**)

[81] K. Singh, C. E. Bradley, S. Anand, V. Ramesh, R. White, and H. Bernien. *Mid-circuit correction of correlated phase errors using an array of spectator qubits*. Science **380**, 1265–1269 (2023). (Cited on page **2**)

[82] T. M. Graham, L. Phuttitarn, R. Chinnarasu, Y. Song, C. Poole, K. Jooya, J. Scott, A. Scott, P. Eichler, and M. Saffman. *Midcircuit Measurements on a Single-Species*

Neutral Alkali Atom Quantum Processor. Physical Review X **13**, 041051 (2023). (Cited on page **2**)

[83] M. A. Norcia, W. B. Cairncross, K. Barnes, P. Battaglino, A. Brown, M. O. Brown, K. Cassella, C.-A. Chen, R. Coxe, D. Crow, J. Epstein, C. Griger, A. M. W. Jones, H. Kim, J. M. Kindem, J. King, S. S. Kondov, K. Kotru, J. Lauigan, M. Li, M. Lu, E. Megidish, J. Marjanovic, M. McDonald, T. Mittiga, J. A. Muniz, S. Narayanaswami, C. Nishiguchi, R. Notermans, T. Paule, K. A. Pawlak, L. S. Peng, A. Ryou, A. Smull, D. Stack, M. Stone, A. Sucich, M. Urbanek, R. J. M. Van De Veerdonk, Z. Vendeiro, T. Wilkason, T.-Y. Wu, X. Xie, X. Zhang, and B. J. Bloom. *Midcircuit Qubit Measurement and Rearrangement in a* ^{171}*Yb Atomic Array*. Physical Review X **13**, 041034 (2023). (Cited on page **2**)

[84] L. Su, A. Douglas, M. Szurek, A. H. Hébert, A. Krahn, R. Groth, G. A. Phelps, O. Marković, and M. Greiner. *Fast single atom imaging for optical lattice arrays*. Nature Communications **16**, 1017 (2025). (Cited on page **2**)

[85] A. Muzi Falconi, R. Panza, S. Sbernardori, R. Forti, R. Klemt, O. Abdel Karim, M. Marinelli, and F. Scazza. *Microsecond-Scale High-Survival and Number-Resolved Detection of Ytterbium Atom Arrays*. Physical Review Letters **135**, 203402 (2025). (Cited on page **2**)

[86] S. Anand, C. E. Bradley, R. White, V. Ramesh, K. Singh, and H. Bernien. *A dual-species Rydberg array*. Nature Physics **20**, 1744–1750 (2024). (Cited on page **2**)

[87] P. Scholl, A. L. Shaw, R. B.-S. Tsai, R. Finkelstein, J. Choi, and M. Endres. *Erasure conversion in a high-fidelity Rydberg quantum simulator*. Nature **622**, 273–278 (2023). (Cited on pages **2** and **27**)

[88] Y. Wu, S. Kolkowitz, S. Puri, and J. D. Thompson. *Erasure conversion for fault-tolerant quantum computing in alkaline earth Rydberg atom arrays*. Nature Communications **13**, 4657 (2022). (Cited on page **2**)

[89] A. L. Shaw, P. Scholl, R. Finkelstein, R. B.-S. Tsai, J. Choi, and M. Endres. *Erasure cooling, control, and hyperentanglement of motion in optical tweezers*. Science **388**, 845–849 (2025). (Cited on pages **2**, **27**, and **107**)

[90] Q. Xu, J. P. Bonilla Ataides, C. A. Pattison, N. Raveendran, D. Bluvstein, J. Wurtz, B. Vasić, M. D. Lukin, L. Jiang, and H. Zhou. *Constant-overhead fault-tolerant quantum computation with reconfigurable atom arrays*. Nature Physics **20**, 1084–1090 (2024). (Cited on page **2**)

[91] K. Sahay, J. Jin, J. Claes, J. D. Thompson, and S. Puri. *High-Threshold Codes for Neutral-Atom Qubits with Biased Erasure Errors*. Physical Review X **13**, 041013 (2023). (Cited on pages **2** and **3**)

[92] L. Pecorari, S. Jandura, G. K. Brennen, and G. Pupillo. *High-rate quantum LDPC codes for long-range-connected neutral atom registers*. Nature Communications **16**, 1111 (2025). (Cited on page **2**)

[93] C. Ryan-Anderson, N. C. Brown, M. S. Allman, B. Arkin, G. Asa-Attuah, C. Baldwin, J. Berg, J. G. Bohnet, S. Braxton, N. Burdick, J. P. Campora, A. Chernoguzov, J. Esposito, B. Evans, D. Francois, J. P. Gaebler, T. M. Gatterman, J. Gerber, K. Gilmore, D. Gresh, A. Hall, A. Hankin, J. Hostetter, D. Lucchetti, K. Mayer, J. Myers, B. Neyenhuis, J. Santiago, J. Sedlacek, T. Skripka, A. Slattery, R. P. Stutz, J. Tait, R. Tobey, G. Vittorini, J. Walker, and D. Hayes. *Implementing Fault-tolerant Entangling Gates on the Five-qubit Code and the Color Code*. arXiv:2208.01863 (2022). (Cited on page **3**)

[94] Google Quantum AI, R. Acharya, I. Aleiner, R. Allen, T. I. Andersen, M. Ansmann, F. Arute, K. Arya, A. Asfaw, J. Atalaya, R. Babbush, D. Bacon, J. C. Bardin, J. Basso, A. Bengtsson, S. Boixo, G. Bortoli, A. Bourassa, J. Bovaird, L. Brill, M. Broughton, B. B. Buckley, D. A. Buell, T. Burger, B. Burkett, N. Bushnell, Y. Chen, Z. Chen, B. Chiaro, J. Cogan, R. Collins, P. Conner, W. Courtney, A. L. Crook, B. Curtin, D. M. Debroy, A. Del Toro Barba, S. Demura, A. Dunsworth, D. Eppens, C. Erickson, L. Faoro, E. Farhi, R. Fatemi, L. Flores Burgos, E. Forati, A. G. Fowler, B. Foxen, W. Giang, C. Gidney, D. Gilboa, M. Giustina, A. Grajales Dau, J. A. Gross, S. Habegger, M. C. Hamilton, M. P. Harrigan, S. D. Harrington, O. Higgott, J. Hilton, M. Hoffmann, S. Hong, T. Huang, A. Huff, W. J. Huggins, L. B. Ioffe, S. V. Isakov, J. Iveland, E. Jeffrey, Z. Jiang, C. Jones, P. Juhas, D. Kafri, K. Kechedzhi, J. Kelly, T. Khattar, M. Khezri, M. Kieferová, S. Kim, A. Kitaev, P. V. Klimov, A. R. Klots, A. N. Korotkov, F. Kostritsa, J. M. Kreikebaum, D. Landhuis, P. Laptev, K.-M. Lau, L. Laws, J. Lee, K. Lee, B. J. Lester, A. Lill, W. Liu, A. Locharla, E. Lucero, F. D. Malone, J. Marshall, O. Martin, J. R. McClean, T. McCourt, M. McEwen, A. Megrant, B. Meurer Costa, X. Mi, K. C. Miao, M. Mohseni, S. Montazeri, A. Morvan, E. Mount, W. Mruczkiewicz, O. Naaman, M. Neeley, C. Neill, A. Nersisyan, H. Neven, M. Newman, J. H. Ng, A. Nguyen, M. Nguyen, M. Y. Niu, T. E. O'Brien, A. Opremcak, J. Platt, A. Petukhov, R. Potter, L. P. Pryadko, C. Quintana, P. Roushan, N. C. Rubin, N. Saei, D. Sank, K. Sankaragomathi, K. J. Satzinger, H. F. Schurkus, C. Schuster, M. J. Shearn, A. Shorter, V. Shvarts, J. Skruzny, V. Smelyanskiy, W. C. Smith, G. Sterling, D. Strain, M. Szalay, A. Torres, G. Vidal, B. Villalonga, C. Vollgraff Heidweiller, T. White, C. Xing, Z. J. Yao, P. Yeh, J. Yoo, G. Young, A. Zalcman, Y. Zhang, and

N. Zhu. *Suppressing quantum errors by scaling a surface code logical qubit*. Nature **614**, 676–681 (2023). (Cited on page **3**)

[95] M. A. Norcia, H. Kim, W. B. Cairncross, M. Stone, A. Ryou, M. Jaffe, M. O. Brown, K. Barnes, P. Battaglino, T. C. Bohdanowicz, A. Brown, K. Cassella, C.-A. Chen, R. Coxe, D. Crow, J. Epstein, C. Griger, E. Halperin, F. Hummel, A. M. W. Jones, J. M. Kindem, J. King, K. Kotru, J. Lauigan, M. Li, M. Lu, E. Megidish, J. Marjanovic, M. McDonald, T. Mittiga, J. A. Muniz, S. Narayanaswami, C. Nishiguchi, T. Paule, K. A. Pawlak, L. S. Peng, K. L. Pudenz, D. Rodríguez Pérez, A. Smull, D. Stack, M. Urbanek, R. J. M. Van De Veerdonk, Z. Vendeiro, L. Wadleigh, T. Wilkason, T.-Y. Wu, X. Xie, E. Zalys-Geller, X. Zhang, and B. J. Bloom. *Iterative Assembly of* ^{171}*Yb Atom Arrays with Cavity-Enhanced Optical Lattices*. PRX Quantum **5**, 030316 (2024). (Cited on pages **3** and **4**)

[96] F. Gyger, M. Ammenwerth, R. Tao, H. Timme, S. Snigirev, I. Bloch, and J. Zeiher. *Continuous operation of large-scale atom arrays in optical lattices*. Physical Review Research **6**, 033104 (2024). (Cited on pages **3**, **4**, and **60**)

[97] Y. Li, Y. Bao, M. Peper, C. Li, and J. D. Thompson. *Fast, continuous and coherent atom replacement in a neutral atom qubit array*. arXiv:2506.15633 (2025). (Cited on pages **3** and **4**)

[98] D. Bluvstein, A. A. Geim, S. H. Li, S. J. Evered, J. P. Bonilla Ataides, G. Baranes, A. Gu, T. Manovitz, M. Xu, M. Kalinowski, S. Majidy, C. Kokail, N. Maskara, E. C. Trapp, L. M. Stewart, S. Hollerith, H. Zhou, M. J. Gullans, S. F. Yelin, M. Greiner, V. Vuletić, M. Cain, and M. D. Lukin. *A fault-tolerant neutral-atom architecture for universal quantum computation*. Nature **649**, 39–46 (2026). (Cited on page **3**)

[99] M. N. H. Chow, V. Buchemmavari, S. Omanakuttan, B. J. Little, S. Pandey, I. H. Deutsch, and Y.-Y. Jau. *Circuit-Based Leakage-to-Erasure Conversion in a Neutral-Atom Quantum Processor*. PRX Quantum **5**, 040343 (2024). (Cited on page **3**)

[100] Y. Li and J. D. Thompson. *High-Rate and High-Fidelity Modular Interconnects between Neutral Atom Quantum Processors*. PRX Quantum **5**, 020363 (2024). (Cited on page **3**)

[101] S. Saha, M. Shalaev, J. O'Reilly, I. Goetting, G. Toh, A. Kalakuntla, Y. Yu, and C. Monroe. *High-fidelity remote entanglement of trapped atoms mediated by time-bin photons*. Nature Communications **16**, 2533 (2025). (Cited on page **3**)

[102] M. Schioppo, R. C. Brown, W. F. McGrew, N. Hinkley, R. J. Fasano, K. Beloy, T. H. Yoon, G. Milani, D. Nicolodi, J. A. Sherman, N. B. Phillips, C. W. Oates, and A. D. Ludlow. *Ultrastable optical clock with two cold-atom ensembles*. Nature Photonics **11**, 48–52 (2017). (Cited on page **3**)

[103] R. Kaubruegger, P. Silvi, C. Kokail, R. Van Bijnen, A. M. Rey, J. Ye, A. M. Kaufman, and P. Zoller. *Variational Spin-Squeezing Algorithms on Programmable Quantum Sensors*. Physical Review Letters **123**, 260505 (2019). (Cited on pages **3** and **4**)

[104] B. Koczor, S. Endo, T. Jones, Y. Matsuzaki, and S. C. Benjamin. *Variational-state quantum metrology*. New Journal of Physics **22**, 083038 (2020). (Cited on pages **3** and **4**)

[105] R. Kaubruegger, D. V. Vasilyev, M. Schulte, K. Hammerer, and P. Zoller. *Quantum Variational Optimization of Ramsey Interferometry and Atomic Clocks*. Physical Review X **11**, 041045 (2021). (Cited on pages **3** and **4**)

[106] L. Pezzè, A. Smerzi, M. K. Oberthaler, R. Schmied, and P. Treutlein. *Quantum metrology with nonclassical states of atomic ensembles*. Reviews of Modern Physics **90**, 035005 (2018). (Cited on page **3**)

[107] W. J. Eckner, N. Darkwah Oppong, A. Cao, A. W. Young, W. R. Milner, J. M. Robinson, J. Ye, and A. M. Kaufman. *Realizing spin squeezing with Rydberg interactions in an optical clock*. Nature **621**, 734–739 (2023). (Cited on page **3**)

[108] C. D. Marciniak, T. Feldker, I. Pogorelov, R. Kaubruegger, D. V. Vasilyev, R. Van Bijnen, P. Schindler, P. Zoller, R. Blatt, and T. Monz. *Optimal metrology with programmable quantum sensors*. Nature **603**, 604–609 (2022). (Cited on page **3**)

[109] M. Tse, H. Yu, N. Kijbunchoo, A. Fernandez-Galiana, P. Dupej, L. Barsotti, C. D. Blair, D. D. Brown, S. E. Dwyer, A. Effler, M. Evans, P. Fritschel, V. V. Frolov, A. C. Green, G. L. Mansell, F. Matichard, N. Mavalvala, D. E. McClelland, L. McCuller, T. McRae, J. Miller, A. Mullavey, E. Oelker, I. Y. Phinney, D. Sigg, B. J. J. Slagmolen, T. Vo, R. L. Ward, C. Whittle, R. Abbott, C. Adams, R. X. Adhikari, A. Ananyeva, S. Appert, K. Arai, J. S. Areeda, Y. Asali, S. M. Aston, C. Austin, A. M. Baer, M. Ball, S. W. Ballmer, S. Banagiri, D. Barker, J. Bartlett, B. K. Berger, J. Betzwieser, D. Bhattacharjee, G. Billingsley, S. Biscans, R. M. Blair, N. Bode, P. Booker, R. Bork, A. Bramley, A. F. Brooks, A. Buikema, C. Cahillane, K. C. Cannon, X. Chen, A. A. Ciobanu, F. Clara, S. J. Cooper, K. R. Corley, S. T. Countryman, P. B. Covas, D. C. Coyne, L. E. H. Datrier, D. Davis, C. Di Fronzo, J. C. Driggers, T. Etzel, T. M. Evans, J. Feicht, P. Fulda, M. Fyffe, J. A. Giaime, K. D. Giardina, P. Godwin, E. Goetz, S. Gras, C. Gray, R. Gray, A. Gupta, E. K. Gustafson, R. Gustafson, J. Hanks, J. Hanson, T. Hardwick, R. K. Hasskew, M. C. Heintze, A. F. Helmling-Cornell, N. A. Holland, J. D. Jones, S. Kandhasamy, S. Karki, M. Kasprzack, K. Kawabe, P. J. King, J. S. Kissel, R. Kumar, M. Landry, B. B. Lane, B. Lantz, M. Laxen, Y. K. Lecoeuche, J. Leviton, J. Liu, M. Lormand, A. P. Lundgren, R. Macas, M. MacInnis, D. M. Macleod, S. Márka, Z. Márka, D. V. Martynov, K. Mason, T. J. Massinger, R. McCarthy, S. McCormick, J. McIver, G. Mendell,

K. Merfeld, E. L. Merilh, F. Meylahn, T. Mistry, R. Mittleman, G. Moreno, C. M. Mow-Lowry, S. Mozzon, T. J. N. Nelson, P. Nguyen, L. K. Nuttall, J. Oberling, R. J. Oram, B. O'Reilly, C. Osthelder, D. J. Ottaway, H. Overmier, J. R. Palamos, W. Parker, E. Payne, A. Pele, C. J. Perez, M. Pirello, H. Radkins, K. E. Ramirez, J. W. Richardson, K. Riles, N. A. Robertson, J. G. Rollins, C. L. Romel, J. H. Romie, M. P. Ross, K. Ryan, T. Sadecki, E. J. Sanchez, L. E. Sanchez, T. R. Saravanan, R. L. Savage, D. Schaetzl, R. Schnabel, R. M. S. Schofield, E. Schwartz, D. Sellers, T. J. Shaffer, J. R. Smith, S. Soni, B. Sorazu, A. P. Spencer, K. A. Strain, L. Sun, M. J. Szczepańczyk, M. Thomas, P. Thomas, K. A. Thorne, K. Toland, C. I. Torrie, G. Traylor, A. L. Urban, G. Vajente, G. Valdes, D. C. Vander-Hyde, P. J. Veitch, K. Venkateswara, G. Venugopalan, A. D. Viets, C. Vorvick, M. Wade, J. Warner, B. Weaver, R. Weiss, B. Willke, C. C. Wipf, L. Xiao, H. Yamamoto, M. J. Yap, H. Yu, L. Zhang, M. E. Zucker, and J. Zweizig. *Quantum-Enhanced Advanced LIGO Detectors in the Era of Gravitational-Wave Astronomy*. Physical Review Letters **123**, 231107 (2019). (Cited on page **3**)

[110] E. Pedrozo-Peñafiel, S. Colombo, C. Shu, A. F. Adiyatullin, Z. Li, E. Mendez, B. Braverman, A. Kawasaki, D. Akamatsu, Y. Xiao, and V. Vuletić. *Entanglement on an optical atomic-clock transition*. Nature **588**, 414–418 (2020). (Cited on page **3**)

[111] L. I. R. Gil, R. Mukherjee, E. M. Bridge, M. P. A. Jones, and T. Pohl. *Spin Squeezing in a Rydberg Lattice Clock*. Physical Review Letters **112**, 103601 (2014). (Cited on page **3**)

[112] V. Borish, O. Marković, J. A. Hines, S. V. Rajagopal, and M. Schleier-Smith. *Transverse-Field Ising Dynamics in a Rydberg-Dressed Atomic Gas*. Physical Review Letters **124**, 063601 (2020). (Cited on page **4**)

[113] Y. C. Liu, Z. F. Xu, G. R. Jin, and L. You. *Spin Squeezing: Transforming One-Axis Twisting into Two-Axis Twisting*. Physical Review Letters **107**, 013601 (2011). (Cited on page **4**)

[114] W. Petrich, M. H. Anderson, J. R. Ensher, and E. A. Cornell. *Stable, Tightly Confining Magnetic Trap for Evaporative Cooling of Neutral Atoms*. Physical Review Letters **74**, 3352–3355 (1995). (Cited on page **4**)

[115] A. J. Olson, R. J. Niffenegger, and Y. P. Chen. *Optimizing the efficiency of evaporative cooling in optical dipole traps*. Physical Review A **87**, 053613 (2013). (Cited on page **4**)

[116] C. Weitenberg, M. Endres, J. F. Sherson, M. Cheneau, P. Schauß, T. Fukuhara, I. Bloch, and S. Kuhr. *Single-spin addressing in an atomic Mott insulator*. Nature **471**, 319–324 (2011). (Cited on page **4**)

[117] A. Mazurenko, C. S. Chiu, G. Ji, M. F. Parsons, M. Kanász-Nagy, R. Schmidt, F. Grusdt, E. Demler, D. Greif, and M. Greiner. *A cold-atom Fermi–Hubbard antiferromagnet*. Nature **545**, 462–466 (2017). (Cited on page **4**)

[118] R. Yamamoto, J. Kobayashi, T. Kuno, K. Kato, and Y. Takahashi. *An ytterbium quantum gas microscope with narrow-line laser cooling*. New Journal of Physics **18**, 023016 (2016). (Cited on page **4**)

[119] S. Hollerith, J. Zeiher, J. Rui, A. Rubio-Abadal, V. Walther, T. Pohl, D. M. Stamper-Kurn, I. Bloch, and C. Gross. *Quantum gas microscopy of Rydberg macrodimers*. Science **364**, 664–667 (2019). (Cited on page **4**)

[120] S. Buob, J. Höschele, V. Makhalov, A. Rubio-Abadal, and L. Tarruell. *A Strontium Quantum-Gas Microscope*. PRX Quantum **5**, 020316 (2024). (Cited on pages **4** and **82**)

[121] B. J. Lester, N. Luick, A. M. Kaufman, C. M. Reynolds, and C. A. Regal. *Rapid Production of Uniformly Filled Arrays of Neutral Atoms*. Physical Review Letters **115**, 073003 (2015). (Cited on page **4**)

[122] G. Pichard, D. Lim, É. Bloch, J. Vaneecloo, L. Bourachot, G.-J. Both, G. Mériaux, S. Dutartre, R. Hostein, J. Paris, B. Ximenez, A. Signoles, A. Browaeys, T. Lahaye, and D. Dreon. *Rearrangement of individual atoms in a 2000-site optical-tweezer array at cryogenic temperatures*. Physical Review Applied **22**, 024073 (2024). (Cited on page **4**)

[123] A. W. Young, W. J. Eckner, N. Schine, A. M. Childs, and A. M. Kaufman. *Tweezer-programmable 2D quantum walks in a Hubbard-regime lattice*. Science **377**, 885–889 (2022). (Cited on pages **4**, **59**, **63**, and **104**)

[124] E. L. Raab, M. Prentiss, A. Cable, S. Chu, and D. E. Pritchard. *Trapping of Neutral Sodium Atoms with Radiation Pressure*. Physical Review Letters **59**, 2631–2634 (1987). (Cited on page **9**)

[125] J. Dalibard and C. Cohen-Tannoudji. *Laser cooling below the Doppler limit by polarization gradients: Simple theoretical models*. Journal of the Optical Society of America B **6**, 2023 (1989). (Cited on page **9**)

[126] W. Petrich, M. H. Anderson, J. R. Ensher, and E. A. Cornell. *Behavior of atoms in a compressed magneto-optical trap*. Journal of the Optical Society of America B **11**, 1332 (1994). (Cited on page **9**)

[127] H. J. Metcalf and P. Van Der Straten. *Laser Cooling and Trapping*. Graduate Texts in Contemporary Physics. Springer New York, New York, NY (1999). ISBN 978-0-387-98728-6 978-1-4612-1470-0. (Cited on page **9**)

[128] R. Grimm, M. Weidemüller, and Y. B. Ovchinnikov. *Optical Dipole Traps for Neutral Atoms*. In *Advances In Atomic, Molecular, and Optical Physics*, volume 42, pages 95–170. Elsevier (2000). ISBN 978-0-12-003842-8. (Cited on page **9**)

[129] S. Kuhr. *Quantum-gas microscopes: A new tool for cold-atom quantum simulators*. National Science Review **3**, 170–172 (2016). (Cited on pages **9** and **59**)

[130] H. Ott. *Single atom detection in ultracold quantum gases: A review of current progress*. Reports on Progress in Physics **79**, 054401 (2016). (Cited on page **9**)

[131] S. Stellmer, F. Schreck, and T. C. Killian. *DEGENERATE QUANTUM GASES OF STRONTIUM*, volume 2, pages 1–80. WORLD SCIENTIFIC (2014). ISBN 978-981-4590-16-7 978-981-4590-17-4. (Cited on page **9**)

[132] J. h. A. Park. *Towards quantum simulations with strontium in cavity-enhanced optical lattices*. Ph.D. thesis, Ludwig-Maximilians-Universität München (2021). (Cited on page **9**)

[133] L. R. Hunter, W. A. Walker, and D. S. Weiss. *Observation of an atomic Stark – electric-quadrupole interference*. Physical Review Letters **56**, 823–826 (1986). (Cited on page **9**)

[134] M. A. Norcia, A. W. Young, and A. M. Kaufman. *Microscopic Control and Detection of Ultracold Strontium in Optical-Tweezer Arrays*. Physical Review X **8**, 041054 (2018). (Cited on pages **9**, **11**, **13**, **15**, and **32**)

[135] N. Schine, A. W. Young, W. J. Eckner, M. J. Martin, and A. M. Kaufman. *Long-lived Bell states in an array of optical clock qubits*. Nature Physics **18**, 1067–1073 (2022). (Cited on page **9**)

[136] R. Tao. *Scalable neutral-atom arrays and high-fidelity universal quantum gates on metastable qubits*. Ph.D. thesis, Ludwig-Maximilians-Universität München (2025). (Cited on pages **10**, **23**, **58**, **64**, and **107**)

[137] H. Levine, A. Keesling, A. Omran, H. Bernien, S. Schwartz, A. S. Zibrov, M. Endres, M. Greiner, V. Vuletić, and M. D. Lukin. *High-Fidelity Control and Entanglement of Rydberg-Atom Qubits*. Physical Review Letters **121**, 123603 (2018). (Cited on page **10**)

[138] A. Cooper, J. P. Covey, I. S. Madjarov, S. G. Porsev, M. S. Safronova, and M. Endres. *Alkaline-Earth Atoms in Optical Tweezers*. Physical Review X **8**, 041055 (2018). (Cited on pages **11**, **12**, **13**, **15**, **32**, and **45**)

[139] F. Le Kien, P. Schneeweiss, and A. Rauschenbeutel. *Dynamical polarizability of atoms in arbitrary light fields: General theory and application to cesium*. The European Physical Journal D **67**, 92 (2013). (Cited on page **11**)

[140] X. Zhou, X. Xu, X. Chen, and J. Chen. *Magic wavelengths for terahertz clock transitions*. Physical Review A **81**, 012115 (2010). (Cited on page **11**)

[141] A. Kiruga, C. Cheung, D. Filin, P. Barakhshan, A. Bhosale, V. Badhan, B. Arora, R. Eigenmann, and M. S. Safronova. *Portal for high-precision atomic data and computation*. arXiv:2506.08170 (2025). (Cited on pages **12** and **47**)

[142] J. Trautmann. *The magnetic quadrupole transition in neutral strontium*. Ph.D. thesis, Ludwig-Maximilians-Universität München (2022). (Cited on page **12**)

[143] J. P. Covey, I. S. Madjarov, A. Cooper, and M. Endres. *2000-Times Repeated Imaging of Strontium Atoms in Clock-Magic Tweezer Arrays*. Physical Review Letters **122**, 173201 (2019). (Cited on page **15**)

[144] R. Taïeb, R. Dum, J. I. Cirac, P. Marte, and P. Zoller. *Cooling and localization of atoms in laser-induced potential wells*. Physical Review A **49**, 4876–4887 (1994). (Cited on page **16**)

[145] A. M. Kaufman, B. J. Lester, and C. A. Regal. *Cooling a Single Atom in an Optical Tweezer to Its Quantum Ground State*. Physical Review X **2**, 041014 (2012). (Cited on page **16**)

[146] J. D. Thompson, T. G. Tiecke, A. S. Zibrov, V. Vuletić, and M. D. Lukin. *Coherence and Raman Sideband Cooling of a Single Atom in an Optical Tweezer*. Physical Review Letters **110**, 133001 (2013). (Cited on pages **16** and **45**)

[147] Y. T. Chew, M. Poitrinal, T. Tomita, S. Kitade, J. Mauricio, K. Ohmori, and S. De Léséleuc. *Ultraprecise holographic optical tweezer array*. Physical Review A **110**, 053518 (2024). (Cited on page **23**)

[148] S. D. Leseleuc de Kerouara. *Quantum simulation of spin models with assembled arrays of Rydberg atoms*. Theses, Université Paris Saclay (COmUE) (2018). (Cited on pages **23** and **59**)

[149] P. Zupancic, P. M. Preiss, R. Ma, A. Lukin, M. Eric Tai, M. Rispoli, R. Islam, and M. Greiner. *Ultra-precise holographic beam shaping for microscopic quantum control*. Optics Express **24**, 13881 (2016). (Cited on page **23**)

[150] S. Snigirev, A. J. Park, A. Heinz, I. Bloch, and S. Blatt. *Fast and dense magneto-optical traps for strontium*. Physical Review A **99**, 063421 (2019). (Cited on page **24**)

[151] R. Finkelstein, R. B.-S. Tsai, X. Sun, P. Scholl, S. Direkci, T. Gefen, J. Choi, A. L. Shaw, and M. Endres. *Universal quantum operations and ancilla-based read-out for tweezer clocks*. Nature **634**, 321–327 (2024). (Cited on page **27**)

[152] N. Hinkley, J. A. Sherman, N. B. Phillips, M. Schioppo, N. D. Lemke, K. Beloy, M. Pizzocaro, C. W. Oates, and A. D. Ludlow. *An Atomic Clock with* 10^{-18} *Instability*. Science **341**, 1215–1218 (2013). (Cited on page **27**)

[153] E. M. Kessler, P. Kómár, M. Bishof, L. Jiang, A. S. Sørensen, J. Ye, and M. D. Lukin. *Heisenberg-Limited Atom Clocks Based on Entangled Qubits*. Physical Review Letters **112**, 190403 (2014). (Cited on page **27**)

[154] S. P. Carman, J. Rudolph, B. E. Garber, M. J. Van De Graaff, H. Swan, Y. Jiang, M. Nantel, M. Abe, R. L. Barcklay, and J. M. Hogan. *Collinear Three-Photon Excitation of a Strongly Forbidden Optical Clock Transition*. Physical Review X **15**, 031051 (2025). (Cited on pages **27**, **32**, and **37**)

[155] J. He, B. Pasquiou, R. G. Escudero, S. Zhou, M. Borkowski, and F. Schreck. *Coherent three-photon excitation of the strontium clock transition*. Physical Review Research **7**, L012050 (2025). (Cited on page **27**)

[156] T. Zanon-Willette, F. Impens, E. Arimondo, D. Wilkowski, A. V. Taichenachev, and V. I. Yudin. *Engineering quantum control with optical transitions induced by twisted light fields*. Physical Review A **108**, 043513 (2023). (Cited on page **28**)

[157] A. Taichenachev, V. Yudin, C. Oates, C. Hoyt, Z. Barber, and L. Hollberg. *Magnetic Field-Induced Spectroscopy of Forbidden Optical Transitions with Application to Lattice-Based Optical Atomic Clocks*. Physical Review Letters **96**, 083001 (2006). (Cited on page **28**)

[158] E. D. Black. *An introduction to Pound–Drever–Hall laser frequency stabilization*. American Journal of Physics **69**, 79–87 (2001). (Cited on pages **28** and **57**)

[159] A. Prehn, R. Glöckner, G. Rempe, and M. Zeppenfeld. *Fast, precise, and widely tunable frequency control of an optical parametric oscillator referenced to a frequency comb*. Review of Scientific Instruments **88**, 033101 (2017). (Cited on page **29**)

[160] W. Gunton, M. Semczuk, and K. W. Madison. *Method for independent and continuous tuning of N lasers phase-locked to the same frequency comb*. Optics Letters **40**, 4372 (2015). (Cited on page **29**)

[161] J. Jost, J. Hall, and J. Ye. *Continuously tunable, precise, single frequency optical signal generator*. Optics Express **10**, 515 (2002). (Cited on page **29**)

[162] T. Fordell, A. E. Wallin, T. Lindvall, M. Vainio, and M. Merimaa. *Frequency-comb-referenced tunable diode laser spectroscopy and laser stabilization applied to laser cooling*. Applied Optics **53**, 7476 (2014). (Cited on page **29**)

[163] T. Sala, D. Gatti, A. Gambetta, N. Coluccelli, G. Galzerano, P. Laporta, and M. Marangoni. *Wide-bandwidth phase lock between a CW laser and a frequency comb based on a feed-forward configuration*. Optics Letters **37**, 2592 (2012). (Cited on page **29**)

[164] R. Holzwarth, Th. Udem, T. W. Hänsch, J. C. Knight, W. J. Wadsworth, and P. St. J. Russell. *Optical Frequency Synthesizer for Precision Spectroscopy*. Physical Review Letters **85**, 2264–2267 (2000). (Cited on page **29**)

[165] R. B.-S. Tsai, X. Sun, A. L. Shaw, R. Finkelstein, and M. Endres. *Benchmarking and Fidelity Response Theory of High-Fidelity Rydberg Entangling Gates*. PRX Quantum **6**, 010331 (2025). (Cited on pages **35**, **39**, **113**, and **119**)

[166] B. E. King. *Angular Momentum Coupling and Rabi Frequencies for Simple Atomic Transitions*. arXiv:0804.4528 (2008). (Cited on pages **35** and **124**)

[167] E. Rubiola. *Phase Noise and Frequency Stability in Oscillators*. Cambridge University Press (2008). ISBN 978-0-521-88677-2 978-0-521-15328-7 978-0-511-81279-8. (Cited on page **39**)

[168] G. Unnikrishnan, P. Ilzhöfer, A. Scholz, C. Hölzl, A. Götzelmann, R. K. Gupta, J. Zhao, J. Krauter, S. Weber, N. Makki, H. P. Büchler, T. Pfau, and F. Meinert. *Coherent Control of the Fine-Structure Qubit in a Single Alkaline-Earth Atom*. Physical Review Letters **132**, 150606 (2024). (Cited on pages **41** and **45**)

[169] B. Richards and E. Wolf. *Electromagnetic diffraction in optical systems, II. structure of the image field in an aplanatic system*. Proc. R. Soc. Lond. **253**, 358–379 (1959). (Cited on page **45**)

[170] S. Veroni, A. Paler, and G. Giudice. *Universal Quantum Computation via Scalable Measurement-Free Error Correction*. PRX Quantum **6**, 040337 (2025). (Cited on pages **50** and **104**)

[171] T. Denecker, Y. T. Chew, O. Guillemant, G. Watanabe, T. Tomita, K. Ohmori, and S. De Léséleuc. *Measurement and feedforward correction of the fast phase noise of lasers*. Physical Review A **111**, 042614 (2025). (Cited on pages **51**, **57**, **120**, and **121**)

[172] PyRPL documentation (2025). Website at https://pyrpl.readthedocs.io/en/latest/index.html. (Cited on page **53**)

[173] Y.-X. Chao, Z.-X. Hua, X.-H. Liang, Z.-P. Yue, C. Jia, L. You, and M. K. Tey. *Robust suppression of high-frequency laser phase noise by adaptive Pound-Drever-Hall feedforward*. Physical Review Applied **23**, L011005 (2025). (Cited on pages **56** and **120**)

[174] N. Friis, G. Vitagliano, M. Malik, and M. Huber. *Entanglement certification from theory to experiment*. Nature Reviews Physics **1**, 72–87 (2018). (Cited on page **58**)

[175] M. Boll, T. A. Hilker, G. Salomon, A. Omran, J. Nespolo, L. Pollet, I. Bloch, and C. Gross. *Spin- and density-resolved microscopy of antiferromagnetic correlations in Fermi-Hubbard chains*. Science **353**, 1257–1260 (2016). (Cited on page **59**)

[176] C. Zhang, V. W. Scarola, and S. Das Sarma. *Initializing a quantum register from Mott-insulator states in optical lattices*. Physical Review A **75**, 060301 (2007). (Cited on page **59**)

[177] D. Greif, M. F. Parsons, A. Mazurenko, C. S. Chiu, S. Blatt, F. Huber, G. Ji, and M. Greiner. *Site-resolved imaging of a fermionic Mott insulator*. Science **351**, 953–957 (2016). (Cited on page **59**)

[178] G. Bornet, G. Emperauger, C. Chen, B. Ye, M. Block, M. Bintz, J. A. Boyd, D. Barredo, T. Comparin, F. Mezzacapo, T. Roscilde, T. Lahaye, N. Y. Yao, and A. Browaeys. *Scalable spin squeezing in a dipolar Rydberg atom array*. Nature **621**, 728–733 (2023). (Cited on page **59**)

[179] L.-M. Steinert. *Spatially tunable spin interactions with Rydberg atoms in optical tweezers*. Ph.D. thesis, Universität Tübingen (2024). (Cited on pages **59** and **82**)

[180] H. Labuhn, D. Barredo, S. Ravets, S. De Léséleuc, T. Macrì, T. Lahaye, and A. Browaeys. *Tunable two-dimensional arrays of single Rydberg atoms for realizing quantum Ising models*. Nature **534**, 667–670 (2016). (Cited on page **59**)

[181] T. Wilk, A. Gaëtan, C. Evellin, J. Wolters, Y. Miroshnychenko, P. Grangier, and A. Browaeys. *Entanglement of Two Individual Neutral Atoms Using Rydberg Blockade*. Physical Review Letters **104**, 010502 (2010). (Cited on page **59**)

[182] R. Tao, M. Ammenwerth, F. Gyger, I. Bloch, and J. Zeiher. *High-Fidelity Detection of Large-Scale Atom Arrays in an Optical Lattice*. Physical Review Letters **133**, 013401 (2024). (Cited on pages **60** and **71**)

[183] Private communication (2023). Similar results were also reported by the strontium experiments of the Caltech, JILA and Columbia groups. (Cited on page **60**)

[184] D. Wei. *Microscopy of spin hydrodynamics and cooperative light scattering in atomic Hubbard systems*. Ph.D. thesis, Ludwig-Maximilians-Universität München (2023). (Cited on pages **67**, **71**, and **86**)

[185] J. Koepsell. *Quantum simulation of doped two-dimensional Mott insulators*. Ph.D. thesis, Ludwig-Maximilians-Universität München (2021). (Cited on page **78**)

[186] M. Martinez-Dorantes, W. Alt, J. Gallego, S. Ghosh, L. Ratschbacher, and D. Meschede. *State-dependent fluorescence of neutral atoms in optical potentials*. Physical Review A **97**, 023410 (2018). (Cited on page **80**)

[187] T. Hilker. *Spin-resolved microscopy of strongly correlated fermionic many-body states*. Ph.D. thesis, Ludwig-Maximilians-Universität München (2017). (Cited on page **80**)

[188] J. Trautmann, D. Yankelev, V. Klüsener, A. J. Park, I. Bloch, and S. Blatt. $^1S_0 - {}^3P_2$ *magnetic quadrupole transition in neutral strontium*. Physical Review Research **5**, 013219 (2023). (Cited on pages **80** and **82**)

[189] S. Wili, T. Esslinger, and K. Viebahn. *An accordion superlattice for controlling atom separation in optical potentials*. New Journal of Physics **25**, 033037 (2023). (Cited on page **82**)

[190] H. Zhang, Y. Miao, Y. Cao, X. Liang, M. Jing, and L. Zhang. *Tunable accordion optical lattice for precise control of Rydberg atom interactions in magneto-optical traps (MOTs)*. Review of Scientific Instruments **96**, 033201 (2025). (Cited on page **82**)

[191] H. Kim, W. Lee, H.-g. Lee, H. Jo, Y. Song, and J. Ahn. *In situ single-atom array synthesis using dynamic holographic optical tweezers*. Nature Communications **7**, 13317 (2016). (Cited on pages **82** and **101**)

[192] R. Lin, H.-S. Zhong, Y. Li, Z.-R. Zhao, L.-T. Zheng, T.-R. Hu, H.-M. Wu, Z. Wu, W.-J. Ma, Y. Gao, Y.-K. Zhu, Z.-F. Su, W.-L. Ouyang, Y.-C. Zhang, J. Rui, M.-C. Chen, C.-Y. Lu, and J.-W. Pan. *AI-Enabled Parallel Assembly of Thousands of Defect-Free Neutral Atom Arrays*. Physical Review Letters **135**, 060602 (2025). (Cited on pages **82** and **101**)

[193] I. Knottnerus, Y. C. Tseng, A. Urech, R. Spreeuw, and F. Schreck. *Parallel assembly of neutral atom arrays with an SLM using linear phase interpolation*. SciPost Physics **19**, 118 (2025). (Cited on pages **82**, **95**, and **101**)

[194] H. Kim, M. Kim, W. Lee, and J. Ahn. *Gerchberg-Saxton algorithm for fast and efficient atom rearrangement in optical tweezer traps*. Optics Express **27**, 2184 (2019). (Cited on page **82**)

[195] M. Ammenwerth, H. Timme, V. Giardini, R. Tao, F. Gyger, O. Lib, D. Berndt, D. Kourkoulos, T. Rom, I. Bloch, and J. Zeiher. *Dynamical spatial light modulation in the ultraviolet spectral range*. Physical Review Applied **24**, 034031 (2025). (Cited on pages **82** and **96**)

[196] A. Impertro, S. Karch, J. F. Wienand, S. Huh, C. Schweizer, I. Bloch, and M. Aidelsburger. *Local Readout and Control of Current and Kinetic Energy Operators in Optical Lattices*. Physical Review Letters **133**, 063401 (2024). (Cited on page **85**)

[197] A. La Rooij, C. Ulm, E. Haller, and S. Kuhr. *A comparative study of deconvolution techniques for quantum-gas microscope images*. New Journal of Physics **25**, 083036 (2023). (Cited on page **85**)

[198] A. Impertro, J. F. Wienand, S. Häfele, H. Von Raven, S. Hubele, T. Klostermann, C. R. Cabrera, I. Bloch, and M. Aidelsburger. *An unsupervised deep learning algorithm for single-site reconstruction in quantum gas microscopes*. Communications Physics **6**, 166 (2023). (Cited on pages **85**, **86**, and **88**)

[199] L. Phuttitarn, B. M. Becker, R. Chinnarasu, T. M. Graham, and M. Saffman. *Enhanced measurement of neutral-atom qubits with machine learning*. Physical Review Applied **22**, 024011 (2024). (Cited on page **85**)

[200] L. R. B. Picard, M. J. Mark, F. Ferlaino, and R. Van Bijnen. *Deep learning-assisted classification of site-resolved quantum gas microscope images*. Measurement Science and Technology **31**, 025201 (2020). (Cited on pages **85** and **86**)

[201] O. Ronneberger, P. Fischer, and T. Brox. *U-Net: Convolutional Networks for Biomedical Image Segmentation*. arXiv:1505.04597 (2015). (Cited on page **86**)

[202] A. Géron. *Hands-On Machine Learning with Scikit-Learn, Keras, and TensorFlow*. (2022). ISBN 978-1-0981-2247-8. (Cited on page **86**)

[203] R. H. Dicke. *Coherence in Spontaneous Radiation Processes*. Physical Review **93**, 99–110 (1954). (Cited on pages **86** and **105**)

[204] P. Isola, J.-Y. Zhu, T. Zhou, and A. A. Efros. *Image-to-Image Translation with Conditional Adversarial Networks*. In *2017 IEEE Conference on Computer Vision and Pattern Recognition (CVPR)*, pages 5967–5976, Honolulu, HI (2017). IEEE. ISBN 978-1-5386-0457-1. (Cited on pages **88** and **94**)

[205] J.-Y. Zhu, T. Park, P. Isola, and A. A. Efros. *Unpaired Image-to-Image Translation using Cycle-Consistent Adversarial Networks*. arXiv:1703.10593 (2017). (Cited on pages **88** and **94**)

[206] T. Park, A. A. Efros, R. Zhang, and J.-Y. Zhu. *Contrastive Learning for Unpaired Image-to-Image Translation*. arXiv:2007.15651 (2020). (Cited on pages **88** and **94**)

[207] D. Schäffner, T. Preuschoff, S. Ristok, L. Brozio, M. Schlosser, H. Giessen, and G. Birkl. *Arrays of individually controllable optical tweezers based on 3D-printed microlens arrays*. Optics Express **28**, 8640 (2020). (Cited on page **95**)

[208] L. Pause, L. Sturm, M. Mittenbühler, S. Amann, T. Preuschoff, D. Schäffner, M. Schlosser, and G. Birkl. *Supercharged two-dimensional tweezer array with more than 1000 atomic qubits*. Optica **11**, 222 (2024). (Cited on page **95**)

[209] A. W. Young, S. Geller, W. J. Eckner, N. Schine, S. Glancy, E. Knill, and A. M. Kaufman. *An atomic boson sampler*. Nature **629**, 311–316 (2024). (Cited on pages **104** and **106**)

[210] S. J. Masson, J. P. Covey, S. Will, and A. Asenjo-Garcia. *Dicke Superradiance in Ordered Arrays of Multilevel Atoms*. PRX Quantum **5**, 010344 (2024). (Cited on page **104**)

[211] Z. Yan, J. Ho, Y.-H. Lu, S. J. Masson, A. Asenjo-Garcia, and D. M. Stamper-Kurn. *Superradiant and Subradiant Cavity Scattering by Atom Arrays*. Physical Review Letters **131**, 253603 (2023). (Cited on page **105**)

[212] S. J. Masson and A. Asenjo-Garcia. *Universality of Dicke superradiance in arrays of quantum emitters*. Nature Communications **13**, 2285 (2022). (Cited on page **105**)

[213] S. J. Masson, I. Ferrier-Barbut, L. A. Orozco, A. Browaeys, and A. Asenjo-Garcia. *Many-Body Signatures of Collective Decay in Atomic Chains*. Physical Review Letters **125**, 263601 (2020). (Cited on page **105**)

[214] J. Rui, D. Wei, A. Rubio-Abadal, S. Hollerith, J. Zeiher, D. M. Stamper-Kurn, C. Gross, and I. Bloch. *A subradiant optical mirror formed by a single structured atomic layer*. Nature **583**, 369–374 (2020). (Cited on page **105**)

[215] A. Heinz, A. J. Park, N. Šantić, J. Trautmann, S. G. Porsev, M. S. Safronova, I. Bloch, and S. Blatt. *State-Dependent Optical Lattices for the Strontium Optical Qubit*. Physical Review Letters **124**, 203201 (2020). (Cited on pages **106** and **124**)

[216] W. J. Eckner, T. L. Yelin, A. Cao, A. W. Young, N. D. Oppong, L. Pollet, and A. M. Kaufman. *Assembling a Bose-Hubbard superfluid from tweezer-controlled single atoms*. arXiv:2512.24374 (2025). (Cited on pages **106** and **107**)

[217] I. Bloch, J. Dalibard, and W. Zwerger. *Many-body physics with ultracold gases*. Reviews of Modern Physics **80**, 885–964 (2008). (Cited on page **107**)

[218] T. Hong, C. Cramer, W. Nagourney, and E. N. Fortson. *Optical Clocks Based on Ultranarrow Three-Photon Resonances in Alkaline Earth Atoms*. Physical Review Letters **94**, 050801 (2005). (Cited on pages **109** and **123**)

[219] F. Reiter and A. S. Sørensen. *Effective operator formalism for open quantum systems*. Physical Review A **85**, 032111 (2012). (Cited on page **110**)

[220] A. Pastore. *An introduction to Bootstrap for nuclear physics*. Journal of Physics G: Nuclear and Particle Physics **46**, 052001 (2019). (Cited on page **120**)

[221] M. Endo and T. R. Schibli. *Residual phase noise suppression for Pound-Drever-Hall cavity stabilization with an electro-optic modulator*. OSA Continuum **1**, 116 (2018). (Cited on page **120**)

[222] L. Li, W. Huie, N. Chen, B. DeMarco, and J. P. Covey. *Active Cancellation of Servo-Induced Noise on Stabilized Lasers via Feedforward*. Physical Review Applied **18**, 064005 (2022). (Cited on page **120**)

List of figures

Acknowledgements

I would like to take this opportunity to express my sincere gratitude to all those who supported and encouraged me throughout the completion of this thesis.

First of all, I would like to thank Immanuel Bloch and Johannes Zeiher for creating such an enthusiastic working atmosphere and for the great support during the last years and guidance during the construction of the new Strontium Rydberg Lab. I am grateful for the opportunity to join the group and deeply appreciate the freedom in setting new goals and planning new measurements in the team together. Finding pragmatic solutions to develop the lab further was a highly instructive and engaging experience. I have learned a lot in countless discussions, in particular with Johannes, and it was fascinating to brainstorm about new upgrades, the possibility of overcoming technical limitations or the feasibility of physical concepts.

Setting up a new lab is teamwork, and I am very grateful to Renhao Tao and Flavien Gyger, with whom I spent most of the time in the lab, for the very enjoyable, intriguing, and fruitful building phase. Building a new apparatus together was a rewarding experience, thanks to your enthusiasm, patience, and constant motivation.

In addition, I am very grateful to Hendrik Timme and Ohad Lib, who joined the team, for the data-taking together and your great motivation in advancing and running the experiment. Also, I am thankful to Shijia Sun, who joined the team recently, and brought some fresh energy. I am curious about the next upgrades and exciting results ahead.

Over the past years, our lab has benefited from the assistance of many bachelor's and master's students as well as interns and visitors, who joined the team. I would like to thank Aron Lloyd, Fabian Grübel, Alexandra Beikert, Maurice Zeuner, Niklas Zischka, Benedict Rücken, Taylan Firat as well as Efe Ersoy, Hannah Seabrook, Pranav Kulkarni, Jacopo de Santis, Elias Trapp, Esha Umbarkar, Mason Bates, Simon Fecherolle, Taylor Briggs, Yağiz Murat, and Veronica Giardini, and Vladislav Gavryusev for many valuable contributions to the experiment and the enjoyable lab work.

Constructing the lab benefited greatly from the invaluable work of our mechanical engineers - Anton Mayer, Milan Antic, Felix Friedrichs, and Thomas Haselbach. Thanks, Anton, for fixing all my drawings and all the pragmatic solutions you suggested. In addition, I want to thank the electrical engineers - Karsten Förster, Herbert Kästle, Olivia Mödl, Thomas Klink, and Stefan Hofinger - for all the essential electronic components, custom circuits, and help with electronic problems.

Furthermore, I am thankful to Kristina Schuldt, Veronica Seidl, Ildiko Kecskesi, and Doreen Seidl for their support with many organizational tasks and the planning of several group events, including the very pleasant and intriguing annual group retreat. In addition, I am thankful to Yulia Borozdina for support with many purchasing-related tasks and also to the purchasing and warehouse team at MPQ - Christoph Mey, Manuel Backe, Noah Glöckner, Christine Poeschko, Carina Steinkrebs, Michael Boyus, Katharina Pappas, and Cornelia Kreitmeier - for processing a countless number of packages, purchase orders, and repairs.

I would like to thank David Wei for providing the kernel-based lattice reconstruction algorithm and Jonas Winklmann for translating it from Python to C for improved performance. Also, I would like to thank Christopher Bülte, Si Wang, Hannah Lange, and Alexander Impertro for insightful discussions regarding machine-learning-based atom detection.

The great environment at MPQ, with a large number of new labs being set up, offers a very helpful support across all the different labs, and I would like to thank the entire group, in particular the MQV and FermiQP teams, for the regular exchange of equipment and many intriguing discussions.

This thesis would not have been possible without the assistance of numerous people, and I am very grateful for their support in its many forms. I had a great time and enjoyed working on our various projects together!

Finally, I want to thank my parents for their unconditional support and encouragement, and my friends for making the time out of the lab so enjoyable and fun!

Thank you all!